Modelling Tongue Mechanics

Yikun Wang

Supervised by:
Prof. Martyn Nash
Prof. Oliver Röhrle

A thesis submitted in partial fulfilment of the requirements for the degree of
Doctor of Philosophy in Bioengineering

Auckland Bioengineering Institute
University of Auckland
New Zealand

March 10, 2014

Abstract

Few studies have attempted to quantify the relative contributions of individual tongue muscles to the overall function of the tongue during swallowing, speech or respiration. The aim of this thesis is to analyse the multi-fibre mechanics of the tongue using an anatomically-realistic Finite Element (FE) tongue model. Outcomes of this thesis include new methods to investigate the underlying mechanisms of tongue muscle mechanics during various functional activities.

The FE model of the tongue was first applied to find the optimal motion sensor placement for electromagnetic articulography during tongue elongation and retraction based on a forward problem analysis. Two optimal criteria for selecting sensor arrays were proposed: (1) the largest displacements containing the most information and (2) the largest displacements in the anatomical axial and overall directions. The inverse problem method was adopted to derive the contractile state of muscles for given kinematic data and thus, test the quality of sensor placement. The results showed that, under the influence of machine-inherent noise, the first optimality criteria was superior to the second, and the average bias and coefficient of variation decreased with an increasing number of sensors from 2, 4 to 6. In a second study, the FE tongue model was applied to identify possible muscle activity patterns during propulsion of dry swallowing based on an extended inverse problem analysis and tagged-MRI data from the literature. The computational results suggested: (1) previous literature hypotheses lacked consideration of the heterogeneous orientation of the transversus muscle in the posterior region compared to the middle and anterior regions, and (2) co-contractions of the hyoglossus, mylohyoid, styloglossus and the anterior-middle part of the transversus resulted in the best match of tongue deformation during propulsion of dry swallowing when compared with the experimentally acquired strain data from the literature.

Two applications in this work demonstrate that the anatomically-realistic FE tongue model enables the quantitative study of muscular activities and geometric deformations of the tongue for various physiological activities. The future application of the FE model to broader areas, such as pathological tongue function or model-aided instrumentation design, is feasible.

Acknowledgments

The author wishes to express his gratitude to his supervisors, Prof. Martyn Nash and Jun.-Prof. Oliver Röhrle, who were abundantly helpful and offered invaluable assistance, support and guidance. Deepest gratitude also goes to the members of the supervisory committee, Prof. Jules Kieser from the University of Otago and Dr. Kylie Foster from Massey University. This research would not have been successful without Prof. Kieser's knowledge in tongue anatomy and swallowing mechanism, and his assistance in the human tissue dissection, and without the assistance of Prof. Foster to provide access to the electromagnetic articulograph. Special thanks also go to Prof. Poul Nielsen and late Andrew Pullan from the Auckland Bioengineering Institute, the graduate students, Hongyan Yao from Massey University, Prasad Babarenda Gamage, Shannon Li and Vicky Wang from the Auckland Bioengineering Institute, Thomas Heidlauf and Michael Sprenger from University of Stuttgart for sharing literature and invaluable assistance. The author would also like to acknowledge the financial support from the Auckland Bioengineering Institute and Ministry for Science and Innovation for the duration of his PhD study.

Lastly, the author wishes to thank his family for his upbringing in a different language, their understanding and endless love through the duration of his PhD research.

千言万语的感谢难以回报家人对我的博士研究期间的支持。我希望将此文献给我挚爱的父亲王斐和母亲冯跃华。他们在背后的默默支持是我前进的动力，为了论文和计算，四年中我很少能有机会回家看望他们，担当起一个儿子的责任，心中甚感愧疚。我要感谢我的妻子罗佳，没有她的体谅、包容和支持，相信这年年的博士生生活将是很不一样的光景。我也将此文献给我的女儿王嘉怡。我博士研究期间最好的结果就是在即将完成论文之际迎接女儿来到这个世界上。

Contents

List of Figures

List of Tables

THE UNIVERSITY OF AUCKLAND
SCHOOL OF GRADUATE STUDIES

Co-Authorship Form

Graduate Centre
ClockTower – East Wing
22 Princes Street, Auckland
Phone: +64 9 373 7599 ext 81321
Fax: +64 9 373 7610
Email: postgraduate@auckland.ac.nz
www.postgrad.auckland.ac.nz

This form is to accompany the submission of any PhD that contains research reported in published or unpublished co-authored work. **Please include one copy of this form for each co-authored work.** Completed forms should be included in all copies of your thesis submitted for examination and library deposit (including digital deposit), following your thesis Acknowledgements.

Please indicate the chapter/section/pages of this thesis that are extracted from a co-authored work and give the title and publication details or details of submission of the co-authored work.

Chapter 5 of this thesis was based on the following publication:

Wang, Y. K., Nash, M. P., Pullan, A. J., Kieser, J. A., and Röhrle, O. Model-based identification of motion sensor placement for tracking retraction and elongation of the tongue. Biomechanics and Modeling in Mechanobiology, 12(2):383-399, 2013

Nature of contribution by PhD candidate	Identifying the necessity and scope of study, literature search and review, design the entire study and research, implementing computational experiments, interpreting the results, writing the manuscript.
Extent of contribution by PhD candidate (%)	70%

CO-AUTHORS

Name	Nature of Contribution
Martyn P. Nash	Reviewing the study, co-designing of the methology, supervision.
Andrew J. Pullan	Before he passed away, he initially co-designed the study and was involved in the supervision.
Jules A. Kieser	Clinical consultant identifying the necessity and scope of the study, identifying constraints, writing, supervision.
Oliver Röhrle	Identifying the necessity and scope of study, co-designing the entire study and research, interpreting the results, writing, supervision.

Certification by Co-Authors

The undersigned hereby certify that:

- the above statement correctly reflects the nature and extent of the PhD candidate's contribution to this work, and the nature of the contribution of each of the co-authors; and
- In cases where the PhD candidate was the lead author of the work that the candidate wrote the text.

Name	Signature	Date
Yikun Wang	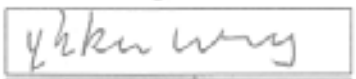	Click here 12/6/13
Martyn P. Nash		Click here 12/6/13
Andrew J. Pullan	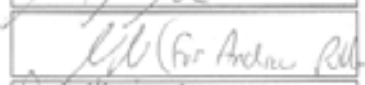	Click here 12/6/13
Jules A. Kieser		Click here 12.6.13
Oliver Röhrle	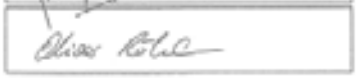	Click here 12.6.13

Last updated: 25 March 2013

Chapter 1

Introduction and overview

1.1 Motivation

1.1.1 Background

Swallowing and speech are two important activities in the everyday lives of humans. Swallowing is a complex vital process for the intake of food, while speech is the primary method of communication between individuals in human society. The human tongue is a highly complex muscular organ whose action is central to swallowing and speech.

The tongue is a muscular organ with fine motor skills consisting of of an interwoven series of muscle groups. The relationships between tongue anatomy, physiology, diet, and dental morphology are topics of significant interest to speech pathologists, ear, nose and throat surgeons, and dentists. The activities of the tongue comprise an intricately orchestrated series of shape changes that contain and then propel the food bolus from the incisor region of the mouth to the pharynx [Nicosia and Robbins, 2001, Felton et al., 2007]. However, abnormal tongue function can result in a range of disorders such as swallowing difficulties (dysphagia), or sleep apnoea [Fujiu et al., 1995, Cheng et al., 2002, Oliven et al., 2007, Proffit et al., 2007]. In the case of human tongue movement disorders, difficulties in swallowing, for example, can cause sig-

nificant morbidity and mortality [Jennifer et al., 2000]. Abnormal tongue function is also a serious population health issue. According to Domenech and Kelly [1999], approximately 10 million Americans are evaluated each year with swallowing difficulties (dysphagia), and the prevalence of dysphagia may be as high as 22% in members of the population aged over 50 [Howden, 2004]. Moreover, Volonte et al. [2002] reported that 20% to 40% of patients with Parkinson's disease have symptoms of swallowing difficulties, whilst lacking awareness of the cause.

The normal and abnormal behaviours of the tongue during swallowing and speech production are still not fully understood. In order to understand the tongue's various shape changes in relation to the underlying muscular activities, it is necessary to identify the functional roles of individual muscles in both normal and abnormal conditions. A considerable amount of experimental effort has previously been dedicated to better understand the correlation between the movement of the tongue and its function during various physiological activities. However, current technological methods are limited in monitoring muscular activity while simultaneously tracking the full motion of the tongue. A biophysical computational model of the tongue is required to understand the relationship between tongue movement and its fibrous structure.

1.1.2 Biomechanics

Biomechanics is the study of the structure and function of biological systems such as those of humans, animals, plants or organs, by means of mechanical engineering. The first biomechanical investigations were conducted in the era of Leonardo da Vinci (1452 - 1519), who employed standard engineering principles to quantify the kinematic patterns of biological movement [Mason, 1962]. For the last 30 years, an increasing number of studies have adopted the principles of continuum mechanics to model and analyse the function of whole organs. This approach is commonly referred to as continuum biomechanics. In general, studies in continuum biomechanics have adopted the Finite Element Method (FEM) as the chosen numerical method to approximate the shape of the organ. The motion of each element (subdomain) is then calculated by defining material parameter values and rigorously complying to the physical laws of

motion (kinematic laws) to derive the overall movement of the entire organ.

Finite element modelling allows more accurate capture of the organ geometry. However, with an increasing number of geometric elements, the number of calculations increases, and thus, the computational costs. Recent advances in computational technologies provide new opportunities to analyse organ function by using complex mechanical models. With the dramatic development of computing hardware during the past decade, complex computations can be performed in a reasonable amount of time, and larger data sets can be handled and stored for post-processing. In addition, High Performance Computers (HPC) have become less expensive and have been extensively deployed in engineering research programmes. Parallel distributed computing on HPC platforms has accelerated the calculation speed for complex computing tasks that were not solvable in the past.

The tongue, as a muscular organ, can be studied by applying the principles of continuum biomechanics. As such, the tongue can be modelled using a finite element geometrical model with specific tissue properties, the movement of which is driven according to the physical law of motion. A geometric model of the tongue has to be developed based on anatomical data to fully incorporate geometric and structural features. To accurately simulate tongue deformation, the mechanical behaviour of muscle tissue needs to be experimentally tested on tongue tissue, or tissue with similar properties. A continuum model of the tongue based on anatomical data and experimentally derived tissue properties would allow the prediction of tongue deformation during various activities, thereby assisting others in analysing the correlation between muscular activities and motion or deformation.

1.2 Thesis objectives

The main aim of this thesis is to gain a better understanding between the fibrous muscle structure of the tongue and the mechanics of the tongue by developing a computational mechanical modelling framework. The main objective is divided into three separate goals:

1. To construct an anatomical-based finite element model of the tongue that can predict the deformation of the tongue by specifying the contractile state of tongue muscles and enable investigation of the relationship between structure and mechanical function of the tongue;

2. To investigate the envelopes of tongue motion caused by co-contraction of multiple muscle fibre families using the tongue model in a forward problem approach;

3. To develop a computational framework, in which experimental data can be used to predict the muscular activation states by using the mechanical tongue model in an inverse problem approach.

The first goal is to develop a FE tongue model which allows the prediction of tongue deformation by specifying the activation of either one muscle or of multiple muscle families simultaneously. The model-generated deformations associate directly with the anatomical structure and muscular activities. Thus, the tongue deformations can be interpreted as a consequence of the varying contractile properties of the spatially variable muscle fibre arrangements. In other words, the modelling procedure idealizes the tongue mechanics as a ”function” which outputs the kinematics of the tongue, i.e. strain and displacement, once the contractile properties of the various tongue muscles are specified.

This type of biophysical modelling framework will provide new means to predict tongue deformation and analyse the envelopes of the tongue over varying contractile states of the tongue muscles. This will provide useful new information, such as the most sensitive geometric points on the tongue envelope in a particular deformation state. Such insights will assist experimentalists to better capture tongue surface motion, for example, using electromagnetic articulography.

On the other hand, if the characteristics of tongue motion have been experimentally captured, they can be fed back into the model to quantitatively estimate the state of muscular activities in an inverse problem approach.

The third goal is to develop a computational framework to quantitatively derive mechanical parameters of the tongue, i.e. muscle contractile properties (muscular activities), using an anatomically-realistic tongue model in combination with experimentally collected kinematic data, i.e. displacement or strain. The computational model is aimed to be applied to state-of-the-art tongue research in two different ways:

- Firstly, the model is applied to the material point displacement tracking system, for example, electromagnetic articulography (EMA system) in oral research. Thereby, the tongue model is first used in a forward problem approach to enhance the reliability of the material point displacement tracking system (e.g. EMA system) by finding the optimized motion sensor placement. The optimized sensor placement design will improve the experimentally acquired motion information, resulting in a more accurate inverse calculation of muscle activation patterns.

- Secondly, the model is used in an inverse problem approach to derive muscular activity patterns based on reported strain values from tagged-MRI. This will help to (1) verify existing hypotheses in the literature related to the mechanics of tongue propulsion in the condition of dry swallowing, and (2) to explore hidden muscular activities that experimentalists may not have previously identified.

1.3 State of the art in tongue research

A group of muscular organs from various animals, such as the tongue of humans and the appendages of the cephalopod, share some common mechanical and structural features, i.e. in that the tissues of these organs can perform large deformations without any skeletal support, depending only on the fibrous arrangements of the relevant tissues [Smith and Kier, 1989].

The human tongue consists of many muscular fibrous groups. The complex arrangements of multiple muscular families enable the tongue to achieve various deformations for the ingestion of food and in speech production. The ability to selectively and independently activate the different muscle fibre groups provides the basis for the complex movements of the tongue. Several clinical studies provide evidence that the dysfunction of single muscle fibre groups can be linked to diseases such as dysphagia [Fujiu et al., 1995], or sleep apnoea [Oliven et al., 2007, Proffit et al., 2007].

A better understanding of the principles underlying the activation of muscle fibre groups during specific tasks would provide a significant step forward in the analysis and treatment of diseases associated with unusual tongue movements. Within this section, previous experimental and modelling approaches which aimed to improve the understanding of tongue mechanics will firstly be reviewed; and secondly, the limitations and disadvantages of these approaches will be addressed.

1.3.1 Imaging of tongue motion

Imaging techniques, including X-ray based imaging, ultrasound imaging and magnetic resonance imaging (MRI) have been used to identify the shape or the internal motion of muscular organs. In oral related research, those imaging techniques have often been used to identify the movement of the tongue during activities such as swallowing and speech. The motion from the image data has commonly been interpreted as a consequence of muscular activities based on empirical knowledge in anatomy.

X-ray imaging technique

The X-ray technique was initially applied to studies of tongue shapes in early oral research. Kent [1972], Kent and Moll [1972] used 2D X-ray images to diagnose speech production under abnormal conditions. Lindblom et al. [2002] applied X-ray techniques to understand the motor control in tongue muscles. Itoh et al. [1980] used an X-ray micro-beam technique to capture

a cluster of surface points movements of the lip, tongue tip and velum for diagnosing patients with speech impairments. Cineradiographic techniques have also been widely used to study the intra-oral movements, for instance, Perkell [1969] and Bothorel et al. [1986] applied these methods to the study of speech production, Barbiera et al. [2002] studied the swallowing of 220 patients.

Ultrasound imaging technique

Ultrasound imaging is another inexpensive method for ascertaining the tongue shape in a variety of situations. For instance, Sonies et al. [1981] and Steele and Van Lieshout [1986] employed the ultrasound imaging technique to observe tongue movements in speech on a 2D plane. Later, Stone [1990] combined X-ray beams with ultrasound imaging and additional assistance of a geometrical tongue model to reveal the dynamic 3D motion of the tongue including changes to its surface. By using ultrasound imaging, Peng et al. [2000] derived the tongue's largest displacement point to be on the mid-sagittal plane during the process of swallowing.

Magnetic Resonance Imaging

Several studies have attempted to directly visualize aspects of tongue movement by means of MRI. Various types and configurations of MRI provide the opportunity to explore the geometrical, structural and kinematic information pertaining to the tongue in various physiological tasks. One of the most fundamental applications of MRI in the study of the tongue is to outline its geometric shape. Badin et al. [2002] used digitized data from a stack of head sagittal MR images to reconstruct 3D geometric shapes of the tongue, lips and face under relaxed conditions.. They creatively applied a series of linear articulators to simulate the possible underlying muscle activities of the tongue's 3D geometric shape. Through the adjustment of the linear articulators, they aimed to reproduce the consequential deformation of the geometric tongue shape. Baer et al. [1991], Narayanan et al. [1997], Ong and Stone [1998] and Honda [1996] have all explored the tongue shapes in speech productions using MRI. Stone et al. [2001, 2004]

reconstructed the position of the deformed shape of the tongue during the production of the syllable |k| through MRI scanning. Later, Narayanan et al. [2004] proposed a sequence (spiral k-space acquisitions with a low flip-angle gradient echo pulse sequence) with an acquisition rate of 89 images per second and reconstruction rates of 20 to 24 images per second, which brought about the possibility for reconstructing tongue movements in speech production. Apart from reproducing the outer shape of the tongue by standard MRI, diffusion-based MRIs have been used to image the interior muscular structures within the tongue [Wedeen et al., 2001, Gilbert et al., 2006].

Standard MRI has a very limited ability to capture the internal movement of tissue. Tagged-MRI is used to quantitatively record the internal motion of the tissue through tracking a grid of signal saturation planes ("tags") in the images. For instance, Napadow et al. [1999a,b], Felton et al. [2007] studied the movement of the tongue in the cases of swallowing and other simple functional tasks, such as bending or elongating. Based on the empirical knowledge of anatomy, they attempted to explain the causes of the deformation driven by muscular contractions. The fibrous arrangement of the tongue muscles (i.e. orientation and distribution) varies spatially, resulting in heterogeneous deformation patterns as shown using strain mapping. Based on these findings, a series of activation patterns of tongue muscles during oral activities such as swallowing have been proposed.

Limitations of imaging techniques in tongue research

Imaging techniques, such as X-ray, ultrasound and MRI, provide visual information with regards to tissue movement in a series of 2D image planes. Although X-ray based imaging techniques may provide a cost effective method of imaging, the risk of exposing the subject to harmful radiation cannot be ignored. In order to collect sufficient data to reconstruct a full 3D view, the subject has to maintain a desired tongue configuration for a prolonged amount of time, or has to attend several repeated scans, which further extends the time of radiation exposure [Stevens, 2000]. A longer acquisition time is needed during ultrasound imaging and MRI to achieve higher image resolution. This may result in an uncomfortable experience for

the subjects, which may impact the quality of the collected data.

X-ray and MRI imaging are limited in capturing swift movements occurring within a very short space of time. Hence, reconstruction of the tongue's 3D motion based on the image data becomes very challenging. The experimental studies of Napadow et al. [1999a,b] and Felton et al. [2007] demonstrated that the derivation of quantitative interior motion information on a single imaging plane is feasible through a visualization technique called tagged MRI. A major limitation of this method is that it is mainly an analogue analysis on single slice images. A further verification of the results from tagged MRI from a 3D perspective would be necessary; however, this remains challenging. Furthermore, existing imaging techniques are unable to provide direct evidence of the link between muscular contraction and motion.

1.3.2 EMG, EMA and contact pressure measurement

EMG studies of tongue muscular activity

A muscle contraction (activation) is reflected in a change of the electrical activity within the skeletal muscle. Electromyography (EMG) provides a reliably measurement technique to record the electric activity in skeletal muscles. Two types of EMG techniques are widely used in experiments, namely, surface EMG and intramuscular (needle and fine-wire) EMG. Surface EMG is a non-invasive way to measure muscle activity on the outer surface, whereas intramuscular EMG is an invasive measurement method in which the probe needle penetrates the tissue to reach the target muscle. Since the tongue comprises a complex 3D fibrous structure, measurements from surface EMG only provide limited information with respect to multiple muscles of the tongue. Therefore, intramuscular EMG is more suitable for studying the tongue. However, this must be weighed up against the invasive nature of the measurements.

in-vivo measurements have been conducted to analyse the electrical activity of tongue muscles in human subjects, such as Honda and Alfonsao [1983] and Baer et al. [1988]. Most EMG experiments in the study of the tongue have been conducted on animal subjects (e.g. pig). Kay-

alioglu et al. [2007b] and Liu et al. [2007] measured the comprehensive pattern of the muscular activities of a pig's tongue during swallowing. They concluded that the deformed configurations of the tongue at most stages of swallowing were achieved through activation of multiple muscles.

EMA studies for tracking tongue movement

The electromagnetic articulography (EMA) is a tracking system that uses coils as motion sensors placed in the field of an electromagnetic transmitter. A standard EMA system is able to simultaneously record a cluster of sensor trajectories. By placing the sensors on the desired tissue surface, i.e. the facial area or the tongue dorsum, the movements of the sensors can be interpreted as the motion of the material points on the tongue surface. One major EMA application is the analysis of tongue motion during normal and impaired speech [Goozee et al., 2003, Lee et al., 2006, Li et al., 2010]. Murdoch and Goozée [2003] applied EMA to study the tongue movements of children with dysarthria following severe traumatic brain injury (TBI); Cheng et al. [2009] introduced a general EMA measurement protocol to identify abnormal motion of the tongue. The recorded spatial motion from EMA was used to evaluate malfunctioning of the tongue muscles.

Ideally, spatial motion data of the entire vocal tract area is considered when studying tongue motion during speech production. To achieve this goal, there is a recent trend in research to combine EMA with other measurement technologies, e.g. imaging techniques, to gain a more comprehensive view of tongue motion. Engwall [2003] combined MRI, EMA, electropalatography (EMP) data and geometrical tongue modelling (outer shape of the tongue) to reproduce deformed configurations of the tongue during the production of vowels and consonants. In Engwall [2003]'s study, the sensor trajectory from EMA was used to correct the digitised contour lines from MR images, and the model predictions were verified using pressure array measurements. Later, Aron et al. [2006] adopted a similar method of coupling EMA with ultrasound imaging techniques, to study the 3D surface of the tongue. For the first time in oral research, Aron et al. [2006] used ultrasound images to reproduce the tongue's geometric contour, and

subsequently, corrected the tongue shape near the apex using EMA recorded data. Thus, the tongue curve could be interpolated to match the best tongue contour and the recorded EMA spatial data. Aron et al. [2006]'s study provided an interpolation-based approximation of the tongue surface contour. As such, the proposed method offers an opportunity to construct the full 3D tongue surface with a cluster of 3D spatial points and incomplete image data, such that the analysis of the surface variations of the entire tongue in various phonetic tasks becomes possible.

Contact pressure measurements

While most attention in oral research is on the direct measurement of tongue motion, a few studies have analysed tongue function indirectly through the measurement of intra-oral pressure points using an array of pressure sensors [Ono et al., 2004, Steele and Van Lieshout, 2008, Kieser et al., 2008, Kennedy et al., 2010]. The tongue has significant interactions with the surrounding oral structures during swallowing. Therefore, these interactions, e.g. contact pressures, of the tongue can be interpreted as a reflection of the tongue movement during those activities. One primary interest in measuring the tongue-upper palate contact pressure has been the functional role of the tongue during the swallowing process. Ono et al. [2004] firstly outlined a contact pattern of the tongue during swallowing in which the tongue touches the upper palate from anterior to posterior. Kieser et al. [2008] and Kennedy et al. [2010] verified this observation in the case of swallowing water.

Limitations of EMA, EMG and contact measurement

EMA allows for tracking the movements of true material points on the tongue dorsum. However, only the trajectories of a limited number of sensor positions in a certain time domain are commonly collected. The sensors are hard-wired to the signal receiver. This set-up adds more challenges to deploy more sensors in the subject's oral cavity, which also give subjects very un-comfortable experiences and therefore influence the quality of experimental data. As a re-

sult, only a cluster of point movements are generally available, which may not provide enough information to understand the 3D behaviour. Similar disadvantages apply to contact measurements on the tongue-upper palate interaction. The pressure sensor array-based measurement device provides a set of discrete 2D measurement points of the contact area between the tongue and bony structures (upper palate). Contact pressure measurements merely provide partial kinematic measurements which cannot fully explain the functional roles of tongue muscles in specific events. EMG is commonly used to record electrical activities of muscles for improved understanding of the muscular contractile properties. However, EMG requires the pinpointing of target muscles in an invasive way. The tongue's limited visibility, relatively small size and complex interior structure make it almost impossible to accurately locate individual muscles, especially for the interwoven intrinsic fibres, e.g., styloglossus, verticalis, transversus muscle fibre groups.

Another major limitation of most experimental studies is the lack of an effective way of combining all collected experimental measurements to present direct evidence of the muscular activation patterns corresponding to various tongue shapes. Most of the analysis and interpretations of the experimental data have drawn on the knowledge and experience of individual researchers. Hence, conclusions based on experimental information from empirical analyses may be subjective, and very possibly, inaccurate. Thus, a quantitative analysis, incorporating data from different measurement techniques, is much desired to draw more accurate conclusions.

The selection of sensor locations in EMA is a challenging task. It requires careful sensor placement to capture the features of tongue motion, and in some cases, this motion data need to reflect the underlying muscular activity.

1.3.3 Modelling tongue mechanics

Previous tongue models

Mathematical modelling of tongue biomechanics provides a quantitative description of tongue movement. From a modelling point of view, the tongue is generally treated as elastic continuum governed by the physical laws of motion.

One of the first computerised tongue models was developed by Kakita and Fujimura [1977], who adopted the finite element technique to outline the general shape of the tongue with linear elements. Kakita and Fujimura [1977] accounted already for the role of fibres in tongue mechanics, and coupled the geometric model with fibres from different muscular groups. The local fibre contractile stress within the tongue model was evaluated with the fibre direction. The contractile stress from various muscles were used to drive the deformation of the tongue model.

Payan et al. [1995] and Payan and Perrier [1997] modelled the 2D tongue shape on a mid-sagittal plane with the deformation of the tongue governed by the dynamical system equations. In Payan and Perrier's model, the mechanics of the tongue tissue was modelled as a system that relied on muscle fibre shortening or lengthening. The elastic contribution in the tissue was modelled using spatially varying Young's moduli, the values of which were influenced by the composition and the direction of the local fibres. The tongue model was activated using recruitment thresholds for each family of muscle fibres. The model was then manually adjusted for comparison with experimental data in which subjects were asked to pronounce a series of vowels. Payan and Perrier [1997]'s model approximated the tongue's behaviours in a variety of phonetic tasks from the perspective of treating the tongue as a mechanical actuator.

Wilhelms-Tricarico [1995] adopted a different approach in the development of a tongue model. Within Wilhelms-Tricarico [1995]'s study, the tongue was considered as a solid incompressible continuum with multiple embedded fibres. The tissue properties of the model were studied using continuum mechanics principles. The overall stress of the tongue tissue body was modelled

as a sum of stress contributions from multiple parts, including the elastic and viscous parts of the tissue and a sum of fibre active stresses which were influenced by fibre direction and scaled by a series of activation level parameters.

Later, Buchaillard et al. [2009] proposed a customized 3D tongue model with a geometry that was based on a variety of data sources, e.g. x-ray, computed tomography images and acoustic data. The interior fibrous structures from the visible human data set digitized by Wilhelms-Tricarico [1995] was morphologically mapped into the geometric shape to reproduce general features of fibre arrangement. A functional model of muscle force generation (i.e. λ-model of the equilibrium point hypothesis) was applied to drive the deformation of the tongue model.

Using a different approach, Napadow et al. [2002] proposed a simple 3D analogue model to investigate the mechanism of tongue bending. The deformation arising from tongue bending was analysed with regards to the structural fibrous arrangements, the material stiffness and the temperature in the oral cavity environment. It was verified that the primary cause of upward tongue bending was the co-contraction of several tightly compacted and interwoven muscles. The model of Napadow et al. [2002] simplified the geometry and the fibrous structure of the tongue. The acquisition of anatomical data requires large efforts in image-based digitization. Thus, the advantage of the methodology by [Napadow et al., 2002] is that, instead of reproducing the actual tissue deformation using an anatomically-based computational model, a simplified conceptual model with essential structural features (e.g. the fibrous arrangement) was adopted to analyse the structure-motion relationship of the tongue in a cost-effective manner.

Pelteret and Reddy [2012] coupled a FE model of the tongue with a neural-excitation model to study the relationship between tongue mechanics and neural control. In Pelteret and Reddy [2012]'s work, muscle contraction was simulated by an additional neural system model which was coupled with the contractile stress of the FE model. The input from the neural model replaced a simple constant scalar force which had been the most common approach in previous models. The neural controlling system was modelled as a time-dependent ordinary differential equation, simulating the frequency of the electrical impulse transmitted to the muscle. The model was used to investigate the importance of the genioglossus muscle's activation pattern

and neural signals in maintaining a particular tongue position. The research by Pelteret and Reddy [2012] improved the understanding of the relationship between the mechanical muscular actuator (tongue) and the neural system from a mathematical perspective.

Stavness et al. [2011] proposed another 3D modelling framework which coupled the upper palate, lower jaw and tongue in a dynamical system. They creatively considered the rigid body motion and the soft-hard tissue interaction, e.g. tongue-jaw motion, as two important parts of oral biomechanics. In their numerical solver (i.e. ArtiSynth software package), both motions were solved simultaneously. Hence, their approach made it possible to investigate the interactions between the tongue and surrounding oral structure.

Limitations of previous tongue models

Modelling of the tongue has largely aimed at reproducing the deformation of the tongue in a mathematical manner. Thereby, the tongue tissue (skeletal muscle) has most commonly been treated as a nonlinear material, and the tongue's material and geometric non-linearity have been represented by combining the principles of continuum mechanics with the FE method. Early models of the tongue lacked an accurate representation of the tongue's geometric and tissue material properties. For example, Kakita and Fujimura [1977] did not consider the nonlinear relationship between active stress and fibre stretch, and details of the passive effect of fibres in the overall stress-strain behaviour of the tissue were lacking. Payan et al. [1995], Payan and Perrier [1997] introduced a 2D dynamical model which is not able to capture the 3D deformation of the tongue, under volume preserving condition of the muscular tissue. The fibrous structure in the tongue model by Buchaillard et al. [2009] was morphologically mapped into a geometric shape. Such interior structure may not be an accurate representations of the fibre arrangement. For instance, as illustrated by Figure 1 in Buchaillard et al. [2009], the transversus and verticalis muscles were distributed throughout the entire tongue body and connect to the hyoid bone, which were imperfect representation of those intrinsic muscles. These approximate representation may cause issues when analysing any fibre-motions relationship with these two intrinsic muscles.

The geometry and fibre distribution used by Payan et al. [1995] and Payan and Perrier [1997]'s model lacked anatomical detail. In Payan et al. [1995] and in Payan and Perrier [1997]'s model, linear elasticity theory was used to model the tongue; however, the Young's modulus cannot account for nonlinear tissue properties. The mechanical framework for linear materials results in inaccurate predictions when modelling large tissue deformations, and thus, many studies in biomechanics have moved to the field of large deformation (finite elasticity theory). Most of the recently developed models, such as the models by Wilhelms-Tricarico [1995] and Pelteret and Reddy [2012], have adopted finite deformation theory to model the large deformations of the tongue. However, no experimental verification of the resulting predictions have been made. Further a clear linkage between computational models of the tongue and experimental data remains lacking.

In the modelling framework proposed by Stavness et al. [2011], the tissue mechanical properties were modelled as an incompressible hyperelastic material. Theoretically, when solving the dynamical system, coupling two conditions together implies an infinitely large stress wave velocity in the tissue body during the deformation process, which, however, is not numerically solvable [Kolsky, 1963]. To deal with this, they adopted the mixed u-p formulation by Hughes [2000] that introduces an artificial factor (damper). This additional factor might bring comparatively large error to the model prediction.

1.3.4 Justification of the objective of this research

Most tongue movement studies have provided empirical analyses based on experimental data. Conclusions based on empirical analyses may be inaccurate and unreliable due to limited experimental data or biased experience of individual researchers. Computational models of the tongue, which are based on anatomical data and comply to physical mechanical laws, provide an opportunity to quantify tongue deformation and draw more accurate conclusions for an improved understanding of tongue deformation in various cases. The key towards a better understanding of tongue deformation is to clarify the contractile properties of each tongue muscle fibre and derive its activation pattern for different configurations. Preferably, a me-

chanical model of the tongue, as an idealised organ system, allows the quantitative predictions of the interior mechanical changes for any given experimentally-measured data, e.g. strain or displacement, and reveals a structure-motion relationship of the tongue. From a mathematical point of view, muscle activity patterns are dependent variables which need to be derived by an inverse modelling approach.

1.4 Thesis structure

The thesis is structured as follows:

Chapter 2 presents the basic anatomy of the tongue from the muscular fibre to the whole organ level, and outlines its physiological behaviour in a variety of cases, e.g. swallowing and speech. The organisation of multiple muscular groups is presented; and the function of tongue muscles as reported in the literature is summarized. The information in Chapter 2 provides detail on tongue anatomy that help to define appropriate boundary conditions for modelling the tongue's exterior and interior structure and the tissue's mechanical behaviours.

Chapter 3 aims to clarify the theoretical foundation of the computational modelling of the tongue. The fundamentals of continuum mechanics and the implementation of the FE method are summarised.

Chapter 4 outlines the development of the FE model of the tongue. The construction of the geometrical model with internal fibre distribution and orientation is presented at the beginning of the chapter. Then, the fundamentals of soft tissue modelling, the passive mechanical behaviour of tongue tissue and the mathematical form of active stress are explained. The computational implementation is described based on the framework of the in-house software CMISS. Accurate modelling of the interaction between the tongue superior surface and the hard palate is critical to study the swallowing process. The penalty method of contact mechanics is introduced to model the mechanical interactions between the tongue and the hard palate.

Chapter 5 presents a model-based motion sensor placement optimization scheme for tracking

the tongue movement. This chapter aims to demonstrate an application of the tongue model in giving the recommendation of EMA sensor placements. The basic optimization principle and algorithm is described and the quality of the sensor placement scheme is tested through a standard parameter estimation procedure (inverse problem). The optimization scheme is applied to two specific cases, namely the elongation and the retraction of the tongue. The case studies endeavour to outline the potential conditions that may influence the reliability of motion tracking. These conditions include machine noise, the number of motion sensors and the mode of tongue deformation. The optimization procedure provides a methodology of model-aided instrumentation design and a possible non-invasive way of deriving muscular activity by using a computerised mechanical organ model in combination with kinematic information.

Chapter 6 introduces a MRI image-based inverse methodology for the reconstruction of tongue deformation and the estimation of its contractile properties. This application of the tongue model provides a way to enhance the interpretation of 2D tagged MRI image data in a more rigorous manner. Firstly, the methodology is adopted to analyse the accuracy of empirical conclusions related to muscular activities during propulsion previously reported in the literature. Secondly, a comprehensive testing of multiple muscle selections is presented. The application of the inverse methodology to multiple muscle groups requires a large number of calculations to be performed. Thus, methods and strategies for using a multi-core high performance computer are reviewed, and issues related to solving strategies of the FE system are discussed.

Chapter 7 concludes by summarising the significance of the presented modelling of the tongue, its applications, as well as current limitations. Future research on model validation and on the framework inverse problem are discussed.

Appendices consist of multiple supplementary materials related to previous chapters. First, the development of the tongue model customization is introduced. It starts with the digitizing process of MR images, and is followed by remodelling techniques and the underlying assumptions of the geometrical model, including customisation of the internal tissue structure and outer shape of the tongue. Secondly, a convergence analysis of the tongue model is given. Third, the numerical verification of various strategies to solve the contact mechanics problem of muscu-

lar activation is presented. Finally, a performance test of the inverse procedure for estimating the contractile properties using a muscle model is provided.

Chapter 2

Anatomy and mechanics of the tongue

2.1 The structure of the tongue

2.1.1 Anatomical position and coordinate system

Prior to describing the anatomical structure of the tongue, it is necessary to introduce the scientific notation to describe anatomical features. The scientific anatomical notation and terms for orientation aim to fully describe the anatomy of animals (humans) based on particular body locations and directions. Figure 2.1 illustrates the specific directional terms with respect to the human body.

2.1.2 Tongue anatomy

As illustrated in Figure 2.2, the tongue is located in the oral cavity and is covered by mucus on the tongue dorsum. The base of the anterior part of the tongue is attached to the mandible; the posterior-inferior part of the tongue is attached to the hyoid bone. The hyoid bone is not a fixed bony structure, but is rather floating with its own movement trajectories, for example, in deglutition [Kaneko, 1992, Yabunaka et al., 2011]. The movement of the tongue body, attached to the hyoid bone, is not spatially fixed. Instead, the tongue is a deformable body that connects

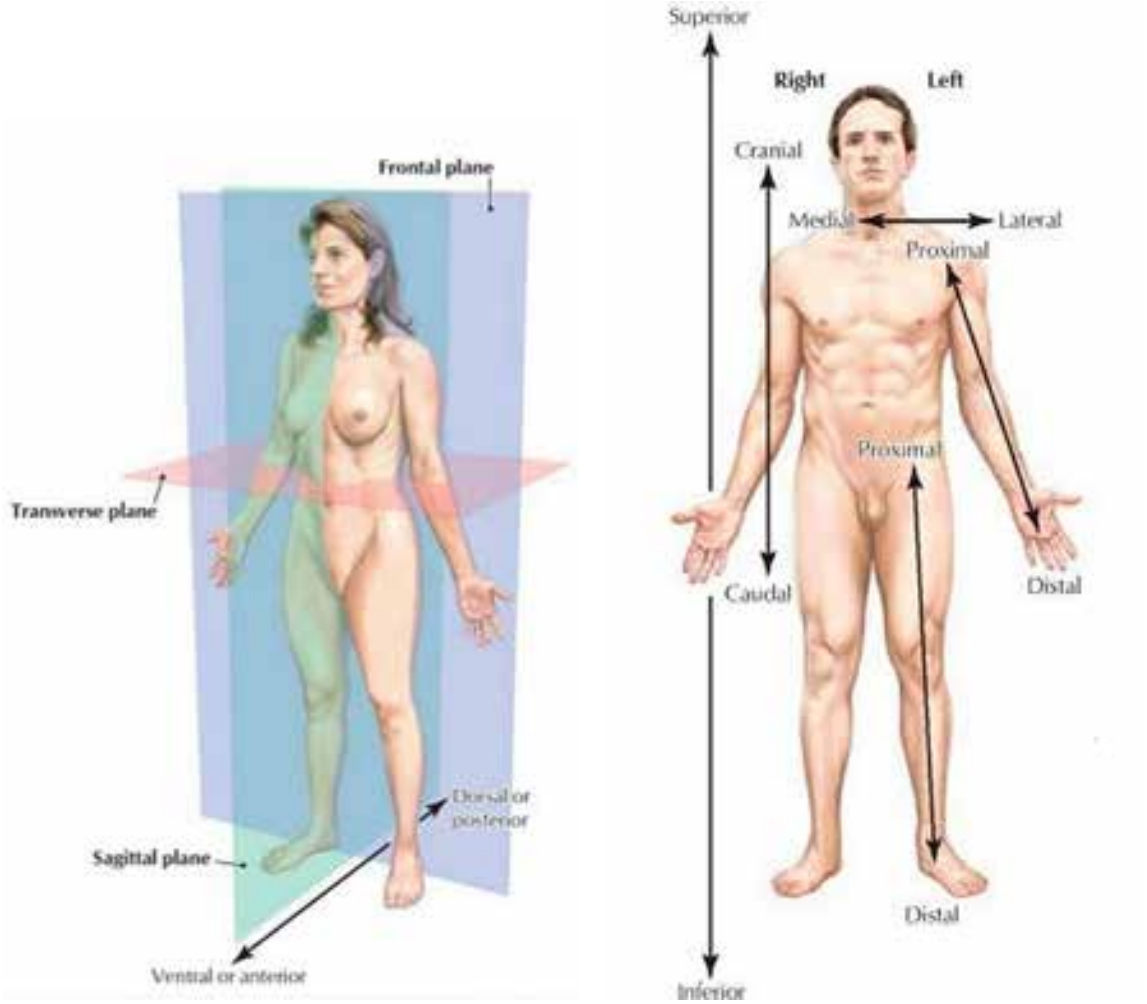

(a) Anatomical planes (b) Anatomical directions

Figure 2.1: Illustrations for anatomical positions and directions. Figures are reproduced from Hansen [2009].

.

to a rigid-body-like object.

The tongue strongly interacts with surrounding oral structures, which participate in a wide range of physiological tasks, for instance, in swallowing a bolus [Ono et al., 2004, Hori et al., 2006, Kieser et al., 2008, Kennedy et al., 2010]. The area above the top of the tongue dorsum is also known as the upper palate, which consists of two parts, namely, the hard palate and soft palate (Figure 2.2). The former is a thin horizontal maxillary bone that forms the roof of the mouth; and the latter, also known as the velum or the muscular palate, is a soft tissue plate located in the posterior side of the upper palate. The teeth define the vertical boundary surrounding the oral cavity. Even though a tooth is formed from the hardest tissue in the human body, it can be gradually corrupted due to pressure produced by the tongue-tooth interaction [Pytlik, 1982, Steedle and Proffit, 1985].

Classification of the tongue muscles

In the human body, there are three major types of muscles, the cardiac muscle, smooth muscles and skeletal muscles. From a structural perspective on the micro-level, the cardiac and skeletal muscles are composed of a series of structurally connected sarcomeres, that are absent in smooth muscles. The main function of skeletal muscles is to drive the skeleton, or body movements of the skeleton or tissue, through a contraction process (i.e. shape changing).

The tongue is traditionally believed to be a collection of skeletal muscles. In a electron microscopic study, Mauro [1961] first observed in the tongue muscles of white rat the same satellite cells as found in the skeletal muscle fibres of the frog. Later, Muir et al. [1965] found further evidence of a similar composition of cells in the tongue muscles and other skeletal muscles.

Skeletal muscles can be classified by the straining intensity of myofibrillar ATPase (mATPase) in acid and alkaline preincubations, namely type I and type II with subtypes IIA, IIAB, IIB, IIC and IM [Essen et al., 1975, Lexell et al., 1983, Schiaffino et al., 1989, Pette and Staron, 2000]. The composition of muscle fibres governs its mechanical properties. Type II fibres possess a faster shortening rate than type I fibres. The sequential order of stimulated activations of

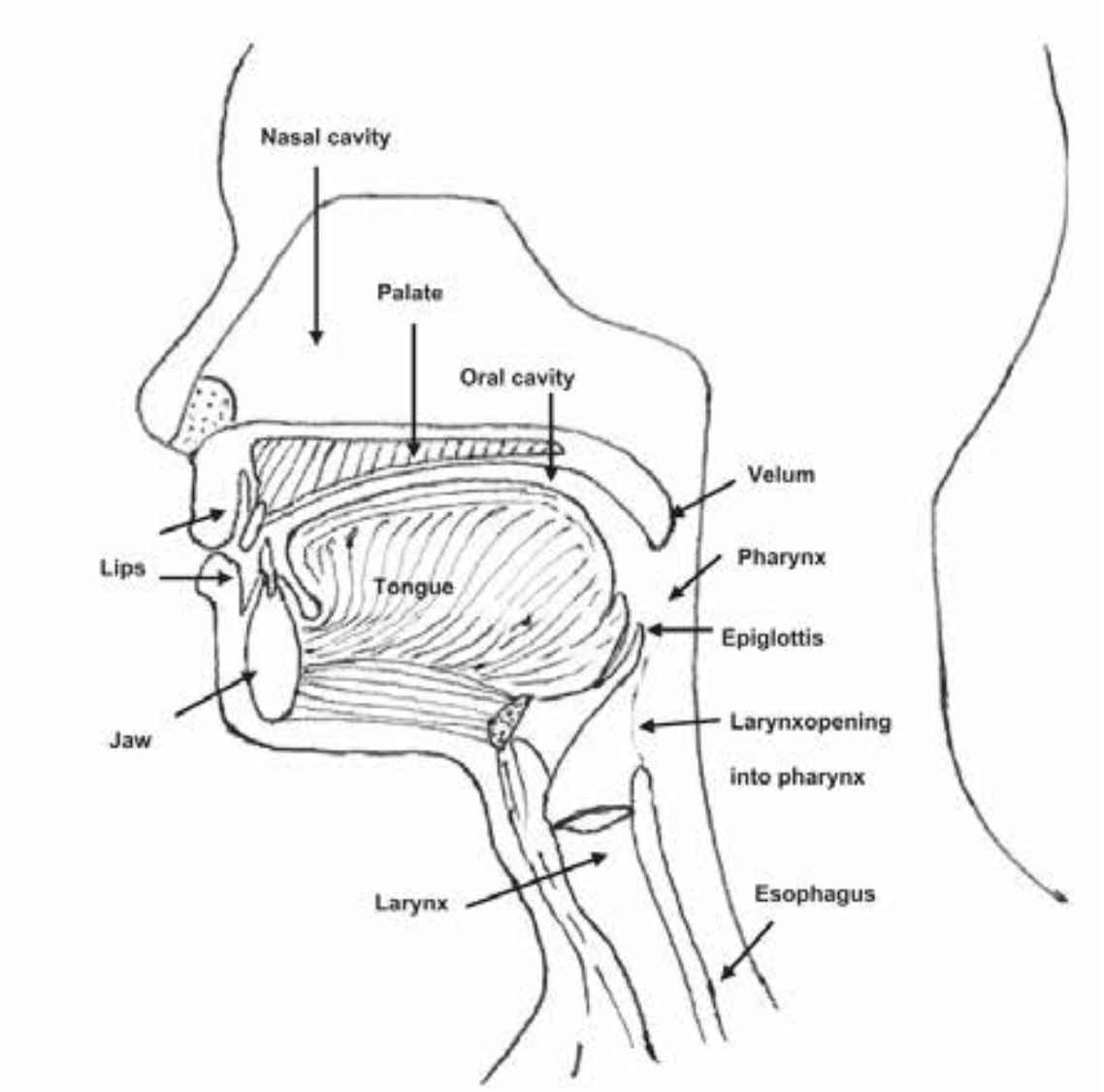

Figure 2.2: An artistic impression of the anatomy of the tongue and surrounding structures through the mid-sagittal plane of the human head. The upper palates (labelled as ”palates”) consist of the hard palate and soft palate. The hyoid bone is attached to the underside posterior of the tongue, which is connected to the digastric and hyoglossus muscles. (Reproduced from Chen [2009])

different fibre types determine the actual resultant shortening effect [Lieber, 1986].

Stål et al. [2003] firstly identified quantitative proportions of type I, IIA and IM/IIC fibres in the muscles of the tongue body through examination of set of samples from subjects of various ages and genders. Within the tongue tissue, type II fibres make up 60% of the total composition. However, the regional difference in fibre type distribution is significant. In contrast to the anterior section of the tongue, which consists mainly of type II fibres (71%), the posterior section of the tongue is comprised of a greater proportion of type I and IM /IIC fibres (66%). The muscles of the tongue possess very similar fibre classifications to other skeletal muscles, and also have the same micro-level structural features. Consequently, the mechanical properties of the tongue fibres can be ascertained by referencing to previously reported studies of skeletal muscle fibres.

Structure of skeletal muscles

Since tongue muscles fall into the category of skeletal muscles, their structural composition is reviewed from the more comprehensively researched perspective of skeletal muscles. A bundle of skeletal muscles consists of many single muscle fibres, each one consisting of multiple myofibrils that comprise a series of connected sarcomeres [Silverthorn, 2009], as shown in Figure 2.3. According to the classical sliding filament theory, myosin bridges pull the thin filaments towards the centre of the sarcomeres, and thus, the myfibril is shortened and the entire muscle is contracted along the direction of the fibre [Silverthorn, 2009]. A variety of energy sources provide the support for such mechanical movement and heat production, including adenosine triphosphate (ATP), glucose and oxygen, through aerobic respiration or anaerobic respiration [Silverthorn, 2009, Zaidi et al., 2013].

Saito and Itoh [2003] used electron scanning microscopy (SEM) measurements to scan human tongue tissue, and firstly observed the detailed tongue fibrous arrangements. The scale of tongue muscle fibre bundles was reported to range from 45 μm to 300 μm in diameter, with an individual fibre variation between 6 μm to 12 μm. They also observed that connective tissue

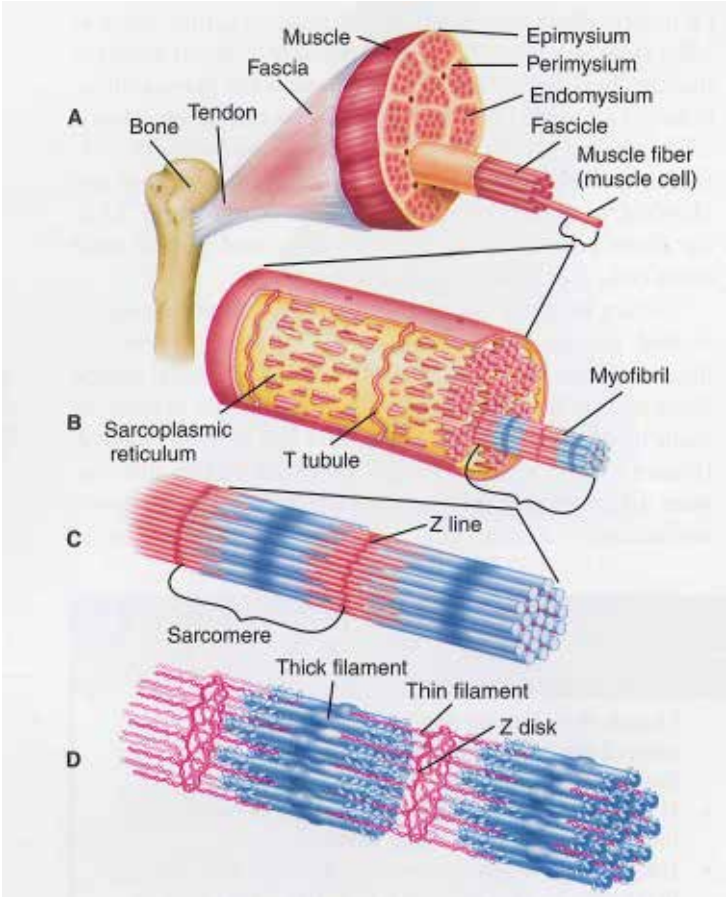

Figure 2.3: A structural illustration of the skeletal muscle composition, reproduced from Thibodeau and Patton [2003]. The basic mechanical unit is the sarcomere which is composed of filaments. A series of connected sarcomeres make up a myofibril, which is the major element of a muscle fibre. During activation, the sarcomeres contract in the direction of the filament, and hence, drive the entire contraction of the muscle fibre, and consequently, the muscle body.

filled the space (about 50 μm to 500 μm) between the fibrous bundles in different layers of the sample.

Distributions of tongue muscles

The tongue possesses a sophisticated fibrous architecture which includes various muscle families, namely,

- genioglossus anterior and posterior (gg),
- styloglossus anterior and posterior (s),
- hyoglossus (h),
- transversus (t),
- verticalis (v),
- superior longitudinalis (sl),
- inferior longitudinalis (il),
- digastric (dig),
- mylohyoid (m), and
- geniohyoid (gh).

The classical definitions of tongue muscles generally classify two types of muscles: intrinsic and extrinsic muscles. From the perspective of classical anatomy, the extrinsic muscles, including genioglossus, styloglossus and hyoglossus muscles, mainly drive the tongue body to perform large spatial movement; whereas the intrinsic muscles, such as the longitudinalis, transversus and verticalis, alter the shape of the tongue [Altschuler et al., 1994, Bailey et al., 2006, Shawker et al., 1984]. The digastric, mylohyoid and geniohyoid muscles are considered external muscles. These muscles are tightly attached to the genioglossus and hyoglossus, which are connected to the mandible, hoiyd bone and tongue body.

In general, the extrinsic muscles are distributed around the visible tongue body, and connect to skeletal structures as listed in the following.

- The genioglossus, including its anterior and posterior parts, is a fan-shaped extrinsic muscle located deep in the body of the tongue. The anterior part of the muscle connects to the mental spine of the mandible, whereas the posterior side attaches to the hyoid bone. Figure 2.4(a) illustrates the distribution of the genioglossus muscle within the tongue body.

- The styloglossus originates from the lower part of the styloid process and inserts at the middle of the tongue body. It passes through the lateral side of the tongue and ends, as illustrated in Figure 2.4(b), at the anterior side of the tongue tip.

- The hyoglossus runs almost vertically upwards between the styloglossus and the longitudinalis inferior. It enters the posterior side of the tongue as shown in Figure 2.4(c). The hyoglossus is attached to the hyoid bone and controls its movement in many physiological activities.

The visible tongue body is mainly composed of intrinsic muscles that gradually merge into the surrounding extrinsic and external muscles. These muscles have no connection with any skeletal structure.

- The transversus and verticalis muscles are orthogonally aligned to each other to form an interlaced woven type of texture (shown in Figure 2.5). The transversus muscle of the tongue originates from the median fibrous septum and passes laterally into the sides of the tongue body; whereas the verticalis muscle generally arranges in a superior-inferior direction.

- The longitudinalis muscle lies under the mucous membrane on the dorsum of the tongue, and arises from the anterior tongue body; the muscle eventually ends close to the epiglottis. Figure 2.6 shows the arrangement of the longitudinalis muscle along with two other interlaced intrinsic muscles.

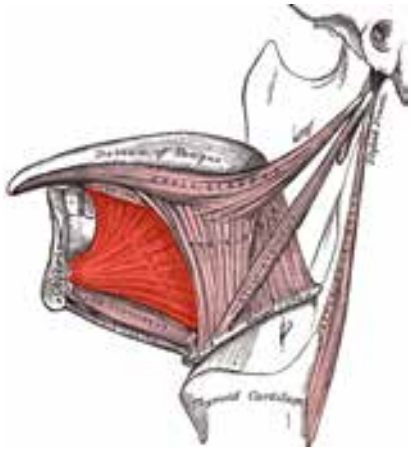

(a) Genioglossus

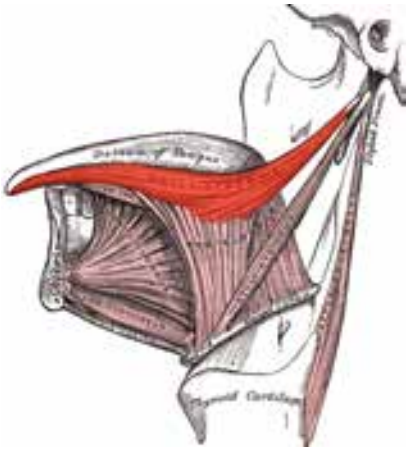

(b) Styloglossus

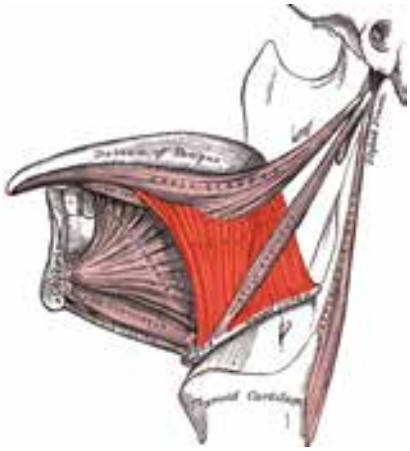

(c) Hyoglossus

Figure 2.4: Locations and distributions of the genioglossus, styloglossus and hyoglossus muscles. Figures reproduced from Grey [1918].

In classical anatomy, the external muscles are not considered part of the tongue. However, the physiological roles of these muscles with respect to tongue function cannot be ignored since these muscles tightly connect to both intrinsic and extrinsic muscles. The digastric muscle falls into the category of the suprahyoid muscle. It is located beneath the mandible and connects the mandible and the mylohyoid muscle. The mylohyoid muscle is situated above the anterior digastric muscle. The superior part of its medial border attaches to the geniohyoid muscle, which largely arises from the inferior mental spine, and runs backward to connect to the anterior surface of the hyoid bone. Figure 2.7 presents a graphical interpretation of the external muscles' distributions and arrangements.

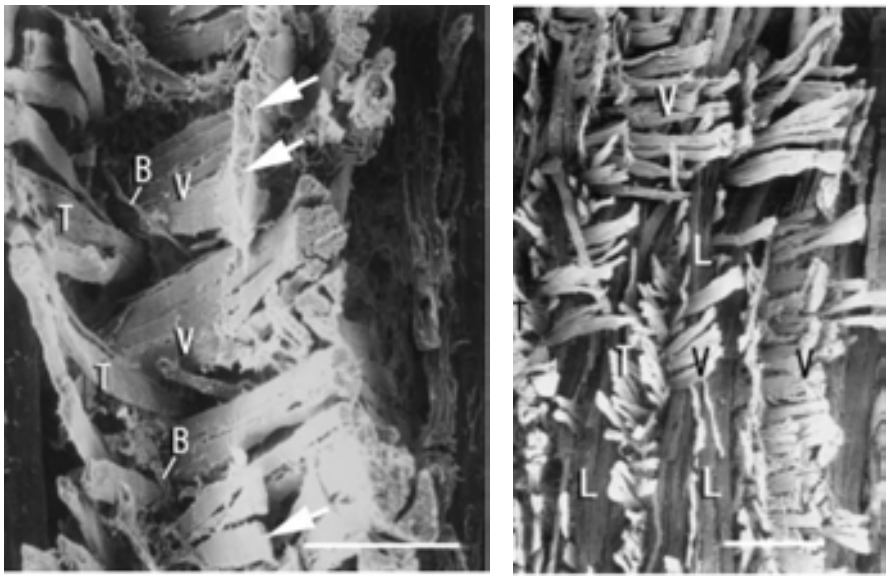

(a) (b)

Figure 2.5: The interwoven fibrous structures of the transversus and verticalis, labelled as T and V respectively. Label L and B indicate the longitudinalis muscles and the blood vessels. Bar on Figure 2.5(a), 250 μm; Bar on Figure 2.5(b), 100 μm. Figures reproduced from Saito and Itoh [2003].

2.2 Overview of food intake and speech

The major physiological roles of the tongue are (1) blending and transporting food by sophisticated deformations of its flexible body, and (2) speech production by reforming the vocal tracking shape. In this section, the major physiological activities of swallowing and speech production are reviewed.

2.2.1 Food intake

From a scientific perspective, food intake is a process of many sub-steps. Each step aims to achieve a specific goal that benefits the next stage of process. Hence, the definition of each sub-step needs to be clarified in order to understand the functional roles of the tongue during these processes. Note that the tongue not only plays an important role in transporting bolus, but it also provides sensory functionality, such as sensing shape and hardness, which helps the central neural system adjust the intra-oral dynamics [Jafari et al., 2003].

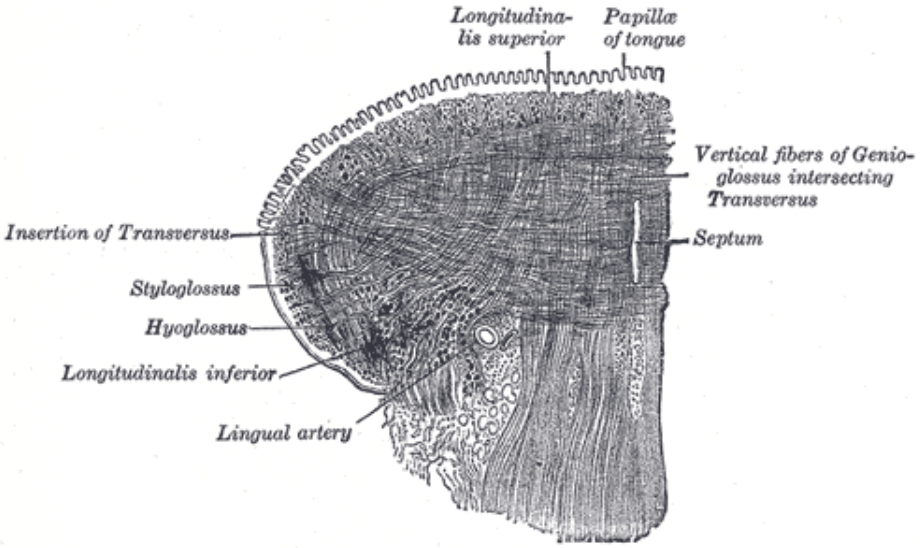

Figure 2.6: An illustration of the arrangements of the transversus, verticalis and longitudinalis muscles on the midfrontal plane of the tongue. Figures reproduced from Grey [1918].

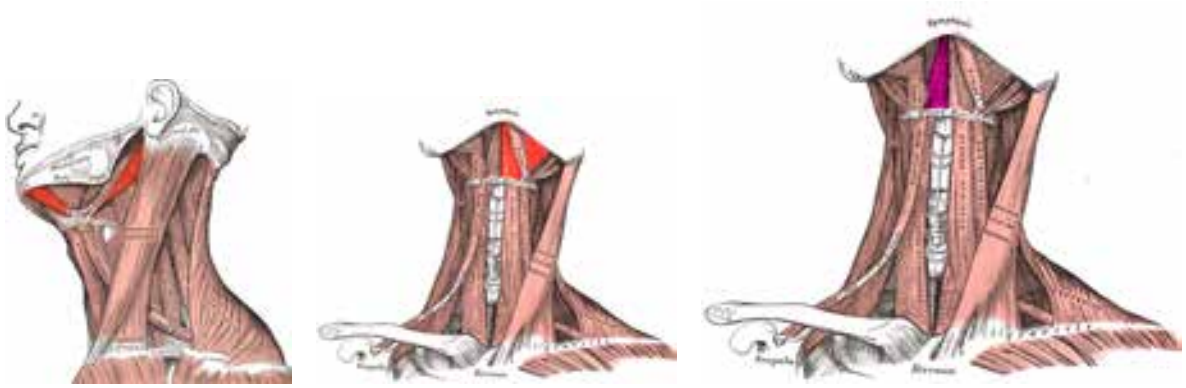

(a) Digastric (b) Mylohyoid (c) Geniohyoid

Figure 2.7: Locations and distributions of the digastric, mylohyoid and geniohyoid muscles. Figures are reproduced from Grey [1918].

Defining the food intake process is challenging due to the involvement of many sub-processes such as mastication, bolus transportation and so on. Two food intake models, proposed by Lucas et al. [2002] and Hiiemae [2004], have been widely accepted for analysis of the oral process of food consumption. Lucas et al. [2002]'s model defines the food intake as a behaviour with multiple steps in sequential order, including gripping, first bite, fracture, size reduction, transportation and swallowing. The transition between any consecutive step is determined by a decision making process that assesses the size and formation of the bolus. To terminate the process of food intake, the size of the bolus needs to be at a certain level of suitability. In short, a series of complex decision making events are re-assembled in an organised sequential form.

Hiiemae [2004]'s model describes the food intake from the perspective of the functional role of each event. The model consists of two major transportation processes, one to manage the size of the bolus and the other one to reformat the bolus in general. An advantage of the model by Hiiemae [2004] is that it clarifies the differences in movement between liquid and solid food intake. As such, it provides means to describe how liquid substances, e.g., water, can shift to the second stage of transport without prior size reduction. As in the model by Lucas et al. [2002], a certain level and shape of the bolus must be achieved before it is transported to the next stage for digestion [Hiiemae, 2004].

In both models, swallowing is the last step in oral food processing. The functional objective of swallowing is to transport a suitably sized bolus from the oral cavity to the oesophagus. This is mainly achieved by the tongue. Complete swallowing consists of a series of complex individual phases with different functional purposes, namely an oral phase, a pharyngeal phase and an oesophageal phase. In the oral phase, the bolus is fractured and reformatted by the tongue pushing the bolus against the hard palate; the tongue then shifts the broken food particles to the posterior side of the oral cavity in the pharyngeal phase; and, with the assistance of striated muscles, the food particles are propelled downwards to the oesophagus (oesophageal phase) before entering the stomach.

2.2.2 Speech production

Speech production is a sound generation process. The entire process is complex and involves three major parts of the human body: the airway system below the larynx, the larynx and its surrounding structures, and the structures and the airways above the larynx [Stevens, 2000]. The airways below the larynx consist of the trachea, the bronchi and the lungs, all of which actively deform, and hence, produce an airflow through the larynx. The larynx, and in particular the vocal folds, are then functionalised to generate sound waves through vibration. The actual sound, such as spoken words, is finally formed in the vocal tract above the larynx. The vocal tract is enveloped in the oral structures, i.e., the upper hard palate, tooth and the tongue. The tongue deforms into a variety of shapes during different phonetic tasks to assist in the construc-

tion of a variety of boundaries for the intake or outlet of air during annunciation [Hardcastle et al., 1999, Stevens, 2000].

Studies of speech have had a strong interest in the description of motion and shape of the tongue corresponding to different sound elements, i.e. consonants and vowels. A large amount of prior research has been undertaken to describe the tongue shape and speech activities. These studies have attempted to give simple descriptions/approximations of the change in tongue shape during speech production using a few parameters. The parameter values have commonly been adjusted to reproduce different shapes while pronouncing a particular sound. In general, these mathematical descriptions have not incorporated the tongue's anatomical features, but merely provided a simple mathematical expression obtained by data fitting.

For instance, the early research undertaken by Lindblom and Sundberg [1971] noted that the contour lines of the tongue's mid-sagittal plane vary with different sound elements, and introduced a semi-polar coordinate system to quantitatively describe the various tongue contours. Based on their measurements, Lindblom and Sundberg [1971] presented a simple mathematical description of the correlations between the shapes of lips, the tongue and the larynx with the sounds elements. Maeda [1990] analysed more than 1000 frames of cineradiographic and labiofilm data corresponding to 10 French sentences uttered by 2 subjects. They concluded that the mandibular, tongue dorsal position, dorsal shape and the position of apex are the main factors controlling the variation in sound. Moreover, Maeda [1990] believed a limited number of parameters, i.e. 7, can be employed to accurately predict and describe the variations in shapes corresponding to different pronunciations. The idea of measuring the trajectories of particular points on the tongue to describe various articulation has commonly been accepted in later studies, such as those of Hombert et al. [1979], Lindblom and Maddieson [1988], Gafos [1999], Stone [2005] and many more.

2.3 Functions of the tongue

The tongue's various deformations and movements define its functional role in phonetic or digestive processes. From a mechanical point of view, the tongue can be considered as a mechanical actuator that drives the motion of tissue and skeletal structures through a self-contracting deformation process stimulated by neural signals [Schneider, 1994, Huijing, 1999]. In this section, the functional role of the tongue is addressed from a mechanical perspective. The mechanical properties of tongue tissue are outlined, including the mechanism of muscle activation, its passive response, and the functional role of lingual fibre arrangements. Previously reported insights into the tongue's muscular activities during swallowing and speech are further outlined.

2.3.1 Muscle contraction and passive response

A single muscle fibre can perform a shortening deformation, also known as activation or contraction. The contraction of fibres is directly associated with the excitation level of a muscle fibre controlled by neural signals [Huijing, 1999]. Since the beginning of the 20th century, researchers have dedicated great efforts to develop a theoretical explanation of the contractile mechanism of muscle fibres. Initially, the folding of long protein chains that surround muscle fibres was thought to be responsible for the shortening of muscle fibres, and hence, production of a contraction [Clark, 1927]. The so-called lactic acid theory on folding long protein chains was later substituted by Huxley's theory on sliding filaments. In 1953, Hugh Huxley observed sliding filaments within frog muscles using transmission electron micrographs of transverse muscle sections [Hanson and Huxley, 1953]. The initial theoretical explanation by Huxley et al. [1957] was later extended with a detailed description of the overlapping zones of cross filaments, i.e. cross-bridge theory [Huxley and Simmons, 1971]. The sliding filament mechanism, including cross-bridge theory, has widely been accepted as a valid explanation of muscular contraction.

The passive response of skeletal muscles depends on the arrangement of muscle fibres and

the passive mechanical properties of muscle tissue and surrounding tissues within the muscle body. Huijing [1999] stated that the passive response of a muscle fibre is only apparent when it is passively stretched along its longitudinal direction. Huijing [1999] suggested that the skeletal muscle can be seen as a composite material, which consists of a extracellular matrix with reinforcement of fibrous material. Reinforcement is achieved through active muscle fibre shortening and passive mechanical response of the basal lamina and intermuscular connective tissues. The basal lamina is the coating layer of the myofibre, which enhances the shearing effect between the contact interfaces of myofibres [Huijing, 1999]. Intermuscular connective tissues, including the endomysium, perimysium and epimysium, provide a supporting structure that surrounds the muscle body and the fascicles of myofibres [Huijing, 1999]. Huijing [1999] described the skeletal muscle using a simplified model with 3 contributions from the ground matrix effect (extracellular matrix), active tension and passive fibrous elasticity.

2.3.2 Muscle fibre arrangement

Fibre arrangement refers to the fibre orientation and the distribution of fibre families. The fibre arrangement is the most basic anatomical factor governing the functions of the tongue. As summarised by Smith and Kier [1989] and Gilbert et al. [2007], the tongue tissue, with its complex fibre arrangements, can perform a large number of deformations that suit various situations. Smith and Kier [1989] and Gilbert et al. [2007] concluded that the co-activation of multi-oriented fibre arrangements define the deforming shape of the tongue.

Cheng et al. [2011] presented a series of elastographical images of the mid-sagittal plane of the tongue, showing the so-called storage and loss moduli with a high level of spatial heterogeneity. The storage modulus measures the stored energy due to elastic deformation; while the loss modulus reflects the energy dissipated as heat, or in other words, the viscous portion in viscous elastic materials. The heterogeneity of the elastic properties of the tongue can be explained by the spatial distribution of muscle fibre families.

The particular fibre arrangement of the tongue does not only affect its passive behaviours, but

also profoundly influence its active behaviour, especially in the case of co-activation of various muscle groups, as observed through the MRI technique by Napadow et al. [1999a,b], Felton et al. [2007] and Takano and Honda [2007]. Co-activation of intrinsic muscles alter the shape of the tongue; while large deformations with spatial movement are achieved through a simultaneous activation of intrinsic and extrinsic muscle families. However, details of the mechanical effects of various muscle activation patterns are still unknown due to remaining limitations in simultaneously recording muscular activities and their resulting functional deformations.

Figure 2.5 illustrates the unique interwoven arrangements of the intrinsic transversus and verticalis muscle fibres when compared with other skeletal muscles [Saito and Itoh, 2003]. Saito and Itoh [2003] combined a microscopic technique with a chemical-maceration method to reconstruct detailed images of intrinsic lingual tissue samples from male rabbits. The intrinsic muscle fibres were demonstrated to be organised in a mesh-liked interlaced fibre arrangement. It was hypothesised that this woven-texture structure assists in the hardening of the posterior part of the tongue to transport the bolus during swallowing. Smith and Kier [1989] noticed a similar interlaced fibre structure within other animal tissues, for example, in the mantel of squids and in elephant trunks.

The interlaced fibre structure is assumed to alter the contractile stress field, allowing the soft tissue body to perform large rotational and stretching deformations [Kier and Smith, 1985, Smith and Kier, 1989]. For instance, the elephant trunk, as a very flexible soft tissue system, can perform large rotational deformations through partial muscle contractions [Kier, 1988, Smith and Kier, 1989, Thompson et al., 1998]. The bending and elongation of the tongue body shows similar characteristics. Napadow et al. [2002] reported that the sagittal bending of the tongue body is caused by simultaneous contraction of the longitudinal muscles and the interlaced intrinsic fibres. The active, interlaced fibres cause a contractile force in the anterior tongue body from the superior-inferior and medial-lateral directions, which lengthens (elongates) the tongue body, while activation of the longitudinal muscles shortens the body upwardly.

The co-activation of extrinsic and intrinsic muscles achieve most of the tongue's configurations for the various functional roles. The extrinsic muscles shift the position of the tongue

body, whereas the intrinsic muscles change the shape of the tongue. The phenomenon of co-contracting intrinsic and extrinsic muscles is often observed in food intake or sound articulation. The following two sub-sections will present some of the existing experimental results pertaining to the simultaneous contractions of intrinsic and extrinsic muscles in the process of swallowing and speech.

2.3.3 Co-activation of the tongue muscles in the swallowing process

In swallowing, the tongue needs to perform a variety of deformations to achieve the different physiological tasks, for instance, blending and transporting the bolus. As mentioned above, shape deformation of the tongue is the consequence of the contraction of various combinations of tongue extrinsic and intrinsic muscles.

Bailey and Fregosi [2004], Kayalioglu et al. [2007b] and Liu et al. [2007] studied the relationship between the resultant tongue shape (in rats and pigs) and the co-activation of intrinsic and extrinsic muscles during the swallowing process. They noticed that the resultant tongue configurations for bolus transport were achieved through activation of different combinations of muscles with varying levels of stimulation. Through direct EMG measurement, the animal-based study by Kayalioglu et al. [2007b] reported a comprehensive result of muscle activation during the entire swallowing process. For example, it was found that the verticalis, transversus and genioglossus were stimulated during jaw opening. Meanwhile, the EMG pig study by Liu et al. [2007] further proved that the intrinsic muscles have less association with a change in tongue shape than the extrinsic muscles during food intake.

Others applied tagged MRI to investigate the various deformations of the tongue during dynamic activities such as bending and elongation [Napadow et al., 1999a], as well as in swallowing [Napadow et al., 1999b]. Napadow et al. [1999b]'s study of swallowing focused primarily on the action of the tongue in dry swallowing conditions. Food intake models of dry swallowing have commonly considered food preparation and bolus size reduction as mere transport-swallow steps [Lucas et al., 2002, Hiiemae, 2004]. However, food preparation and bolus size

reduction comprise three major tongue configurations that are early bolus accommodation, later bolus accommodation and propulsions. In Napadow et al. [1999b]'s study, mid-sagittal MRI images of the tongue were divided into four regions, each of which consisted of tagged elements which were traceable in different shape configurations and which represented one, or several parts of individual muscles. The deformed tagged elements during tongue elongation are used to calculate the axial strain patterns within those regions. The third axial strain component, which is perpendicular to the image plane, are computed under the assumption of incompressibility. Combined with the muscles' orientations, Napadow et al. [1999b] outlined a comprehensive muscular activation pattern based on quantitative movement information.

Later, Felton et al. [2007] assessed tongue deformation during the propulsive phase by using phase-contrast MRI. The images were acquired in the sagittal and coronal orientations within 600 ms of the gating pulse during 2.5 ml water bolus swallows. The local principal strains were computed from predefined tags on the images. The authors reported that compressive strain along the direction of the transversus and verticalis muscles occurred in the middle and posterior tongue, obliquely aligned between the anterior-inferior and the posterior-superior regions. They concluded that bolus propulsion may consist of much more complex muscle activation patterns than previously thought. The genioglossus, hyoglossus and styloglossus were considered to play synergistic roles with minor contributions from intrinsic muscles.

Using ultrasound imaging, Stone and Shawker [1986] studied the tongue-palate interaction during swallowing by tracking pre-installed markers (pellet). The tissue deformation was observed to show a wave propagation pattern in bolus propulsion. This was explained by the major movement of the tongue in the superior direction and the subsequent contact with the upper palate. Ono et al. [2004], Kieser et al. [2008] and Kennedy et al. [2010] verified the phenomenon by using a custom-designed pressure measurement device. The measurement palate consisted of a pressure sensor array which was distributed on the surface for capturing potential interaction with the tongue body. Figure 2.8 presents the pressure measurement palate used by Ono et al. [2004]. The resulting data of pressure versus time at each sensor location shows a clear pattern in which the tongue establishes contact with the anterior hard palate, then gradually approaches

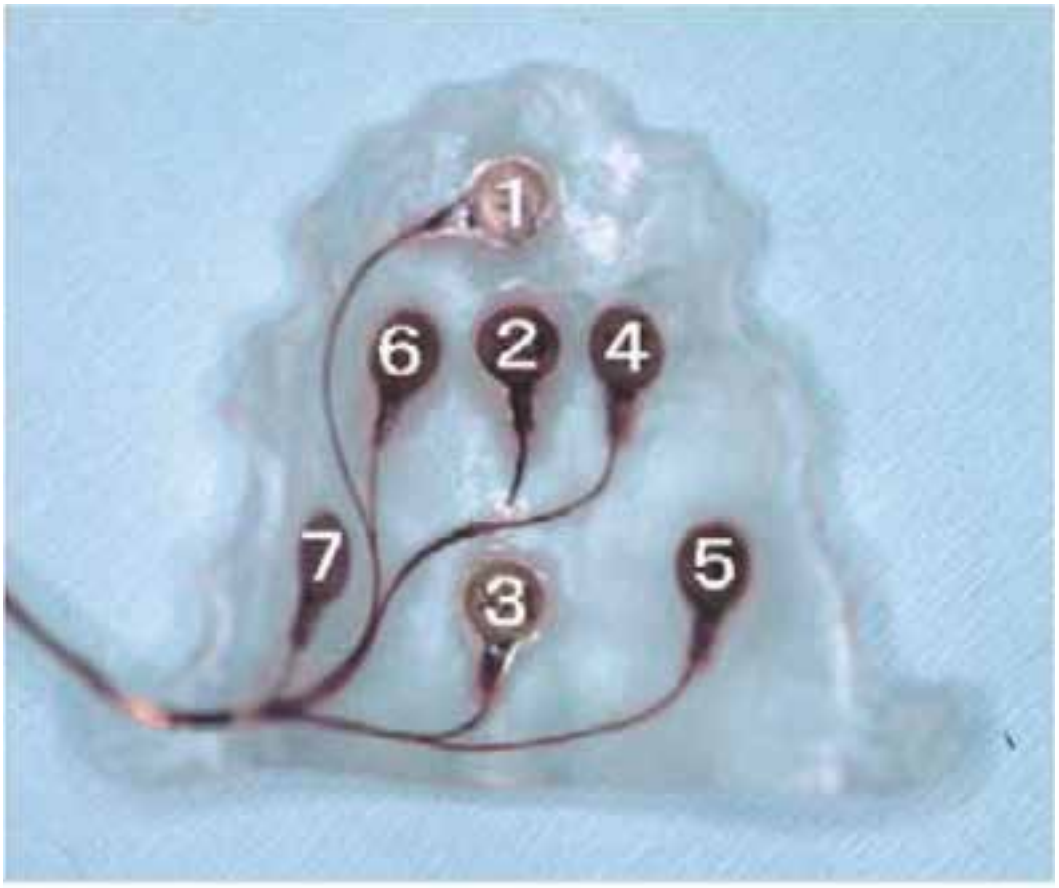

Figure 2.8: The customized plate for measuring upper palate contact pressure, reproduced from Ono et al. [2004]. The numbers on each sensor location labels the sensor index. Kieser et al. [2008], Kennedy et al. [2010] used a similar design for measuring contact pressure patterns during swallowing.

the middle section, and ends with a minor interaction at the posterior side of the upper palate [Ono et al., 2004, Kieser et al., 2008, Kennedy et al., 2010].

In summary, the tongue movements during swallowing can be seen as a consequence of multiple actions of individual muscles and contact between the tongue and surrounding structures. In the present research, it is assumed that food preparation and bolus size reduction comprise three major tongue configurations, i.e. early accommodation, later accommodation and propulsion, as outlined in Napadow et al. [1999b]. Each of these configurations is formed by the co-activation of multiple muscles and and the incompressible nature of muscle tissue. Thereby, the interaction between the tongue and other surrounding oral structures needs to be taken into account. The contact between the tongue and the bony parts, e.g. the hard palate and teeth, constrain the deformation of the tongue due to muscle contraction and result in an external force

which also influences the tissue deformation.

2.3.4 Heterogeneous contraction of the tongue muscle in speech production

As mentioned previously, phonetic research is strongly motivated to elucidate the relationship between phonetic elements, i.e. vowels and consonants, and various tongue shapes. Consequently, observing the motion of the tongue is the primary focus in speech research. MRI studies have led some researchers to conclude that the tongue's deformation during speech is caused by co-activation of multiple muscle families similar to swallowing [Baer et al., 1991, Honda, 1996, Narayanan et al., 1997, Ong and Stone, 1998]. Furthermore, research indicates that the muscle activation patterns during speech may be more complex than the uniform contraction of single muscles. For instance, Takano and Honda [2007] studied the kinematics of the tongue in speech using MR images. It was concluded that, regardless of the anatomical classification of muscle groups, the regional tissue contraction is strongly associated with back vowels and front vowels, indicating heterogeneous contractile muscle properties.

By combining cine-MRI and ultrasound imaging, Stone et al. [2004] reported a functional segment controlling effect in the transversus, verticalis and genioglossus muscles during phonic tasks. Strong evidence was given that the tongue cannot be considered as being simply divided into tip and body, and that tongue muscles may not be activated uniformly during those physiological tasks [Stone et al., 2004]. In the case of the articulation of | k |, the tongue performs a retraction action during which the tongue body shifts backwards [Stone et al., 2004]. Using images of the mid-sagittal plane, the middle portion of the tongue showed a significantly more obvious compression-like deformation compared to the deformation of the tip of the tongue. Based on these findings, Stone et al. [2004] concluded that the verticalis and transversus muscles must share a similar segmental structure as the genioglossus muscle. Furthermore, Stone et al. [2004] concluded that the different movements between anterior and posterior tongue parts suggest at least two different functional segments within the transversus and verticalis

muscles.

Another MRI study on speech, conducted by Parthasarathy et al. [2007], reported a similar phenomenon comprising a non-uniform localised strain pattern of the tongue body during articulation from | u | to | k |. They found that the tongue was gradually elevated from its anterior to its posterior region, which resulted in varying movement directions throughout the tongue body. Similar retractile action has been observed in the propulsive phase of swallowing. In particular, the tongue has been found to contract along the medial-lateral axis, while expanding in the anterior-posterior and superior-inferior directions, constrained by the upper-palate [Napadow et al., 1999b, Ono et al., 2004, Kieser et al., 2008, Kennedy et al., 2010]. Similar observations have been reported by Takano and Honda [2007] in one of their studies on the linkage between regional tissue activity and a variety of vowels. However, no study has yet reported on the functional role of individual tongue segments during the propulsive phase.

Woźniak and Young [1969] and O'Kusky and Norman [1995] reported on the complexity of neuronal muscle innervation in the tongue. At least 6500 motoreurons were estimated on each side of the tongue, leading to a total of 13000 hypoglossal motoneurons to innervate the human tongue. Each layer of interwoven intrinsic muscles, i.e. transversus and verticalis, was found to contain its own motoreurons, and hence, present with an ability to independently control fibre contraction [Miyawaki et al., 1975, Mu and Sanders, 1999, Takemoto, 2001]. As such, it is likely that locally varying contractile properties exist within a single muscle family, particularly within intrinsic muscles.

2.4 Clinical measurement of tongue motion

As mentioned in Section 1.3.2, EMA was originally designed for tracking facial and tongue movements in phonetic research. The EMA system within this thesis refers to an Articulograph AG500 developed by Carstens Medizinelektronik GmbH in Germany[1]. Henceforward, the term of Carstens AG500 refers specifically to this articulography system.

[1] See http://www.articulograph.de

2.4.1 Electromagnetic articulograph setup

As shown in Figure 2.9, a typical EMA system includes a helmet cube, a number of transmitter coils, and a signal processing module that connects the transmitter coils to a computer. The helmet cube consists of a set of 3 large transmitter coil systems mounted in the upper corners of the cube. The coils generate alternating electromagnetic fields of different frequencies. A number of receiver coils (motion sensors) are placed on the subject's articulators (tongue, jaw, lips and teeth). The basic underlying principle of the EMA system is based on the Hall effect [Kaburagi et al., 2005]. During an experiment, the receiver coils influence the magnetic field and electrical currents are passively generated within the transmitter coils. Those electrical currents (a cluster of signals) are subsequently interpreted as the motion sensors' 3D coordinates and orientations (2 angles), which can be visualised on a standard PC.

A standard Carstens AG500 system is equipped with 12 motion sensors of size 2 mm $\times$ 3 mm. which are tracked with a frequency of frequency of 200 frames per second. During an experiment, the motion sensors have to be positioned on the desired motion tracking points (as shown in Figure 2.10). The sensors' trajectories are required to remain inside of the cube. Any sensor motion beyond the measurement range of the helmet cube (300 mm $\times$ 300 mm $\times$ 300 mm) is neglected.

2.4.2 Accuracy assessment of the EMA AG500 system in motion tracking

Yunusova et al. [2009] and Kroos [2012] performed an extensive accuracy assessment of Carstens AG500 in motion tracking. In Yunusova et al. [2009]'s study, the helmet cube was divided into four spatial regions. Each of which was tested with a variety of sensor movements, including (1) the movements of a calibration device, (2) the movements of the motion sensors in a cartridge device, and (3) various articulation tasks. The term "error" referred to the positional error in relation to the sensor location within the measurement field. Yunusova et al. [2009] summarised their findings in two main observations (1) the magnitude of the measurement errors correlated with the recording regions within the helmet cube, and were dependent on

(a) Articulograph AG500

(b) Motion sensors for Articulograph AG500

Figure 2.9: Articulograph AG500 system including motion sensors from Carstens Medizinelektronik GmbH, Germany.

(a) (b)

Figure 2.10: An example deployment of the Articulograph AG500 system motion sensor. In common practice, at least three sensors are used to identify the rotational movement of the head, or a mandible, as shown in Figure 2.10(b).

the particular measurement task; (2) the median error was less than 0.5 mm across various recording tests, with the peak values being between 1 to 2 mm. Testing of ”small movements” showed a median of 0.49 mm with 50% of the error data ranging from 0.18 mm to 0.83 mm and 5% of the error at the high tail of the distribution above 2.43 mm. Moreover, there was a slightly lower error distribution in the central region of the helmet cube (0.5 mm) compared to the surrounding areas.

Kroos [2012] conducted another independent study on the accuracy of the Carstens AG500 by comparing the EMA data with simultaneously acquired data from the Vicon optical motion tracking system. Kroos [2012] reported that the standard deviation of inter-sensor distances (relative error) were below 1 mm, and the standard derivation of the absolute error ranged between 1 mm and 2 mm. Kroos [2012] concluded that any results from EMA have to be interpreted with care due to potentially large measurement errors.

However, the results by Yunusova et al. [2009] and Kroos [2012] do not provide any conclusive

statistical noise patterns within the helmet cube. Thus, a few assumptions need to be drawn to model the noise pattern based on the available data. Based on the studies by Yunusova et al. [2009] and Kroos [2012], it can be assumed that the variance of the noise distribution is finite, and the infinite variance distribution does not apply. Thus, the statistical noise distribution can be assumed to be a multi-variant Gaussian distribution $N(\boldsymbol{\mu}, \boldsymbol{\Sigma})$. According to Yunusova et al. [2009], the median error rate is around 0.49 mm for small movements; while Kroos [2012] measured the absolute and relative errors, which were shown to be less than 1 mm and ranged between 1 mm to 2 mm, respectively. In the scope of the present work, the noise distribution within the helmet cube is assumed to be independent with respect to the 3 spatial directions. The probability density function of the noise distribution with mean $\boldsymbol{\mu}$ is defined as,

$$f(\mathbf{x}) = \frac{1}{(2\pi)^2 |\boldsymbol{\Sigma}|^{1/2}} \exp\left(-\frac{1}{2} (\mathbf{x} - \boldsymbol{\mu})^T \boldsymbol{\Sigma}^{-1} (\mathbf{x} - \boldsymbol{\mu}) \right) \tag{2.1}$$

and with a standard deviation of 0.7 mm in all three axial directions, the diagonal entries of variance are set to $\Sigma_{ii}^2 = 0.49$. Note that, the variances in x-y, y-z and x-z direction are not considered here, i.e. $\sigma_{i,j} = 0$ where $i \neq j$.

2.4.3 Advantages and disadvantages of EMA

The EMA is a point tracking system that captures the positions of a limited number of sensors. There are several advantages and disadvantages to the EMA system when applyed to oral related research.

Advantages

The Articulograph AG500 by Carstens has the following advantages for studying facial and intra-oral motion:

- The motion sensors of the Articulograph AG500 are small compared with optical-based sensor tracking systems. The small size of the sensors allows experimentalists to place

them in the oral cavity to monitor the intra-oral motion, and are especially useful to record tongue deformation.

- The Articulograph AG500 by Carstens can track the 5D kinematic data of each motion sensor, including its spatial coordinates and its orientation (i.e. two additional angles) in 3D space. As such, the EMA system provides a comprehensive kinematic data set of the particular material points.

- The Carstens AG500 is able to sample the motion of a sensor at a rate of 200 times per second. Using the motion data, the velocity of the tongue's shape changes can be approximated at sample rate of 200 Hz.

- The high temporal resolution of the Articulograph AG500 is superior to other measurement techniques. Unlike tagged-MRI, the subject is not required to maintain a posture for a certain amount of time. Thus, short-interval motion (normally less than 1 seconds) such as speech production can be monitored.

Disadvantages

There are several disadvantages of the Articulograph AG500 applied to tracking tongue motion during swallowing:

- The motion tracking ability of the Carstens AG500, or any EMA system, is generally restricted by the number of deployable motion sensors. In practice, only a limited number of motion sensors, e.g. 12 in Carstens AG500, can be deployed. This certainly prohibits a full view of the entire surface deformation. The size of a motion sensor is 2 mm $\times$ 3 mm. This implies that the minimum inter-centre distance between any two sensors ranges from 2 mm to 3 mm.

- Each motion sensor in the EMA system comprises a transmitter coil. Electrical currents produced within those coils may influence the neighbouring sensor signals if their distance is shorter than a certain level [Kroos, 2012]. Consequently, a minimum distance of

3 mm has to be maintained between any two sensors. This fact limits the possibility of approximating the local strain by merely using data from neighbouring motion sensors.

- The Carstens AG500, which was designed for phonetic studies, does not principally support the physiological and experimental conditions in swallowing. The sensors are attached to the dorsum of the tongue using glue; however, the adherence between the sensors and body tissue may weaken due to lubrication of saliva [Kroos, 2012]. Furthermore, the sensors, with wired connections, may lead to an uncomfortable experience for the subject. This could influence the quality of data collected during an experiment.

- In some experimental studies, e.g. the investigation of inter-individual variability, the experimentalist has to reproduce (register) the same sensor positions on different subjects. However, the highly flexible tongue body makes it difficult to locate a precise sensor location in the reference state, making the registration process a challenge task.

- Capturing the characteristic motion (e.g. the largest motion) of the tongue body is the primary application of the EMA system. However, some regions, e.g., posterior dorsum, in the propulsive phase [Napadow et al., 1999b, Felton et al., 2007], are practically inaccessible using the motion sensors provided by Carstens AG500.

- As with any measurement device, the Carstens AG500 has an inherent natural non-uniform machine error [Yunusova et al., 2009, Kroos, 2012]. Kroos [2012] pointed out that such noise could lead to incorrect conclusions when applied to small movements.

It is desirable to reduce measurement errors to a minimum, without having to fundamentally change or reinvent the system. An improvement could be achieved, for instance, with a model-based mathematical optimization of the motion sensor placement.

Chapter 3

Theoretical background for the computational modelling

The tongue is a soft tissue organ and comprises a collection of multiple skeletal muscles. Soft tissues (e.g. skeletal muscles) are commonly modelled using a finite element modelling approach driven by the finite elasticity theory (large deformation theory). The deformation of muscle tissue can be represented by strain tensors, and the corresponding strain-energy function over the entire deformation process. In this section, the theoretical foundation of modelling the soft tissue of the tongue is presented and based on the books by Ogden [1997] and Holzapfel [2000a]. The fundamentals of modelling include the definitions of strain, stress and the strain-energy function in the Lagrangian framework, which describes the movement and other related quantities with respect to the Lagrangian material coordinates in the reference/undeformed state.

3.1 Reference coordinate system and motion

In continuum mechanics, the deformation of a continuum is referred to as the quantitative description of the deformation between two material states, namely, the reference configuration

and the deformed configuration. The undeformed configuration is used as the reference state of the material points within the object domain. Here, the spatial domain of the object in the reference configuration is denoted as Ω_0 where subscript 0 indicates the initial state. The current configuration, or deformed state, refers to a state in which the spatial locations of the material points differ from the initial configuration due to external loads or other forces. In the scope of this work, the spatial domain in the deformed configuration is denoted as Ω_t, where t indicates either a specific time or processing step.

In the analysis of continuum deformations, a series of coordinates systems need to be defined to quantitatively describe the movement (displacement) of material points. A global reference system, called the spatial coordinate system, is used to describe the spatial positions of material points in 3D space. The spatial coordinate system is an independent reference system that remains constant throughout the entire process of deformation. The coordinates of a particle in the spatial coordinate system are denoted by $\mathbf{x}$. Similarly, a material coordinate system is defined to describe the position of material particles with respect to the continuous media, denoted as $\mathbf{X}$. The material coordinate $\mathbf{X}$ remains constant during deformation. In other words, the material coordinate frame deforms simultaneously with the continuum body. The material coordinate system is commonly used to define the mechanical properties of the material (stress-strain relationship).

In the reference state, the material coordinate system can be conveniently aligned with the spatial coordinate system. In the case that the spatial and the material coordinate systems are aligned with each other, the motion of a particle, i.e. displacement, can be defined as

$$\mathbf{u} = \mathbf{x} - \mathbf{X}, \tag{3.1}$$

where $\mathbf{x}$ are the coordinates in the deformed Ω_t configuration of the coordinate of material point $\mathbf{X}$ in Ω_0. In case of modelling skeletal muscles, the material coordinate system is often defined as a curvilinear coordinate system to better quantify the local material properties of muscle

tissue. The conversion of coordinates between two coordinate systems is done through

$$\mathbf{x} = \mathbf{J}(\mathbf{X})\mathbf{X}, \tag{3.2}$$

where $\mathbf{J}$ is the Jacobian matrix.

3.2 Deformation, strain and energy

3.2.1 Deformation and strain tensor

Strain is used to define the relative movements of material particles between two states and is derived from the measurement of deformation. Thereby, the deformation gradient tensor $\mathbf{F}$ is used for mapping an infinitesimal small material line $d\mathbf{X}$ with point $\mathbf{X}$ in the initial configuration Ω_0 to $d\mathbf{x}$ in the deformed configuration Ω_t as follows

$$d\mathbf{x} = \mathbf{F}d\mathbf{X}. \tag{3.3}$$

Further deduction yields

$$\begin{aligned} d\mathbf{u} &= d\mathbf{x} - d\mathbf{X}, \\ &= (\mathbf{F} - \mathbf{I})d\mathbf{X}, \end{aligned} \tag{3.4}$$

with $d\mathbf{u}$ being defined as displacement. Performing the limit, one obtains $\mathbf{F} = \mathbf{I} + \nabla\mathbf{u}$. Further, under realistic physical conditions, the following assumptions can be drawn,

$$\det(\mathbf{F}) \neq 0, \tag{3.5}$$

hence,

$$\mathbf{F}d\mathbf{X} \neq \mathbf{0} \quad \text{for all } d\mathbf{X} \neq \mathbf{0}, \tag{3.6}$$

which implies a non-singular symmetric property of $\mathbf{F}$. A material line ($d\mathbf{X}$ or $d\mathbf{x}$) has to possess a certain length. As a consequence, the following condition applies,

$$d\mathbf{x} \cdot d\mathbf{x} = d\mathbf{X} \cdot (\mathbf{F}^T\mathbf{F})d\mathbf{X} = (\mathbf{F}d\mathbf{X}) \cdot (\mathbf{F}d\mathbf{X}) > 0, \tag{3.7}$$

implying that $\mathbf{F}^T\mathbf{F}$ is positive definite. $\mathbf{F}^T\mathbf{F}$ is also called the right Cauchy-Green tensor denoted as $\mathbf{C}$.

The condition (3.6) can be further used to analyse changes in the local volume. Considering a continuum made up of the triads $d\mathbf{X}^1$, $d\mathbf{X}^2$ and $d\mathbf{X}^3$ in 3D space, its volume dV is defined as

$$dV = \det(d\mathbf{X}^1, d\mathbf{X}^2, d\mathbf{X}^3). \tag{3.8}$$

Similarly, dV in a deformed configuration Ω_t can be written as

$$dv = \det(d\mathbf{x}^1, d\mathbf{x}^2, d\mathbf{x}^3). \tag{3.9}$$

where dV is related to dv via,

$$dv = \det(\mathbf{F})dV. \tag{3.10}$$

Defining $J = \det(\mathbf{C}) = (\det(\mathbf{F}))^2$, any local volumetric change has to satisfy the condition

$$J \equiv \det(\mathbf{C}) > 0, \tag{3.11}$$

in which $\det(\mathbf{C}) = \det(\mathbf{U}\mathbf{U})$. If the material complies to the incompressible condition (volume conservation) during deformation, then $J \equiv 1$. In general, the movement (displacement) of a material line involves a rotation $\mathbf{R}$ and a stretching $\mathbf{U}$. The right polar decomposition of the deformation gradient tensor leads to $\mathbf{F} = \mathbf{R}\mathbf{U}$.

The change in the length of the material line $d\mathbf{X}$ can be described using the so-called Green-Lagrangian strain tensor $\mathbf{E}$, such that $|d\mathbf{x}|^2 - |d\mathbf{X}|^2 = d\mathbf{X} \cdot \mathbf{E}d\mathbf{X}$ where $\mathbf{E} = \mathbf{F}^T\mathbf{F} - \mathbf{I}$. This can

be rewritten in the terms of **C**, such that

$$\mathbf{E} = \frac{1}{2}(\mathbf{C}-\mathbf{I}), \tag{3.12}$$

$$= \frac{1}{2}(\mathbf{F}^T\mathbf{F}-\mathbf{I}), \tag{3.13}$$

E can be written in terms of the displacement gradient tensor $\mathbf{D} = \nabla\mathbf{u} = \mathbf{F}-\mathbf{I}$, thus obtaining

$$\mathbf{E} = \frac{1}{2}(\mathbf{D}+\mathbf{D}^T+\mathbf{D}^T\mathbf{D}). \tag{3.14}$$

Since **C** is positive definite, the spectral decomposition applied to **C** yields

$$\mathbf{C} = \sum_{i=1}^{3} \lambda_i^2 \mathbf{N}_i \otimes \mathbf{N}_i, \tag{3.15}$$

where $\mathbf{N}_i$ is the principal stretch direction with respect to the material (elemental) coordinate system. Consequently, Equation 3.15 can be written in terms of the stretch tensor **U** with respect to the material coordinate system as

$$\mathbf{U} = \sum_{i=1}^{3} \lambda_i \mathbf{N}_i \otimes \mathbf{N}_i. \tag{3.16}$$

A key feature of hyperelastic materials is that their deformation is not dependent on the path of deformation [Ogden, 1997]. In other words, the finial deformed state of a hyperelastic material can be derived directly from its initial configuration without knowledge of its intermediate states. Therefore, the deformation gradient tensor **F** can be used to provide a direct mapping from the initial state to any given deformed configuration; while the right Cauchy-Green tensor **C** and the Green-Lagrangian strain tensor **E** provide direct estimate of the deformed configuration of the material with respect to the initial configuration.

3.2.2 Interior strain energy

In continuum mechanics, the overall deformation is often represented by the total interior stored energy which depends on the Green Lagrangian strain tensor **E**,

$$W_{tissue}(\mathbf{E}), \tag{3.17}$$

where W_{tissue} is the strain energy function returning a scalar value, and subscript '*tissue*' refers to the tissue body (continuous media). The dimensionless scalar energy function is commonly associated with the strain invariants that are

$$\begin{aligned} I_1 &= tr(\mathbf{C}); \\ I_2 &= \frac{1}{2}\left[(tr(\mathbf{C}))^2 - tr(\mathbf{C}^2)\right]; \\ I_3 &= \det(\mathbf{C}). \end{aligned}$$

The three strain invariants are independent of the chosen material coordinate system (frame indifference). For isotropic tissues, the total energy stored in the continuous elastic body can be written in an implicit functional form as

$$W_{tissue}(I_1, I_2, I_3). \tag{3.18}$$

The strain energy function of anisotropic materials (e.g. isotropic materials with fibre reinforcement) is not solely dependent on I_1, I_2 and I_3, but also relies on the composition of the continuous body and the material structure. In Chapter 4.3, a detailed description of the strain-energy function of multiple fibre reinforced materials will be presented.

For composite materials, the interior energy can be considered as being stored in various compositions, known as the constituents. The theory of Helmholtz's free energy suggests that the energy is stored proportionally to the volume, or mass, of each constituent. Assuming that a continuous domain Ω_0 consists of multiple constituents (e.g. muscle families), each occupying a certain spatial domain denoted by $\Omega_{0,i}$ with i representing the constituent index, the volume

occupation of a constituent in a unit block may be represented by the volume fraction

$$d_i = \frac{V_i}{V_{total}}. \tag{3.19}$$

By definition, the summed volume fractions of multiple constituents within such a sample block must satisfy the following condition,

$$\sum_{i=1}^{n} d_i = 1, \tag{3.20}$$

where n is the number of constituents within the sample. The factor d_i is a scalar field reflecting the volume weight of various components in an infinitesimal control volume of tissue.

In an ideal situation, if constituent i occupies the entire domain Ω_0, the strain-energy function represents the total energy stored in the entire domain Ω_0. In reality, however, each constituent i is only distributed within a certain spatial domain $\Omega_{0,i}$. Thus, the interior energy can be expected to vary spatially in accordance with the material composition at each material point. Hence, the total strain energy within the tissue can be formulated in terms of the volume fractions of its constituents and the Green's strain tensor $\mathbf{E}$ as

$$W_{tissue}(\mathbf{E}) = \sum_{i=1}^{N} d_i W_i(\mathbf{E}), \tag{3.21}$$

where $W_{tissue}(\mathbf{E})$ is the total strain energy stored in the biological tissue body and W_i is the energy stored in the *i-th* constituent. The volume fraction functions $d_i(\mathbf{X})$ define the local tissue material compositions. This implies that the spatial domain (Ω_0) possesses heterogeneous material properties, and hence, that the mechanical behaviour of the tissue depends on the distributions of its constituents, as previously assumed in Lanir [1983] and Kim et al. [2009].

3.2.3 Total potential energy

The deformation of a continuous body may be caused by an externally applied load, or, so-called, traction loads, or driven by a far field force, e.g. gravitational force. The traction loads are represented as a vector quantity $\mathbf{t}$. The total energy produced by the traction loads can be

obtained through the surface integral such that

$$W_{traction} = \int_{\partial\Omega_t} \mathbf{t} \cdot \mathbf{u}\, ds, \tag{3.22}$$

where $\partial\Omega_0$ indicates the integration over the boundary surface to which $\mathbf{t}$ is applied on, and $\mathbf{u}$ denotes the displacement. The gravitational force can also be written as a vector force $\mathbf{b}$. The total gravitational energy is then obtained through

$$W_{gravitation} = \int_{\Omega_t} \mathbf{b} \cdot \mathbf{u}\, dv, \tag{3.23}$$

where Ω_t indicates that the gravitational force is applied to all material points, and that the overall integration is with respect to the entire material body. Thus, the total potential energy of the system is calculated as

$$W_{total} = W_{tissue} - W_{traction} - W_{gravitation}. \tag{3.24}$$

Note that, without considering the energy produced by external loads ($W_{traction}$ and $W_{gravitation}$), $W_{total} = W_{tissue}$ is yielded. According to the principles of minimum energy, the system will reach a state of stable equilibrium once the overall potential energy reaches a minimum value ($\min W_{total}$). Thus, a solution needs to be found to minimise the total potential energy of the system, which is done by setting its first variation δW_{total} to zero

$$\delta W_{total} = 0. \tag{3.25}$$

In such a configuration, the entire system needs to be stable and able to converge back to a state of stability even in the presence of of perturbations. The condition of stability leads to

$$\delta W_{total}(\delta \mathbf{u}) = 0, \tag{3.26}$$

where $\delta\mathbf{u}$ denotes the virtual displacement, and it has to satisfy that $\delta\mathbf{u} \mapsto mathbf0$. This formulation is also referred to as the principal of virtual work.

3.3 Stress

Movement of a continuum body gives rise to interactions between material points in the interior of the body. Such interactions are often interpreted as forces or stress. In solid mechanics, the constitutive relation commonly refers to the explicit mathematical formulation that defines the stress tensor in relation to the various components of strain.

3.3.1 Concepts and types of stress

Considering the object domain Ω_0 in an initial state with a boundary $\partial\Omega_0$ and an infinitesimal resultant force $d\mathbf{f}$ applied to a surface element ds in the deformed configuration, the following relationship is obtained

$$d\mathbf{f} = \mathbf{t}ds = \mathbf{T}dS, \tag{3.27}$$

where $\mathbf{t}$ represents a traction vector measured with respect to the deformed state of the material boundary $\partial\Omega_t$, and $\mathbf{T}$ denotes the first Piola-Kirchhoff traction vector that is measured with respect to the undeformed state of the surface element dS. The outward normal vectors with respect to the initial and deformed configurations are denoted as $\mathbf{N}$ and $\mathbf{n}$, respectively. From this, second-order tensor fields can be derived by

$$\mathbf{t} = \boldsymbol{\sigma}\mathbf{n}, \tag{3.28}$$

$$\mathbf{T} = \mathbf{P}\mathbf{N}, \tag{3.29}$$

where $\boldsymbol{\sigma}$ is called the Cauchy stress tensor and $\mathbf{P}$ the first Piola-Kirchhoff stress tensor. Each stress tensor satisfies the following condition

$$\int_{\Omega_t} \boldsymbol{\sigma}\mathbf{n}ds = \int_{\Omega_0} J\mathbf{P}\mathbf{F}^{-T}\mathbf{N}dS, \tag{3.30}$$

Defining the Cauchy stress tensor using the spectral decomposition such that

$$\boldsymbol{\sigma} = \sum_{i=1}^{3} \sigma_i \mathbf{n}_i \otimes \mathbf{n}_i, \tag{3.31}$$

where σ_i is the eignvalue and $\mathbf{n}_i$ is the corresponding eignvector of the tensor (matrix)$\boldsymbol{\sigma}$. The Piola transformation can be reformulated as follows

$$\begin{aligned} \mathbf{P} &= J(\sum_{i=1}^{3} \sigma_i \mathbf{n}_i \otimes \mathbf{n}_i)(\mathbf{RU})^{-T}, & (3.32) \\ &= J(\sum_{i=1}^{3} \sigma_i \mathbf{n}_i \otimes \mathbf{N}_i)(\mathbf{U}^{-1}). & (3.33) \end{aligned}$$

The resulting two point tensor $\mathbf{P}$ links the reference configuration with the current configuration, whereby the Cauchy stress tensor is defined with respect to the global reference coordinates system. However, it is desirable to further define stress with respect to the material coordinate system. This is achieved by applying the inverse Piola transformation (a push-back operation) to the Cauchy stress tensor, resulting in the so-called second Piola-Kirchhoff stress tensor $\mathbf{S}$ as

$$\mathbf{S} = J\mathbf{F}^{-1}\boldsymbol{\sigma}\mathbf{F}^{-T}. \tag{3.34}$$

The second Piola-Kirchhoff stress tensor defines stress with respect to the material coordinate system. The second Piola-Kirchhoff and Cauchy stress tensors represent the same loading state, however, with respect to different coordinate systems. The Cauchy stress tensor describes stress with respect to the current, deformed configuration Ω_t, whereas the second Piola-Kirchhoff stress tensor describes stress with respect to the reference configuration Ω_0.

3.3.2 Derivation of stress

The different stress tensors are obtained by differentiating the strain energy function with respect to different strain tensors. The types of stress tensors deduced from the derivative of the scalar strain energy function rely on the choice of the strain tensor. Differentiation of the strain energy function with respect to the Green strain, that is the strain tensors with respect to the

reference configuration, leads to the second Piola-Kirchhoff stress tensor,

$$\mathbf{S}_{tissue} = \frac{\partial W_{tissue}}{\partial \mathbf{E}}. \tag{3.35}$$

The Cauchy stress tensor is obtained through

$$\boldsymbol{\sigma}_{tissue} = \mathbf{F}\frac{\partial W_{tissue}}{\partial \mathbf{E}}\mathbf{F}^T. \tag{3.36}$$

Using the chain rule, the second Piola-Kirchhoff tensor, for example in the case of isotropic material, can therefore be re-written as

$$\begin{aligned} \mathbf{S}_{tissue} &= \frac{\partial W_{tissue}(I_1, I_2, I_3)}{\partial \mathbf{E}} \\ &= \sum_{i=1}^{3} \frac{\partial W_{tissue}(I_1, I_2, I_3)}{\partial I_i} \frac{\partial I_i}{\partial \mathbf{E}}. \end{aligned} \tag{3.37}$$

A further derivation can be carried out on a deformable body with multiple constituents. To recall, the stored energies within different constituents are added linearly to obtain the total strain energy function. The total stress within a material with multiple constituents has a similar form, with the resultant second Piola-Kirchhoff tensor defined as

$$\begin{aligned} \mathbf{S}_{tissue} &= \frac{\partial W_{tissue}}{\partial \mathbf{E}} \\ &= \sum_{i=1}^{N} \frac{\partial d_i W_i}{\partial \mathbf{E}} \\ &= \sum_{i=1}^{N} d_i \frac{\partial W_i}{\partial \mathbf{E}}. \end{aligned} \tag{3.38}$$

Particular materials exhibit particular functional relationships between stress and strain. Stress-strain relationships are mathematically formulated using constitutive equations. Constitutive equations are usually derived from experimental measurements. Once the stress-strain relationship of a material is defined, the governing energy equation can be readily obtained

$$W_{tissue} = \int_{\Omega_0} \mathbf{S}_{tissue} : \mathbf{E} dV. \tag{3.39}$$

3.4 Summary

This chapter presented the theoretical fundamentals were used to model the tongue mechanics. The computational tongue model was built on the finite deformation theory. The tissue's mechanical behaviour was mathematically represented using the second Piola-Kirchhoff stress tensor. The deformation was described by the governing energy equation. In this dissertation, only deformed geometric shape is of most interest. Therefore, the path of deformation from one state to the other was not considered. In other words, the dynamics of the tongue was not considered or modelled in this study, and a quasi-static system condition was applied to the tongue model.

Chapter 4

Finite element modelling of the tongue

4.1 Modelling conditions and original data

Modelling is an idealisation process for which the underlying assumptions and conditions require clarification. The tongue is treated as a continuous media that can be represented by a volumetric finite element model. The tissue within the tongue body is considered as a nonlinear material in which the mechanical characteristics are influenced by its anatomical structures. As such, the constitutive equations, specifying the contractile properties of either one or multiple muscular families, need to be coupled with the geometric model to accurately reproduce the deformation.

The FE model of the tongue has been developed using a set of images from the female set of the Visible Human data project [Spitzer et al., 1996]. The image set consists of a collection of axial anatomical photographs (transverses plane) of which the spatial resolution is 0.33 mm $\times$ 0.33 mm and the image space is approximately 0.33 mm. The image data of the tongue was manually digitised and originally contributed by Wilhelms-Tricarico [2005]. The digitised data include three parts: a collection of the spatial coordinates of the tongue surface, the direction of each muscle family, and the volume fractions of each fibre family.

The mechanical behaviour of the tongues of different individuals may vary due to subject-

specific variations in anatomical and mechanical properties due to gender or age [Sonies et al., 1984, Pae and Lowe, 1999]. The following key conditions/assumptions are assumed in the scope of this research:

1. Only the interaction between the tongue and the upper palate is considered in the modelling framework for study swallowing.

2. The tongue model in this study aims to reflect the deformation mechanism from a pure mechanical perspective. Other possible variables, for instance the neural control system or the possible influence of temperature, are not taken into consideration.

3. The consideration of subject-specific variability of the tongue shape is limited by the available data. Large subject-specific variations in tongue shape and structure, and their possible effects on tongue mechanics, are not discussed or considered here.

4.2 Geometrical modelling

The anatomical modelling of the tongue includes two parts which are (1) a model of the geometric shape of the tongue and (2) a model of the interior fibrous architecture. The latter is coupled with the geometric shape model to provide the anatomical details of the distributions and spatially varying orientations of various fibre families.

4.2.1 The geometric model

The geometrical FE model of the tongue is used to approximate the volumetric domain of the tongue body. Within this project, cubic Hermite basis functions are used to deal with the complex surface geometry and provide a continuous strain field for the computation of tongue deformations [Bradley et al., 1997]. The fitting procedure called face fitting (FF), proposed by Bradley et al. [1997], is used in this research to refine the surface curvature of the tongue model according to the digitised image data. The face fitting technique has extensively been applied

to muscular organ modelling, for instance, in Nash and Hunter [2000] or Röhrle and Pullan [2007]. Figure 4.1 illustrates the fitted tongue model, for which all derivatives are determined using the face fitting, leading to a smooth surface of the FE mesh.

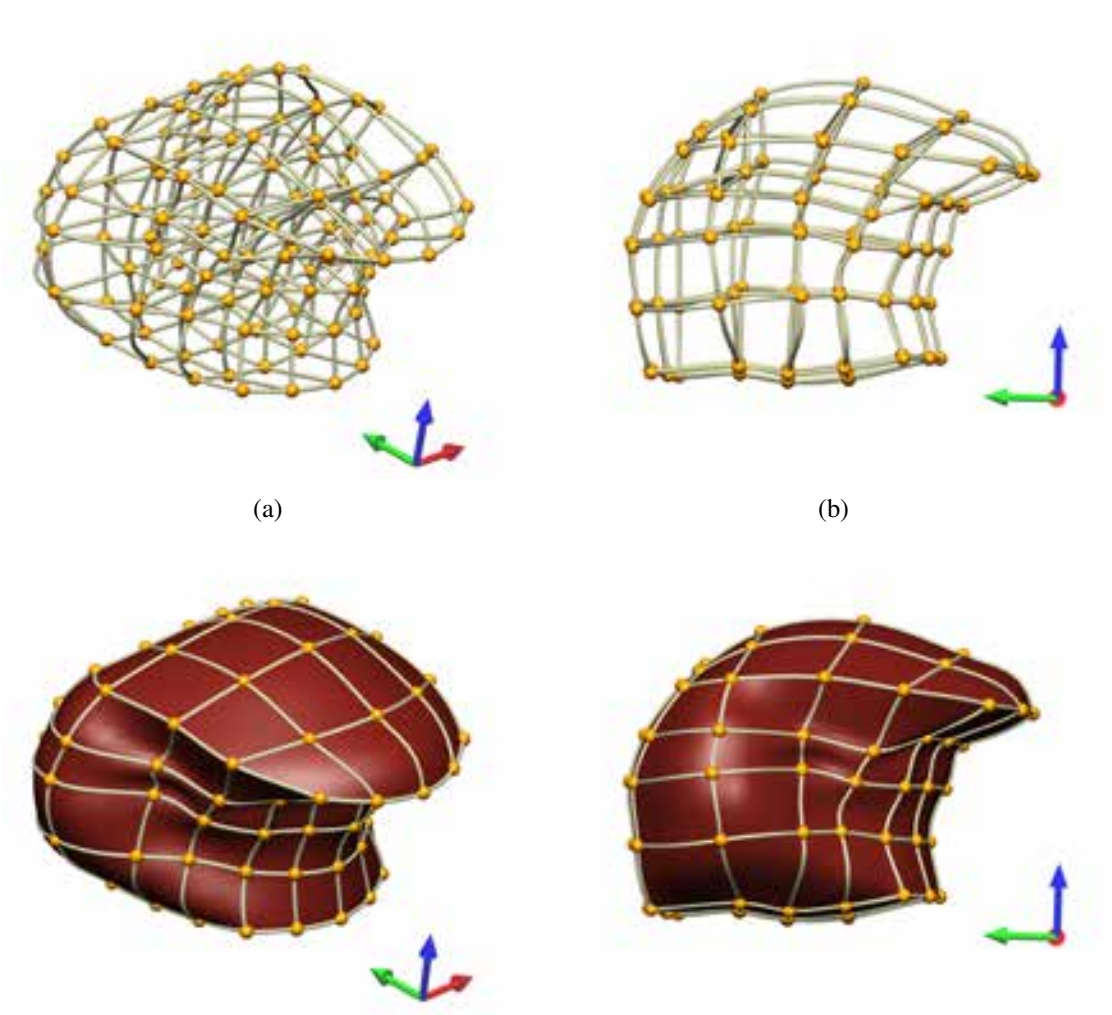

(a) (b)

(c) (d)

Figure 4.1: The geometric tongue model with interior nodes and elements. The golden nodes indicate the elemental nodes that define each element. The connectivities of nodes are represented as white cylindrical lines. The colours of the orthogonal axes outside the tongue model indicate the global coordinate system with the superior (blue), posterior (green) and lateral (red) directions.

.

4.2.2 Modelling the architecture of the tongue tissue

The tongue comprises two groups of constituents: (1) a ground matrix and (2) muscle tissue which is divided into intrinsic muscles (i.e., transversus, verticalis, superior longitudinalis

and inferior longitudinalis) and extrinsic and external muscles (such as the genioglossus anterior, genioglossus posterior, hyoglossus, styloglossus, mylohyoid and digastric). Modelling the architecture of the tongue tissue requires a mathematical description of its fibrous constituents (muscles) and the ground matrix according to their anatomical compositions presented in Chapter 2.

The fibrous constituent (muscle fibre) possesses two anatomical properties: spatially varying fibre orientations and local compositions of fibres within the tongue body. The fibre orientation is modelled as a 3D vector field that defines the fibre directions throughout the 3D geometrical tongue model. The volume composition is modelled as a weighting field throughout the geometric model, and it defines the muscle distributions within the tongue (volume fraction). The remaining substance within the 3D geometrical model is considered to be the ground matrix.

Fibrous structure fields

The anatomical properties of the fibrous constituents refer to the fibrous muscle architecture which is modelled as a collection of separate field variables. The local value of a field variable at each Gauss point can be obtained through standard interpolation.

Fibre composition and architecture fields: The muscle composition of the tongue is modelled for each fibre family i by means of volume fraction $d_{fibre,i}$. The condition $0 < d_{fibre,i} < 1$ holds for regions which contain muscle fibres; while the condition $d_i = 0$ holds for regions without muscles, respectively. At any position within the model, the local constituent composition needs to satisfy the following condition

$$d_{matrix} + \sum_{i \in \mathscr{F} = \{t,v,sl,\ldots\}}^{n} d_{fibre,i} = 1, \tag{4.1}$$

where d_{matrix} denotes the volume fraction of the ground matrix (which includes proteoglycans and fat) [Brandan, 1994, Yanagishita, 1993], and $\mathscr{F}$ is the set of muscle group indices, i.e. $\{t, v, sl, \ldots\}$.

The fibre orientation is a directional property which can be represented by a spatially varying vector field. The vector field describing the fibre orientation, is denoted as $\mathbf{a}_i$ ($||\mathbf{a}_i|| = 1$) where subscript i indicates the index of a particular muscle group. The field parameter $\mathbf{a}_i$ is composed of 3 independent scalar components in 3D space, such that $\mathbf{a}_i = (x, y, z)$. Fibre orientation and composition are described as independent field variables at each node of the geometric FE model. Therefore, a total of 4 parameters directly associates with each fibre family, $(d_{fibre,i}, x, y, z)$. The field values of these independent field variables at each node were calculated using the 3D field fitting procedure [Bradley et al., 1997].

Each fibre family has 4 data fields, including the x, y and z components of the vector $\mathbf{a}_i$, and a scalar value for defining the volume fraction. Since the tri-cubic Hermite basis functions are employed to interpolate the field values of the geometric model, the nodal values consist of 7 additional derivative fields. As a result, besides the the geometrical coordinates, the nodal parameters also include muscle orientations in 3D space with their corresponding volume fractions, and the respective derivatives for the tri-cubic Hermite interpolation scheme. Consequently, each node consists of 40 data field variables with a total of 308 derivative fields for describing the distributions and orientations of the 10 fibre families and the ground matrix.

For each fibre family, an interpolation function is introduced to interpolate the volume fraction and the components of fibre direction at the gauss point. The interpolation function is of the form $f : \mathbb{R}^4 \mapsto \mathbb{R}$ where $\mathbb{R}^4$ consists of the spatial locations $\boldsymbol{\xi}^e$ within the element and the volume fraction d at the location of $\boldsymbol{\xi}^e$. As an example, the volume fraction of the f-th fibre group in the *e-th* element is interpolated by the following functional form

$$d_{fibre,f} = f(\boldsymbol{\xi}^e, \mathbf{d}_{fibre,f}) \tag{4.2}$$

where $\boldsymbol{\xi}^e$ is the interpolated location, and $\mathbf{d}_{fibre,f}$ is the nodal values of volume fraction field of the f-th fibre group. The detailed tri-cubic interpolation scheme can be seen from Bradley et al. [1997]. The same formulation is applied to the components of vector $\mathbf{a}_f$ for each fibre group. Figure 4.2 shows the fitted fibre distribution within the tongue model with tri-cubic Hermite basis functions for all fibre fields. Vectors of the same colour represent the orientation of a

population of muscles with their magnitudes being scaled by the local volume fraction.

The fibre arrangement of the transversus muscle

In the present model, the transversus muscle mainly shows a fan-shape fibrous arrangement towards the posterior direction, see Figure 4.3. An anatomical dissection was carried out in the scope of the present work to ensure this feature is not subject-dependent.

The anatomical dissection was done on a single male cadaver, sectioned horizontally into 2.5 mm slices, and subsequently, processed using a S10 plastination technique [Weber and Henry, 1993]. The cadaver was donated to the Department of Anatomy and Structural Biology, University of Otago, New Zealand, for the purpose of teaching and research under the New Zealand Human Tissues Act 1964. During the E12 sheet plastination, the water and liquids of the tissues were replaced by curable resin at a cellular level [Johnson et al., 2000]. As a result, the *in situ* positions of all the tissues are preserved and could be examined at both macroscopic and microscopic levels.

After fixation in 10% neutral buffered formalin, the cadaver was frozen at -80 °C for more than 24 hours, and subsequently, sectioned at a thickness of 2.5 mm using a band saw. Slices were dehydrated in increasing concentrations of acetone (95% to 100%) at -30 °C for 6 weeks and degreased at 22 °C to 24 °C for 2 weeks. Subsequently, the slices were immersed in a polymer mixture and placed in a vacuum container at 0 °C for 24 hours. The polymer mixture consisted of Biodur E12/E1/AE10/AE30 (100:28:20:5, parts by weight; Biodur, Heidelberg, Germany). Finally, the slices were laid between plastic sheets and cured at 32 °C and 45 °C for 1 week before being examined under a dissecting microscope.

Figure 4.4 shows the horizontal dissection image (transverse plane) of the human tongue tissue. In the posterior region, where the styloglossus and transversus muscles are inter-digitate, the fibrous arrangements can clearly be identified as fan shape towards the posterior direction. The orientations of fibres in this region are not perfectly arranged in the medial-lateral direction. This indicates that the transversus muscle is not orientated along the same direction throughout

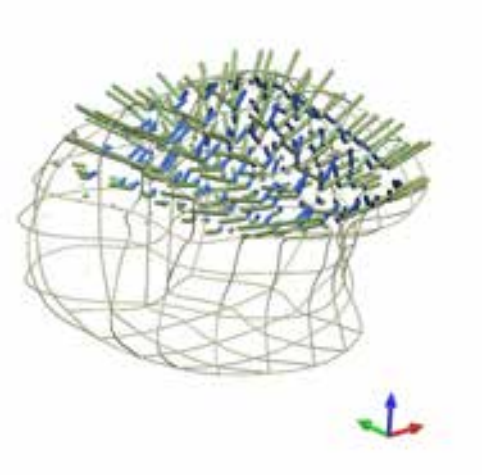

(a) Transversus (green) and verticalis (blue) muscles

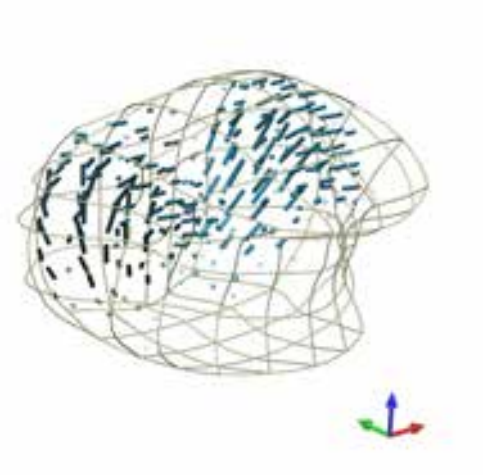

(b) Hyoglossus muscle

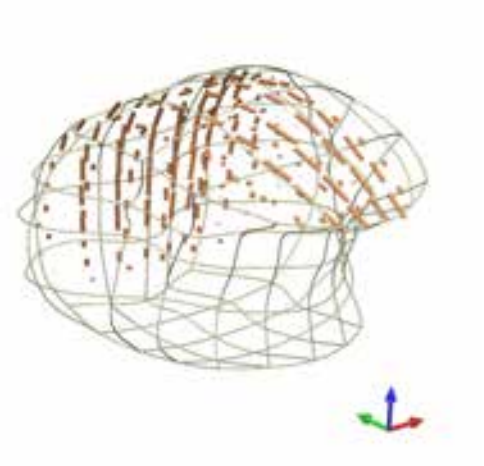

(c) Longitudinalis muscle

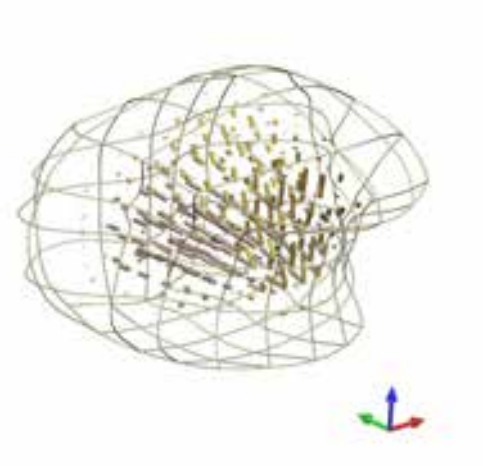

(d) Genioglossus muscle

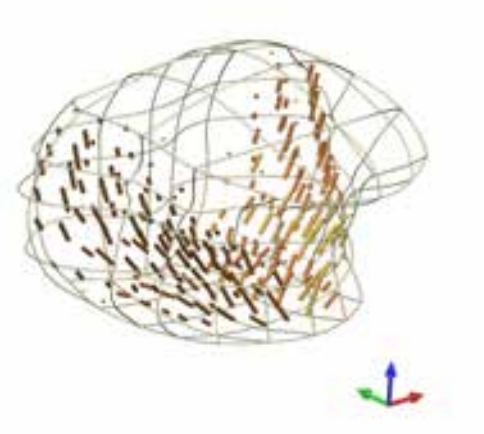

(e) Mylohyoid muscle

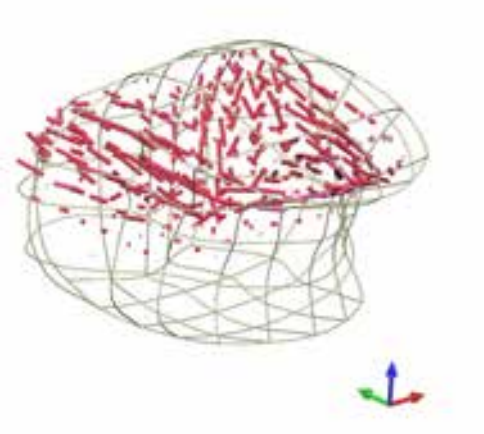

(f) Styloglossus muscle

Figure 4.2: The fibrous structure fitted within the geometric tongue model. The solid cylinder represent the local fibre directions at each spatial location. The length of each cylinder is scaled by the corresponding volume fraction. The colours of the orthogonal axes outside the tongue model indicate the orientation of each sub-figure and have no linkage with the fibres.

.

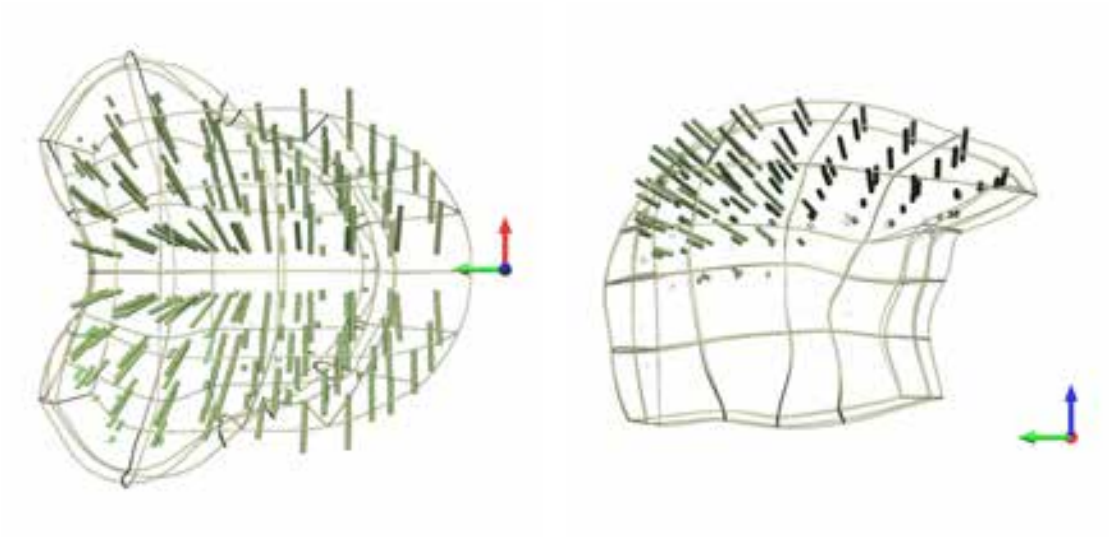

(a) (b)

Figure 4.3: The fibrous structure of the transversus muscle within the geometric tongue model. The solid green cylinders represent the local fibre directions at each spatial location. The length of each cylinder is scaled by the corresponding volume fraction. The colours of the orthogonal axes outside the tongue model indicate the orientation of each sub-figure and have no linkage with the fibres.

.

the entire tongue body, shifting from a medial-lateral to an anterior-posterior direction. Most importantly, the anatomical dissection showed the same fibrous structure of the transversus muscle as observed in the tongue model.

Description of the ground matrix field and functional segments

The ground matrix provides the support structure for the embedded muscle fibres. The stress contribution of the ground matrix depends on the local volumetric compositions d_{matrix}, which can be obtained through $1 - \sum_{i \in \mathscr{F} = \{t,v,sl,\ldots\}} d_{fibre,i}$.

As mentioned in Section 2.3.4, there are some experimental reports showing that, the tongue muscles may exhibit a heterogeneous contraction pattern, the so-called functional segment control, during speech or swallowing. The functional segment of a muscle group can be seen as a series of additional field variables which define the internal stresses due to muscle contraction. The functional segment is thereby commonly considered as a "switch" variable taking 0 and 1 as possible values. The switch variable is denoted by $s_{fibre,i,j}$, where subscript j is the

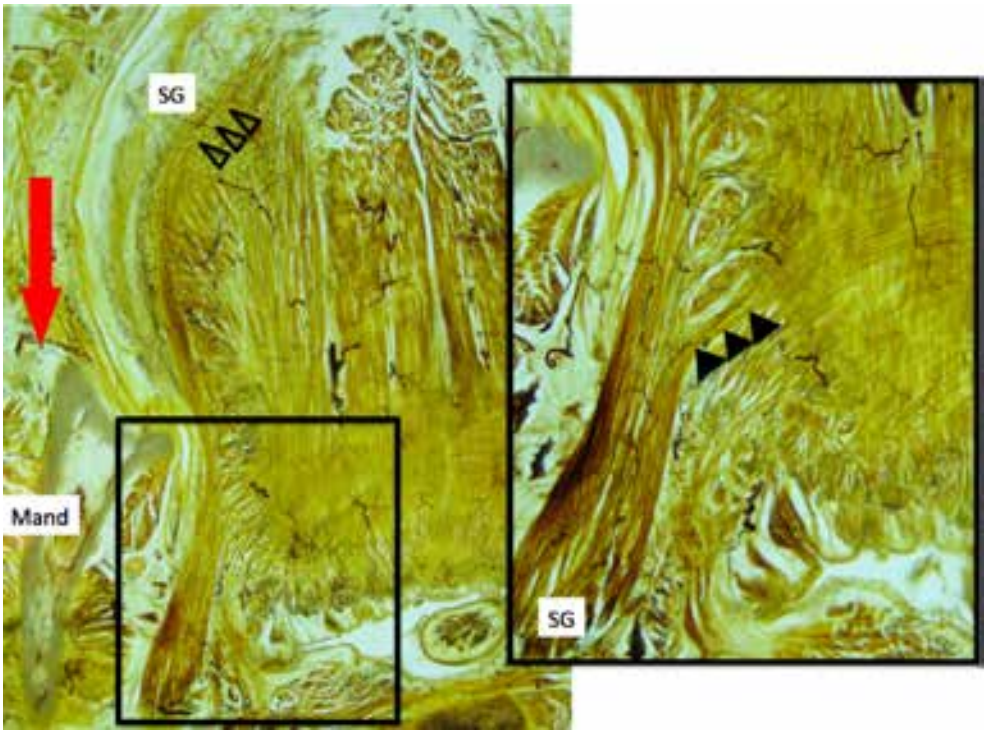

Figure 4.4: Horizontal plastinated section of a human cadaveric tongue, showing styloglossus muscle fibres SG reaching to the tip of the tongue (open arrows). The enlarged area is of the base of the tongue, showing styloglossus fibres branching off to reach across the posterior dorsum (closed arrows). The red arrow points in the posterior direction. Photos taken by Prof. Jules Kieser at University of Otago, used with permission.

segment index of the *i-th* fibre population. The condition $s_{fibre,i,j} = 0$ holds for Gauss points in non-activated segments; while $s_{fibre,i,k} = 1$ with $j \neq k$ holds for Gauss points in activated segments.

Unlike a continuous field, e.g. volume fraction, the functional fields are discontinuous. Therefore, a look-up table is used to define whether the functional segment variable at each Gauss point is switched on or off during computation. A detailed explanation of how the variable influences the muscular mechanical characteristics is presented in Chapter 4.3.3.

4.3 Constitutive modelling

Within the tongue, multiple muscle fibres connect tightly to each other and drive the entire body deformation by means of single or multiple fibre contractions. From a mechanical modelling

point of view, the aim is to reproduce the nodal movement by pre-defining the stress-strain relationship of tongue tissue (constitutive equations). The constitutive equations aim to capture the mechanical characteristics of the fibrous muscle tissue within the tongue, and account for all mechanical factors that could influence the resultant stress due to contraction. In this section, the basic properties of the tongue muscles are summarised first. A constitutive equation, accounting for multiple constituents, which models the contractile properties of muscle fibres and the passive mechanical properties within muscle tissue, is then proposed. Finally, the detailed computational implementation of the constitutive equation is presented.

4.3.1 The mechanical properties of tongue muscles

The first characteristics of the tongue muscle, addressed in this section, is volume conservation. In 1663, Swammerdam provided the first evidence that the volumes of skeletal muscles are maintained during deformation due to active contraction or external loading [Needham and Needham, 1971]. This phenomena is commonly known as the volumetric conversation property of skeletal muscles. Tongue tissue has been hypothesised to possess volumetric conservation properties based on observations by Smith and Kier [1989], Kier [1988], Thompson et al. [1998] and more recently by Kairaitis [2010].

Napadow et al. [1999a] made an initial attempt to verify the volume conservation property of tongue tissue using tagged-MRI. In their study, the local axial and principal strains were deducted through deformed tags on the images. In their case study, it was observed that the axial strain due to tongue elongation possessed predominately positive strains in the anterior-posterior direction, whereas negative strain patterns were present in superior-inferior direction. The authors concluded that, under the assumption of volume conversation of the tissue, the co-activation of the transversus and the verticalis muscles may drive the compressing like deformation in the superior-inferior and medial-lateral directions; and tongue tissue may possibly only expand along the anterior-posterior direction due to its volumetric conversation property.

In addition to the volumetric conversation property, the tongue can be considered as a hypere-

lastic material. Gerard et al. [2005] performed a series of *ex-vivo* indentation testing on human lingual tissue. The experimental data could be approximated using the functional form of the Mooney-Rivilin model, for which the stress levels exponentially increase with the rise in strain levels. The deformation due to indentation did not depend on the loading history, but only on the current loading condition. Once the force was removed, the shape of the tongue resumed its original state. In continuum mechanics, this property is also referred to as hyperelasticity.

In addition to the hyperelastic and volumetric conservation properties, the mechanical properties of multiple muscle groups affect the deformation of the tongue body. Thus, the tongue muscle can be considered an incompressible hyperelastic biological soft tissue with heterogenous mechanical properties due to complex internal fibre arrangements.

4.3.2 Multi-fibre reinforced constitutive model

The constitutive model of soft tissue (e.g. muscle) refers to a mathematical equation that describes the degree of tissue deformation corresponding to a certain level of loading. In case of muscles, loading forces are produced by active contraction or passive response due to stretching. Constitutive models in continuum biomechanics are commonly derived from experimental quantification of the changes in stress with increasing strain, and are referred to as stress-strain relationships. The stress-strain relationship of a tissue is fundamental for modelling its mechanical behaviour.

Two different mathematical forms have been adopted to model the constitutive relationship of a particular tissue: phenomenological forms and structurally-based forms. Phenomenological models were widely used in early research, for instance, in the nonlinear power form of the force-length relationship described in Bogen [1987], Ogden [1997] or the exponential form of the force-length relationship in Fung and Liu [1989]. Phenomenological models provided an initial attempt to quantitatively explain the nonlinear properties of muscle tissue. However, they did not account for the influences of fibrous structures on the overall stress-strain relationship.

A structurally-based modelling has further considered the fibrous influence as a factor in the

mathematical form of the stress-strain relationship. Based on a series of experimental measurements, Burkholder et al. [1994] reported that fibre length and fibre type distribution were the most functionally significant parameters in determining skeletal muscle mechanics, whereas the architectural properties of fibres were found to be the most structurally significant parameters. In a later study, Murray et al. [2000] measured the muscles crossing the human elbow, and presented further evidence that the functional capabilities of a muscle depend on its architecture.

Several studies have aimed to model the anisotropic behaviour of muscle tissue due to its complex fibrous muscle arrangement. Hayashi et al. [1974], Lanir [1983], He and Roach [1994] introduced additional structural weighting factors (so-called volume fractions) to quantify unequal composition ratios of various constituents. [Holzapfel et al., 2000b, Gasser et al., 2006, Holzapfel and Ogden, 2009] and Van Loocke et al. [2008] focused on the development of a structurally-based form of the stress-strain relationship of soft tissues. Based on modelling results, Holzapfel [2000a] concluded that the total stress within biological soft tissue is the sum of the contributions from various muscular constituents, including the ground matrix and individual fibres, and interactions between fibres. Furthermore, previous work by Murray et al. [2000], Huijing [1999], Zajac [1989], Allinger et al. [1996] and Blemker et al. [2005] adopted mechanics models of skeletal muscles to investigate the causes of non-uniform strain patterns within muscles fascicles. In Blemker et al. [2005]'s study, the resulting stress along the fibre direction depend on the strain along the same direction, and stress is concluded to be a linear sum of an activation stress (concentric contraction) and a passive stress.

In this research, it was assumed that multiple muscles within the tongue body can be treated as a whole entity for the structural form of the constitutive relationship. This assumption was drawn because the scale of tongue muscle fibres (12 μm) is far smaller than the resolution of the available image data (0.33 mm $\times$ 0.33 mm $\times$ 0.33 mm). As proposed by Holzapfel [2000a], the strain-energy function of muscle tissue was regarded as a summation of multiple parts: the gel-like ground matrix, the families of muscular fibres, and the interactions between these components [Holzapfel, 2002]. As part of Holzapfel's work on modelling the mechanics of the

arterial wall [Holzapfel et al., 2000b, Holzapfel, 2002], an implicit framework for the stress-strain response of hyperelastic materials with up to two fibre families was introduced. Based on this model, the stress at any material point was derived as the sum of the stress contributions of the two fibres and the ground matrix. In other words, the stress was regarded as elastic energy stored within two major constituents, the isotropic and anisotropic parts.

The modelling framework proposed by Holzapfel has been widely accepted for modelling soft tissues of biological structures [Menzel, 2005, Driessen et al., 2005, Hariton et al., 2007]. In the present study of tongue modelling, the 10 fibre groups and the ground matrix were modelled as a continuum, rather than as a group of discrete components. Therefore, a further extension of Holzapfel et al. [2000b]'s model had to be considered. In particular, it was assumed that the total stored energy can be quantitatively divided according to the tissue composition. Hence, the composition of the tissue at all spatial locations was considered key to understanding its mechanical behaviour during deformation.

Spencer [1972] and Holzapfel [2002] stated that a transverse isotropic material, which is a homogeneous isotropic material with single fibre reinforcement, can be modelled in a functional form as

$$W(I_1, I_2, I_3, I_4, I_5), \tag{4.3}$$

where

$$I_4 = \mathbf{a}_1 \cdot \mathbf{C}\mathbf{a}_1, \tag{4.4}$$

$$I_5 = \mathbf{a}_1 \cdot \mathbf{C}^2\mathbf{a}_1. \tag{4.5}$$

In the deformed configuration Ω_t, the fibre direction $\mathbf{a}_1$ is updated by applying the deformation gradient tensor $\mathbf{F}$ as follows

$$\mathbf{a}_{t,1} = \mathbf{F}\mathbf{a}_1. \tag{4.6}$$

Following the above, the strain energy function of a two fibre-family reinforced, hyperelastic material can be written as

$$W(I_1, I_2, I_3, I_4, I_5, I_6, I_7, I_8, I_9), \tag{4.7}$$

where

$$I_6 = \mathbf{a}_2 \cdot \mathbf{C}\mathbf{a}_2, \tag{4.8}$$

and according to the theory of invariants, e.g. Spencer [1972],

$$I_7 = \mathbf{a}_2 \cdot \mathbf{C}^2\mathbf{a}_2; \tag{4.9}$$

$$I_8 = (\mathbf{a}_1 \cdot \mathbf{a}_2)\mathbf{a}_1 \cdot \mathbf{C}\mathbf{a}_2; \tag{4.10}$$

$$I_9 = (\mathbf{a}_1 \cdot \mathbf{a}_2)^2. \tag{4.11}$$

The stress can simply be derived through differentiating the strain energy function with respect to the invariants. Using the chain rule, one obtains for transversely isotropic materials

$$\begin{aligned} \mathbf{S} = 2\Bigg[&\left(\frac{\partial W}{\partial I_1} + I_1\frac{\partial W}{\partial I_2}\right)\mathbf{I} - \frac{\partial W}{\partial I_2}\mathbf{C} + I_3\frac{\partial W}{\partial I_3}\mathbf{C}^{-1} + \\ &\frac{\partial W}{\partial I_4}\mathbf{a}_1 \otimes \mathbf{a}_1 + \frac{\partial W}{\partial I_5}(\mathbf{a}_1 \otimes \mathbf{C}\mathbf{a}_1 + \mathbf{a}_1\mathbf{C} \otimes \mathbf{a}_1)\Bigg]; \end{aligned} \tag{4.12}$$

and for a material with a two-fibre-family reinforcement,

$$\begin{aligned} \mathbf{S} = 2\Bigg[&\left(\frac{\partial W}{\partial I_1} + I_1\frac{\partial W}{\partial I_2}\right)\mathbf{I} - \frac{\partial W}{\partial I_2}\mathbf{C} + I_3\frac{\partial W}{\partial I_3}\mathbf{C}^{-1} + \\ &\frac{\partial W}{\partial I_4}\mathbf{a}_1 \otimes \mathbf{a}_1 + \frac{\partial W}{\partial I_5}(\mathbf{a}_1 \otimes \mathbf{C}\mathbf{a}_1 + \mathbf{a}_1\mathbf{C} \otimes \mathbf{a}_1) + \frac{\partial W}{\partial I_6}\mathbf{a}_2 \otimes \mathbf{a}_2 + \\ &\frac{\partial W}{\partial I_7}(\mathbf{a}_2 \otimes \mathbf{C}\mathbf{a}_2 + \mathbf{a}_2\mathbf{C} \otimes \mathbf{a}_2) + \frac{\partial W}{\partial I_8}(\mathbf{a}_1 \cdot \mathbf{a}_2)(\mathbf{a}_1 \otimes \mathbf{a}_2 + \mathbf{a}_2 \otimes \mathbf{a}_1)\Bigg]. \end{aligned} \tag{4.13}$$

A similar form may be derived in the case of multiple fibre reinforcements.

It is assumed that a fibre is a line-object. In other words, the deformation of a unit length of fibre will only occur in the along-fibre direction. This assumption is based on the observation that most energy due to stretching is stored in the fibre direction and the energy in the other two orthogonal directions can be neglected, i.e. $\mathbf{I}_8$ and $\mathbf{I}_9$ do not consider here. Since the interaction between fibres is not considered, the total strain energy function of a tissue with 2 fibres can be expressed in a functional form as $W_{tissue}(I_1, I_2, I_3, I_4, I_6)$. The stretch ratio λ of a fibre with unit

length can be obtained through

$$I_{fibre,i} = \lambda_i^2 = \mathbf{F}\mathbf{a}_i \cdot \mathbf{F}\mathbf{a}_i = \mathbf{a}_i \cdot \mathbf{C}\mathbf{a}_i. \tag{4.14}$$

From this, a simplified version of the implicit strain energy function for tissues with multi-fibre reinforcement can be formulated as

$$W_{tissue}(I_1, I_2, I_3, I_{fibre,1}, \cdots I_{fibre,n}), \tag{4.15}$$

where n is the total number of involved fibre families.

Since the interior strain energies of various constituents can be linearly summed, the overall strain energy function with multiple fibres can be written as

$$W_{tissue}(I_1, I_2, I_3, I_{fibre,1}, \cdots I_{fibre,n}) = d_{matrix} W_{matrix}(I_1, I_2, I_3) + \sum_{i \in \mathscr{F}} d_{fibre,i} W_{muscle}(I_{fibre,i}). \tag{4.16}$$

The tissue's stress-strain relationship $\mathbf{S}_{tissue}$ is subsequently obtained through the differentiation of the strain energy function W_{tissue} with respect to strain. By the chain rule, the following is obtained

$$\begin{aligned} \mathbf{S}_{tissue} &= 2 d_{matrix} \sum_{i=1}^{3} \frac{\partial W_{matrix}}{\partial I_i} \frac{\partial I_i}{\partial \mathbf{C}} + 2 \sum_{i \in \mathscr{F}} d_{fibre,i} \frac{\partial W_{fibre}}{\partial I_{fibre,i}} \frac{\partial I_{fibre,i}}{\partial \mathbf{C}} \\ &= d_{matrix} \mathbf{S}_{matrix} + \sum_{i \in \mathscr{F}} d_{fibre,i} \mathbf{S}_i, , \end{aligned} \tag{4.17}$$

where $\mathbf{S}_{matrix}$ represents the constitutive mechanical response of the ground matrix, $\mathscr{F} = \{t, v, sl, \ldots\}$ denotes the set of muscle indices, and $\frac{\partial W_{fibre}}{\partial I_{fibre,i}} \frac{\partial I_{fibre,i}}{\partial \mathbf{C}} = \mathbf{S}_i$ denotes the stress-strain relationship of each group of muscle fibres and can be seen as the passive and active stress contributions to the overall stress.

4.3.3 Passive and active constitutive equations

Passive constitutive equations

The passive constitutive equation is a mathematical representation of the tissue's passive, internal stress response due to external loads or fibre contraction. The overall passive stress of the tongue can be defined as the sum of stress contributions from the various populations of muscle fibres and the gel-like ground matrix as follows

$$\frac{\partial \mathbf{W}_{tissue,passive}}{\partial \mathbf{E}} = d_{matrix}\frac{\partial \mathbf{W}_{matrix}}{\partial \mathbf{E}} + \sum_{i\in\mathscr{F}} d_{fibre,i}\frac{\partial \mathbf{W}_{i,passive}}{\partial \mathbf{E}}$$
$$\mathbf{S}_{tissue,passive} = d_{matrix}\mathbf{S}_{matrix} + \sum_{i\in\mathscr{F}} d_{fibre,i}\mathbf{S}_{i,passive}. \tag{4.18}$$

The ground matrix can only be deformed by being passively stretched through external loading. The ground matrix is assumed to be a rubber-like isotropic material which is modelled using the Mooney-Rivlin stress-strain relationship. The 2$^{\text{nd}}$ Piola-Kirchhoff stress tensor $\mathbf{S}_{matrix}$ for such a material is given by

$$\mathbf{S}_{matrix} = 2(c_1 + c_2 tr(\mathbf{C}))\mathbf{I} - 2c_2\mathbf{C} + p\mathbf{C}^{-1}, \tag{4.19}$$

where c_1 and c_2 are the two material parameters for the Mooney-Rivlin model, and p is the hydrostatic pressure obtained from the constraint condition of incompressibility. Volume conservation of the tongue tissue is a critical assumption in the modelling of its geometrical deformation. From a mathematical perspective, an extra constraint term has to be added to the constitutive equation for modelling the hydrostatic field inside the tissue which accounts for volume conservation. The constraint condition proposed by Nash and Hunter [2000] is adopted in this research to model the volume conservation of the tissue

$$\int_{V_e} (\sqrt{I_3} - 1)\psi^P J \, dV_e = 0, \tag{4.20}$$

where ψ^p is the basis function for interpolating the hydrostatic pressure field, and $J = \det(\mathbf{F})$, evaluated with respect to the reference configuration.

The passive stress contribution from multiple fibres forms the major nonlinear anisotropic part of the overall stress in the tissue. The directional properties of fibres cannot be ignored, given that a portion of input energy from tissue loading will be stored within the deformed fibres. In continuum mechanics, the strain-energy function of a single fibre is considered as $W_{fibre,i}(\mathbf{E}, \mathbf{a}_i)$. Differentiating $W_{fibre,i}(\mathbf{E}, \mathbf{a}_i)$ with respect to $\mathbf{E}$ yields the 2$^{\text{nd}}$ Piola-Kirchhoff stress tensorin 3D space, such as

$$\mathbf{S}_{i,passive} = \frac{\partial W_{fibre,i}(\mathbf{E}, \mathbf{a}_i)}{\partial \mathbf{E}}. \tag{4.21}$$

Note that the fibre is assumed to be a 1D object. By the chain rule, the above equation can be expanded as [Holzapfel, 2000a]

$$\begin{aligned} \mathbf{S}_{i,passive} &= 2\frac{\partial W_{fibre,i}}{\partial I_{fibre,i}}\frac{\partial I_{fibre,i}}{\partial \mathbf{C}} \\ &= \frac{1}{\lambda_i}\frac{\partial W_{fibre,i}}{\partial \lambda_i}\mathbf{a}_i \otimes \mathbf{a}_i \\ &= \frac{\sigma_{i,passive}}{\lambda_i^2}\mathbf{a}_i \otimes \mathbf{a}_i, \end{aligned}$$

where $\sigma_{i,passive}$ is the Cauchy stress along the fibre direction. The Cauchy stress is usually obtained from direct experimental measurements, and it reflects the fibre stresses corresponding to different levels of deformation/strain along the fibre direction.

Based on experimentally measured data, Blemker et al. [2005] proposed the following functional form of the Cauchy stress of a skeletal muscle fibre

$$\sigma_{i,passive} = \sigma_{max}\, f_{passive}(\lambda_i), \tag{4.22}$$

where σ_{max} is the maximum stress in fibre direction, and $f_{passive}(\lambda_i)$ is the normalised passive stress function which depends on the fibre stretch λ. Note that the maximum stress in the fibre direction needs to be experimentally obtained. However, no literature to date has reported

on stress-strain measurements for the tongue. Since tongue muscles fall into the category of skeletal muscles, the experimental results by Blemker et al. [2005] are adopted in the present research. The normalised passive force along fibre direction is then defined as [Blemker et al., 2005]

$$f_{passive}(\lambda) = \begin{cases} 0 & \lambda \leq \lambda_{ofl} \\ P_1(\exp^{P_2(\lambda/\lambda_{ofl}-1)}-1) & \lambda_{ofl} < \lambda \leq \lambda^*, \\ P_3\lambda/\lambda_{ofl} + P_4 & \lambda > \lambda^* \end{cases} \tag{4.23}$$

where P_1, P_2, P_3 and P_4 are parameters ensuring the best fit of the equation to the experimental data, λ^* represents the fibre stretch at which the $f_{passive}$ becomes linear, λ_{ofl} is the optimal fibre stretch occurred when fibres stress reaches σ_{max}. The parameter values used in this project will be presented in Section 4.5.2.

Active constitutive equations

From a mechanical point of view, the activation of muscles can be considered as an additional contractile force produced by muscle fibres. Similar to the functional form of the passive response, active stress relates to tissue strain. Hill [1938] first presented comprehensive results on the relationship between muscle force and muscle length. In Hill [1938]'s model, the contractile stress is idealised by a force which constitutes a contractile element and two non-linear spring elements, one in series and the other in parallel. The Hill-type model has found widespread use to mathematically approximate the contractile stress in muscle fibres due to muscle contraction [Hill et al., 1975, Meijer et al., 1998, Lloyd and Besier, 2003].

Gareis et al. [1992] and Baratta et al. [1993] measured different sample tissues under isometric conditions and found a large variability in the force-length relationship due to differences in the architecture of fibre populations. The following model was proposed by Otten [1987]

$$F = \exp(-(\frac{(\varepsilon+1)^\beta - 1}{w})^p), \tag{4.24}$$

where F is the normalised active force, ε is the muscle fibre strain, and β, p and w are called skewness, roundness and width constants, describing the shape of the force-length relationship. Baratta et al. [1993] proposed a generalised relationship for multiple fibre populations that is

$$F = \sum_j K_j \exp(-(\frac{(\varepsilon+1)^\beta - 1}{w})^p), \tag{4.25}$$

whereby the additional parameter K_j represents the proportional contributions of individual fibre populations to the overall active force. Gareis et al. [1992] and Baratta et al. [1993] noted that the active force is larger than the passive force during contraction, until it reaches a state of equilibrium. Baratta et al. [1993] presented a plot of active muscle force against fibre strain based on fitted experimental data which showed a bell-shaped curve that could be approximated by a second-order function.

In this thesis, contractile stress is considered as an additional superimposed stress along the fibre direction as proposed in Hunter et al. [1997], and the stress contributions from multiple fibrous families are considered as additive as proposed by Gareis et al. [1992] and Baratta et al. [1993]. In other words, contractile stress contributions from activated muscle fibres are treated as an additional energy term, which directly influences the overall strain-energy function as follows

$$W_{tissue} = \sum_{i \in \mathscr{F}} d_{fibre,i} \left(W_{i,passive}(\mathbf{C}, \mathbf{a}_i) + W_{i,active}(\alpha_i, \mathbf{C}, \mathbf{a}_i) \right). \tag{4.26}$$

Differentiating the energy function $W_{i,active}$ with respect to the invariant $I_{fibre,i}$ yields the same functional form of the active stress term as obtained for passive stress, that is

$$\mathbf{S}_{i,active} = \alpha_i \frac{\sigma_{i,active}}{\lambda_i^2} \mathbf{a}_i \otimes \mathbf{a}_i, \tag{4.27}$$

where α_i is the activation level parameter of the *i-th* fibre family, and $\sigma_{i,active} = \sigma_{max}\, f_{active}(\lambda_i)$,

where [Blemker et al., 2005]

$$f_{active}(\lambda) = \begin{cases} -\frac{25}{4\lambda_{ofl}^2}\lambda^2 + \frac{25}{2\lambda_{ofl}}\lambda - 5.25 \\ \qquad 0.6\lambda_{ofl} \leq \lambda < 1.4\lambda_{ofl} \\ 0 \qquad\qquad\qquad\qquad\qquad \text{otherwise.} \end{cases} \tag{4.28}$$

The parameter values used in the tongue model will be presented in Section 4.5.2.

As outlined in Section 4.2.2, a discontinuous functional segment field is added to the geometric model to define the activity level at each Gauss point. The functional segment field relates directly to the internal contractile stress $\mathbf{S}_{i,active}$. Defining the functional segment variable as $s_{fibre,i}$ of the *i-th* fibre family, the active stress in Equation 4.27 can be modified as

$$\mathbf{S}_{i,active} = s_{fibre,i}(\mathbf{X})\alpha_i \frac{\sigma_{i,active}}{\lambda_i^2}\mathbf{a}_i \otimes \mathbf{a}_i \tag{4.29}$$

If the functional segment in the *i-th* muscle group is present, then $s_{fibre,i} = 1$.

In summary, the overall muscle stress can then be represented as

$$\begin{aligned} \mathbf{S}_{tissue} &= d_{matrix}\mathbf{S}_{matrix} + \sum_{i\in\mathscr{F}} d_{fibre,i}\left(\frac{\sigma_{i,passive} + s_{fibre,i}\alpha_i\sigma_{i,active}}{\lambda_i^2}\right)\mathbf{a}_i \otimes \mathbf{a}_i & (4.30) \\ &= d_{matrix}\mathbf{S}_{matrix} + \sum_{i\in\mathscr{F}} d_{fibre,i}\left(\frac{\sigma_{fibre,i}}{\lambda_i^2}\right)\mathbf{a}_i \otimes \mathbf{a}_i. & (4.31) \end{aligned}$$

In a deformed configuration (current configuration) due to activations of multiple or single muscles ($\alpha_i > 0$), the total energy stored in the muscle can be expressed in terms of the active and passive stress components, such that

$$W_{tissue} = \int_{\Omega_0} d_{matrix}\mathbf{S}_{matrix} : \mathbf{E}dV + \sum_{i\in\mathscr{F}} \int_{\Omega_0} d_{fibre,i}\left(\mathbf{S}_{i,passive} + \mathbf{S}_{i,active}\right) : \mathbf{E}dV. \tag{4.32}$$

In the absence of other external loads, such as the gravitational force, the deformed configura-

tion of the muscle satisfies the following condition

$$\min_{\mathbf{u}\in\Upsilon} W_{tissue} = \int_{\Omega_0} \mathbf{S}_{tissue,passive} : \mathbf{E} dV + \sum_{i\in\mathscr{F}} \int_{\Omega_0} d_{fibre,i} \mathbf{S}_{i,active} : \mathbf{E} dV, \tag{4.33}$$

where $\mathbf{u}$ is the stable solution of the geometric degree of freedom, e.g. the displacement, and Υ is the function space of the solution $\mathbf{u}$. The condition in Equation 4.33 implies that, in the deformed configuration, the total energy stored in the muscle is not zero, but a sum of energies produced by passive stretching and active contraction.

4.4 Computational implementation of the constitutive model

The governing equations of finite elasticity for the FE tongue model are solved using the software package CMISS (Continuum Mechanics, Image analysis, Signal processing and System Identification), which is developed and maintained at the Auckland Bioengineering Institute, University of Auckland, New Zealand. The computational core of CMISS is called CM, which allows to assemble the FE system and iteratively solve the linear system of equations. The framework of CM was originally designed for modelling cardiac tissue, only supporting the use of just one family of fibres. In the scope of the present work, further development of the computational platform CM was required for defining the constitutive equation of the non-uniformly distributed, multiple-fibrous structure of the tongue. The source code of CM was modified such that each Gauss point could capture the material properties of the tongue based on the existing computational infrastructure.

4.4.1 Coordinate systems for computation

The computational structure of CM follows the definitions and computational form proposed by Costa et al. [1996a,b] and Nash [1998]. Multiple coordinate systems are designed to define material symmetry (the symmetry of stress and strain), and a series of coordinate transformations have to be performed for the computation of stresses and strains. During computation,

stresses and strains need to be defined with respect to a local, material coordinate system. Thus, the theoretical form of the constitutive equation (Equation 4.31) in the tongue model cannot be directly evaluated, since all stress terms and fibre directions are defined with respect to the global coordinate system. At first, all variables which are related to stress and strain have to be defined with respect to the material coordinate system.

Following Costa et al. [1996a,b] and Nash [1998]'s definition of coordinate systems, let $\mathbf{e}^g = [\mathbf{e}_1^g, \mathbf{e}_2^g, \mathbf{e}_3^g]$ denote the basis vectors of the global coordinate system indicated by superscript g. A material coordinate system $\mathbf{e}^m$ can then be derived from the vectors of the *1st* derivatives along the 3 material lines, such as

$$\mathbf{m}_1 = \frac{\partial \mathbf{x}(\boldsymbol{\xi}^e)}{\partial \boldsymbol{\xi}^e} \cdot \mathbf{e}_1^g, \mathbf{m}_2 = \frac{\partial \mathbf{x}(\boldsymbol{\xi}^e)}{\partial \boldsymbol{\xi}^e} \cdot \mathbf{e}_2^g, \mathbf{m}_3 = \frac{\partial \mathbf{x}(\boldsymbol{\xi}^e)}{\partial \boldsymbol{\xi}^e} \cdot \mathbf{e}_1^g, \tag{4.34}$$

whereby the basis vectors of the material coordinate system ($\mathbf{e}_1^m$, $\mathbf{e}_2^m$ and $\mathbf{e}_3^m$) can be defined as

$$\mathbf{e}_1^m = \mathbf{m}_1; \tag{4.35}$$

$$\mathbf{e}_2^m = \mathbf{m}_1 \times \mathbf{m}_2; \tag{4.36}$$

$$\mathbf{e}_3^m = \mathbf{m}_1 \times \mathbf{e}_2^m. \tag{4.37}$$

The overall stress within the material is assumed to be the sum of the isotropic part from the ground matrix and the anisotropic part from the muscle fibres. As such, the mechanical characteristics of a tissue with a single fibre reinforcement is dominated by one fibre direction that constrains the material stiffness and defines the direction of contraction.

In classical mechanics, it is common to define any additional fibre stress (passive and active) in the diagonal entries of the stress tensor. In the scope of the present work, an additional fibre-embedded coordinate system $\mathbf{e}^f$ is defined with one of its axes parallel to the fibre direction. A transformation of coordinates from the material coordinate system $\mathbf{e}^m$ to the fibre-embedded coordinate system $\mathbf{e}^f$ is then achieved through the transformation matrix $\mathbf{T}_{m,f}$ as follows

$$[\mathbf{e}_1^f, \mathbf{e}_2^f, \mathbf{e}_3^f] = \mathbf{T}_{m,f}[\mathbf{e}_1^m, \mathbf{e}_2^m, \mathbf{e}_3^m], \tag{4.38}$$

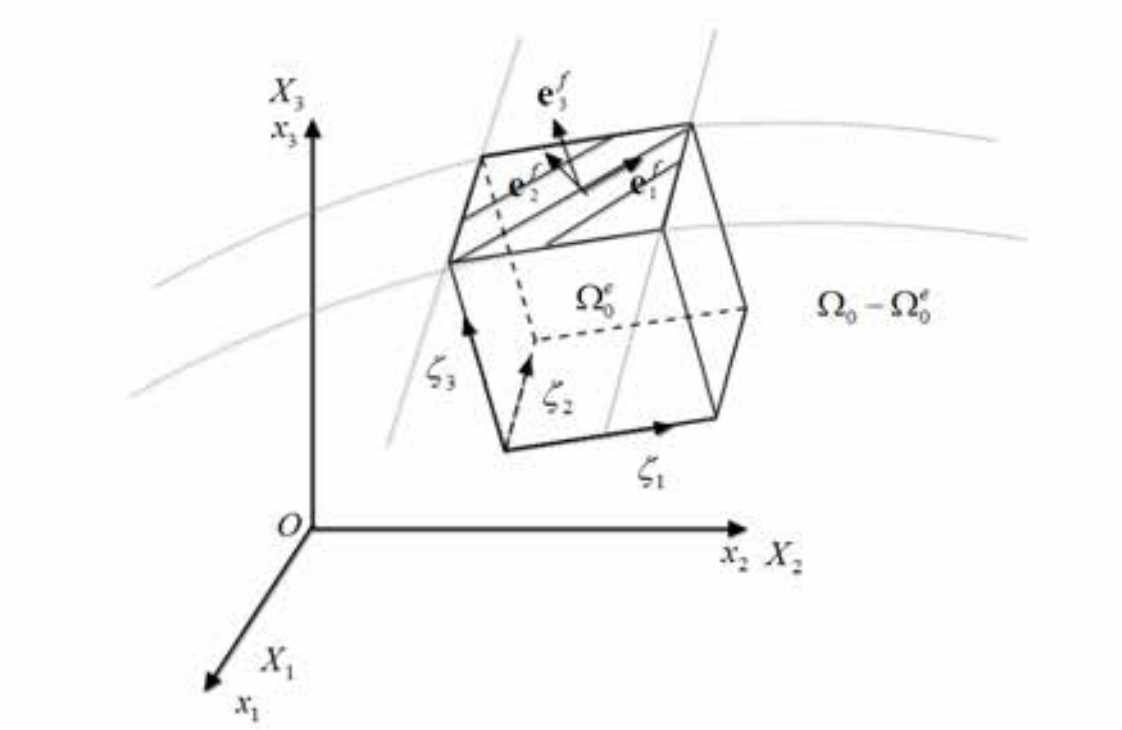

Figure 4.5: Illustration of coordinate systems defined in CM. A group of fibres embedded in an element Ω_0^e. By using the first derivatives of the geometrical shape interpolation, a fibrous coordinate system at any elemental coordinate ($\boldsymbol{\xi}^e$) can be derived with basis vectors $\mathbf{e}_1^f$, $\mathbf{e}_2^f$ and $\mathbf{e}_3^f$.

where subscripts m and f of transformation $\mathbf{T}$ indicate the transformation which aligns the *1st* axis of system $\mathbf{e}^m$ with the fibre direction. In CM, the constitutive equation is evaluated at each Gauss point, and the residual term ($\mathbf{R}$) is subsequently assembled with respect to the local fibrous coordinate system ($\mathbf{e}^f$ coordinate system).

4.4.2 Tensor product form for computing fibrous structure effect

In the geometric model, the fibre direction is represented by a 3D vector with respect to the global coordinate system $\mathbf{e}_i^g$, and each component of this vector is interpolated at each Gauss point. In this research, a computational tensor product form is introduced, which directly uses the fibrous direction from the geometric model. The additional term is introduced to improve the accuracy of the solution and reduce potential numerical errors.

Based on the coordinate systems by Costa et al. [1996a,b] and Nash [1998], a virtual fibre

family (denoted as $\mathbf{a}_0$) is introduced into the model, with its fibre direction along the direction of $\mathbf{e}_1^m$. The virtual fibre does not contribute any stress that lead the fibre stress tensor as $\mathbf{0}$. The second Piola-Kirchhoff stress is then written as

$$[\mathbf{S}_{tissue}]_{\mathbf{e}^m} = [\mathbf{S}_{matrix}]_{\mathbf{e}^m} + [\mathbf{0}]_{\mathbf{e}^m}. \tag{4.39}$$

Note that, the overall stress is defined with respect to the $\mathbf{e}^m$ system, and additionally to the $\mathbf{e}^f$ system; and that no actual stress from $\mathbf{a}_0$ is added to the total stress term. Once $\mathbf{e}_i^m$ is defined, a rotational transformation $\mathbf{T}_{g,m}$ is obtained at each Gauss point through

$$[\mathbf{e}_1^m, \mathbf{e}_2^m, \mathbf{e}_3^m] = \mathbf{T}_{g,m}[\mathbf{e}_1^g, \mathbf{e}_2^g, \mathbf{e}_3^g]; \tag{4.40}$$

or, $\mathbf{T}_{g,m} = [\mathbf{e}_1^m, \mathbf{e}_2^m, \mathbf{e}_3^m]$, since $[\mathbf{e}_1^g, \mathbf{e}_2^g, \mathbf{e}_3^g]$ is the identity matrix.

The constitutive equation (Equation 4.17) can then be transformed with respect to $\mathbf{e}^m$, resulting in

$$\begin{aligned}
[\mathbf{S}_{tissue}]_{\mathbf{e}^m} &= [\mathbf{S}_{matrix}]_{\mathbf{e}^m} + \sum_{i\in\mathscr{F}} \frac{\sigma_{fibre,i}}{\lambda_i^2} \mathbf{T}_{g,m}\mathbf{a}_i \otimes \mathbf{T}_{g,m}\mathbf{a}_i \\
&= \mathbf{T}_{g,m}\mathbf{S}_{matrix}\mathbf{T}_{g,m}^T + \mathbf{T}_{g,m}\Big(\sum_{i\in\mathscr{F}} \frac{\sigma_{fibre,i}}{\lambda_i^2} \mathbf{a}_i \otimes \mathbf{a}_i\Big)\mathbf{T}_{g,m}^T \\
&= \mathbf{T}_{g,m}\Big([\mathbf{S}_{matrix}]_{\mathbf{e}^m} + \sum_{i\in\mathscr{F}} \frac{\sigma_{fibre,i}}{\lambda_i^2} \mathbf{a}_i \otimes \mathbf{a}_i\Big)\mathbf{T}_{g,m}^T \\
&= \mathbf{T}_{g,m}\mathbf{S}_{tissue}\mathbf{T}_{g,m}^T.
\end{aligned} \tag{4.41}$$

The fibre strain can be obtained through $\lambda_i^2 = (\mathbf{T}_{g,m}\mathbf{a}_i)\cdot(\mathbf{T}_{g,m}\mathbf{C}\mathbf{T}_{g,m}^T)(\mathbf{T}_{g,m}\mathbf{a}_i) = \mathbf{a}_i \cdot \mathbf{C}\mathbf{a}_i$ because $T_{g,m}$ is an orthogonal tensor. Note that the ground matrix term $\mathbf{S}_{matrix}$ can only be an isotropic material without specified material orientation. In other words, the ground matrix must have a frame-independent material stress-strain relationship. Equation 4.41 is not valid for other constitutive behaviours, e.g. the ground matrix stress being modelled as an orthotropic material.

The tensor product form (Equation 4.41) does not depend on the fibre coordinate system $\mathbf{e}^f$. Instead, the stress and strain terms are transformed between the local orthogonal coordinate

system ($\mathbf{e}^m$) and the global coordinate system ($\mathbf{e}^g$) in a single computational operation as the summation of all fibre stresses. Consequently, the number of computational operations is reduced, and computational efficiency is improved.

4.5 Modelling tongue deformation by active contraction

Modelling the deformation of the FE tongue model relies on boundary conditions and properly defined material parameters. Within this section, the boundary conditions for modelling tongue movement will be introduced, i.e. restrictions on nodal motion and deformation of geometric curvature; and the material parameters which govern the fundamental characteristics of the tongue's complex fibrous tissue are described and quantified.

4.5.1 Boundary conditions

Two types of boundary conditions are imposed on the model: the so-called Dirichlet boundary conditions and contact boundary conditions. Contact boundary conditions for modelling the interaction between the tongue body and the upper palate are presented in Chapter 4.6. At first, the focus is drawn on the Dirichlet boundary conditions which comprise a series of movement restrictions at selected points in the model. In the context of tongue modelling, the Dirichlet boundary conditions are used to constrain the movement at boundary points where the body of the tongue connects with bony structures. The following areas are considered in the present work

- Nodes are fixed in the area where the bottom anterior tongue body connects to the lower jaw (blue cubes in Figure 4.6(a)). In addition to the nodal positions, the derivatives of these nodes are fixed with respect to the medial-lateral direction (ξ_1 direction). The associated geometric parameters (nodal values) include $\mathbf{X}$ and $\partial\mathbf{X}/\partial\xi_1$, which will remain constant/unchanged during deformation.

- The hyoid bone is a floating bony structure that is attached to the bottom posterior part of the tongue. The hyoid bone is not included in the present anatomical model. The nodes of the tongue in the posterior region, which would attach to the hyoid bone (cf., see the gold cubes in Figure 4.6(b)) are restricted to move in anterior-posterior and superior-inferior directions only. In addition, their geometric derivatives and cross derivatives with respect to the medial-lateral directions are fixed. The associated geometric parameters include $\partial \mathbf{X}/\partial \xi_1$, $\partial^2 \mathbf{X}/\partial \xi_1 \partial \xi_2$, $\partial^2 \mathbf{X}/\partial \xi_1 \partial \xi_3$ and $\partial^3 \mathbf{X}/\partial \xi_1 \partial \xi_2 \partial \xi_3$.

- The attachment of the palatoglossus muscle to the lateral sides of the tongue dorsum forms the connection between the tongue and its surrounding tissues. This connection is modelled by fixing the displacements of the nodes in the attachment area of the palatoglossus (green diamonds in Figure 4.6(b)), while their derivatives are not constrained.

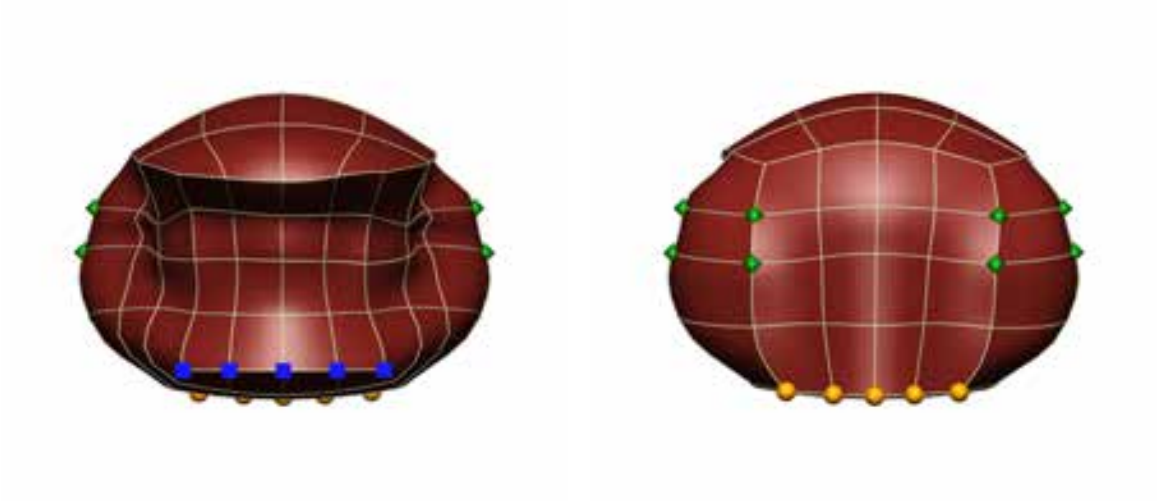

(a) Anterior view (b) Posterior view

Figure 4.6: Illustration of the Dirichlet boundary conditions applied to the geometric tongue model. The golden nodes indicate the elemental nodes within each element. The connectivity between nodes is represented by the white cylindrical lines.

4.5.2 Material parameters

The choice of material parameters will determine the resulting deformation of the continuum-mechanical model. As with all biological tissue, the definition of appropriate constitutive rela-

tionships and material parameters is an extremely challenging task. The anatomical structure and the complex muscle fibre distribution within the tongue add further challenges. Note that, no available literature reported material data may be directly applied to the constitutive equation. Therefore, the material parameters, chosen within this study, were derived from literature:

- In the absence of comprehensive experimental tests in the literature to determine the passive material response of the tongue's ground matrix, the parameter values of Mooney-Rvlin model were approximated based on available literature data. Cheng et al. [2011] reported an *in vivo* measured overall shear modulus for the tongue of 2.67 ± 0.29 kPa (mean $\pm$ standard deviation); Malhotra et al. [2002] reported a similar overall shear modulus 2 kPa; the *ex vivo* compression test by Gerard et al. [2005] showed a shear modulus of tongue tissue about 0.38 kPa. The shear modulus for a Mooney-Rivlin material is twice the sum of the two material parameters, i.e., $2(c_1 + c_2)$. By choosing $c_1 = 0.375$ kPa and $c_2 = 0.175$ kPa for the ground matrix, it is assumed that the shear modulus of ground matrix about 1.1 kPa, and it is also assumed that the ground matrix can contribute up to about 41% to the overall shear *in vivo* measured by Cheng et al. [2011].

- In terms of the maximum active fibre stress (σ_{max}), Titze [1994] reported a maximum active fibre stress of 100 kPa for the laryngeal muscles. De Groot and Van Leeuwen [2004] reported a maximum active fibre stress of 200 kPa in a chameleon tongue. It can be assumed that the maximum active stress of the human tongue lies somewhere between the laryngeal muscle and the chameleon tongue muscle. Thus, a maximum active fibre stress of 150 kPa is assumed in the present work.

- A functional form of the fibre stress-strain relationship was introduced by Blemker and Delp [2005]. In this thesis, the parameter values by Blemker and Delp [2005] were adapted for modelling stress along fibre direction (shown in Table 4.1). The normalised force along the fibre direction is plotted in Figure 4.7.

Deformation of the model is driven by active muscle contraction which is controlled via an activation level parameter α_i. If a non-zero value is assigned to α_i, the discretised governing

Constant	Value	Unit	Constant	Value	Unit
c_1	0.375	kPa	c_2	0.175	kPa
P_1	0.05	-	P_2	6.6	-
P_3	3.4850	-	P_4	-4.2517	-
λ_{ofl}	1.4	-	σ_{max}	150	kPa
λ^*	1.9				

Table 4.1: The constant parameters for the constitutive equation based on values reported in the literature.

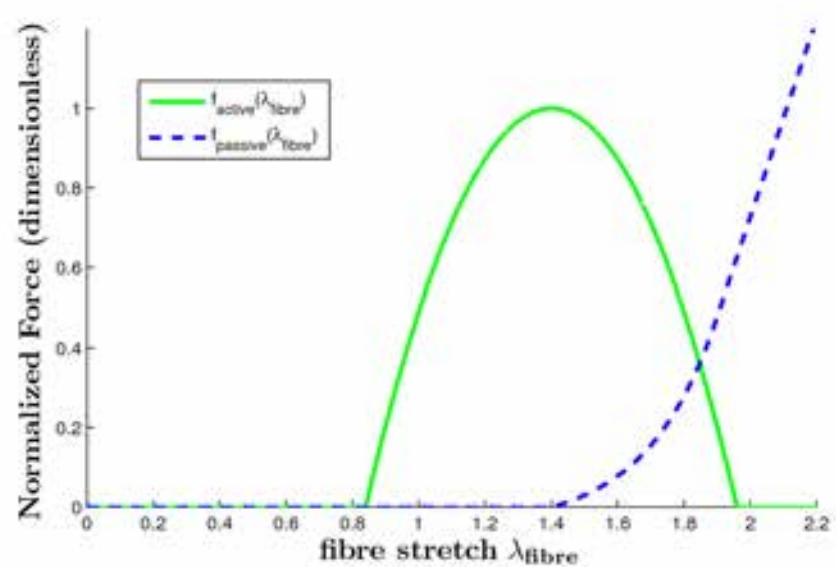

Figure 4.7: Plotting of the normalised stress along fibre direction. The green curve represents the active stress along fibre direction; while the blue curve represents the passive fibre stress.

equation do not satisfy the equilibrium condition any longer, and the solution process will start and continue until it reaches the next equilibrium state.

4.5.3 Illustrative examples

Two deformation states of the tongue were chosen to illustrate the modelling results: tongue retraction and elongation. Tongue retraction comprises a retrograde motion with a large bending deformation occurring within the upper tongue body. Tongue retraction is considered to be a consequence of the co-contraction of the transversus and styloglossus muscles [Gilbert et al., 2007]. To model tongue retraction, the activation level parameters of the involved muscles in the model are assigned values ranging from 0 to 1. Figure 4.8 shows the resulting model deformation by simultaneously updating the activation levels of the transversus and the styloglossus muscles to the maximum level $(\alpha_t, \alpha_s) = (1,1)$.

Elongation is a tongue action that is driven by the verticalis and the transversus muscles [Gilbert et al., 2007]. Figure 4.9 illustrates the resulting deformation of the model with maximum activation levels of the involved muscles ($(\alpha_t, \alpha_v) = (1,1)$). A convergence analysis of tongue retraction and elongation is presented in Appendix C.

4.6 Modelling the interaction of the tongue and the upper palate

The interaction between the tongue body and the upper palate plays a crucial role in tongue mechanics. As experimentally shown by Ono et al. [2004], Steele and Van Lieshout [2008] and Kieser et al. [2008], the interaction between the tongue and the upper palate shows a consistent pattern of contact pressure throughout the entire swallowing process. This additional compressing force from the superior surface to the tongue body cannot be ignored, especially if the mechanical model is applied to swallowing.

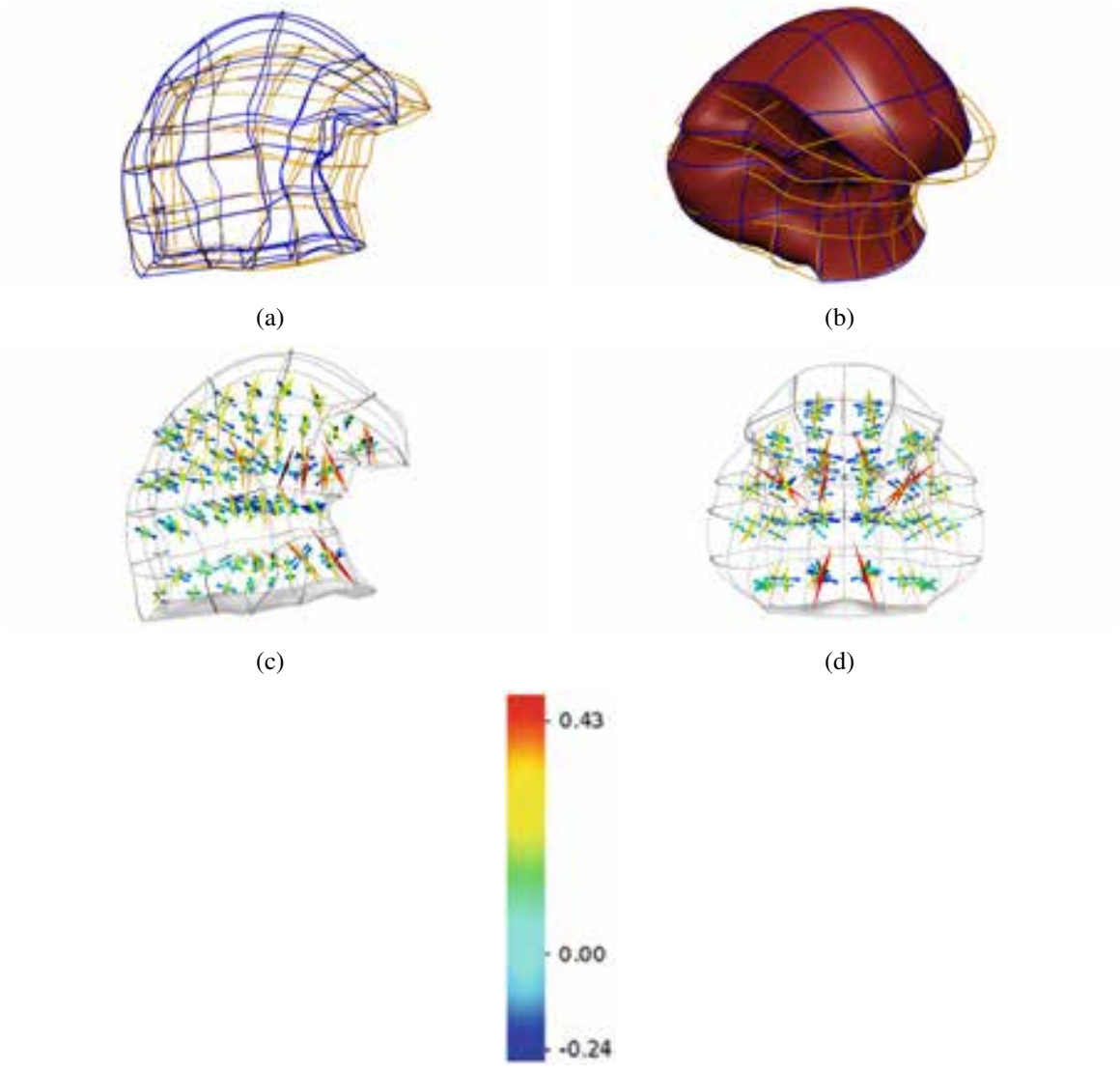

(a) (b)

(c) (d)

(e)

Figure 4.8: Modelling retraction of the tongue by activating the transversus and the styloglossus muscles to the maximum level illustrated from two viewpoints. In sub-figure (a) and (b), the golden line represents the model in undeformed state, whereas the blue line shows the deformed state. In sub-figure (c) and (d), the cones represent the local principal strain directions, and the colour and length indicate the magnitude of the principal strains. Sub-figure (e) shows the spectrum of strain magnitude.

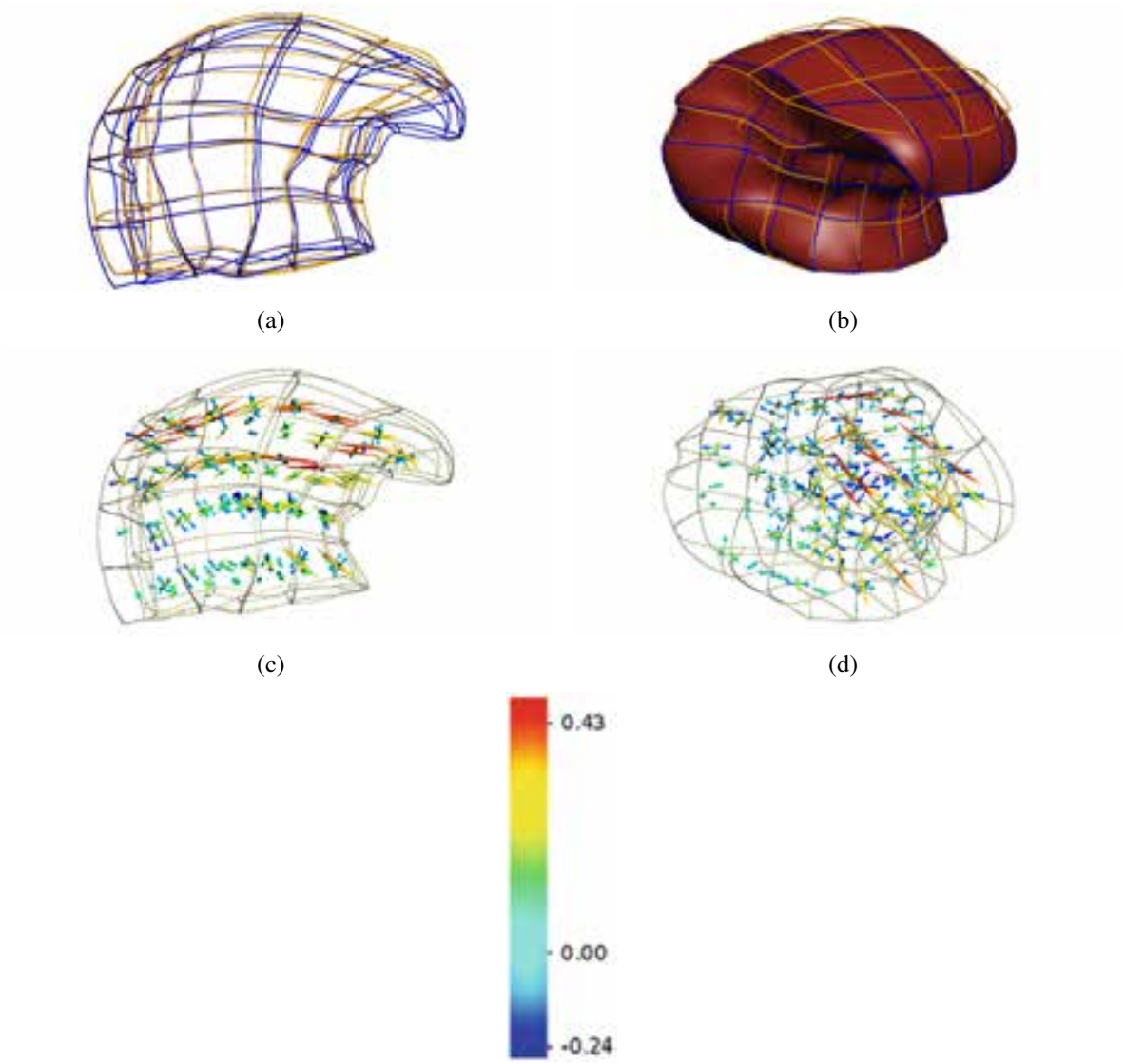

Figure 4.9: Modelling elongation of the tongue by activating the transversus and the verticalis muscles with the maximum level. Colours and glyphs are the same as for Figure 4.8. Sub-figure (e) shows the spectrum of strain magnitude.

In this work, the contact of the tongue with the front bony part (hard palate) is considered within the modelling framework. Zysset et al. [1999] reported that the elastic moduli of human bones (not including cartilage) range from 6.9 ± 4.3 GPa to 25.0 ± 4.3 GPa in older persons aged over 60. Additional measurements by Rho et al. [1999] showed that the elastic moduli of dry human vertebrae (T-12 and L-1) and tibia can reach up to 25.7 ± 1.7 GPa. Based on the reported values in the literature, the deformation of the upper palate is neglected due to the much stiffer material properties of bones compared to muscle soft tissue. The hard palate is considered a rigid body object, and the interaction between the tongue and the hard palate is idealized as frictionless contact between a soft tissue body (tongue) and a rigid body (hard palate).

4.6.1 Contact boundary condition

The interaction of the tongue and the upper palate can be modelled using the principles of contact mechanics [Wriggers, 2006]. Figure 4.10(c) and 4.10(d) presents the geometrical model of the hard palate, the surrounding upper teeth and the contact area.

The teeth are critical to tongue motion during swallowing [Fröhlich et al., 1991], however the female visible human image data set does not contain the teeth on the upper palate. It was assumed that the bony structures shared similar topological features between individuals. The FE mesh of the upper palate in this dissertation was obtained by scaling the model of Essen [2006], which includes teeth but was narrow compared to the palate data from the visible woman images. Thus, Essen's model was scaled only in the medial-lateral direction such that the upper palate fully covered the bi-lateral edges of the tongue.

The contact boundary conditions are applied to selected boundary faces of the FE model to simulate the contact force between the tongue and the upper palate. Figure 4.10(a) and 4.10(b) show the selected contact surfaces on the FE mesh of the tongue and the upper palate. It is assumed that saliva lubricates the oral environment. Thus, the shear stress between tongue and upper palate is neglected, and no frictional force is applied to the contact area. Consequently,

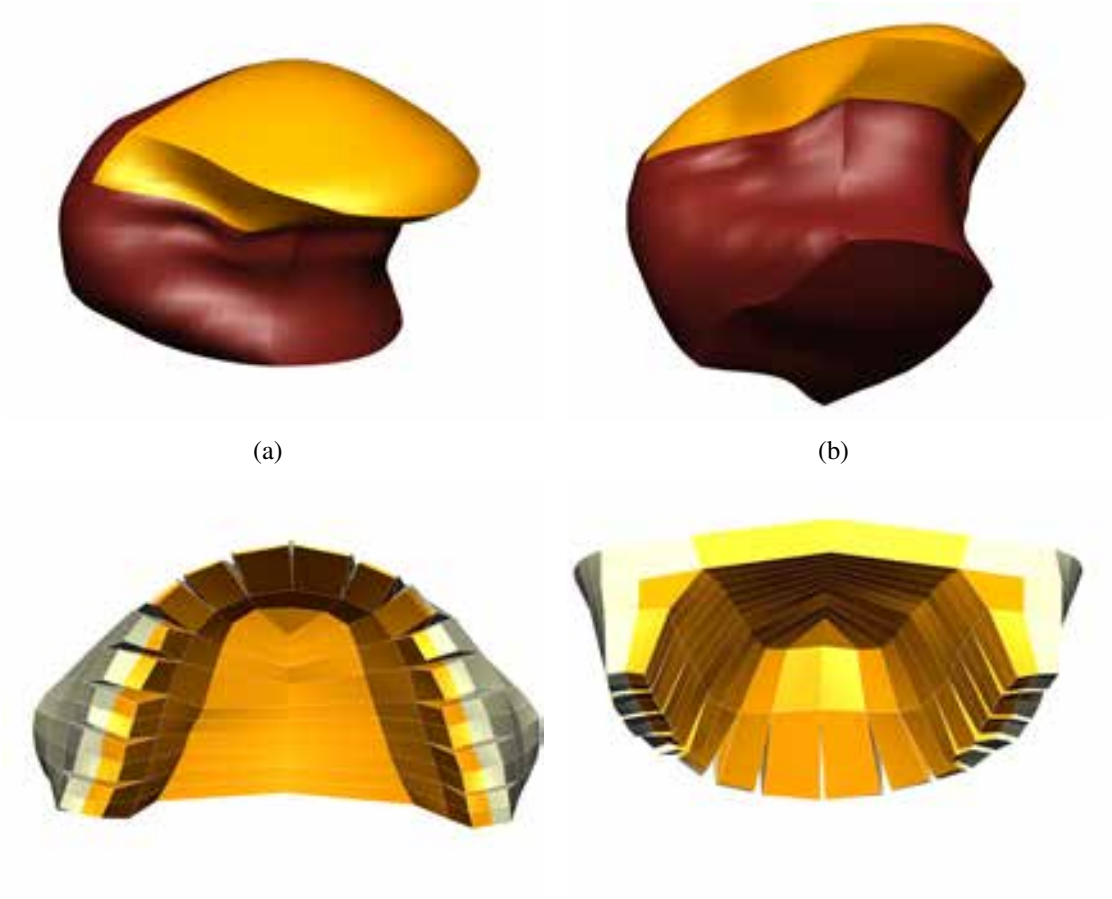

(a) (b)

(c) (d)

Figure 4.10: The contact areas, coloured as golden, on the tongue model (a, b) and the upper palate model (c, d).

the contact force normal to the contact area is modelled using a frictionless penalty method. In general, the penalty boundary condition relies on the amount of overlap between the deformable soft body and the rigid body at contact points. The contact force at a contact point is defined as

$$f(\mathbf{x}_{tissue}) = \begin{cases} \varepsilon_N g_N & \text{if } g_N \geq 0 \\ 0 & \text{otherwise,} \end{cases} \tag{4.42}$$

where ε_N is the contact stiffness parameter; and g_N is the gap function used to calculate the amount of overlap between two contact objects, such that

$$g_N = -\mathbf{n} \cdot (\| \mathbf{x}_{tissue} - \mathbf{x}_{bone} \|). \tag{4.43}$$

In Equation 4.43, $\mathbf{x}_{tissue}$ and $\mathbf{x}_{bone}$ are two contact points on the tissue and the bone, respectively.

Equation 4.43 projects the absolute distance between $\mathbf{x}_{tissue}$ and $\mathbf{x}_{bone}$ onto the normal direction at $\mathbf{x}_{tissue}$.

4.6.2 The pre-contact configuration

In its initial state, the tongue is in a configuration with no muscle contractions, but contact between the tongue body and the bony upper palate may already exist. This initial contact state is also referred to as the pre-contact state. The relative position of the upper palate with respect to the tongue body is important to derive the pre-contact state. Contact of the hard palate with the tongue is considered an additional motion constraint which affects the deformation of the superior outer surface of the tongue model. The pre-contact state can influence the overall resultant deformation, even if the same activation levels are used.

Figure 4.11(a) shows the mid-sagittal images of the head of the female Visible Human. The teeth surrounding the tongue body are missing, as seen in Figure 4.11(a). As a consequence, the anterior part of the tongue in the relaxed state occupies the anterior oral cavity where the teeth are usually located. In reality, the anterior dorsum of the tongue is often in contact with the anterior-inferior surface of the hard palate. In such a case, a force from the superior direction acts on the anterior dorsum of the tongue and presses the tongue tip downward. Therefore, the initial configuration of the tongue resembles a pre-contact state which is caused by external contact forces applied to the anterior tongue dorsum.

The complex geometries of the tongue and the upper palate make it challenging to ascertain the pre-contact condition. The pre-contact configuration is a deformation of the tongue model that is obtained as follows

1. First, the curvatures of the interior mid-sagittal line of the upper palate and the superior mid-sagittal tongue line are digitised on the mid-sagittal images of the Visible Woman data set. The digitised data allow the definition of the relative position of the upper palate with respect to the tongue surface, see Figure 4.11(b);

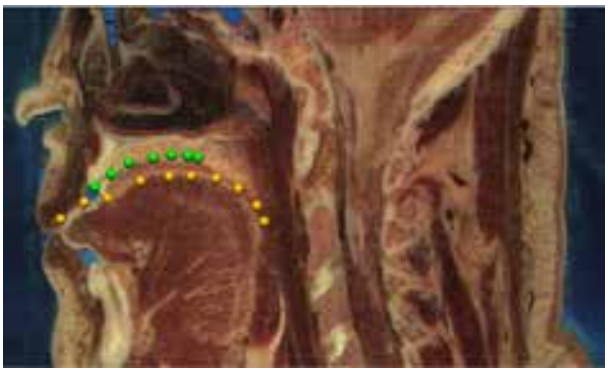

(a) Digitised positions of the upper palate (green dots) and the tongue (gold dots) based on the Visible Human data set to align the model position.

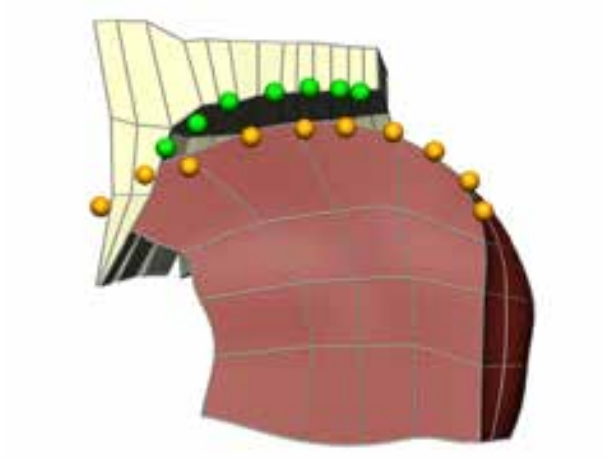

(b) The upper palate and tongue model after alignment.

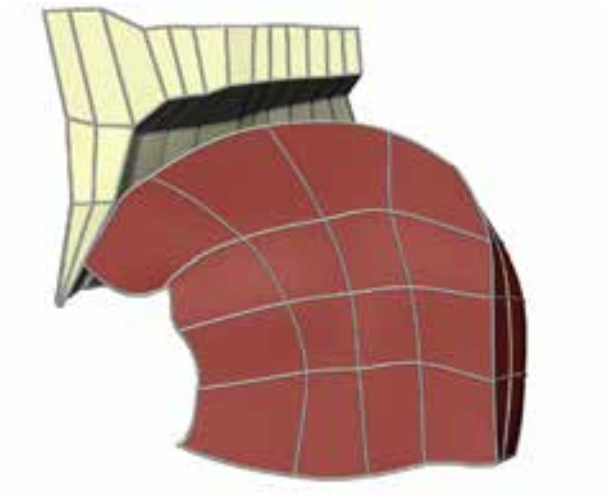

(c) The initial configuration of the tongue model with contact between the tongue and the upper palate.

Figure 4.11: Relative positions of the tongue and the upper palate and initial configuration with pre-contact.

2. Subsequently, the golden nodes in Figure 4.11(b) are aligned with the mid-sagittal line of the tongue model, and the upper palate model is adjusted so that the mid-sagittal line of the upper palate model aligns with the green dots, as shown in Figure 4.11(b);

3. Finally, the pre-contact deformation is obtained by applying the contact boundary condition on the selected contact areas of the FE model. Figure 4.11(c) presents the derived initial state with pre-contact condition.

The tongue muscle is modelled as a nonlinear, multi-fibre reinforced, hyperelastic material. Hyperelasticity coupled with frictionless contact constraints implies that the deformation path is independent, and the deformation history does not influence the resultant target configuration. In other words, different loading strategies can be used to solve the contact problem between the hyperelastic tongue body and the surrounding rigid structures. In the present work, the pre-contact state described above was used as the initial state. This initial state is not the reference configuration, but an intermediate configuration for which there is no muscle contraction. Appendix B presents different loading strategies used to solve the contact problem between a hyperelastic material and a rigid body. All simulations produced the same numerical results, providing verifying that the deformation of hyperelastic materials is path independent. The consequence of this is that if one loading strategy turns out to be numerically unstable, then an alternative loading strategy can be used to find the solution.

4.7 Inverse problem for deriving the contractile properties of muscles

The calculation of tongue deformation based on different levels of muscle activations is also referred to as forward problem method. The forward problem method aims to generate the model-based kinematic data, i.e. strain and displacement, based on different levels of muscle activation. The derivation of muscular activation levels can be done by comparing model output (i.e. strain and displacement) with experimentally collected data. On the other hand, muscular

activation levels can be estimated using an inverse problem method.

The inverse problem of parameter estimation compares the function (i.e. tongue model) in the parameter space (i.e. activation level $\boldsymbol{\alpha}$) with the given kinematic data, and searches the optimal values of the parameters which satisfy the objective function. Denoting the objective function as $\mathfrak{I}$, the derivation of muscular activation levels in the tongue is achieved through

$$\tilde{\boldsymbol{\alpha}} = \underset{\boldsymbol{\alpha}\in[0,1]^N}{\operatorname{argmin}}\ \mathfrak{I}(\boldsymbol{\alpha}). \tag{4.44}$$

where N is the number of estimated parameters. One need note that, the components in parameters $\boldsymbol{\alpha}$ can be beyond 1.0 for representing larger active fibre stresses. In practice, the upper bound limits can be also setup a large number above 1.0, e.g. $\boldsymbol{\alpha} \in [0, 10]^N$. In general, $\operatorname{argmin} \mathfrak{I}(\boldsymbol{\alpha})$ is a typical nonlinear optimisation problem that can be solved using a Newton-Raphson algorithm, e.g. a trust region reflective algorithm, if the numerical behaviour of the objective function is quadratic-like and has a global minimum point.

4.8 Summary

In this chapter, the geometric FE mesh and the constitutive equation for modelling the tongue were presented. The fibrous architecture of the tongue, consisting of the intrinsic, extrinsic and external muscles, was modelled using vectorial and volume composition fields embedded into the geometric FE tongue model. The composition of the tongue tissue was assumed as the sum of multiple constituents, including the fibrous structures. The stress contribution of a fibre family consists of a passive term and a superimposed active stress. Within the present model, the spatially varying distributions of the muscles are treated as a series of scalar fields with different contributions to the mechanical stress. The modelling procedure is simplified without losing mechanical accuracy.

A series of activation level parameters are introduced to control the magnitude of active stress for each muscle family. Contact mechanics between the tongue and the hard palate is intro-

duced to simulate their interaction in both zero and non-zero activation cases. By specifying one or multiple activation levels, the deformation caused by the corresponding muscles can be modelled. Based on the forward problem method, an inverse problem framework is proposed to derive the muscle activation levels through parameter estimation using existing kinematic data. An inverse framework also has been proposed for the applications with only partial motion information available. Details of those applications will presented in the chapter 5 and 6. This inverse procedure is to find an pattern of muscular activities using given motion data and the tongue model. In short, the tongue model, forward method and inverse procedure establish the basic computational framework to study the the mechanics of tongue.

Moreover, the computational efficiency in the implementation of constitutive equations and the derivation of the pre-contact condition is addressed and improved. This will benefit model applications which require large numbers of iteration steps (e.g. the forward and inverse problem) and speed up the entire problem solving procedure.

Chapter 5

Optimal sensor locations and application to articulography

The deformations of the tongue model can be produced by specifying the activation levels of different tongue muscles. The deformation and function of the tongue and the fibrous structures at varying levels of muscle activation can be investigated using a forward problem method. A forward problem study, sampling the envelopes of tongue deformation over the parameter domain, could help to improve the quality of experimentally collected kinematic data, for instance, from the 3D Articulograph AG500. Ideally, the motion of sensors from articulography reflect the characteristics of tongue deformation caused by muscle contraction. However, articulography can suffer from large random noise. The sampled deformation modes of the tongue model from a forward simulation could assist experimentalists to find the most motion-sensitive points on the tongue surface, which reflect the underlying characteristics of muscular activity. In the present study, the forward problem method is used to identify an optimised sensor placement on the tongue surface for collecting kinematic data using the 3D Articulograph AG500. The optimal sensor configuration is later used to derive muscle activation levels for various tongue deformations through an inverse approach. The work presented in this chapter formed the basis for the research article: Wang et al. [2013].

5.1 Articulograph system

5.1.1 Overview of the study

In movement biomechanics, optical motion capture systems are commonly adopted to track surface markers. However, optical surface markers are difficult to use for tracking tongue motion as their visibility is obstructed by the bony walls and the surrounding soft tissues in the oral cavity. In oral research, motion capture systems are commonly adopted which track the positions and angles of specific coils within a magnetic field, e.g. the 3D Articulograph AG500 from Carstens Medizinelektronik (Lenglern, Germany). The big advantage of such magnetic-field-based motion tracking systems is their ability to track sensor locations within the oral cavity. Therefore, electro-magnetic articulography has extensively been used to track the motion of the tongue and other facial features [Jiang et al., 2002, Steele and Van Lieshout, 2009, Goozee et al., 2000, Katz et al., 1999, Steele and van Lieshout, 2004].

In practice, the sensors of the 3D Articulograph AG500 for tracking the movement of the tongue are heuristically placed on the tongue's surface. No recommendations on optimal sensor placement have been made. Furthermore, mechanical noise, inherent to the system, may influence the quality of the recorded data, and hence, produce inaccurate observations and conclusions concerning the deformation of the tongue (see Section 2.4.2). In the present study, a model-based approach based on the tongue's envelope of movement is proposed to determine the optimal sensor placement. The principles of forward dynamics (deriving motion from selective activation of muscle fibres) are applied to the anatomically-realistic computational model of the tongue to determine the tongue's envelope of movement during specific tasks.

The calibration of the motion sensors prior to any experiment is important, as pointed out by Yunusova et al. [2009]. However, the level of difficulty in the calibration may rise with the number of sensors, with a maximum of eight sensors being considered applicable to the entire tongue surface. In this study, 2, 4 and 6 locations are selected in order to accurately capture the movement of the tongue on half of the tongue's surface. The reduction of the dimensionality of

the sensor locations is necessary due to physical constraints of the recording method, e.g. only a small number of recording channels are available, and only a small number of sensors can be placed in the mouth due to their size and connecting wires.

5.2 Sensor location optimisation

The main aim of this section is to describe the methodology to determine an optimal set of sensor locations on the tongue's surface during retraction and elongation. Retraction and elongation of the tongue are chosen within this context, since the muscle fibre groups involved in these movements are believed to be known. Gilbert et al. [2007] and Napadow et al. [1999a,b] reported that based on observation and empirical analysis, the retraction is caused by contractions of the transversus and styloglossus muscle fibre groups, while elongation is caused by contractions of the transversus and verticalis muscle fibre groups, respectively. The tongue's envelope of movement can be determined from a representative sample of different combinations of activation levels, which are input into the anatomically-realistic, continuum-mechanical model of the tongue. Following the forward simulation of tongue movement, an optimal set of sensor locations can be derived from the computed tongue envelope using an optimisation criterion that reflects key movement characteristics. The following subsections outline the methodology in detail.

5.2.1 Computing the tongue's envelope of motion

Two case studies, namely the elongation and retraction of the tongue, were undertaken to assess the robustness of the proposed method in deriving the optimal set of surface markers based on the activation levels for a particular tongue deformation. The elongation of the tongue is driven by the simultaneous contraction of the transversus and verticalis muscles; while, retraction is driven by the contraction of the transversus and styloglossus muscles. It is believed that tongue elongation and retraction only involve the activation of two muscles. Thus, the parameter search

spaces for the two case studies each consists of only two dimensions. All numerical studies were carried out under the assumption that the level of activation is spatially homogeneous for the entire muscle fibre group. Furthermore, a symmetric arrangement of the muscle fibre groups within the tongue was assumed. The symmetry assumption provided justification to restrict the analysis to one half of the tongue.

For each type of movement, e.g. retraction or elongation, the tongue's envelope of motion is determined by utilising the generic continuum-mechanical model outlined in Chapter 4 and principles of forward dynamics, i.e. by choosing a specific set of activation parameters ($\boldsymbol{\alpha}$). In the case of retraction, different levels of activation for the transversus muscle fibre group, α_t, and the styloglossus muscle fibre group, α_s, are chosen to derive the various modes of deformation. For the forward simulation, the respective levels of activation are multiples of $\Delta\alpha = 0.1$ and range from 0 (inactive) to 1 (fully activated). The activation levels for the remaining muscle fibre groups are set to 0 (inactive). The set of all computed modes of deformation form the envelope of movement. The same procedure is followed to determine the envelope of motion for elongation. In this case, the levels of activation for all muscle fibre groups remain 0 except for the transversus muscle fibre group, α_t, and the verticalis muscle fibre group, α_v, which are again chosen to be multiples of $\Delta\alpha = 0.1$, ranging from 0 to 1.

5.2.2 Possible sensor locations

Sensors can only be placed on the external surface of the tongue. Within this work, a total of 48 potential sensor locations are evenly distributed over half of the tongue's surface. The detailed discussion and justification on this condition are provided in Section 5.6. The number of potential sensor locations correspond to four nodes per surface face of the FE model and are generated with respect to the undeformed state (reference configuration). Figure 5.1 shows all potential sensor locations on the deployable area on the dorsum of the tongue. Each potential sensor location is identified with a unique numeric index. The set of all sensor locations is denoted by $\mathscr{S}$.

Based on the general theory of continuum mechanics, each material point P in the reference configuration (denoted by $\mathbf{X}$) has its unique position over time/level of activation (denoted by $\mathbf{x}(\boldsymbol{\alpha})$), which is determined by the placement function χ such as

$$\mathbf{x}(\boldsymbol{\alpha}) = \chi(P, \boldsymbol{\alpha}), \quad \mathbf{X} = \chi(P, \boldsymbol{\alpha}_0), \tag{5.1}$$

and $\boldsymbol{\alpha}_0 \equiv \mathbf{0}$. Hence, the displacement at a material point P is derived from the difference between the actual position $\mathbf{x}(\boldsymbol{\alpha})$ and its initial position $\mathbf{X}$,

$$\mathbf{u}(P, \boldsymbol{\alpha}) = \chi(P, \boldsymbol{\alpha}) - \chi(P, \boldsymbol{\alpha}_0). \tag{5.2}$$

Hence, χ defines for all $\boldsymbol{\alpha}$ the motion and the displacement of each sensor in $\mathscr{S}$.

5.2.3 General optimization procedure for sensor placement

The optimisation of motion sensor placements on the tongue is a typical location-measurement problem. The set of all potential sensor combinations, consisting of n different sensors $\boldsymbol{s}_i \in \mathscr{S}$, can be described by

$$\mathrm{SL(n)} = \left\{ \; (\boldsymbol{s}_1, \ldots, \boldsymbol{s}_n) \;\middle|\; \boldsymbol{s}_i \in \mathscr{S}, \boldsymbol{s}_i \neq \boldsymbol{s}_j \text{ and } i \neq j \; \right\}. \tag{5.3}$$

The cardinality of $\mathrm{SL(n)}$ is given as

$$\mathrm{card}\left(\mathrm{SL(n)}\right) = \begin{pmatrix} N \\ n \end{pmatrix} = \frac{N!}{n!(N-n)!}, \tag{5.4}$$

and denotes the number of possible sensor combinations that could be placed on half of the upper tongue surface ($N = 48$). Based on Equation 5.4, the numbers of feasible sensor arrangements for n=2, 4, and 6 sensors are equal to 1 128, 194 580 and 12 271 512, respectively. The movement of each sensor can be obtained through sampling the model configuration over the parameter domain (the range of activation levels).

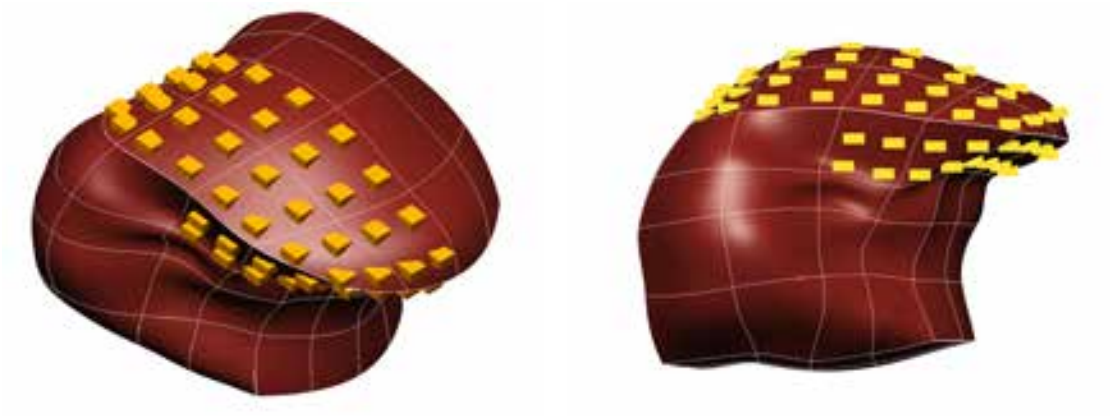

(a) (b)

Figure 5.1: Possible sensor locations on half of the tongue dorsum.

A 3-step optimisation procedure is proposed based on the available information:

1. Generate the admissible sensor locations on the tongue surface;
2. Evaluate the criteria values for all combinations of possible sensor locations;
3. Select the combination of sensor locations with the optimal criteria value.

The key to success is the design of an optimisation criteria that reflects the quantities to be optimised. Two different optimisation criteria are considered in this work for selecting the optimal sensor locations on the surface of the tongue. The first criteria is based on the assumptions that sensor locations with large displacements contain the most information regarding the tongue's movement and are less susceptible to measurement errors. The second criteria also focuses on the displacement of motion sensors, yet, its objective function aims to distinguish between movement in anterior-posterior, superior-inferior and medial-lateral direction.

5.2.4 Optimality criteria I: Fisher information matrix

For a given group of n sensors with the sensor locations $\boldsymbol{s}_1, \ldots, \boldsymbol{s}_n$ configured by the activation level $\boldsymbol{\alpha}$, the displacement vector of all selected sensors can be written in a compact form as

$$\delta^{\boldsymbol{\beta}}(\boldsymbol{\alpha}) = \Big[\mathbf{u}(\boldsymbol{s}_1, \boldsymbol{\alpha}), \ldots, \mathbf{u}(\boldsymbol{s}_n, \boldsymbol{\alpha})\Big]^T. \tag{5.5}$$

Note that the noise influence remains constant. Thus, the index array $\delta^{\boldsymbol{\beta}}$ forms an n-variate multivariate distribution in which a sensor may appear in several different positions during repeated experiments.

The movement sensitivity of a set of sensor locations is measured by the Fischer Information matrix. The concept of using the Fischer Information matrix to determine optimal sets of sensor locations is not new. It has previously been applied to many engineering-type applications, e.g., in civil engineering for structural monitoring [Papadimitriou et al., 2000], in environmental engineering for air quality monitoring [Ucinski, 2000], or in aerospace engineering for on-orbit identification and correlation of large space structures [Kanner, 1991].

For an n-variate multivariate distribution, the Fischer Information matrix $\mathbf{M}(\boldsymbol{\alpha},\boldsymbol{\beta})$ with $\boldsymbol{\alpha} \in [0,1]^{10}$ and $\boldsymbol{\beta} \in \mathrm{SL(n)}$, is defined in the explicit form as

$$\mathbf{M}(\boldsymbol{\alpha},\boldsymbol{\beta}) = \left(\frac{\partial\,\delta^{\boldsymbol{\beta}}(\boldsymbol{\alpha})}{\partial\,\boldsymbol{\alpha}}\right)^{T} \boldsymbol{\Sigma}^{-1} \left(\frac{\partial\,\delta^{\boldsymbol{\beta}}(\boldsymbol{\alpha})}{\partial\,\boldsymbol{\alpha}}\right) + \frac{1}{2}\,\mathrm{tr}\left(\frac{\partial\boldsymbol{\Sigma}}{\partial\boldsymbol{\alpha}}\boldsymbol{\Sigma}^{-1}\frac{\partial\boldsymbol{\Sigma}}{\partial\boldsymbol{\alpha}}\right), \tag{5.6}$$

whereby $\boldsymbol{\Sigma}$ is a diagonal matrix $\sigma^2\mathbf{I}$, with σ^2 being the variance of the noise distribution. The derivative of the the displacement vector $\delta^{\boldsymbol{\beta}}$ with respect to the activation level $\boldsymbol{\alpha}$ is numerically computed using a Newton's difference quotient with $\Delta\alpha = 0.1$. The differentiation is only performed for the non-zero activation parameters. According to the assessment by Yunusova et al. [2009] and Kroos [2012], there is no clear evidence of a statistical pattern of error distribution between the x-y, x-z and y-z directions. Therefore, the noise influence in different axial directions are considered independent but with the same statistical pattern. This leads to a reduced form of Equation 5.6 as follows

$$\mathbf{M}(\boldsymbol{\alpha},\boldsymbol{\beta}) = \left(\frac{\partial\,\delta^{\boldsymbol{\beta}}(\boldsymbol{\alpha})}{\partial\,\boldsymbol{\alpha}}\right)^{T} \boldsymbol{\Sigma}^{-1} \left(\frac{\partial\,\delta^{\boldsymbol{\beta}}(\boldsymbol{\alpha})}{\partial\,\boldsymbol{\alpha}}\right). \tag{5.7}$$

Consequently, finding the optimal placement of the sensor array is equivalent to obtaining the Fischer Information matrix which is $\mathbf{M}(\boldsymbol{\alpha},\boldsymbol{\beta}^*) \succeq \mathbf{M}(\boldsymbol{\alpha},\boldsymbol{\beta})$, where $\boldsymbol{\beta}^*$ is the optimal scheme and $\boldsymbol{\beta}$ the remaining combinations. Various criteria exists to quantitatively assess the performance

of the output, including:

- The determinant optimality (D-optimality) criterion: $\det(\mathbf{M})$
- The largest eigenvalue (E-optimality) criterion: $\lambda_{\max}(\mathbf{M}^{-1})$
- The trace optimality (A-optimality) criterion: $\mathrm{tr}(\mathbf{M}^{-1})$

D-optimality aims to maximise the uncertainty ellipsoid formed by a cluster of recorded positions for estimation; E-optimality minimises the length of the largest axis of the same ellipsoid; and A-optimality aims to obtain the best average variance of the estimates. Thus, D-optimality is adopted to quantify the performance of the sensor array. To maximise the information contained within the envelope of movement over a pre-described parameter space (here the level of activation for the respective muscle fibre groups) of all muscle groups, the optimal set of sensor locations is found by solving the following optimisation problem:

$$\boldsymbol{\beta}^* = \underset{\beta \in \mathrm{SL(n)}}{\operatorname{argmax}} \left[\det \left(\sum_{\alpha_1=0}^{1/\Delta\alpha} \cdots \sum_{\alpha_9=0}^{1/\Delta\alpha} \sum_{\alpha_{10}=0}^{1/\Delta\alpha} \mathbf{M}(\Delta\alpha \cdot \boldsymbol{\alpha}, \boldsymbol{\beta}) \right) \right], \tag{5.8}$$

where $\alpha_1, \cdots, \alpha_{10}$ correspond to the respective activation levels of the muscle fibre groups, e.g. , t, v, $\cdots$. Note that, the summations in Equation 5.8 can be reduced by specifying the muscles involved in specific action. For instance, for the study of retraction, only styloglossus and transversus muscles are involved. Other muscles are not playing any roles. Hence, only two summations corresponding to styloglossus and transversus muscles are applied in this case (see Section 5.4.1). A similar argument holds for the case of elongation.

5.2.5 Optimality criteria II: Axial displacement

The optimisation criteria II is based on the assumption that the largest movements in each spatial direction contain the most relevant information regarding a particular 3D motion pattern. The second optimality criterion aims to distinguish between movements in anterior-posterior, superior-inferior and medial-lateral directions. Therefore, the first three markers are chosen

based on the maximal displacements in the anterior-posterior (AP), superior-inferior (SI) and medial-lateral (ML) directions, respectively:

$$\mathfrak{s}_1 = \underset{\mathfrak{s}\in\mathscr{S}}{\operatorname{argmax}} \sum_{\alpha_1=0}^{1/\Delta\alpha} \cdots \sum_{\alpha_9=0}^{1/\Delta\alpha} \sum_{\alpha_{10}=0}^{1/\Delta\alpha} \| \mathbf{u}_{\mathrm{AP}}(\mathfrak{s}, \Delta\alpha \cdot \boldsymbol{\alpha}) \|_2, \tag{5.9}$$

$$\mathfrak{s}_2 = \underset{\mathfrak{s}\in\mathscr{S}\setminus\{\mathfrak{s}_1\}}{\operatorname{argmax}} \sum_{\alpha_1=0}^{1/\Delta\alpha} \cdots \sum_{\alpha_9=0}^{1/\Delta\alpha} \sum_{\alpha_{10}=0}^{1/\Delta\alpha} \| \mathbf{u}_{\mathrm{SI}}(\mathfrak{s}, \Delta\alpha \cdot \boldsymbol{\alpha}) \|_2, \tag{5.10}$$

$$\mathfrak{s}_3 = \underset{\mathfrak{s}\in\mathscr{S}\setminus\{\mathfrak{s}_1,\mathfrak{s}_2\}}{\operatorname{argmax}} \sum_{\alpha_1=0}^{1/\Delta\alpha} \cdots \sum_{\alpha_9=0}^{1/\Delta\alpha} \sum_{\alpha_{10}=0}^{1/\Delta\alpha} \| \mathbf{u}_{\mathrm{ML}}(\mathfrak{s}, \Delta\alpha \cdot \boldsymbol{\alpha}) \|_2. \tag{5.11}$$

In the case of $n = 4$ sensors, the fourth sensor location $\mathfrak{s}_4$ is chosen such that

$$\mathfrak{s}_4 = \underset{\mathfrak{s}\in\mathscr{S}\setminus\{\mathfrak{s}_1,\mathfrak{s}_2,\mathfrak{s}_3\}}{\operatorname{argmax}} \sum_{\alpha_1=0}^{1/\Delta\alpha} \cdots \sum_{\alpha_9=0}^{1/\Delta\alpha} \sum_{\alpha_{10}=0}^{1/\Delta\alpha} \| \mathbf{u}(\mathfrak{s}, \Delta\alpha \cdot \boldsymbol{\alpha}) \|_2. \tag{5.12}$$

Similar as the optimality criteria I, the summations in optimality criteria II correspond to the muscles involved in specific tongue action. For $n > 4$, the set of potential sensor combinations SL(n) is restricted so that each element of the restricted set contains all of the 4 previously selected sensors. The restricted set is then used in the above-described selection procedure (FIM based selection) to determine the remaining sensors. In the instance of $n < 4$, a selection of the criteria given in Equations 5.9 - 5.12 has to be chosen. Within this work, the optimality criteria II is only used for sets of 4 sensors.

5.3 Quality measures for selected sensor locations

The ultimate goal of motion tracking is to predict the movement of the entire moving body (such as the tongue) based on a few sensor locations. In the present study, the movement of the sensors are used in a first step to derive the muscle activation levels, which are causing the particular movement, by solving the inverse problem. In a second step, the solution of the inverse problem, in this case the activation levels of particular muscle fibre groups, is used to derive the motion of the entire tongue based on the continuum-mechanical model in a forward

simulation.

To measure the robustness of a particular set of sensor locations, i.e. for a $\boldsymbol{\beta} \in \mathrm{SL(n)}$, the respective sensor locations are subjected to a motion-tracking-system-specific measurement error, i.e., $\mathbf{e}^{\mathfrak{s}}$, where $\mathbf{e}^{\mathfrak{s}} = [e_1^{\mathfrak{s}}, e_2^{\mathfrak{s}}, e_3^{\mathfrak{s}}]^T$. Given a set of sensor locations $\boldsymbol{\beta} \in \mathrm{SL(n)}$ and the (measured error-prone) locations of these sensors for a given deformation, denoted by $\tilde{\boldsymbol{\beta}} = (\tilde{\boldsymbol{s}}_1, \ldots, \tilde{\boldsymbol{s}}_n)$, the inverse problem is given by

$$\tilde{\boldsymbol{\alpha}} = \underset{\alpha \in \mathscr{A}}{\operatorname{argmax}} \sum_{j=1}^{n} \| \tilde{\boldsymbol{s}}_j - \boldsymbol{\chi}(\boldsymbol{s}_j, \boldsymbol{\alpha}) \|^2, \tag{5.13}$$

with $\mathscr{A} = [0,1]^{10}$, where $\tilde{\boldsymbol{\alpha}}$ are the estimated results, $\tilde{\boldsymbol{s}}_j = \boldsymbol{s}_j + \mathbf{e}^{\boldsymbol{s}_j}$ and $\mathbf{e}^{\boldsymbol{s}_j}$ is the random noise at the sensor location $\boldsymbol{s}_j$.

The Monte Carlo method is introduced in this study to simulate random noise $\mathbf{e}^{\boldsymbol{s}_j}$ since $\boldsymbol{s}_j$ is the measured error-induced sensor location. The Monte Carlo method is a procedure for generating random data that follows the mean, the variance, and the predefined probability distribution. Details on the method can be found in Metropolis and Ulam [1949] and Rubinstein and Kroese [2007].

Note, the inverse problem is solved for sufficient sensor locations $\tilde{\boldsymbol{\beta}}^k = (\tilde{\boldsymbol{s}}_1, \ldots, \tilde{\boldsymbol{s}}_n)$ to derive a statistically relevant estimate of the activation levels. The robustness of a set of sensor locations is subsequently investigated by comparing, for a $\boldsymbol{\beta} \in \mathrm{SL(n)}$, the computed activation value with the original activation level, $\boldsymbol{\alpha}$, that was chosen to determine the ground truth sensor locations in the deformed configuration. Clearly, the better the computed activation level matches the original value, the more robust can the set of sensor locations be considered. The standard deviation is a further measure for comparing the robustness of different sets of sensor locations. The smaller the standard deviation of the computed activation level, the more robust, and hence, the less sensitive the estimates are for a given set of sensor locations to the measurement error. Hence, the quality of a selected set of sensor locations is evaluated in this work based on the robustness of the inverse method to determine the initial activation levels of the different muscle fibre groups.

The inverse problem is numerically solved using the *Trust-Region-Reflective* algorithm as implemented in MATLAB's (V7.8, R2009a) optimisation toolbox. The Trust-Region Reflective algorithm is based on the approximation of an objective function with its Taylor series truncated after the second-order derivative term (Hessian). A Newton-like algorithm is applied to obtain the optimal solution which minimises the function value of the truncated Taylor series. For more details about trust-region algorithms, the reader is referred to Moré and Sorensen [1983] and Yuan [2000] and references therein. The algorithm is terminated if the objective function values for two consecutive iterates, i.e. all components of $\boldsymbol{\alpha}_k$ and $\boldsymbol{\alpha}_{k+1}$, differ by less than 10^{-5}. In the present work, the continuum-mechanics modelling software CMISS is directly linked to MATLAB to compute the deformation of the tongue, here $\mathbf{u}(\boldsymbol{s}_j, \boldsymbol{\alpha})$ for $i = 1, \ldots, n$ for a specific $\boldsymbol{\alpha}_k$. Note that the optimisation problem, as given in Equation 5.13, is not an 10-dimensional optimisation problem. In case of retraction and elongation, all α_i except for the activation levels of two muscle fibre groups are 0. This restriction is taken into account when solving Equation 5.13.

5.4 Cases studies of tongue elongation and retraction

The results of the numerical analysis are presented in Section 5.4.1 for the case of retraction and in Section 5.4.2 for the case of elongation.

5.4.1 Case study I: Retraction

In the first case study, the retraction were analysed based on Optimality Criterion I and II. For each $\boldsymbol{\beta} \in \mathrm{SL(n)}$, the objective function for Optimality Criterion I,

$$\mathscr{M}(\boldsymbol{\beta}) = \det\left(\sum_{\alpha_t=0}^{1/\Delta\alpha}\sum_{\alpha_s=0}^{1/\Delta\alpha} \mathbf{M}(\Delta\alpha \cdot \boldsymbol{\alpha}, \boldsymbol{\beta})\right), \tag{5.14}$$

was evaluated with $\Delta\alpha = 0.1$. Each $\boldsymbol{\beta} \in \mathrm{SL(n)}$ was associated with an index l, such that $\mathscr{M}(\boldsymbol{\beta}_1) < \ldots < \mathscr{M}(\boldsymbol{\beta}_l) < \ldots < \mathscr{M}(\boldsymbol{\beta}_{\max})$.

The results for $\mathscr{M}(\boldsymbol{\beta})$ with $\boldsymbol{\beta} \in \mathrm{SL}(4)$ are depicted in Figure 5.2, plotting index l versus $\mathscr{M}(\boldsymbol{\beta}_l)$. Within Fig. 5.2, three different choices of sensor arrangements are plotted (green

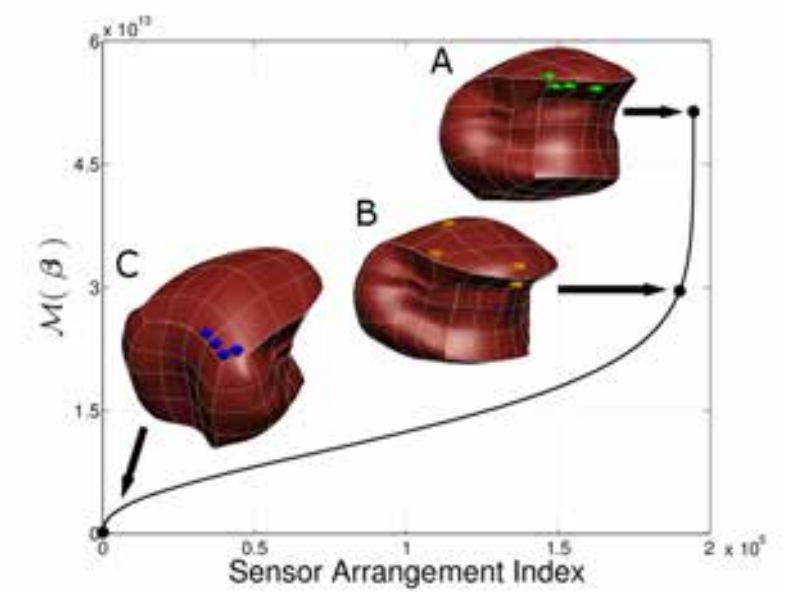

Figure 5.2: Ranking of feasible sensor arrangements, $\boldsymbol{\beta}_l \in \mathrm{SL}(4)$, for retraction based on Equation (5.14). The locations for the best (A) and worst (C) choices based on the Optimality Criterion I, as well as the index for the best choice based on the Optimality Criterion II (B), are indicated. For A, B, and C, the respective sensor locations on the tongue surface are depicted.

squares). Arrangement A (Case A), depicts the optimal set of sensors if the Optimality Criterion I is employed. The optimal set of sensors is denoted by $\boldsymbol{\beta}_{\mathrm{I}}^{\mathrm{opt}}$. Sensor arrangement B (Case B) represents the optimal choice, $\boldsymbol{\beta}_{\mathrm{II}}^{\mathrm{opt}}$, for the Optimality Criterion II. Based on the Optimality Criterion I, marker arrangement B relates to the 4555-th rank (index 190025 out of 194580). Additionally, sensor arrangement C (Case C) represents the worst set of sensors to capture retraction of the tongue, denoted by $\boldsymbol{\beta}_{\mathrm{I}}^{\mathrm{worst}}$.

A sensitivity analysis was carried out, as described in Section 5.3, to make sure that the proposed sensor arrangement in Case A is indeed a better choice than in Case B or C. One particular state during tongue movement is arbitrarily chosen by computing the resulting deformations of the tongue using $\alpha_t = 0.75$ and $\alpha_s = 0.25$. The particular choices of activation levels is associated with a (generic) mode of deformation, which is likely to occur during the retraction of the tongue (this assumption is based on the fact that the only active muscle fibre groups during retraction are the transversus and the styloglossus muscle fibre groups). A forward simulation

is used to determine the exact sensor locations for the different sensor arrangements, i.e., Case A, B, and C.

To investigate the practicability of the proposed sensor optimisation criteria, the sensor locations is subjected to machine-inherent noise, i.e., $\mathbf{e}_i^{\boldsymbol{s}} = [e_1^{\boldsymbol{s}}, e_2^{\boldsymbol{s}}, e_3^{\boldsymbol{s}}]^T$ with $e_i^{\boldsymbol{s}} \sim \mathcal{N}(\mu, \sigma^2)$, $\mu = 0$, and $\sigma^2 = 0.49$ (see also Section 5.3). A total of 41 different perturbations are computed for the sensor arrangements in Case A and B, containing 2 and 6 sensors, respectively. Similarly, 41 different perturbations are applied to the 4 sets of sensor locations in Case A, B, and C. The aim of perturbing the sensor locations is to test the ability of estimating the actual muscle activity levels α_t (transversus) and α_s (styloglossus) based on sensor locations that are prone to errors. The results of the estimated activation levels α_t and α_s are presented in Figure 5.3(a) as scatter plots for 2 sensors, in Figure 5.3(b) for 4 sensors, and in Figure 5.3(c) for 6 sensors, respectively. Table 5.1 lists the estimated values and the respective standard deviations of the sensitivity analysis.

	α_t		
	Case A	Case B	Case C
2 sensors	0.7702 ± 0.1542		0.6992 ± 0.2889
4 sensors	0.7532 ± 0.1244	0.7547 ± 0.1120	0.8056 ± 0.1694
6 sensors	0.7412 ± 0.0761		0.7928 ± 0.1349
	α_s		
	Case A	Case B	Case C
2 sensors	0.3149 ± 0.2801		0.6125 ± 0.3764
4 sensors	0.2655 ± 0.1176	0.3065 ± 0.1421	0.3135 ± 0.2991
6 sensors	0.2578 ± 0.0639		0.4507 ± 0.3051

Table 5.1: Sensitivity results for tongue retraction: Reported are the estimated values and the standard deviations of the activation levels α_t and α_s, derived through inverse analysis using perturbed sensor locations. The respective sensor locations were perturbed (see Section 5.3) based on the results of the forward problem analysis, with $\alpha_t = 0.75$ and $\alpha_s = 0.25$. The results for a sample size of 41 is depicted for Case A, B, and C.

The standard deviation of the estimated activation levels decreased with an increasing number of deployed sensors in all cases, except for Case C with 4 compared to 6 sensors, see Table 5.1. However, the difference in the standard deviation between 4 and 6 sensors in Case C was marginal (0.2991 in case of 4 sensors compared to 0.3051 in case of 6 sensors). The difference between the computed values from the inverse problems, $E(\hat{\alpha}_t)$ and $E(\hat{\alpha}_s)$, and the associated

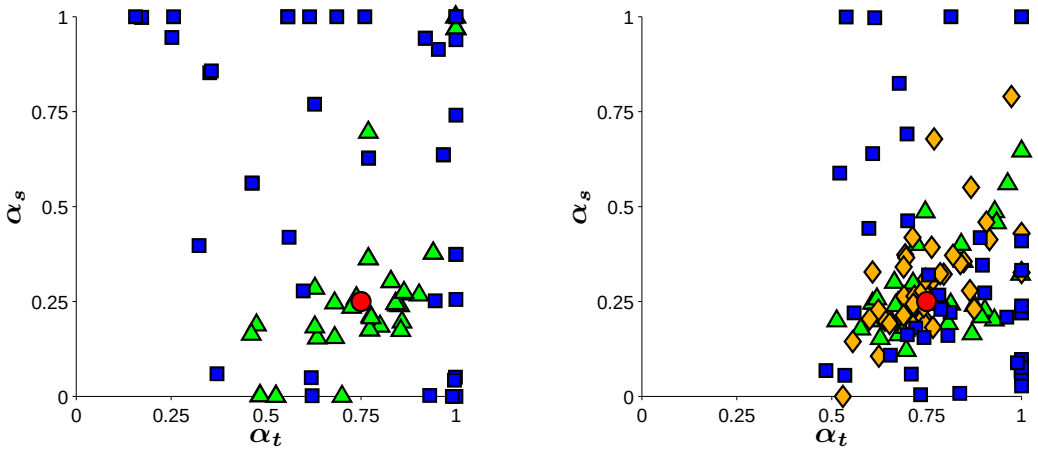

(a) 2 sensors

(b) 4 sensors

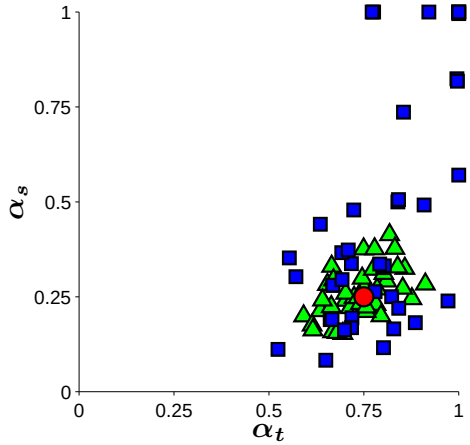

(c) 6 sensors

Figure 5.3: Scatter plots visualising the estimated levels of activation of the transversus (α_t) and styloglossus (α_s) muscle fibre groups for one deformation mode during tongue retraction. The green triangles depict the (α_t,α_s) levels obtained by solving the inverse problems under the assumption that the sensor locations conform with Case A, the yellow diamonds represent the results for Case B, and the blue squares show the resulting activation levels for Case C. The red circle indicates the chosen (ground truth) activation level for the forward problem.

.

activation levels from the forward problem (α_t and α_s) decreased with an increasing number of sensors, except for $\hat{\alpha}_t$ in Case A with 4 compared to 6 sensors. In Case A, the difference between the computed values of the estimator $\hat{\alpha}_t$ and the activation level of the forward problem, $\alpha_t = 0.75$, increased from 0.0032 for 4 sensors to 0.0088 with 6 sensors. However, the associated standard deviations of the estimated activation levels decreased significantly from 0.1244 to 0.0761.

Since the estimated activation levels, α_t and α_s, are obtained based on an inverse problem analysis, the values of the estimators and the respective standard deviations should not be considered independently. Therefore, two additional measures, combining the estimations for α_t and α_s, are introduced. Firstly, the scaled bias of an estimator $\hat{\theta}_i$ is computed from

$$\mathscr{B}_i(\hat{\theta}_i) = s_i \cdot \left\| \frac{E(\hat{\theta}_i) - \theta_i}{\theta_i} \right\|, \tag{5.15}$$

where θ_i is either α_t or α_s of the forward problem, i.e., $\alpha_t = 0.75$ and $\alpha_s = 0.25$; $E(\hat{\theta}_i)$ are the estimated values reported in Table 5.1; and s_i is a scaling factor that depends on the volume fraction of the respective muscle fibre group. The scaling factors for the bias of the transversus muscle fibre group, s_t, and the stylogoluss muscle fibre group, s_s, are defined as

$$s_t = \frac{\int_\Omega d_t(\mathbf{x})\, dV}{\int_\Omega \sum_{j \in \mathscr{F}} d_j(\mathbf{x})\, dV} \tag{5.16}$$

and

$$s_s = \frac{\int_\Omega d_s(\mathbf{x})\, dV}{\int_\Omega \sum_{j \in \mathscr{F}} d_j(\mathbf{x})\, dV}, \tag{5.17}$$

whereby Ω represents the volume of the entire tongue and d_j is the volume fraction of muscle fibre group j. The integrals in Equation 5.16 and 5.17 are approximated by summing up the respective volume fractions at all Gauss points. Note that for each $\mathbf{x} \in \Omega$, the sum of all volume fractions equals 1. Hence, the respective scaling parameters are computed from

$$s_t \approx \frac{\sum_i^{\#\text{ of GP}} d_t(\mathbf{x}_i)}{\sum_i^{\#\text{ of GP}} 1} = 0.1772 \tag{5.18}$$

and

$$s_s \approx \frac{\sum_i^{\#\text{ of GP}} d_s(\mathbf{x}_i)}{\sum_i^{\#\text{ of GP}} 1} = 0.1063. \tag{5.19}$$

In a similar way, the averaged bias, an overall measure for the standard deviation, is introduced through an averaged coefficient of variation. The coefficient of variation $c_v(\hat{\theta}_i)$ for an estimator $\hat{\theta}_i$ is a normalised measure of dispersion of a probability distribution, i.e.

$$c_v(\hat{\theta}_i) = \frac{\sigma(\hat{\theta}_i)}{E(\hat{\theta}_i)}. \tag{5.20}$$

The variation of coefficients for the two different estimators is combined in one measure by taking into account the scaling parameters of the respective muscle fibre groups.

Thus, the average bias and the average coefficient of variation are defined for the case of retraction in the following way:

$$\bar{\mathscr{B}}^p = \frac{1}{s_t + s_s} \left[\sum_{i=\{t,s\}} \mathscr{B}_i(\hat{\theta}_i) \right] \tag{5.21}$$

and

$$\bar{c}_v^p = \frac{1}{s_t + s_s} \left[\sum_{i=\{t,s\}} s_i \frac{\sigma(\hat{\theta}_i)}{E(\hat{\theta}_i)} \right]. \tag{5.22}$$

The average bias, $\bar{\mathscr{B}}^p$, and the average coefficient of variation, $\bar{c}_v^p$, as defined in Eqs. 5.21 and 5.22, are given in Table 5.2 based on the data reported in Table 5.1. The average bias and

	Case A		Case B		Case C	
	$\bar{\mathscr{B}}^p$	$\bar{c}_v^p$	$\bar{\mathscr{B}}^p$	$\bar{c}_v^p$	$\bar{\mathscr{B}}^p$	$\bar{c}_v^p$
2 sensors	0.1142	0.4587			0.5860	0.6826
4 sensors	0.0259	0.2693	0.0887	0.2666	0.1416	0.4892
6 sensors	0.0190	0.1571			0.3367	0.3601

Table 5.2: Average bias and average coefficient of variation calculated based on the expectation values and respective standard deviations reported in Table 5.1.

coefficient of variation constitute two measures to estimate the material parameters, α_t and α_s, in instances where sensor locations are subject to machine-inherent measurement errors.

In the present study of tongue retraction, the bias decreased for all cases, if the number of sen-

sors was increased, except for Case C with 4 sensors (0.1416) compared to 6 sensors (0.3367). Furthermore, the bias and the coefficient of variation increased from Case A to Case C if the number of sensors was kept fixed, except for 4 sensors in Case A (0.2693) compared to Case B (0.2666). However, the bias of Case A (0.0259) was (much) smaller than the bias of Case B (0.0887) with 4 sensors. Overall, the results in Table 5.2 support the results shown in Figure 5.2, suggesting that the Optimality Criterion I is, at least for the case of tongue retraction, superior to the Optimality Criterion II.

To conclude with case study I, the optimal and worst sensor locations for $n = 2$, 4 and 6 deployable sensors, as well as the 4 optimal sensor locations based on the Optimality Criterion I and II, are depicted in Figure 5.4.

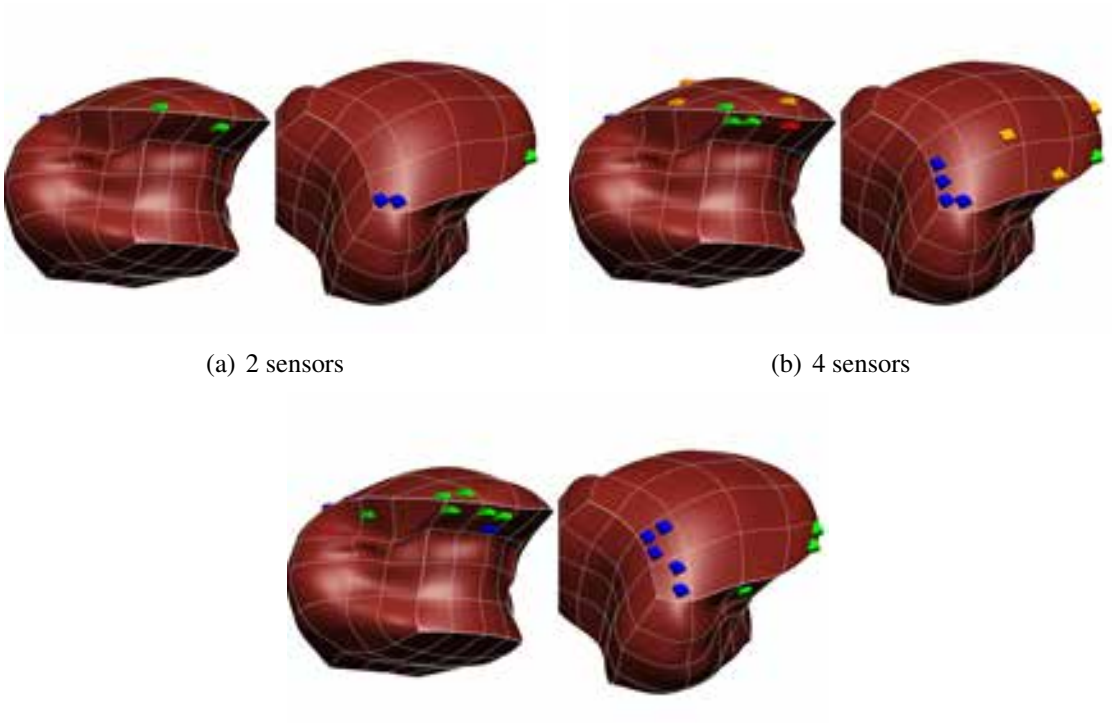

(a) 2 sensors

(b) 4 sensors

(c) 6 sensors

Figure 5.4: Sensor placements for tracking tongue retraction using 2, 4, and 6 sensors based on the Optimality Criterion I and II. The green cubes represent the sensor locations for Case A (optimal), the golden cubes show the locations for Case B (heuristic), and the blue cubes depict the sensor locations for Case C (worst). The location of one sensor, out of four sensors, coincided in Case A and B. This sensor is highlighted in panel (b) in red.

5.4.2 Case study II: elongation

In the second case study, muscle activation levels during tongue elongation are analysed in a similar fashion as presented in Section 5.4.1 to further assess the robustness of the optimal marker locations based on Optimality Criterion I and II. The primary muscle fibre groups responsible for the elongation of the tongue are thought to be the transversus and verticalis muscle fibre groups [Napadow et al., 1999a]. In the present work, the different deformation modes of tongue elongation are computed by choosing the activation levels of $\alpha_t = \alpha_v = 0.5$ for transversus and verticalis muscle groups, respectively. Based on the resulting deformation from the forward problem analysis, the muscle activation levels are estimated using an inverse problem approach with 2 and 6 sensors in Case A and C, and 4 sensors in Case A, B and C. Additionally, a sensitivity analysis is carried out for perturbed sensor locations due to machine-inherent measurement errors. Again, for each case and for each sensor arrangement, a total of 41 perturbed sensor locations are considered. For each perturbed sensor location an inverse problem is solved to estimate the respective levels of activation. The search space of the inverse problem hereby is restricted to $0 \leq \alpha_t \leq 1$ and $0 \leq \alpha_v \leq 1$. All other activation level parameters are considered to be 0.

Similar to the case of tongue retraction, the best and worst sensor arrangements for elongation were determined for both the Optimality Criterion I and the Optimality Criterion II. The best and worst sensor arrangements based on Optimality Criterion I with 2 and 6 sensors are denoted by Case A and Case C respectively. The best sensor arrangement based on the Optimality Criterion II with 4 deployable sensors is denoted by Case B. The sensor arrangements in all cases are obtained by evaluating a similar objective function as proposed for tongue retraction. The only differences between the objective function for tongue elongation, and the objective function defined in Equation 5.14, are the values of the non-zero activation levels (α_t and α_v instead of α_t and α_s for retraction). To extract the desired sensor locations, the respective sensor arrangement indices are ordered by the magnitudes of the evaluated objectives function values. Again, sensor location arrangements with larger values of the objective function are considered to be more suitable for capturing the motion of the tongue during elongation. Figure

5.5 presents the objective function values for $n = 4$ sensors and the locations of the sensors for Case A, B, and C.

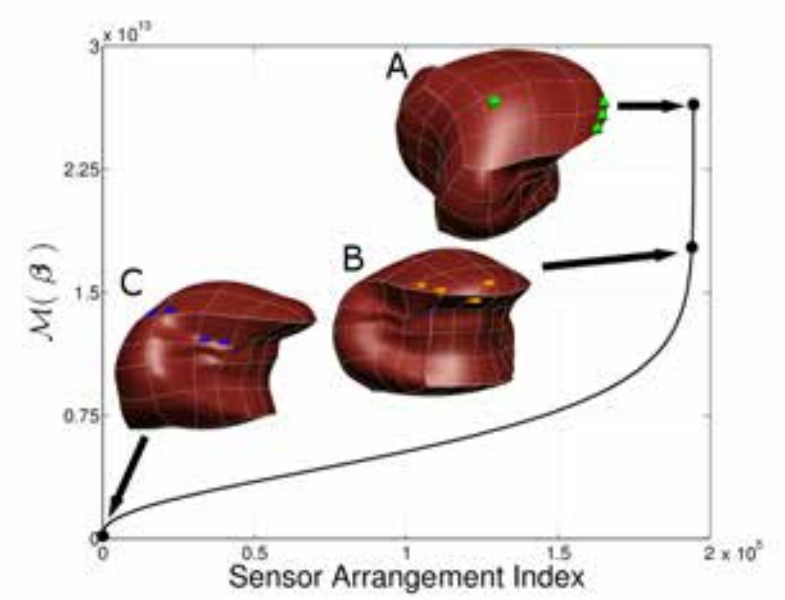

Figure 5.5: Ranking of feasible sensor arrangements, $\boldsymbol{\beta}_l \in \mathrm{SL}(4)$, for elongation based on the respective objective function values. Further included are the locations for the best (A) and worst (C) choices, based on the Optimality Criterion I, as well as the best choice based on the Optimality Criterion II (B). The respective sensor locations on the tongue surface are depicted for Case A, B, and C.

Figure 5.6 depicts the solutions for all cases of the inverse problem analysis. The green triangles depict the estimated activation levels (α_t, α_v) obtained by solving the respective inverse problems for the best sensor placements based on Optimality Criterion I, the yellow diamonds represent the estimates based on the best sensor placements obtained by Optimality Criterion II, and the blue squares refer to the estimates based on the worst sensor placements obtained by Optimality Criterion I. The red circle indicates the ground truth activation levels to determine a mode of deformation during tongue elongation using the forward problem analysis (α_t, α_v)=$(0.5, 0.5)$.

The more closely the estimates of the inverse problem were clustered around (α_t, α_v)=$(0.5, 0.5)$, the less sensitive were the estimated activation levels to measurement errors due to machine-inherent recording errors. A statistical analysis was carried out to make a comparison between Case A, B and C. Table 5.3 presents the computed values of the estimators, $E(\hat{\alpha}_t)$ and $E(\hat{\alpha}_v)$ and their standard deviations based on the results shown in Figure 5.6.

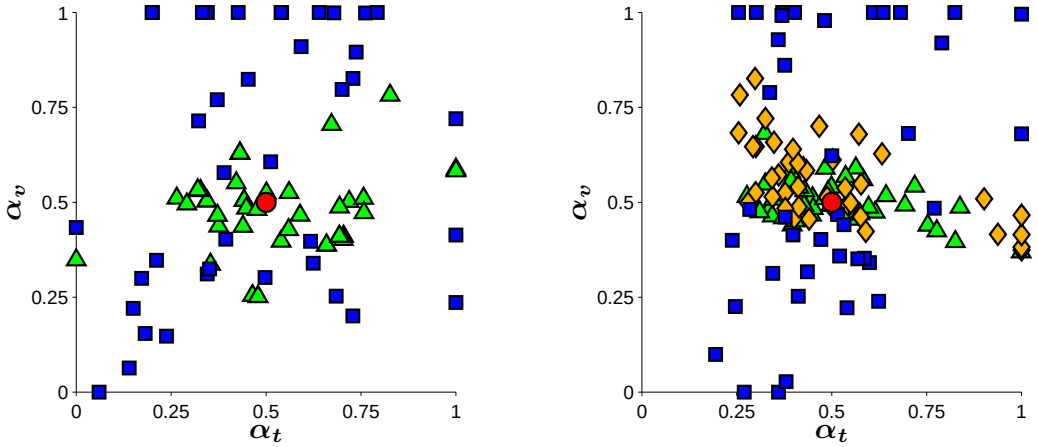

(a) 2 sensors

(b) 4 sensors

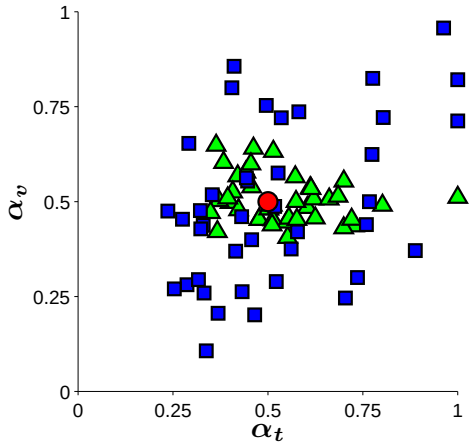

(c) 6 sensors

Figure 5.6: The scatter plots visualise the estimated levels of activation of the transversus (α_t) and verticalis (α_v) muscle fibre groups for one deformation mode during tongue elongation. The green triangles depict the estimated activation levels (α_t,α_v) obtained by the solving the respective inverse problem with the sensor locations as in Case A, the yellow diamond represent the results for Case B, and the blue squares show the estimated activations levels for Case C. The red circle indicates the chosen ground truth level of activation for the forward problem analysis.

	α_t		
	Case A	Case B	Case C
2 sensors	0.5284 ± 0.1998		0.4923 ± 0.2807
4 sensors	0.5107 ± 0.1639	0.5028 ± 0.2208	0.4889 ± 0.1965
6 sensors	0.5403 ± 0.1368		0.5225 ± 0.2165
	α_v		
	Case A	Case B	Case C
2 sensors	0.4792 ± 0.1112		0.6022 ± 0.3420
4 sensors	0.5036 ± 0.0588	0.5531 ± 0.1054	0.5878 ± 0.3414
6 sensors	0.5049 ± 0.0621		0.4927 ± 0.2102

Table 5.3: Sensitivity results for tongue elongation: Reported are the estimated values and the standard deviations of the activation levels α_t and α_v obtained through an inverse problem analysis using perturbed sensor locations. The respective sensor locations were perturbed (see Chapter 5.3) based on the results of the forward problem analysis with ground truth values of $\alpha_t = \alpha_v = 0.5$. The results for a sample size of 41 is depicted for Case A, B, and C.

For a fixed number of deployable sensors, the standard deviations are smaller in Case A than in Case C, as seen in Table 5.3. The standard deviation only decreases from Case B to Case C for α_t with 4 deployed sensors. However, the standard deviation increases substantially from Case B to Case C for α_v with 4 deployed sensors. No clear behaviour with respect to the estimated activation levels, i.e. α_t and α_v, can be deducted by statistically analysing each level of activation independently, as seen in Table 5.4. However, the estimated values of α_t vary less compared to α_v. The range for $E(\hat{\alpha}_t)$ is between 0.4889 and 0.5403, while the range for $E(\hat{\alpha}_v)$ spread from 0.4792 to 0.6022.

Instead of analysing the estimated values and standard deviations of the different activation levels independently, two combined statistical measures are defined like in the case of tongue retraction. The average bias and the coefficient of variation for tongue elongation are computed from

$$\bar{\mathscr{B}}^e = \frac{1}{s_t + s_v} \left[\sum_{i=\{t,v\}} \mathscr{B}_i(\hat{\theta}_i) \right] \tag{5.23}$$

and

$$\bar{c}_v^e = \frac{1}{s_t + s_v} \left[\sum_{i=\{t,v\}} s_i \frac{\sigma(\hat{\theta}_i)}{E(\hat{\theta}_i)} \right], \tag{5.24}$$

where θ_i is either α_t or α_v and the scaling factors for the transversus and the verticalis muscle fibre group are $s_t = 0.1772$ and $s_v = 0.2087$, respectively.

The results of the average bias and the coefficient of variation for tongue elongation are given in Table 5.4. The average bias and coefficient of variation increases from Case A to Case C, provided that the number of deployable sensors remain constant (Table 5.4).

	Case A		Case B		Case C	
	$\mathscr{B}^e$	$\bar{c}_v^e$	$\mathscr{B}^e$	$\bar{c}_v^e$	$\mathscr{B}^e$	$\bar{c}_v^e$
2 sensors	0.0486	0.2991			0.1176	0.5690
4 sensors	0.0137	0.2105	0.0600	0.3047	0.1052	0.4987
6 sensors	0.0423	0.1828			0.0286	0.4210

Table 5.4: Average bias and average coefficient of variation calculated based on the estimated values and standard deviations reported in Table 5.3.

This strengthened the hypothesis that Case A provided suitable optimality criteria for sensor placement to calculate muscle fibre activation levels from inverse analysis given noise-afflicted sensor measurements. For Case C, the average bias and coefficient of variation decreases if the number of deployable sensors increases. Similarly, the average bias and coefficient of variation decreased for Case A if the number of deployable sensors increases from 2 to 4. In contrast, the average bias in Case A increases from 0.0137 for 4 sensors to 0.0423 for 6 sensors; while the average coefficient of variation decreases from 0.2105 (4 sensors) to 0.1828 (6 sensors).

For tongue elongation, the optimal and worst sensor locations for $n = 2$, 4 and 6 deployable sensors, as well as the 4 optimal sensor locations based on Optimality Criterion II, are depicted in Figure 5.7.

5.5 Numerical behaviour of the estimation process

Computing for a specific set of sensor locations, the respective activation levels are based on solving the optimisation problem given in Equation 5.13. For the *Trust-Region-Reflective* algorithm, as for most other optimisation algorithms, a convex objective function with a global minimum is desired. In the following, the visual characterisation of the objective function is presented. To do so, the objective function, which is minimised with respect to the level of activation (cf. Equation 5.13), was evaluated over the parameter space subject to different sce-

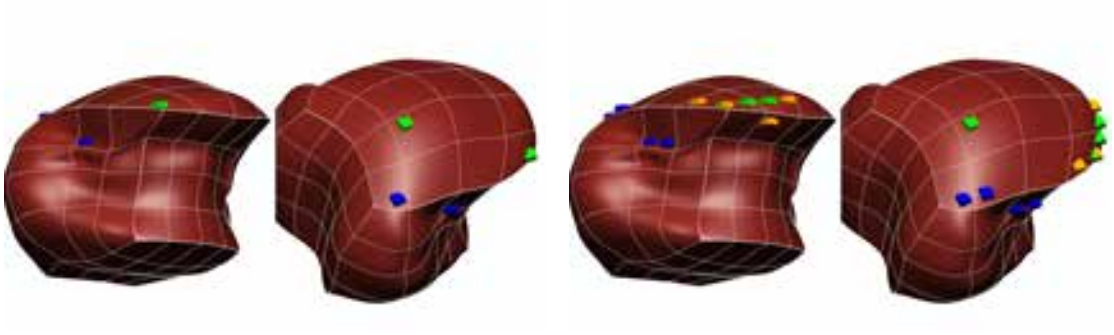

(a) 2 sensors

(b) 4 sensors

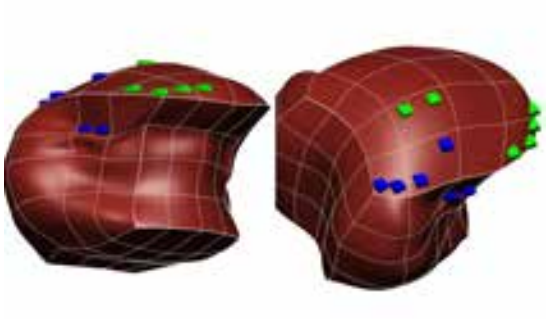

(c) 6 sensors

Figure 5.7: Sensor placements for tracking tongue elongation using 2, 4, and 6 sensors based on Optimality Criterion I and II. The green cubes represent the locations for Case A, the golden cubes show the locations of Case B, while the blue cubes depict the sensor locations of Case C.

.

narios, e.g. for retraction and elongation and different sensor arrangements. Figure 5.8 depicts the contour plots for retraction with 2, 4 and 6 sensors based on the previously-computed sensor locations in Case A (Figure 5.8(a), 5.8(c) and 5.8(e)) and Case C (Figure 5.8(b), 5.8(d) and 5.8(f)). Figure 5.9 presents the respective contour plots for tracking elongation with 2, 4 and 6 sensors. Case A for elongation is depicted in Figure 5.9(a), 5.9(c) and 5.9(e) and Case C in Figure 5.9(b), 5.9(d) and 5.9(f), respectively. In all cases, the sensors are not subjected to any noise.

The contour line of the objective function emcompassed a much larger area in case of the worst sensor placement (Case C) compared to the best sensor placement (Case A), see Figure 5.8. The objective function represents the sum of the L_2-norms of the differences between the measured sensor locations and the computed sensor locations. Thus, perturbing sensor , subject to "bad" sensor placements (adding measurement noise), had a greater effect than for sensors with "good" placement. Figures 5.8 and 5.9 provide visual insights as to why non-optimal sensor placement lead to more variations in predicting the respective activation levels. Furthermore, an increase in the number of sensors led to a rise in the numerical difference between neighbouring contours lines, in case of good or bad sensor placement. This behaviour of the objective function is associated with a greater convergence rate during the inverse estimation procedure, and implies an increased chance of reaching the optimal solution (the actual configuration).

5.6 Discussion

Motion tracking systems are commonly used to study the dynamics (and indirectly the biomechanical behaviour) of an object. The challenge of all motion tracking systems is to find suitable marker placements that completely characterise the motion of all points throughout the object. In gait analysis, for example, the challenge is to deduce the relative motion of the bones within the musculoskeletal systems from a (small) set of markers. Skin artefacts [e.g., Karlsson and Tranberg, 1999] and wobbling masses [e.g., Schmitt and Günther, 2011] can play a crucial role in tracking gait and have the potential to introduce significant errors to the analysis. In

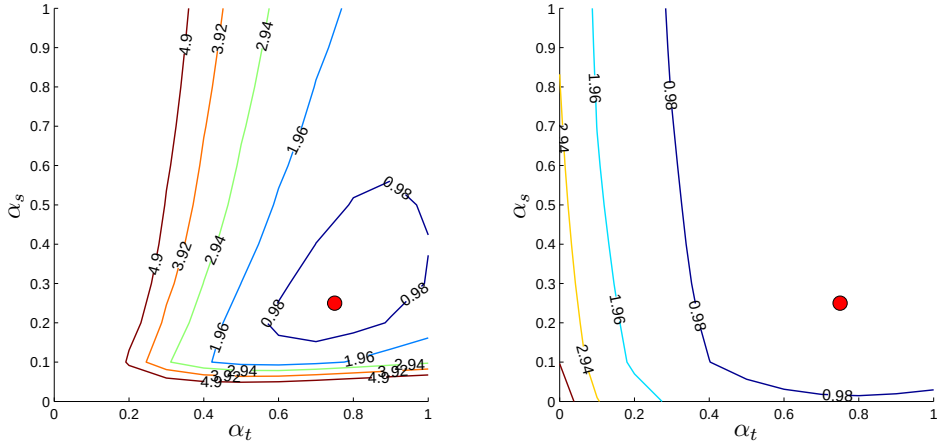

(a) Retraction, Case A, 2 sensors

(b) Retraction, Case C, 2 sensors

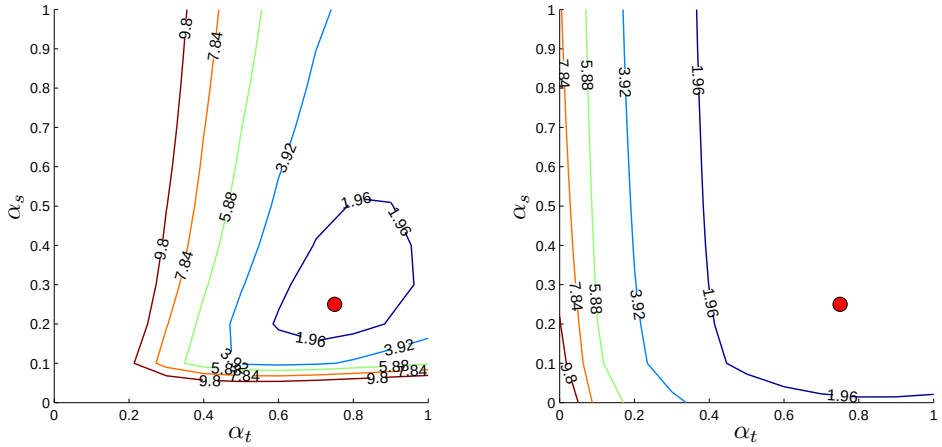

(c) Retraction, Case A, 4 sensors

(d) Retraction, Case C, 4 sensors

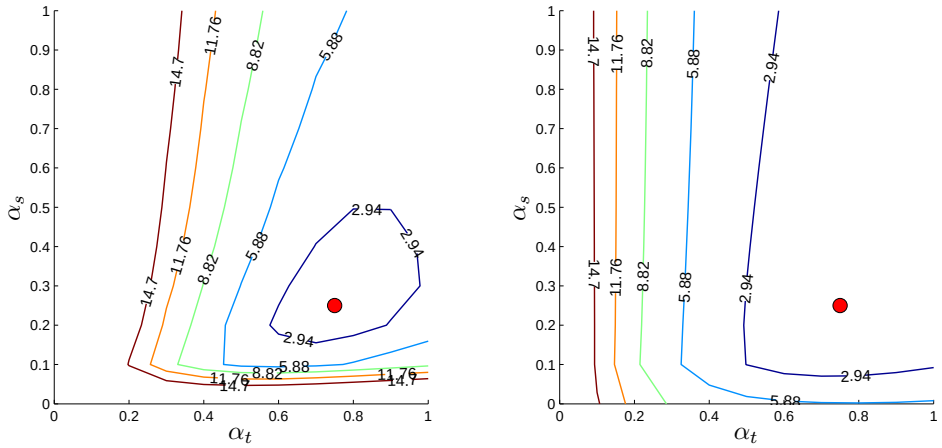

(e) Retraction, Case A, 6 sensors

(f) Retraction, Case C, 6 sensors

Figure 5.8: Contour plot of the objective function given by Equation 5.13 with zero noise. The red dots show the ground truth values of the activation parameters configuration with the objective function being 0. Panels (a), (c) and (e) depict the objective function in case of tracking retraction with 2, 4 and 6 sensors, respectively, subject to the best sensor placement (Case A); while Panels (b), (d) and (f) depict the objective function for the worst sensor placement (Case C).

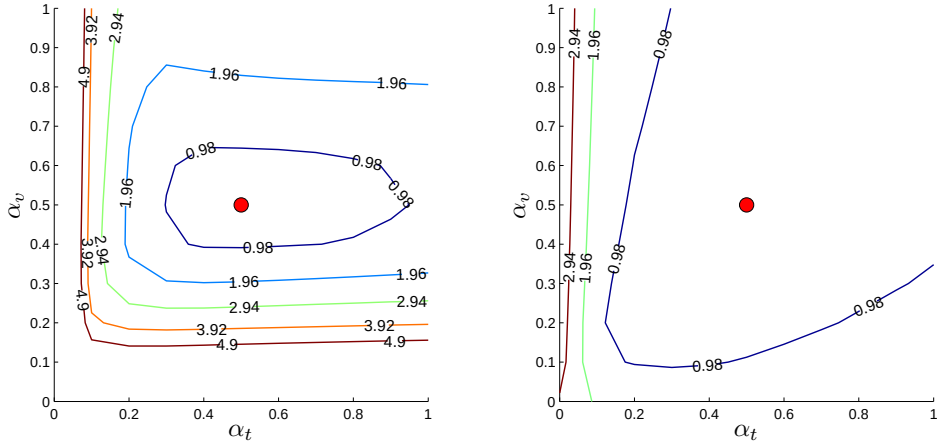

(a) Elongation, CASE A, 2 sensors

(b) Elongation, CASE C, 2 sensors

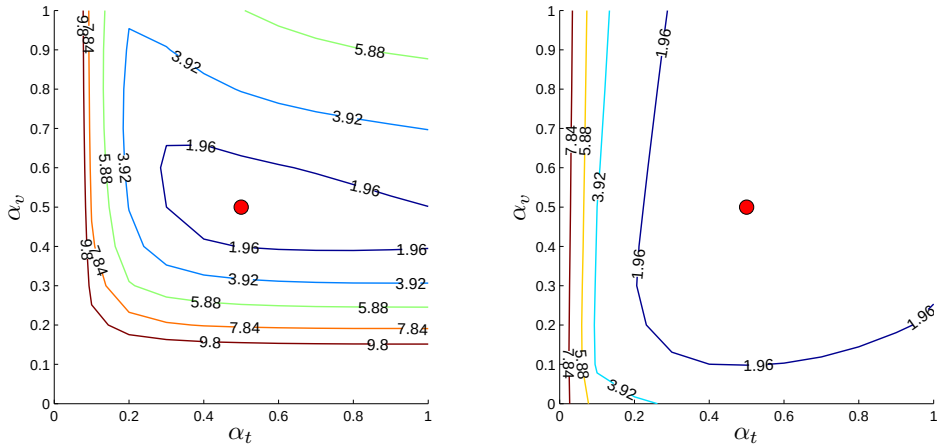

(c) Elongation, CASE A, 4 sensors

(d) Elongation, CASE C, 4 sensors

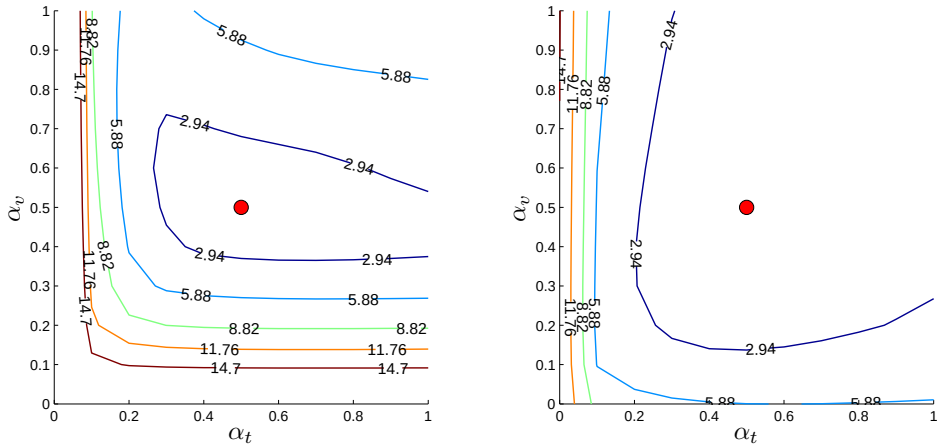

(e) Elongation, CASE A, 6 sensors

(f) Elongation, CASE C, 6 sensors

Figure 5.9: Contour plot of the objective function given by Equation 5.13 with zero noise. The red dots show the ground truth values of the activation parameters configuration for which the objective function is 0. Panels (a), (c) and (e) depict the objective function in case of tracking elongation with 2, 4 and 6 sensors, respectively, subject to the best sensor placements (Case A); while Panels (b), (d) and (f) depict the objective function for the worst sensor placements (Case C).

the case of the tongue, the first challenge is to obtain reasonable marker movements as the tongue is largely hidden within the oral cavity. This can be achieved using electromagnetic articulography.

To obtain further insights into the biomechanical behaviour of the tongue, one has to study it's structural and mechanical properties, in addition to its motion. This poses further challenges as the tongue is a complex, extremely flexible and dexterous mechanical object, consisting of many interlaced muscle fibre groups. The present study provides, for the first time, a model-based identification method for the optimal placement of Articulograph sensors on the accessible parts of the tongue surface to track different movements, e.g., tongue retraction and elongation. The model-based identification draws on a pre-computed envelope of tongue motion for the cases of retraction and elongation. Apart from oral research, the present methodology may provide a suitable tool to improve sensor locations for other motion tracking applications, such as gait analysis.

As an alternative to articulography, MRI techniques have been employed to track the deformation of the tongue [Stone et al., 2001, Hiiemae and Palmer, 2003, Honda et al., 2010]. In contrast to motion tracking systems, which are limited to the external surface of the tongue, MRI has the advantage to allow the tracking of the tongue's internal structures. For example, diffusion tensor MRI can provide interesting insights into the fibre distribution of the tongue; tagged MRI allows one to analyse the muscle deformation during motion [Napadow et al., 1999a,b, 2002]; and other MRI scanning sequences can provide ways of investigating strain [e.g., Zhong et al., 2008, for skeletal muscles]. However, the acquisition of MRI data is generally time-consuming; while tongue movement, e.g. swallowing, happens quickly. Thus, the acquisition of high-quality MRI data of the tongue in motion is challenging. The subject would need to hold a desired pose for a long period of time or would need to be able to perform the process of swallowing extremely slowly or in a very repetitive fashion.

In the present study, the tongue was considered as an isolated structure/organ, which is a drawback of the proposed modelling technique. The interaction of the tongue with the surrounding structures of the oral cavity is not considered in computing the envelope of motion using the

forward continuum-mechanical model. It is clear that interactions of the tongue with the palate and teeth have an influence on the tongue's mode of deformation. However, since interactions with surrounding structures only occur in cases of high muscle activation levels, e.g. in the case where the tip of the tongue is elongated far out of the mouth, the drawbacks of not considering those interactions are limited.

The mechanical model is not only the basis for determining the optimal set of sensor locations based on the envelope of movement (forward analysis); it is also used to derive the activation levels based on a particular set of sensors for an actual tongue configuration (inverse analysis). The ability to perform the inverse problem analysis depends on the robustness of the mechanical model and the choice of objective function. Within this work, the objective function of the inverse problem was based solely on minimising the Euclidean distances between predicted sensor locations for the given estimate of activation levels, and the ground truth sensor locations obtained from the forward dynamics simulations (using specified activation levels). A major issue with inverse problems for tissue parameter estimation is that the optimal constitutive parameters may not be unique, particularly given the sparse nature of the articulograph measurements. In the present study, the inverse analysis only comprise the estimation of two muscle activation levels for the cases of elongation and retraction. Thus, the proposed objective function seems to be adequate. However, other objective functions, which further account for inter-marker distances or strain measures, might be needed in future research to estimate muscle activation parameters for more complex tongue movements.

The restriction to two muscle activation parameters, while subjecting the sensor locations to a Gaussian-distributed measurement error, may result in the inability to find the optimal activation parameters within the search space. For example, if the error-prone sensor locations are not within the range of the envelope of motion obtained through the parameter space (i.e., allowing the activation parameters to range from 0 and 1), the optimal solution cannot be found. In such a case, the optimal solution might be derived by extending the parameter search space to include more muscle fibre groups or increasing the range of activation parameters beyond the interval [0,1]. Increasing the search space to other muscle fibre groups is feasible. However,

retraction or elongation are assumed to be driven by only two muscle fibre groups. If no optimal solution is found, the inverse estimation procedure outputs activation levels at the fringe of the parameter space.

The inverse estimation procedure is sensitive to the initial values of the activation parameters. The objective function may exhibit a plateau or areas with very flat gradients. In such case, the optimal parameters can vary widely for a given optimality tolerance. The variability can be reduced if suitable sensor locations are chosen, as demonstrated in the present results. For example, the estimated activation levels of Case C (worst sensor locations) were spread over almost the entire admissible parameter space, while the activation levels for Case A (best sensor locations) were contained within a much smaller region (see Figures 5.3 and 5.6).

The numerical results in Section 5.4 further demonstrate that the optimal sensor locations based on the Optimality Criterion I have better expectation values/average bias than those based on Optimality Criterion II. In addition, this study demonstrates that an increase in the number of sensors improves the estimated levels of activation for all cases except one (increased bias in Case A for 6 sensors compared to 4, which might be due to added noise). In a post-analysis, an additional test was undertaken with 12 additional test samples

In multi-parameter optimisation, the accuracy of a specific optimisation parameter is often influenced by scaling. Thus, additional care needs to be taken when interpreting the results of the inverse problem because the mechanical model contains intrinsic scaling through the volume fraction and the level of activation. The computed activation levels and standard deviations might be more error-afflicted for muscle fibre groups with small volume fractions. Muscle fibre groups with small volume fractions are likely to have a smaller effect on overall deformation patterns compared to the larger muscle fibre groups. Therefore identifying parameters of the smaller fibre groups will likely be ill-posed, yielding non-unique estimates.

Due to the complex muscle fibre architecture and its associated mechanical behaviour, only two specific motions (tongue retraction and elongation) are considered in this research. Furthermore, symmetry assumptions are exploited to reduce the computational time. In particular,

it is assumed that the symmetric arrangement of the muscle fibre groups within the tongue leads to symmetric contractions and to symmetric deformations. Additionally, the present computational analyses are based on the assumption that the level of activation is constant throughout the entire muscle fibre group. Only symmetric movements, including tongue elongation or retraction, are considered, and hence, the symmetry assumptions are considered realistic and justify the restriction of the analysis to one half of the tongue.

The number of sensors for each half of the tongue is limited to a maximum of 6 sensors due to the physical limitations in the recording channels of the articulograph. A typical setup of an AG500 consists of 12 recording channels. However, placing all 12 sensors on the tongue is not advisable. To isolate the specific tongue deformation, the movement of the mandible needs to be taken into account. To obtain the mandible movement with six degrees of freedom, at least three markers need to be utilised on the head, e.g., adhering them to the maxillary teeth, and three markers on the mandible, e.g., on the mandibular teeth [compare, for example, Röhrle et al., 2009, Saini et al., 2009]. The initial distribution of potential sensor locations (48 per half tongue) was evenly distributed over the accessible tongue surface. The distances between sensors were big enough to avoid overlapping regions of two neighbouring sensors after the application of noise, i.e. machine-inherent error. An overlap of sensor locations would pose additional challenges in obtaining the levels of activation by means of an inverse problem analysis.

The application of the present modelling framework to the entire tongue would likely result in a different optimal sensor arrangement compared to half of the tongue. For example, in the case that one sensor is located on the line of symmetry, it would make no sense to add another sensor at the same location when considering the entire tongue. Nevertheless, the present approach may be utilised to determine the optimal sensor locations on the entire tongue; however, the number of deployable sensor locations would need to be reduced. Choosing a total of 96 sensor locations (twice as many as for half of the tongue) would result in too many combinations of sensor arrangements. Thus, some sensor arrangements would need to be ruled out a priori to provide a computationally tractable problem.

Some computed sensor locations might not be practical for experimental data acquisition. Thus, recommendations from this work should be considered qualitative in nature. A great deal of variability exists between the tongue's shape and muscle fibre distribution of different subjects. Nevertheless, the outcome of the present study provides clear evidence for a recommendation of sensor placements if the aim is to track tongue retraction or elongation (see Figures 5.2 and 5.5). Several sensible choices of sensor locations are identified, while unsuitable choices are pointed out. Based on the results of the present work, it can be concluded that sensor locations for articulography should not be chosen arbitrarily or heuristically. In particular, a heuristic criterion such as the Optimality Criterion II, aiming to account for the magnitude and maximal variation of the displacement in each spatial direction, exhibited high average bias and coefficient of variation. The overall method, presented in this work, is well suited for application to other cases, which aim to determine an optimal set of sensor locations for capturing the key characteristics of mechanical deformation, e.g., in gait analysis.

5.7 Summary

The deformations of the tongue model, sampled in the parameter (activation level) domain, are used to identify the best sensor locations to improve the tracking of motion features of the tongue. The present study introduces a forward problem method to derive the envelopes of the tongue motion for improved design of sensor locations during articulography. The optimal sensor locations are subsequently used to quantitatively identify the muscle contractile state by conducting an inverse problem analysis using the tongue model, under the conditions of large machine-inherent errors. A possible extension of the inverse problem may help in the identification of muscular activity for a particular tongue motion. Such insights can benefit the understanding of the mechanism behind the tongue's various deformations during different physiological tasks (e.g. swallowing) in a model-based quantitative manner.

Chapter 6

Identification of tongue muscle fibre group contraction from MR images

The literature regarding muscle activation levels during tongue motion is sparse, and the physiological roles of different muscle groups involved in tongue function are poorly understood. One objective of the present study is to use the tongue model, developed in Chapter 4, to study the correlation between tongue motion and tongue muscular activity. The results of the inverse problem, summarised in Chapter 5, demonstrate that the relationship between muscle structure and tongue function can be analysed using the proposed modelling framework.

In the following, the inverse problem framework is applied to investigate the physiological roles of tongue muscles during propulsion in dry swallowing using kinematic data reported by Napadow et al. [1999b]. The associated computational experiments consist of two parts

- Firstly, the empirical conclusions drawn by Napadow et al. [1999b] are tested using an inverse problem framework.
- Secondly, more comprehensive inverse testing of the given data is conducted to identify additional muscle activity patterns during propulsion, which might have been ignored previously.

Note that, comprehensive inverse testing requires extensive computational resource. Thus, a special emphasis is placed on improving efficiency of the inverse framework outlined in Section 4.7 prior to any analysis.

6.1 Tongue imaging experiments by Napadow et al. [1999b]

MRI tissue tagging makes it possible to fully characterise the deformation of the tongue during different activities by tracking material points within the tongue body. Napadow et al. [1999b] studied the *in-vivo* deformation of the tongue during different food intake tasks, and provided a quantitative description of the internal tissue movements during these activities. The same study further attempted to explain the different muscle activation patterns by combining muscle motion, derived from MR images, with spatial distributions and orientations of muscle fibres.

In Napadow et al. [1999b]'s study, a series of tagged MR images in the mid-sagittal plane of the tongue was obtained from 7 healthy adults during propulsion under dry swallowing conditions (i.e. swallowing saliva only). The MR images were obtained using a 1.5 Tesla Siemens Vision MRI system, and an anterior neck coil with an ultrafast asymmetric gradient echo pulse sequence (TurboFlash). The imaging parameters were defined as follows: image slice thickness 10mm, effective spatial resolution 1.33×1.33mm, and matrix size 80×128.

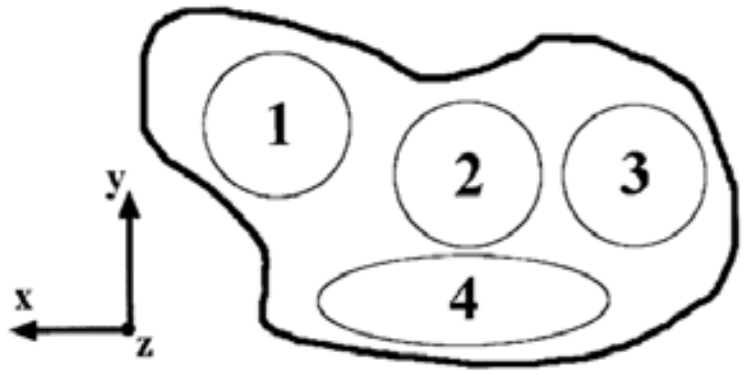

Figure 6.1: Four functional regions defined in the mid-sagittal image plane by Napadow et al. [1999b]. The axes on the left hand sides indicate the anterior-posterior direction (x), the superior-inferior direction (y) and the medial-lateral direction (z). Reproduced from Napadow et al. [1999b].

	Region 1	Region 2	Region 3	Region 4
AP	0.034 ± 0.053	0.065 ± 0.081	$0.173 \pm 0.045 *$	$0.064 \pm 0.044 *$
SI	$0.083 \pm 0.067 *$	0.050 ± 0.093	$0.098 \pm 0.050 *$	0.008 ± 0.058

Table 6.1: Measured axial strain data (mean $\pm$ standard deviation; $* P < 0.01$) taken from Napadow et al. [1999b] estimated within four predefined regions in the tongue during dry swallowing. AP and SI denote the anterior-posterior and superior-inferior directions, respectively.

	Region 1	Region 2	Region 3	Region 4
ML	-0.031 ± 0.064	-0.014 ± 0.08	$-0.109 \pm 0.040 *$	-0.004 ± 0.061

Table 6.2: Derived ML (medial-lateral) axial strain data (mean $\pm$ standard deviation; $* P < 0.01$) taken from Napadow et al. [1999b] using the assumption of tissue incompressibility.

In Napadow's experiment, the mid-sagittal area of the tongue was divided into four non-overlapping regions (see Figure 6.1 in Napadow et al. [1999b]), with each region including several muscle fibre families. The average local axial strains were derived for each region by tracking the deformation of the MRI tags based on the image stacks. For each region, the mean $\pm$ standard deviation of the axial strains in anterior-posterior (AP) and superior-inferior (SI) directions were derived. The resulting strain values in the AP and SI directions are given in Table 6.1. Table 6.2 shows the average axial strains in the medial-lateral (ML) direction, which were derived using the assumption of tissue incompressibility.

The observations by Napadow et al. [1999b] (Table 6.1) indicate that the tongue expands along the AP and SI directions during propulsion in dry swallowing. Since muscle contraction is the only driving force leading to tongue deformation, Napadow et al. [1999b] postulated that the geometrical arrangements of different tongue muscles greatly influence the resultant shape of the tongue. Based on the experimental data, Napadow et al. [1999b] concluded that the AP and SI expansions of the tongue are most likely due to contraction of the transversus or verticalis intrinsic muscles (both of which are believed to align orthogonally in the coronal image plane according to classical anatomy, as shown in Figure 4.2(a)). It was further hypothesised that the retrograde motion of the tongue in propulsion is due to muscle activation of the styloglossus (shown in Figure 4.2(f)).

6.2 Computational simulations of tongue mechanics

Deriving the muscular activities of various tongue muscles using the developed model from Napadow's data is an inverse problem. In this section, the details of the objective function and the computational experiments of muscular activity identification are presented.

6.2.1 Objective function

The four regions in the mid-sagittal plane of the tongue, described in Napadow et al. [1999b], are identified on the tongue model as shown in Figure 6.2. Each region is identified using a set of spatial data points. The local strain tensor $\mathbf{E}$ is evaluated at each point by $\mathbf{E} = 1/2(\nabla\mathbf{u} + \nabla\mathbf{u}^T + \nabla\mathbf{u}^T\nabla\mathbf{u})$, and the average axial strains in the AP and SI directions for the *j-th* region of the tongue model are denoted as $E_{\mathrm{AP}}^{(j,\mathrm{model})}$ and $E_{\mathrm{SI}}^{(j,\mathrm{model})}$, respectively.

In order to estimate the muscle activation levels ($\boldsymbol{\alpha}$), the difference between the modelling results from the inverse problem and the experimentally collected image data is minimised. The following objective function was introduced to compare the average axial strains within each region

$$f(\boldsymbol{\alpha}) = \sum_{j=1}^{4}\left[\frac{E_{\mathrm{AP}}^{(j,\mathrm{expt})} - E_{\mathrm{AP}}^{(j,\mathrm{model})}(\boldsymbol{\alpha})}{\sigma_{\mathrm{AP}}^{(j,\mathrm{expt})}}\right]^2 + \sum_{j=1}^{4}\left[\frac{E_{\mathrm{SI}}^{(j,\mathrm{expt})} - E_{\mathrm{SI}}^{(j,\mathrm{model})}(\boldsymbol{\alpha})}{\sigma_{\mathrm{SI}}^{(j,\mathrm{expt})}}\right]^2, \qquad (6.1)$$

where superscript j denotes the region index, superscript *expt* represents the experimental data, $\sigma_{\mathrm{AP}}^{(j,\mathrm{expt})}$ and $\sigma_{\mathrm{SI}}^{(j,\mathrm{expt})}$ denote the standard deviations of the average axial strain in AP and SI directions, respectively, which are given in Table 6.1. The standard deviation of the measured data $\sigma_{\mathrm{AP}}^{(j,\mathrm{expt})}$ and $\sigma_{\mathrm{SI}}^{(j,\mathrm{expt})}$ were used to scale the differences between the mean strain values of the model and the experimental data, respectively. Smaller standard deviations imply less variations in the measured strain distributions between different individuals, and are thus given a higher weight in the matching process.

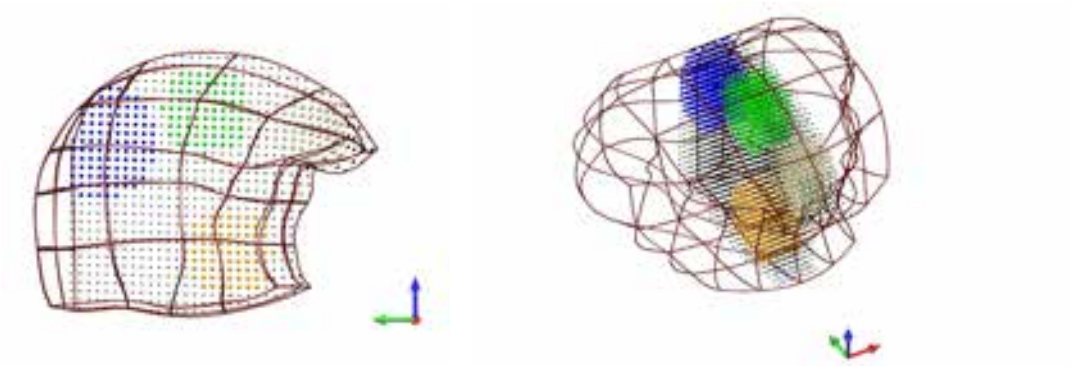

(a) (b)

Figure 6.2: Four regions defined in the tongue model in the initial state correspond to the four imaging regions in Napadow et al. [1999b]. The black dots demarcate the mid-sagittal plane from which Napadow imaged the tongue. The white, green, blue and gold data points represent Region 1, 2, 3 and 4, respectively.

6.2.2 Inverse simulations

Two sets of simulations consisting of five case studies were designed to identify the muscle activation patterns which best matched the experimental strain data in Table 6.1. The inverse problem framework developed in Section 4.7 is used to estimate the levels of activation with in the parameter space that upper bound may beyond 1.0, i.e. $\boldsymbol{\alpha} \in [0,3]^N$, where N is the number of estimated parameters. Firstly, the following three cases were tested assuming homogenous muscle contraction,

- Case study I: Testing of Napadow's hypothesis that the tongue propulsion, as characterised using MRI, is due to the co-contraction of the muscles of styloglossus and transversus or a combination of styloglossus and verticalis muscles (2 parameters);
- Case study II: Testing of 35 other possible activation patterns involving 3 muscles (3 parameters) to see if a better match between model and experimental data can be found.
- Case study III: Testing of one possible activation pattern involving 4 muscles (4 parameters) to see if a better match between model and experimental data can be found.

Secondly, two heterogeneous muscle activation patterns were tested (functional segment control) to best match the experimental strain data,

- Case study IV: Testing of Napadow's hypothesis related to the transversus and styloglossus muscles plus a heterogeneous contraction of the transversus muscle;
- Case study V: Testing of the muscle activation pattern with 4 muscles (Case study III) with a heterogeneous contraction of the transversus muscle.

The design of the five case studies is detailed in Section 6.4.

Napadow's experimental data in Table 6.1 are based on a group of 7 subjects. It is assumed that the data sufficiently represent the statistical variation in tongue deformation during propulsion within the population. The number of standard deviations (NSD) is introduced to compare the differences in modelling output with the experimental data in a statistical sense. The NSD is defined as

$$\text{NSD} = \frac{|E_{\text{direction}}^{(j,\text{expt})} - E_{\text{direction}}^{(j,\text{model})}(\boldsymbol{\alpha})|}{\sigma_{\text{direction}}^{(j,\text{expt})}}, \tag{6.2}$$

where the subscript labelled as "direction" indicates either AP or SI direction, and the superscript j is the region index.

6.3 Method: Accelerating the inverse problem

The inverse problem framework, presented in Section 4.7, is employed for the computational experiments outlined above. The inverse problem is solved using a Newton-like method. In the context of optimization, this sort of method in general requires the construction of multiple components including the objective function, its first derivative (i.e. the gradient vector) and its second derivative (i.e. the Hessian matrix) [Greig, 1980]. Each component is defined with respect to one, or multiple, configurations of the tongue model and is found through the forward difference method in incremental step sizes of 0.001 ($\delta\alpha_i = 0.001$, $\delta\alpha_i$ is the *i-th* component of $\delta\boldsymbol{\alpha}$).

In order to obtain the global minimum in the parameter domain in the present work, each combination of muscles is tested with 6 initial start values. For each value, the parameter estimation

procedure requires the evaluation of multiple configurations to derive the objective function and the first and the second derivatives of the objective function. For instance, in the case of estimating 3 parameters, the forward difference method requires a total of 10 computations. In a conventional solution strategy, the incremental path of each parameter (i.e. levels of activation, $\boldsymbol{\alpha}$) is tracked from the undeformed to the target configuration. Thereby, the big O notation $O(N)$ is introduced to denote the time spent on the entire solution procedure of the FE model. Thus, in the case of the estimation of 3 parameters, the time needed for one iteration becomes $60 \times O(N)$. With the pre-set maximum number of iterative steps of 100 steps in this study, in the worst scenario, a total solution time is $6000 \times O(N)$ for the combination with 3 muscles. Given these estimates, a reduction of the the total solution time for one iterative step of the inverse procedure becomes necessary and critical.

For improving the computational efficiency, the following strategy was employed. Firstly, parallel computing techniques were applied to simultaneously evaluate different tongue deformations for solving the objective function and its derivatives (the gradient vector and Hessian matrix), as presented in Section 6.3.1. Secondly, the time costs for deriving the model deformation ($O(N)$) is reduced using a so-called warm start technique with pre-sampled deformed configurations (i.e. pre-computed deformed configurations or solutions) of the tongue model to avoid unnecessary repetitions in the incremental path. This is discussed and presented in Section 6.3.2 and 6.3.3.

6.3.1 Parallel computing

Parallel computing is a computational technique using multiple physical CPUs to simultaneously carry out the computations, and hence, reduce the total processing time. To solve the inverse problem using parallel computing, the overall problem needs to be treated as multiple independent parts, where each part is solved separately. In the present study, the forward difference method is adopted to compute the gradient vector and Hessian matrix of the inverse problem. Since the components (i.e. model configurations) for assembling the derivatives are independent to each other, thus they can be processed independently using an embarrassing

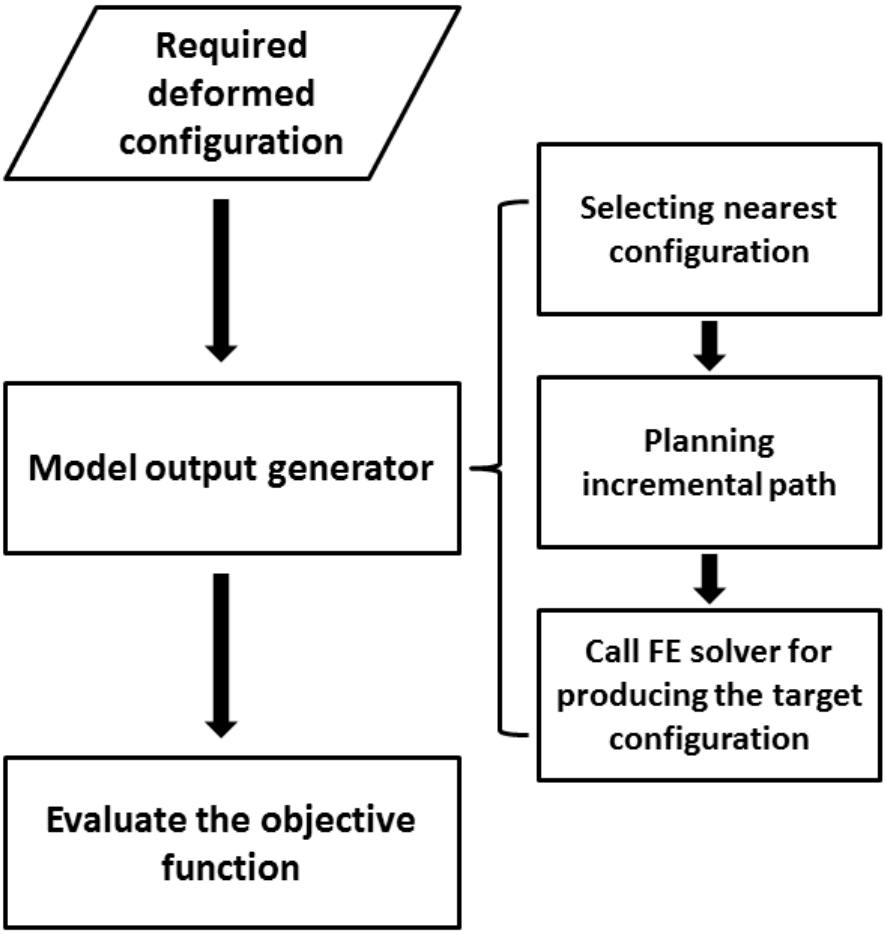

Figure 6.3: Flow chart of a single thread to evaluate the inverse problem of one tongue configuration.

parallel computing technique. Figure 6.3 illustrates the flow of single thread to evaluate the inverse problem of one tongue configuration.

In the present study, the parameter estimation procedure was implemented in Python v2.6 with Numpy v1.6 and Scipy v0.11 packages. The numerical solver for the optimization problem was based on the limited memory Broyden-Fletcher-Goldfarb-Shanno bounded (L-BFGS-B) optimisation algorithm [Byrd et al., 1995, Zhu et al., 1997]. In general, a Newton-Raphson type iterative method was used to find the global minimum of the objective function in the defined parameter domain, e.g. $\boldsymbol{\alpha} \in [0,1]^2$ in the case of two involved muscles. To deal with the large computational complexity, the computational experiments (Case studies I-V) were simultaneously evaluated using the NeSI (New Zealand eScience Infrastructure) Pan cluster

supercomputer. The NeSI Pan cluster is equipped with 160 computing nodes, each with 16 cores at speed of 2.70 GHz (a total of 1960 cores) with up to 88 GB memory.

6.3.2 Improving the FE solution procedure

Solving for the deformed model configuration caused by muscle contraction is not straightforward. In a typical FE problem, the deformation of a continuum body is subject to prescribed boundary conditions, such as stretching or compressing of the FE model at desired nodes, lines or faces. The same strategy using incrementally rising levels of activation is applied in the forward method to solve the deformation caused by a muscular contraction.

For convenience, the deformed configuration of the tongue model is denoted as $\Omega(\boldsymbol{\alpha})$, which is to represent the deformed state corresponding to an activation level vector. In the case of a conventional FE problem, an incremental path of the material parameter (e.g. the activation level) from the reference configuration to the target configuration is used to incrementally and iteratively derive the target deformed configuration. The first step of the incremental solution procedure is to compute the configuration with the first activation levels in the incremental path, using the reference configuration. The activation level vector is subsequently increased and the corresponding deformed configuration is solved starting from previously computed solutions. The new computed solution will become the starting configuration for the next required configuration in the incremental path. This iterative process is terminated when it reaches the target activation levels.

In the inverse problem framework, multiple deformation solutions for different activation states are required in each iterative step of the parameter estimation procedure. Using the conventional solution strategy means all required target configurations have to be solved from the reference state. Repeating this process at each iterative step of the parameter estimation reduce the overall performance due to high computational costs.

As the tongue tissue is assumed to be a hyperelastic material, the configuration does not depend on the deformation history. Thus, any deformed state of the model, i.e. the nodal displacement

$\mathbf{u}$, might be used as an initial guess for deriving a particular target state. Hence, a wisely chosen pre-sampled configuration is expected to reduce the computational time for solving the inverse problem in comparison with a conventional strategy that always uses the reference configuration as initial estimate of the solution. This solution strategy is referred to as a warm start technique.

Given a pre-sampled configuration $\Omega(\boldsymbol{\alpha}_{t-1})$, the aim of the warm start technique is to derive $\Omega(\boldsymbol{\alpha}_t)$ from $\Omega(\boldsymbol{\alpha}_{t-1})$, where $\boldsymbol{\alpha}_{t-1}$ is non-zero in general. Recalling that the linearised form of the FE system without considering the role of activation level parameters is

$$\mathbf{K}\left[\mathbf{u}^s\right]\delta\mathbf{u}^s = \delta\mathbf{R}\left[\mathbf{u}^s\right], \tag{6.3}$$

where $\mathbf{u}^s$ denotes the model state (displacement at each node) of the *s-th* iterative step. The nodal displacement at the *(s+1)-th* step is obtained through $\mathbf{u}^{s+1} = \mathbf{u}^s + \delta\mathbf{u}^s$. The nodal displacements $\mathbf{u}$ depend on a given activation level vector $\boldsymbol{\alpha}_{t-1}$, and the stress tensor $\mathbf{S}$ that assembles the stiffness matrix ($\mathbf{K}$) and residual vector ($\mathbf{R}$) that also depends on the given activation level vector $\boldsymbol{\alpha}_{t-1}$. Thus, Equation 6.3 can be seen as

$$\mathbf{K}\left[\mathbf{u}^s(\boldsymbol{\alpha}_{t-1}), \boldsymbol{\alpha}_{t-1}\right]\delta\mathbf{u}^s = \delta\mathbf{R}\left[\mathbf{u}^s(\boldsymbol{\alpha}_{t-1}), \boldsymbol{\alpha}_{t-1}\right]. \tag{6.4}$$

Equation 6.4 can then be solved iteratively, i.e. find a final displacement vector $\mathbf{u}$ through iteratively determining $\mathbf{u}^{s+1} = \mathbf{u}^s + \delta\mathbf{u}^s$ until the sequence satisfies the convergence criteria.

Given a target configuration with $\boldsymbol{\alpha}_t = \boldsymbol{\alpha}_{t-1} + \delta\boldsymbol{\alpha}$, the FE system will move away from the balanced state since the muscle activation level is changing by ($\delta\boldsymbol{\alpha} = \boldsymbol{\alpha}_t - \boldsymbol{\alpha}_{t-1}$). Therefore, in the first iterative step ($s = 1$), the linear system (Equation 6.4) is transformed into the following form

$$\mathbf{K}\left[\mathbf{u}^1(\boldsymbol{\alpha}_{t-1}), \boldsymbol{\alpha}_t\right]\delta\mathbf{u}^1 = \delta\mathbf{R}\left[\mathbf{u}^1\left(\boldsymbol{\alpha}_{t-1}\right), \boldsymbol{\alpha}_t\right]. \tag{6.5}$$

Equation 6.5 is then iteratively solved until it reaches equilibrium. The pre-computed nodal displacements $\mathbf{u}^1$ of the configuration $\Omega(\boldsymbol{\alpha}_{t-1})$, i.e. $\mathbf{u}^1(\boldsymbol{\alpha}_{t-1})$, can thereby used as initial guess to find target deformation $\Omega(\boldsymbol{\alpha}_t)$. This warm start technique will slightly reduce the required

computational time. Note that, warm start techniques depend on the choosing reasonable configurations of the deformed tongue model to serve as initial states. Furthermore, the warm start technique may use the pre-computed configurations to reduce the incremental path, hence the total computational time. However, the definition of appropriate incremental steps is still needed to obtain the target configuration from the pre-computed solutions/configurations.

6.3.3 Stability conditions and incremental path planning

The above proposed strategy (i.e. the warm start technique) requires (1) the definition of a pre-sampled configuration as initial estimate of the the solution process, and (2) the planning of incremental steps that lead from the pre-computed configuration to the target state. Inappropriate definition of incremental activation levels for a given starting configuration could trigger failure in the solution of the system equations. In the following, the criteria for system stability of multi-fibre contraction is discussed.

Stability conditions

Condition 1: The total strain-energy function with respect to the target configuration Ω_t is written as

$$W_\Omega = \int_{\Omega_0} \mathbf{S}(\boldsymbol{\alpha}_{t-1} + \delta\boldsymbol{\alpha}) : \mathbf{E} dV, \tag{6.6}$$

where $W_\Omega = W_{\text{passive},\Omega} + W_{\text{active},\Omega}$. By applying the Taylor expansion on the total strain energy function, one obtains [Ibrahimbegović, 2009]

$$W_\Omega(\boldsymbol{\alpha}_{t-1} + \delta\boldsymbol{\alpha}) \approx W_\Omega(\boldsymbol{\alpha}_{t-1}) + D'(W_\Omega(\boldsymbol{\alpha}_{t-1}))[\delta\boldsymbol{\alpha}] + D''(W_\Omega(\boldsymbol{\alpha}_{t-1}))[\delta\boldsymbol{\alpha}, \delta\boldsymbol{\alpha}], \tag{6.7}$$

where operator D denotes the Frechet directional derivative in the direction $\delta\boldsymbol{\alpha}$. The second order derivative can be then further rewriten as

$$D''(W_\Omega(\boldsymbol{\alpha}_{t-1}))[\delta\alpha, \delta\alpha] = \delta\boldsymbol{\alpha}^T \mathbf{K} \delta\boldsymbol{\alpha} \tag{6.8}$$

If $W_\Omega(\boldsymbol{\alpha}_{t-1} + \delta\boldsymbol{\alpha})$ is in an equilibrium state, $D'(W_\Omega(\boldsymbol{\alpha}_{t-1}))[\delta\boldsymbol{\alpha}] = 0$. The difference in total potential strain energy between $\boldsymbol{\alpha}_{t-1}$ and $(\boldsymbol{\alpha}_{t-1} + \delta\boldsymbol{\alpha})$ is then controlled by the second term $\delta\boldsymbol{\alpha}^T \mathbf{K} \delta\boldsymbol{\alpha}$.

If the muscle activation level increases, the overall potential energy will increase, and one yields the inequality $W_\Omega(\boldsymbol{\alpha}_{t-1} + \delta\boldsymbol{\alpha}) > W_\Omega(\boldsymbol{\alpha}_{t-1})$ where $\delta\boldsymbol{\alpha} > \mathbf{0}$. From a mathematical point of view, this condition leads to $\delta\boldsymbol{\alpha}^T \mathbf{K} \delta\boldsymbol{\alpha} > \mathbf{0}$ with $\mathbf{K}$ positive definite; if $W_\Omega(\boldsymbol{\alpha}_{t-1} + \delta\boldsymbol{\alpha}) < W_\Omega(\boldsymbol{\alpha}_{t-1})$, $\mathbf{K}$ is negative definite [Ibrahimbegović, 2009]. In such a situation, it would be highly likely that the linear system would fail without converging to a solution [Ibrahimbegović, 2009]. This leads to the first critical condition of the warm start procedure: the total energy of any neighbouring configuration needs to be smaller than the target configuration.

The deformation of the tongue model is driven by different levels of muscle activation. Thus, the selection of initial muscle activation levels is crucial for Newton's method to be successful.

Condition 2: As shown in Equation 4.33, finding a target deformation of the tongue model based on given boundary conditions and varying muscle activation levels can be seen as a searching procedure within the admissible solution space (displacement). Equation 4.33 is solved using Newton's method. One critical condition of Newton's method is that the initial starting point (configuration) is close to the actual solution. Otherwise, the method is likely to fail and not converge to the root. Theoretically, a large active stress will produce a large deformation. Large active stresses imply a rapid change of the internal stress; and resulting in an initial guess for Newton's method that might be not sufficiently close to the solution. This might cause deteriorating convergence rates or no convergence at all. Hence, the incremental activation level vector shall maintain in a comparatively small level.

An applied additional condition is that each component of incremental activation level vector $\delta\alpha_i$ (the *i-th* component of $\delta\boldsymbol{\alpha}$ corresponding to α_i in $\boldsymbol{\alpha}$), is chosen in such a way that two active stresses are close. In this work, the magnitude of the incremental activation level of each muscle between two neighbouring configurations is restricted to

$$\log_{10}(\alpha_i) = \log_{10}(\delta\alpha_i). \tag{6.9}$$

This restriction is based on empirical tests. Note that, $\boldsymbol{\alpha}$ may not be the activation level vector of the pre-sampled configuration, it could be an activation level vector along the incremental path.

Incremental path planning and sampling strategy

Planning the incremental path from the initial to the target configuration relies on the two conditions outlined above. To derive the target configuration $\Omega(\boldsymbol{\alpha}_t)$, a neighbouring configuration $\Omega(\boldsymbol{\alpha}_{t-1})$, which every component $\alpha_{i,t-1}$ in $\boldsymbol{\alpha}_{t-1}$ needs to be bigger than the corresponding components in $\boldsymbol{\alpha}_t$ to satisfy Condition 1, is required to be selected. To satisfy Condition 2, the incremental steps of the single components in activation levels, $\delta\boldsymbol{\alpha}$, needs to be restricted to the same orders of magnitudes as the level of activation in the incremental path.

To construct the incremental steps, i.e. a series of activation level vectors, the following two functions are defined to extract useful numerical information from each component of activation level vector $\boldsymbol{\alpha}_{t-1}$. For a given scalar level of activation α_i in $\boldsymbol{\alpha}$, the following two functions are used to compute the order of magnitude and the fractional part of α_i:

- $f_{\text{order}}(\alpha_i)$ returns the order of magnitude of α, and is defined as

$$f_{\text{order}}(\alpha_i) = \text{floor}(\log_{10}(\alpha_i)), \tag{6.10}$$

  where the function floor rounds $\log_{10}(\alpha_i)$ to the nearest integer less than or equal to $\log_{10}(\alpha_i)$;

- $f_{\text{head}}(\alpha_i)$ returns the fractional part of α_i in a normalised scientific notation, that is

$$f_{\text{head}}(\alpha_i) = \frac{\alpha_i}{10^{f_{\text{order}}(\alpha_i)}}, \tag{6.11}$$

For any α_i, one thus obtains

$$\alpha_i = f_{\text{head}}(\alpha_i) \times 10^{f_{\text{order}}(\alpha_i)}. \tag{6.12}$$

Theoretically, to derive the target configuration $\Omega(\boldsymbol{\alpha}_t)$ from $\Omega(\boldsymbol{\alpha}_{t-1})$, a generic incremental sequence for every component α_i can be constructed, such that

$$\{f_{\text{head}}(\alpha_{i,t-1}) \times 10^{f_{\text{order}}(\alpha_{i,t-1})}, \cdots, 10^{f_{\text{order}}(\alpha_{i,t})}, \cdots, f_{\text{head}}(\alpha_{i,t}) \times 10^{f_{\text{order}}(\alpha_{i,t})}\}. \tag{6.13}$$

The incremental factor $\delta\alpha$ between two neighbours in the incremental path depends the previous activation level α_{t-1}, i.e. $\delta\alpha = f_{\text{order}}(\alpha_{i,t-1})$. Note that, the subscript $t-1$ here is not for denoting the pre-computed solution, but an intermediate activation level in the incremental path. The above condition for $\delta\alpha$ is to ensure that Condition 2 is satisfied and large stress increments are avoided during the solution process. In practice, the solution of the forward problem within the inverse problem procedure, the procedure reuses the levels of activation in the sequence, and use the previous solution as the initial guess for deriving the next deformed configuration in the sequence, until reaching the final target configuration.

The actual incremental path relies on the selection of the nearest configuration from a pre-computed set of solution. The selected pre-computed model configuration, i.e. the pre-computed solution, serves as the starting configuration to solve for the target configuration in the warm start procedure of the inverse problem. A "good" selection of the starting configuration can effectively reduce the total computational costs, and lead to a more robust solution of the linear system. In other words, a wisely planed sampling strategy can improve the overall performance and reduce the total time spent on executing less incremental steps.

One intuitive idea to reduce the number of incremental steps is to increase the coverage of sample points over the parameter domain. A high coverage of sample points implies less incremental steps are necessary to compute the respective model deformations. However, a high sampling density, e.g. the evenly distributed mesh grid, implies long computational times for determining the pre-computed solutions. Consequently, the overall computational time would dramatically increase to a level in which the entire problem cannot be solved in a reasonable amount of time.

Given the above dilemma, the sample points can be constrained to the diagonal of the param-

eter domain. More precisely, the activation levels of all stimulated muscles are defined to be identical, e.g. $(0.1, 0.1, 0.1, \ldots)$. Thus, for example, a model configuration with two stimulated muscles only requires to the solutions for the deformations resulting from

$$\alpha_1 = \alpha_2 = \{0.00001, 0.0001, 0.001, 0.01, 0.1, 0.2, 0.3, \cdots, 0.9, 1.0\}$$

prior to the actual parameter estimation. Note that, in practice, the configuration with $\boldsymbol{\alpha} = \mathbf{0.00001}$ (i.e. the components in $\boldsymbol{\alpha}$ corresponding to involved muscles are equal to 0.00001) is quite close to the initial configuration, since the deformation with this level of activation is negligible. In other words, the inverse problem procedure does not need to solve the intermediate configurations from the reference configuration to the configuration with $\boldsymbol{\alpha} = \mathbf{0.00001}$.

The strategy, that samples the deformation along the diagonal path of the domain of the activation level, leads to a loss of the full coverage in the parameter domain. However, the distances between neighbouring configurations remain relatively small compared with other sampling strategies with less sampling points. Appendix D outlines a computational experiment for testing the performance of the improved inverse procedure.

6.4 Case studies of estimating the muscular activity in tongue propulsion

6.4.1 Homogeneous muscular activity

Case study I: Testing Napadow et al. [1999b]'s hypothesis

Two test cases were analysed to test Napadow's hypothesis. For each case study, the activation parameters of two sets of muscle combinations were considered, including the combination of the transversus and styloglossus muscles ($\boldsymbol{\alpha} = (\alpha_t, \alpha_s)$), and the combination of the verticalis and styloglossus muscles ($\boldsymbol{\alpha} = (\alpha_v, \alpha_s)$).

Results: The optimal activation levels for each muscle combination (i.e. (α_s, α_t) and (α_s, α_v)), which minimised the RMS difference between the modelling results and the experimental data (objective function f in Equation 6.1), are shown in Table 6.3. Combined activation of the styloglossus and transversus muscles resulted in a closer match ($f(\alpha_t, \alpha_s) = 19.9$) with the experimental strain data in Table 6.1 compared to the combined activation of the verticalis and styloglossus muscles ($f(\alpha_v, \alpha_s) = 23.1$).

$\hat{\boldsymbol{\alpha}}$	$f(\hat{\boldsymbol{\alpha}})$
$(\alpha_s, \alpha_t) = (1.512, 0.496)$	19.907
$(\alpha_s, \alpha_v) = (0.228, 0.046)$	24.697

Table 6.3: Parameter estimation results for case study I, testing of the Napadow's hypothesis. The sub-indices s, t and v on the left hand side denote the styloglossus, transversus and verticalis muscles, respectively. The optimal activation levels $\hat{\boldsymbol{\alpha}}$ for the two sets of muscular combinations are listed in the middle column. The values of the objective function f at the optimal solutions are shown in the last column.

Table 6.4 lists the predicted regional strains with $(\alpha_s, \alpha_t) = (1.512, 0.496)$. The simultaneous contraction of the styloglossus and transversus muscles produce the most dominant stretching deformation along the SI direction in Region 1. At the same time, Region 3 showed a compressive deformation in the AP direction, which is unlike the observation by Napadow (Table 6.1). The NSDs of the average strain in the AP and SI directions in Region 3 are 4.14 and 0.951 respectively, indicating a large difference compared to the experimental data.

Table 6.5 lists the predicted regional strains with $(\alpha_s, \alpha_v) = (0.228, 0.046)$. Apart from Region 4, all other regions exhibit NSDs higher than 1, indicating significant differences to the experimental data. Interestingly, the average strain in the AP direction of Region 3 shows a slightly lower NSD (3.388) compared to the first activation case $(\alpha_s, \alpha_t) = (1.512, 0.496)$ (NSD=4.14).

	Region 1	NSD	Region 2	NSD	Region 3	NSD	Region 4	NSD
AP	-0.016	0.95	0.047	0.218	-0.013	4.14	0.046	0.416
SI	0.133	0.747	0.035	0.165	0.05	0.951	0.031	0.397

Table 6.4: The average axial strains and the standard deviation (NSD) and the number of standard deviations (NSD) away from the experimental data for the four regions of the deformed tongue model obtained by choosing $(\alpha_s, \alpha_t) = (1.512, 0.496)$.

	Region 1	NSD	Region 2	NSD	Region 3	NSD	Region 4	NSD
AP	-0.094	2.422	-0.025	1.121	0.021	3.388	0.040	0.553
SI	0.025	0.873	-0.044	1.001	-0.001	1.980	-0.011	0.322

Table 6.5: The average axial strains in the four regions of the deformed tongue model obtained by choosing $(\alpha_s, \alpha_v) = (0.228, 0.046)$. NSD: number of standard deviations between the model predictions and experimental strain estimates.

This implies that the contraction of the verticalis muscle, with its vertical fibre arrangement (superior-inferiorly), might contribute to the expansion of the tongue in the AP direction in Region 3. However, the difference in NSD between the two activation cases is small.

For both activation cases (α_t, α_s) and (α_v, α_s), the solutions of the objective function are not substantially reduced compared to the value in the initial state ($f = 24.8$). In other words, neither combination (the transversus and styloglossus muscles, or the verticalis and styloglossus muscles) could drive the deformation of the tongue model sufficiently close to the experimental data. These results suggest that the experimental data cannot be reproduced using the tongue model in combination with the muscle activity proposed by Napadow.

Case study II: Comprehensive testing of combinations with 3 muscles

Comprehensive testing was performed to determine if other muscle combinations could better match Napadow's experimental data. Hrycyshyn and Basmajian [1972], Kayalioglu et al. [2007a] and Felton et al. [2007] hypothesised that 7 muscles might be involved in the propulsion of swallowing. The muscles included transversus (t), verticalis (v), superior longitudinalis (sl), genioglossus (gg, both anterior and posterior parts), styloglossus (s), hyoglossus (h) and mylohyoid (m). To reduce the computational complexity, we tested whether the tongue deformation during propulsion could be produced by simultaneous contraction of any combination of 3 out of these 7 muscles, e.g. $\boldsymbol{\alpha} = (\alpha_s, \alpha_t, \alpha_v)$. Thus, 35 different combinations of 3 active muscles were tested.

Results: The results for testing the objective function f in Equation 6.1 with combinations of 3 muscles are shown in Figure 6.4. Simultaneous activation of the hyoglossus (h), styloglossus (s)

and transversus (t) muscles produced the best match (with the experimental data, i.e. minimal f).

Table 6.6 (Figure 6.6) shows the AP and SI axial strains in the four regions of the tongue. The overall best watch was given by $(\alpha_h, \alpha_m, \alpha_t) = (0.6420.7760.171)$. In general, the AP axial strains in Region 3 and 4, and the SI axial strains in Region 1 and 3, match the sign of the corresponding experimental data in Table 6.1. However, the values of the NSDs indicate that large differences remain between the model prediction and the experimental data. The average AP axial strain in Region 3 showed the largest NSD (3.550). High NSD values are also obtained for the average AP axial strain in Region 1 (1.445). The average strain values in the AP direction of Region 1 (-0.043) indicate an opposite deformation compared to the corresponding experimental data in Table 6.1.

	Region 1	NSD	Region 2	NSD	Region 3	NSD	Region 4	NSD
AP	-0.043	1.445	0.008	0.706	0.013	3.550	0.049	0.336
SI	0.101	0.266	0.013	0.402	0.043	1.082	0.035	0.468

Table 6.6: The average axial strains in the four regions of the tongue model for $(\alpha_h, \alpha_m, \alpha_t) = (0.6420.7760.171)$. NSD: number of standard deviations between the model predictions and experimental strain estimates.

In summary, the comprehensive testing of combinations with three muscles shows that the simultaneous activation of the hyoglossus, styloglossus and transversus muscles produce the smallest values of the objective function f. It was observed that the hyoglossus, mylohyoid and styloglossus muscles could influence the deformation in the observational imaging plane (the mid-sagittal plane), even though these muscles are largely located outside of this region. In short, none of the tested combinations of 3 muscles lead to a model deformation that fully matched with the experimental data in all regions. However, as shown in Table 6.4, the largest activation levels among all the combinations are seen for the hyoglossus, mylohyoid, styloglossus and transversus muscles, which indicates that each of these four muscle groups may play an important role during propulsion. This raised the question as to whether the combined action of all four of these muscle groups might improve the match between the model predictions and experimentally measured deformations during tongue propulsion.

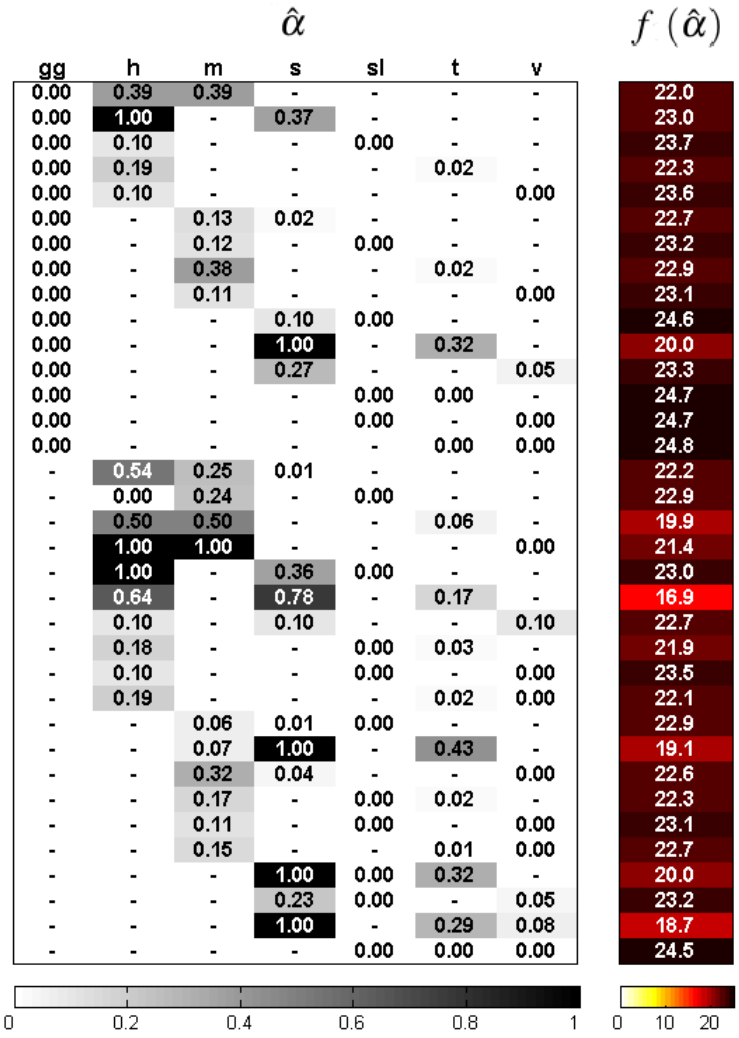

Figure 6.4: The estimated activation levels $\hat{\boldsymbol{\alpha}}$ for the corresponding combinations with three muscles, with $f(\hat{\boldsymbol{\alpha}})$ being the values of the objective function at optimal activation levels $\hat{\boldsymbol{\alpha}}$. Each row corresponds to a different muscle combination, the symbol "-" denotes muscles which were not selected (their values were set to zero.). The grey-scale shading indicates the magnitude of the estimated activation levels; whereby, darker colours denote stronger contraction. The colour spectrum represents the values of the objective function; whereby, warmer colours indicate a closer match of the model with the given experimental data. The test includes genioglossus (gg), hyoglossus (h), mylohyoid (m), styloglossus (s), superior longitudinalis(sl), transversus (t) and verticalis (v) muscles.

Case study III: Testing of the combination of hyoglossus, mylohyoid, styloglossus and transversus muscles

The results from the previous two case studies indicated that the hyoglossus, mylohyoid, styloglossus and transversus muscles may play important roles in the deformation of the tongue during propulsion. In the following case study III, these four muscles were selected, and it was tested if their co-activation could lead to a tongue deformation that fully matched the experimental data listed in Table 6.1.

Results: Table 6.7 show the optimal activation levels for the 4 muscle groups. Table 6.8 shows the regional axial strain with the hyoglossus, mylohyoid, styloglossus and transversus muscles activated at the optimal level. The resulting tongue deformation shows a better match with Napadow's experimental data compared to the results from case studies I and II. This is reflected through a smaller value of the objective function (16.875). The NSDs of all regions were reduced compared to the previous case studies, which implies a better match to the experimental data, however this improvement is rather insubstantial.

$\hat{\boldsymbol{\alpha}}$	$f(\hat{\boldsymbol{\alpha}})$
$(\alpha_h, \alpha_m, \alpha_s, \alpha_t) = (0.719, 0.133, 0.610, 0.158)$	16.825

Table 6.7: Parameter estimation results for case study III, testing of the combination of hyoglossus (h), mylohyoid (m), styloglossus (s) and transversus (t) muscles. The optimal activation levels ($\hat{\boldsymbol{\alpha}}$) indicate that all four muscle groups were active, and this reduced the objective function value ($f_1(\hat{\boldsymbol{\alpha}})$) compared to the previous case studies.

	Region 1	NSD	Region 2	NSD	Region 3	NSD	Region 4	NSD
AP	-0.057	1.723	0.009	0.685	0.016	3.494	0.077	0.308
SI	0.112	0.436	0.007	0.458	0.043	1.099	-0.041	0.486

Table 6.8: The average axial strains in the four regions of the deformed tongue model obtained obtained using the optimal values of $(\alpha_h, \alpha_m, \alpha_s, \alpha_t) = (0.719, 0.133, 0.610, 0.158)$. NSD: number of standard deviations between the model predictions and experimental strain estimates.

6.4.2 Heterogeneous muscular activity

This subsection reports the testing results of the possible muscle combinations that involved the heterogeneous muscular activities.

Heterogeneous activity of the transversus muscle

Section 4.2.2 shows an anatomical dissection that demonstrates that the orientations of the transversus muscle fibres vary spatially. This histological image in Figure 4.4 shows that the muscle fibres are oriented transversely in the anterior and central parts of the tongue body, whereas the posterior fibres of transversus muscle shows a fan-shape arrangement toward the posterior side. Based on the results from case studies I, II and III, and the anatomical features of transversus muscle, it was hypothesised that the co-activation of the hyoglossus, mylohyoid and styloglossus muscles in combination with a partial activation of the transversus muscle, i.e. anterior and middle parts corresponding to Regions 1 and 2, respectively, might be responsible for the tongue deformation during propulsion of dry swallowing. In the following case studies, this hypothesis of heterogeneous muscular activity is tested.

Stone et al. [2004] reported that the tongue's intrinsic muscles, i.e. the transversus and verticalis muscles, may possess three functional muscular segments in the AP direction, suggesting the possibility of heterogeneous muscle contraction. Very little attention has previously been drawn on the precise definition of these functional segments. In the present study, the conceptual ideas proposed by Stone et al. [2004] were adopted to define the functional segments of the transversus muscle in the tongue model. Figure 6.5 illustrates the three functional segments, i.e., anterior (yellow), middle (red) and posterior (blue) segments, defined in the present FE model.

In order to test the hypothesis of heterogeneous muscular activity during propulsion, only the anterior and middle segments of the transversus muscle are simultaneously activated, while the posterior part is kept in a resting state. Note, the activation levels in the anterior and middle parts of the transversus muscle are assumed to have the same magnitude. More precisely, the

activation level parameters of the transversus muscle in these two regions are continued to be equal, while the posterior segment (blue region) is kept in a zero activation state for all tests.

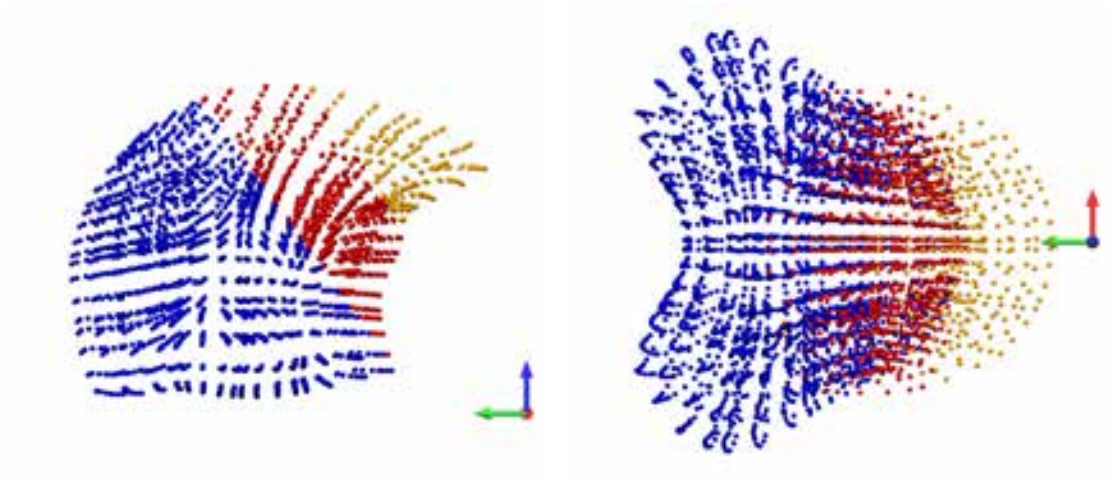

(a) (b)

Figure 6.5: The Gauss points associated with the functional segments of the transversus muscle, highlighted in yellow (anterior), red (middle) and blue (posterior). The functional segments were defined in accordance with the reported observations by Stone et al. [2004].

Heterogeneous activity of the genioglossus muscle

The genioglossus muscle has a fan-shaped fibre arrangement in the mid-sagittal plane of the tongue. This muscle has been modelled as at least two subdivisions in many previous tongue modelling works, e.g. Perkell [1974], Hashimoto and Suga [1986], Wilhelms-Tricarico [1995], Payan and Perrier [1997], Sanguineti et al. [1997], Dang and Honda [2004] and Buchaillard et al. [2009]. Those subdivisions allowed the models to have more flexibility to produce complex deformations in studies of speech production. However, the definitions of boundaries of those subdivisions were not clearly defined. In order to investigate the possibility of heterogeneous muscle activation, the genioglossus muscle was divided as two functional segments, i.e. anterior and posterior, in accordance with Wilhelms-Tricarico [2005]'s definitions, as illustrated in Figure 6.6.

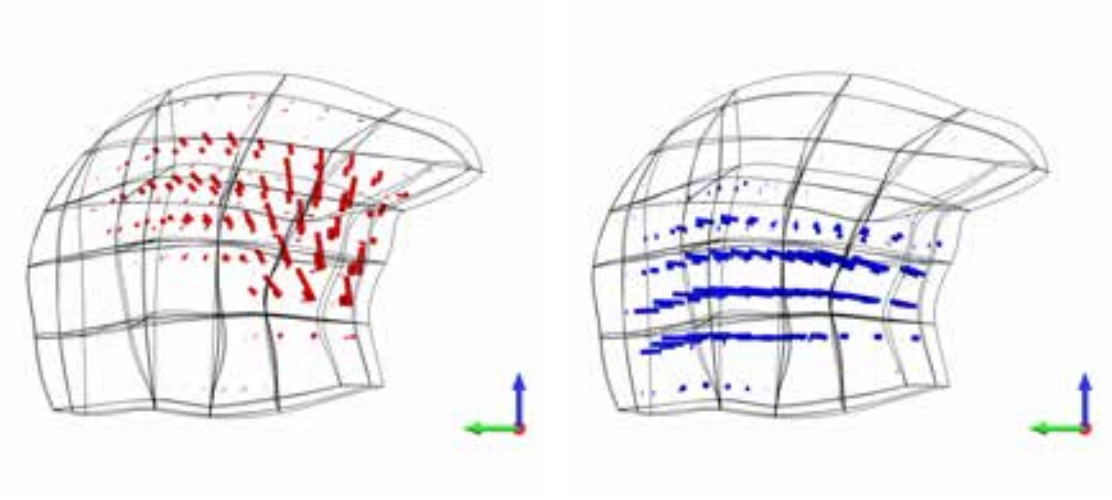

(a) Genioglossus anterior (b) Genioglossus posterior

Figure 6.6: The spatial definitions of the genioglossus anterior (red) and genioglossus posterior (blue). These functional segments were defined in accordance with the original digitization by Wilhelms-Tricarico [1995].

$\hat{\boldsymbol{\alpha}}$	$f(\hat{\boldsymbol{\alpha}})$
$(s, \text{Partial } t) = (1.295, 1.26)$	13.866

Table 6.9: Parameter estimation results for case study IV, combined muscle activation of styloglossus (s) and anterior and middle parts of transversus (Partial t) muscles.

Case study IV: Testing of the combination of styloglossus and partial transversus muscles

In this case, Napadow's hypothesis is retested using only a partially activated transversus muscle, i.e. the anterior and middle parts of the tongue.

Results: Table 6.9 shows the optimal activation levels for the styloglossus and transversus muscles with the corresponding minimum values of the objective function. Compared with homogenous activation in case study I (Table 6.3), the value of the objective function is slightly reduced (13.866) with the activation $(\alpha_s, \alpha_t) = (1.295, 1.26)$.

Table 6.10 presents the results for case study IV with $(\alpha_s, \text{Partial } \alpha_t) = (1.295, 1.26)$. The NSDs in the AP and SI directions of Regions 1, 2 and 3 indicate smaller differences to the experimental data compared to homogeneous activation in case study I. The heterogeneous, higher activation of the transversus muscle compared to case study I lead to further deformation in the anterior and middle part of the transversus muscle, resulting in a closer prediction

of the experimental data by Napadow. Region 3 still presented with high NSDs in AP and SI directions, that are 3.40 and 1.102 respectively. Clear indications are given that the heterogeneous contraction of the transversus muscle in the anterior and middle area strongly influences the deformation of the tongue in Region 1 and 2.

	Region 1	NSD	Region 2	NSD	Region 3	NSD	Region 4	NSD
AP	0.023	0.209	0.075	0.128	0.020	3.40	0.056	0.178
SI	0.150	1.01	0.046	0.040	0.043	1.102	0.020	0.203

Table 6.10: The average axial strains in the four regions of the deformed tongue model obtained using the optimal values of $(\alpha_s, \text{Partial } \alpha_t) = (1.295, 1.26)$. Partial α_t represents the activation levels of the anterior and middle functional segments of the transversus muscle, as defined in Figure 6.5.

Case study V: Testing for heterogeneous activity of genioglossus muscle

The speech study by Maeda and Honda [1994] reported that co-activation of the genioglossus posterior, hyoglossus and styloglossus muscles is known to be at the origin of tongue movement in upward and front-back direction. Case study V tested whether this muscular combination could improve the match to the data reported by Napadow.

Results: Table 6.11 presents the optimal levels of contractile stresses when activating genioglossus posterior, hyoglossus and styloglossus. The genioglossus posterior muscle remained in an inactive state ($\alpha_{ggp} = 0$), whereas the hyoglossus and styloglossus muscles reached high activation levels. The objective function value at the optimal point (i.e. $f(\hat{\boldsymbol{\alpha}}) = 23$) was not reduced significantly compared with case study IV. Table 6.12 shows the averages of axial strains in regions and corresponding NSDs. The NSDs of the average axial strains in the regions 1, 2 and 3 (i.e. 2.891, 1.854 and 3.029, respectively) indicated large differences between the tongue model predications and experimental data.

$\hat{\boldsymbol{\alpha}}$	$f(\hat{\boldsymbol{\alpha}})$
$(\alpha_{ggp}, \alpha_h, \alpha_s) = (0.0, 0.9, 0.36)$	23.00

Table 6.11: Parameter estimation results for case study VI: testing of the combination of genioglossus posterior, hyoglossus, styloglossus muscles. The ggp, h and s on the left hand side denote the genioglossus posterior, hyoglossus and styloglossus muscles, respectively.

	Region 1	NSD	Region 2	NSD	Region 3	NSD	Region 4	NSD
AP	-0.119	2.891	-0.085	1.854	0.037	3.029	0.039	0.579
SI	0.071	0.178	0.023	0.293	0.035	1.253	0.008	0.015

Table 6.12: The average axial strains in the four regions of the deformed tongue model obtained using the optimal activation levels $(\alpha_{ggp}, \alpha_h, \alpha_s) = (0.0, 0.9, 0.36)$.

Case study VI: Testing of the combination of hyoglossus, mylohyoid, styloglossus and partial transversus muscles

Case study VI is set up to find the optimal level of activation of hyoglossus, mylohyoid, styloglossus and the anterior and middle parts of transversus muscles to best match the experimental data in Table 6.1. The same muscles had been activated in case study III, yet in a homogeneous manner.

Results: Table 6.14 shows the optimal activation levels (α_h, α_m, α_s, Partial α_t) = (0.915,0.216, 0.353,0.637) of the regional average directional strains and the corresponding NSD. In general, the values of the objective function at the optimal configuration were slightly reduced, with $f = 11.104$ (Table 6.13).

The NSDs in Region 1 and 2 are slightly reduced to a level below 1 compared to the case studies I, II and IIII, see Table 6.14. In Region 3, the average strain in the AP direction is reduced to 2.756 which is smaller than the corresponding values of 3.956, 3.578 and 3.494 in the case studies I, II and III, respectively. The average strain in the SI direction in Region 3 remain at a similar level of mismatch compared to previous solutions, with a NSD of 1.240 compared to all previous optimal solutions. Furthermore, in Region 4, the differences between the experimental data and the average strains in the AP and SI direction are higher compared to the other case studies (a higher NSD, 1.045 in the AP direction, 1.638 in the SI direction). In

$\hat{\boldsymbol{\alpha}}$	$f(\hat{\boldsymbol{\alpha}})$
$(\alpha_h, \alpha_m, \alpha_s, \text{Partial } \alpha_t) = (0.915, 0.216, 0.353, 0.637)$	11.104

Table 6.13: Parameter estimation results for case study VI: testing of the combination of hyoglossus, mylohyoid, styloglossusand partial transversus muscles. The *h*, *m* and *s* on the left hand side denote the hyoglossus, mylohyoid and styloglossus muscles, respectively. The partial *t* represents the anterior and middle functional segments of transversus muscle.

	Region 1	NSD	Region 2	NSD	Region 3	NSD	Region 4	NSD
AP	0.008	0.491	0.058	0.086	0.049	2.756	0.082	0.409
SI	0.116	0.493	0.021	0.312	0.036	1.240	-0.056	1.103

Table 6.14: The average axial strains in the four regions of the deformed tongue model obtained using the optimal activation levels $(\alpha_h, \alpha_m, \alpha_s, \text{Partial } \alpha_t) = (0.9149, 0.2163, 0.3533, 0.6373)$. Partial α_t represents the activation level in the anterior and middle functional segments of the transversus muscle, as shown in Figure 6.5.

short, the results from case study VI show the best match to the experimental data in Table 6.1 compared with the other case studies, with smaller values obtained for the objective function and the NSDs in most regions of the tongue.

6.5 Discussion

Napadow's hypothses

Case study I aimed at testing the combinations of muscle activation during propulsion in dry swallowing as proposed by Napadow et al. [1999b]. The results of case study I suggest to reject the proposed combinations involving the intrinsic muscles, interleaving with the styloglossus muscle, as they could not produce expansions in the AP and SI directions in the posterior mid-sagittal plane. Although the transversus and verticalis muscles were activated at low levels (0.496 and 0.046 respectively) compared to the styloglossus muscle, the comparatively high values of the objective function imply that these two muscles as they have been modelled in case study I play minor role comparing with styloglossus muscle in reproducing the deformation shown in Table 6.1. The regional average axial strains did not match the experimental data in Table 6.1.

Napadow et al. [1999b]'s hypotheses were based on the conventional knowledge of tongue anatomy, whereby the transversus muscle is oriented in the lateral to the medial direction throughout the entire tongue body and the arrangement of the verticalis muscle is along the superior-inferior direction. In this context, it is natural to assume that stretching in the AP and SI direction may be caused by the contraction of one of the interlaced muscles. However, more recent data indicate a slightly different arrangement of the transversus muscle in the posterior region of the tongue (see Section 4.2.2). These new data were incorporated into the tongue model for the present studies. The observed arrangement of the transversus muscle can only cause a negative axial strain in AP direction. In other words, the present tongue model cannot produce stretching in the AP and SI directions by activating one of the intrinsic muscles in the posterior region.

The anatomical dissection presented in Section 4.2.2 provides further evidence of the variations in the local fibrous arrangement in the posterior region of the tongue. In Figure 4.4, the horizontal imaging plane shows a fan-shaped fibrous arrangement in the posterior area, which may comprise parts of the styloglossus and transversus muscles. In particular, the results from the anatomical dissection in Section 4.2.2 indicate that the transversus muscle is distributed along the length of the tongue and provides further evidence that its fibres cross over in the dorsal plane towards the posterior region of the tongue and fan out across the posterior surface (Figure 4.4). Such details on fibre arrangement in the tongue have not been previously reported. They do appear to offer support for the mathematical model of tongue function in the present study (see Figure 4.3 and 4.4); and potentially explain the negative axial strain in AP direction, resulting from the co-contraction of the styloglossus and transversus muscles in case study I.

Homogeneous muscular activities

A primary aim of this work was to determine the muscle (or muscles) that can achieve the propulsion of the tongue by matching Napadow's experimental data. In the scope of case study II, 35 combinations of three muscles were tested using the same inverse procedure and objective function as for case study I. The resulting values of the objective function f at the optimal acti-

vation levels (shown in Figure 6.4) were remained relatively unchanged values, if compared to the initial value. This implied that the objective function over the defined parameter domain is comparatively flat. The numerical behaviour of f caused the searching algorithm to stop when the numerical tolerance of the optimisation procedure was reached. This could explain why the resulting activation levels for some muscles were only slightly larger than zero. However, it could also mean that the activation of those muscles did not directly influence the strain values in the four regions of the tongue model. In any case, several initial estimates were chosen to ensure the global minimum (i.e. best match) was obtained.

Some general patterns could be identified based on the results of case study II. Although the muscle combination of the hyoglossus, mylohyoid and transversus muscles achieved the smallest value of f if compared to all other cases (Figure 6.4), the hyoglossus, mylohyoid, styloglossus and transversus muscles were shown to have the most dynamic roles in driving the deformation observed in Table 6.1. The hyoglossus, mylohyoid and styloglossus muscles share similar features in their fibre distributions. Firstly, all muscles exhibit a left-to-right symmetry; and secondly, the major proportion of these muscles are located outside of the mid-sagittal plane. During model deformation, a non-zero activation level parameter triggers these muscles to simultaneously contract on both sides. Thus, the regional deformation in the bilateral area compresses the tissue towards the mid-sagittal area due to the incompressible nature of the tissue. Felton et al. [2007] provided more comprehensive observations of tongue deformation during swallowing based on multiple images from various angles. Felton et al. [2007] concluded that the extrinsic muscle groups, i.e. the styloglossus, hyoglossus and mylohyoid muscles, may be simultaneously activated to drive the posterior tongue deformation. Moreover, the tongue body deformation was considered to be due to the contractile stress from the intrinsic core muscles (e.g. longitudinalis superior muscles).

None of the combinations of three muscles in case study II led to a model deformation that fully matched the experimental data. However, hyoglossus, mylohyoid, styloglossus and transversus muscles presented strong dynamical roles, i.e. highly variable activation levels, throughout the analysis. Thus, case study III aimed at further investigating the combined activation of the

hyoglossus, mylohyoid, styloglossus and transversus muscles (four parameters). It was demonstrated that the additional contraction of the transversus muscle had a strong influence on the deformation in Region 1 and 2, as shown in Table 6.8. However, its activation led to an opposite deformation in the posterior region compared to the experimental data in Table 6.1. It was also noted that the deformation in the AP direction of Regions 1 and 2 did not match the experimental data in Table 6.1.

Heterogeneous muscular activities

Due to the possible existence of functional segments previously reported by Stone et al. [2004], we considered the partial activation of the transversus muscles in the anterior and middle part of the tongue body. Thus, the transversus muscle was sub-divided into three functional segments, which were partially activated in the anterior and middle regions in case studies IV and VI. In other words, a heterogeneous contraction pattern was introduced into the intrinsic muscles in the current modelling framework.

The estimated activation levels of the combination of the partial transversus and styloglossus muscles led to a slightly improved optimal solution, i.e. $f(\alpha_s, \text{Partial } \alpha_t) = 13.866$ compared with the homogeneous activation in case study I ($f((\alpha_s, \alpha_t)) = 19.9$). These results provided some suggestions for the involvement of only the anterior and middle part of the transversus muscle. The additional activation of the hyoglossus and mylohyoid muscles in case study VI led to a further reduction of the NSDs in the AP direction compared to the NSDs of the optimal configuration in the case study I, II and III. Although Region 4 (inferior region) showed a larger NSD, the NSDs in all other directions of the four regions were slightly lower and were more balanced for case study VI. In fact, the smallest NSDs for all case studies were obtained in the AP and SI directions of Region 3 for the muscle combination in case study VI, indicating a best match to the experimental data (Table 6.1).

The results from case studies IV and VI are consistent with the notion that the transversus muscle may possess multiple functional segments which enable regional contractions, for in-

stance, in the anterior and middle part of the tongue during propulsion of dry swallowing. Case study VI provides further evidence that the combined activation of hyoglossus, mylohyoid and styloglossus with partial activation of the transversus muscle can produce a deformation that matches the experimental data reported by Napadow et al. [1999b]. However, the definition of functional segments in the present study was based on a visual observation of an illustration in the literature due to a lack of previously reported data. Thus, the spatial distribution of the functional segments might be inaccurate, requiring further quantitative identification through anatomical dissections in future work. Comparing the results of case study IV with case study VI, it is clear that the values of the objective function were only slightly reduced. This might suggest that the transversus and styloglossus muscles play major roles in propulsion, while the hyoglossus and mylohyoid muscles merely make minor contributions to the overall deformation.

In case study V, the genioglossus posterior part was in an inactive state. This is consistent with the data showed in case II for which the activation levels of genioglossus muscle in all combinations were zeros. It can be explained by its fan shape fibre arrangements on the mid-sagittal plane of the tongue. The contraction of such fibrous arrangement could only produce negative axial strains in AP and SI directions. That, however, is contrary to the Napadow's data - the positive strains in the AP and the SI direction, as shown in Table 6.1. The genioglossus muscle thus remains in an inactive state, rather than contributing to the objective function through contraction.

Moreover, the estimated results in the case study V can be further interpreted as an evidence that the experimentally observed motion (i.e. displacement with respective the global coordinate system) is not representative of the strains. In other words, in the context of tongue related motion/deformation study, strain is a more typical quantity of the local material deformation, whereas the displacement is a consequence of the overall deformation. Thus, the motion from experiments, i.e. displacement, has to be re-interpreted as a synergistic consequence of multi-fibre co-contraction, rather than an indication of a particular fibre activity.

Further improvements

None of the estimated results in any of case studies completely matched the experimental data in Table 6.1, which is likely due to a combination of limitations in modelling, study design and experimental data. Limitations of the tongue modelling framework include approximations of the constitutive behaviours of the tissue and insufficient anatomical information. It was assumed that that various muscle fibres of the tongue model share the same material properties, e.g., the material constants of ground matrix. This assumption ignores possible differences in passive material response amongst tongue muscles, which could influence individual fibre performance. In short, the passive response was assumed to be the same, although this is probably a reasonable assumption.

Second, there is a clear need for further inverse testing, comprising more comprehensive computational experiments which incorporate more muscle fibres and additional functional segments in other muscle families. In the current study, the influence of only 7 muscles was investigated. However, the tongue deformation during propulsion might be due to active stress contributions from further muscles. Hence, more muscles would need to be introduced into the inverse problem, thereby raising the number of estimated muscle activation levels. Unfortunately, an increasing number of estimated parameters will raise the computational complexity to evaluate the objective function, the gradient vector and the Hessian matrix. Hence, a new computational technique, which improves the overall performance of solving the model deformation, would need to be developed. In addition, the boundaries between subdivisions, e.g. genioglossus anterior and posterior, remain unclear throughout literatures. In this dissertation, due to a lack of clear definitions of boundaries of anterior and posterior portions, the genioglossus anterior and posterior were defined using Wilhelms-Tricarico [2005] definitions that were based on observation of the muscle fibre; the transversus muscle was divided due to the fibre orientation. The definitions of those subdivisions in both muscles were not based on experimentally obtained data. In order to improve understanding of subdivisions of each muscle in swallowing, e.g. genioglossus muscle, a future research on geometric definitions of subdivisions needs to be investigated. Each segment can be then treated independently in the

improved tongue model, and their roles can be re-assessed subsequently.

Third, the objective function f may not be able to fully capture the differences between the model output and the actual tongue deformation. Deformations are likely to occur in regions other than the mid-sagittal plane, e.g., the lateral side (tongue edge). However, such deformations were not taken into account due to the lack of imaging data. For instance, the deformations of the tongue in the frontal and transverse plane, as observed by Felton et al. [2007], may give more detailed indications of the muscle involvement during propulsion in dry swallowing. The tongue deformation during propulsion is complex due to the sophisticated, spatially varying fibre orientation and distribution of the tongue muscles. In order to fully understand the mechanism of tongue deformation during the propulsive phase of swallowing, richer data sets, e.g. the strain data from images with multiple angles, need to be incorporated into the present modelling framework.

6.6 Summary

In this chapter, the inverse modelling approach was applied to estimate the muscular activity during propulsion of dry swallowing using the strain data reported in the literature [Napadow et al., 1999b]. A series of strategies were introduced to improve the overall performance of the parameter estimation procedure, including the warm start technique and a sampling strategy. With the help of the new computational framework, Napadow's hypothesized muscle combinations were tested (2 parameters). Furthermore, the resulting deformations from all possible combinations of 3 muscles, and a combination of hyoglossus, mylohyoid, styloglossus and transversus muscles (4 parameters), were compared with the experimental data. Although the modelling predictions did not fully match the experimental data, the model output still provided useful new insights into the possible mechanism of tongue propulsion under the condition of dry swallowing. Finally, the output from the combined, heterogeneous activation of the hyoglossus, mylohyoid, styloglossus and anterior-middle part of the transversus muscle was compared with the experimental data. The final results suggest that the hyoglossus, mylohyoid,

styloglossus and anterior-middle part of the transversus muscle are very likely involved as the major driving forces producing the deformation of the tongue during propulsion as reported in Napadow et al. [1999b].

Chapter 7

Conclusion and future research

7.1 Summary

Investigating of the relationship between tongue function and its complex structural muscle arrangements remain challenging due to the comparatively small size of the tongue and limited visibility using conventional measurement techniques. The aim of the present research was the development of an anatomically-realistic, physiologically-driven computational model of the tongue to provide a method for investigating tongue mechanics.

The tongue model was built using the FEM technique in continuum mechanics together with anatomical data of the tongue from the Visible Human image set. The modelling framework consisted of two major parts, a geometrical model and a computational mechanics model. The geometrical FE model provided a mathematical description of the tongue's shape and interior fibrous architecture using standard spline interpolation of the image data; while the computational mechanics model comprised a description of the mechanical tissue behaviour based on the principles of continuum mechanics. According to the theory of classical mechanics, the deformation of the tongue model is driven by active muscle contraction and reached an equilibrium state once the balance of the internal and external stresses is satisfied.

The stress state of the tongue was modelled at any spatial point in the model as the sum of

stresses from two local tissue constituents, that are the ground matrix and the muscle fibres. Based on experimental results from the literature, all constituents were considered to be hyperelastic materials, with any current deformation being independent of the deformation history. The contractile stress from each fibre family was modelled as an additional reinforced stress component along fibre direction, which was scaled by an activation level parameter. An anatomical model of the upper palate, and contact boundary conditions between the tongue and the upper bony structures, were added to simulate tongue deformation due to contact. In summary, the tongue model combined anatomical image data, realistic material properties, physiologically-based deformation mechanisms and realistic boundary conditions to simulate tongue deformation due to muscle contraction.

Measurements of kinematic motion generally comprise the quantification of two parameters: strain and displacement. In speech research, the EMA system allows to capture facial expressions or tongue motion by tracking the coordinates and displacements of a cluster of motion sensors. In the present study, it was demonstrated that a computational model of the tongue can aid in determining the placement of motion tracking sensors for EMA measurements. The results of an inverse test showed that an optimised design of sensor placement can significantly improve the identification of tongue deformation under machine inherent noisy conditions.

The aim of the motion sensor optimization was to find the cluster of sensors which are most sensitive to displacement with respect to varying muscle activation levels in quasi-static conditions, and subsequently, derive a particular tongue configuration based on the identified sensors. In other words, the optimization procedure seeked a combination of sensor locations that achieved the best identification of the muscle activation levels using the displacement information (the Fisher information matrix). Even though the collected spatial information was affected by machine inherent noise, the optimised sensor scheme achieved more reliable results in capturing the actual tongue configuration compared to other schemes.

The quality of sensor array placement is tested using the inverse problem formulation to derive the muscle activity levels based on the given displacement data. In other words, the derivation of muscle activity levels was transformed into a parameter estimation problem using the tongue

model as function of the given kinematic data (e.g. strain and displacement) with the activation levels of different muscles as input variables. The results from the inverse problem formulation revealed the potential application of the tongue model in deriving muscle activation levels using a limited number of material points (i.e. sensors). The anatomically-realistic mechanical tongue model, in combination with a few material points, led to a vastly simplified experimental set-up to estimate the contractile properties of tongue muscles.

To better understand muscle activity of the tongue during swallowing, the inverse problem formulation was applied to strain data reported in the literature. A warm start technique was implemented into the modelling framework to improve the computational efficiency and deal with the large computational task. Based on the improved inverse problem framework and given strain data from the literature, the influence of different combinations of muscles on tongue deformation during propulsion in dry swallowing was analysed. Based on the computational experiments, the empirical conclusion of muscular activities based on classical anatomical knowledge (i.e. styloglossus, transversus and verticalis muscles proposed by Napadow et al. [1999b]) seemed unlikely to drive the propulsive deformation of the tongue during dry swallowing. Following these results, more comprehensive tests with 3 and 4 muscles, were conducted. However, none of the tests with homogeneous muscle activation could achieve a tongue deformation that fully matched with the reported data.

The resulting muscle activity levels from the initial computational experiments suggested that the propulsive deformation of the tongue is likely driven by the simultaneous activation of the hyoglossus, mylohyoid and styloglossus muscles, with a partial activation of the transversus muscle in the anterior and middle parts of the tongue. Thus, further computational experiments were carried out to test the hypothesis of heterogeneous muscle activation during propulsion of dry swallowing, i.e. a combination of styloglossus and anterior and middle parts of the transversus and a combination of the hyoglossus, mylohyoid, styloglossus and anterior and middle parts of the transversus, respectively. Compared to the initial testing with homogeneous muscle activation (i.e. case studies I and IV), the model's predictions in case of heterogeneous activation of the transversus muscle resulted in a slightly better match with the experimental

data reported by Napadow et al. [1999b]. This was seen by the decreased values of the objective function and the NSDs in most regions of the tongue.

The present research provides the first attempt to quantitatively explain the mechanism of tongue propulsion using a computational tongue model and existing experimental data reported in the literature. The inverse problem formulation, and conclusions drawn from the model-based estimations, help to better understand tongue muscle activities in the propulsive phase of dry swallowing. The present modelling framework provides quantitative means to analyse and interpret image-based observations, which extend traditional observations based on medical images.

In summary, the computational mechanical tongue model, developed in this work, shows a potential application in studying the co-relation between the tongue's fibrous structures and the tongue body deformation. The computational experiments in the present work demonstrate that the tongue model can be used to re-interpret experimental measurements based on mathematical and mechanical modelling. Unlike empirical analyses based on experimental data, the anatomically-realistic tongue model, in combination with the parameter estimation scheme and experimental strain data, provide new means to reveal the muscle activities of the tongue in a quantitative manner.

7.2 Original contributions and implications

The primary scientific contributions, made through this project, are:

- An anatomically-based, mechanics-driven FE model of the tongue was developed. A multi-fibre reinforced, hyperelastic constitutive equation was coupled with the geometric model of the tongue to accurately capture the material properties of the tongue tissue (i.e. mechanical behaviour). The active contractile properties of muscle fibres were incorporated as additional stress parameters in the continuum mechanics formulation. Each muscle group of the tongue model can be independently activated to explore the resulting

deformation of various muscle combinations.

- The most robust motion sensor locations for EMA measurements of tongue retraction and elongation under noisy conditions were successfully identified using a sample of deformation modes based on the forward problem method.
- The general application of the anatomically-realistic tongue model in estimating muscular activity using only a limited number of measured spatial points was demonstrated based on the results from the model-based sensor optimization.
- The tongue model was used to identify and quantify the muscular activities during propulsion of dry swallowing. For the first time, a mathematical model was introduced into swallowing research to better understand the roles of various tongue muscles and quantify their activation levels based on measured strain data.

7.3 Limitations and future research

Based on the current progress and remaining limitations in modelling tongue mechanics, future research may be directed towards the following:

The tongue model

Several areas of the geometric tongue model can be improved. First, the surrounding bony structures, i.e. the mandibular, the teeth on the lower jaw and the hyoid bone, could further be incorporated into the modelling framework. The posterior bottom of the tongue is attached to the hyoid bone, which moves due to the contraction of tongue muscles. The tongue also interacts with the oral cavity floor, which is composed of various types of soft tissue. The interaction of the tongue with the hyoid bone and the oral cavity floor is expected to influence the tongue deformation, and thus, the modelling results. This may not be so important for propulsion, but may be more important for other tongue functions. Modelling the distribution and orientations

of the palatoglossus muscle may be required. This would enhance the boundary conditions in the upper posterior side of model such that these areas shall be freely moveable and deformable.

The current geometric model of the tongue is based on the Visible Human image data, and merely represents the anatomy of a female cadaver. As such, the geometric model does not reflect anatomical differences amongst individuals. Future research should aim to develop a customised model using population-based anatomical data, which enables the incorporation of statistically significant features of the shape and interior fibrous structure of the tongue.

The constitutive equation, implemented into the current modelling framework, can further be improved. In reality, muscle fibres are 3D cylindrical objects. However, the constitutive equation in the present work only captured the stress contribution along fibre direction (1D). The mechanical characteristics in the other two directions, which are orthogonal to the fibre direction in the context of stress sensors, were not taken into account. The 3D contractile properties of muscle fibres might significantly influence tissue deformation. Further experimental studies and an extension of the constitutive equations are necessary to investigate the influence of 3D muscle fibre contraction on tongue deformation.

Further validation of the model's accuracy is crucial for future development. To verify the robustness and accuracy of the model's predications, experimental measurements of the tongue's movement and corresponding stresses are needed. Novel validation techniques, including a combination of experimental measurements and computational modelling methods, should be developed in future work.

The inverse problem

The framework of the inverse problem can further be improved in two areas: (1) the choice of objective function and (2) the procedure for evaluating the model deformation. In the current inverse framework, the difference between the modelling results (nodal displacements) and given kinematic data is minimised. In order to improve the objective function, it is further necessary to investigate the most sensitive kinematic and kinetic quantities (i.e., strain, dis-

placement, energy expenditure, total system energy) with regards to varying activation levels. Future research may instead focus on combining minimising the total of energy and the total displacement error. A challenge task is to determine the appropriate mathematical representations and weightings of these two elements of the objective function. That could be achieved using the sum of a normalized global amount energy and a normalized displacement error term.

In the scope of the inverse problem formulation, the tongue model is treated as an independent function that, for any target level of muscle activation, returns the corresponding model deformation. Thereby, the tongue model has to be deformed in each iterative step. Thus, most of the time is consumed to solve for the deformation of the FE model. The complexity of the problem, including the computation time, significantly raises with an increasing number of identification parameters (i.e. activation level parameter α for each fibre group). Recent developments of the so-called reduced basis method could lead to a close solution compared to the target configuration without solving the actual FE system [Prudhomme et al., 2002, Ito and Ravindran, 1998]; and thus, reduce the required computational costs. Future investigation and implementation of the reduced basis method for solving the tongue model deformation could benefit the overall efficiency of the inverse procedure.

Sensor optimization

The current algorithm of sensor placement optimization may lead to high computational costs when a higher number of candidate locations is required. Increasing the number of candidates will raise the total number of possible combinations, and thus, the number of comparisons between combinations. One strategy to reduce the computational costs is to study the correlation between different selections of single sensors and groups of sensors, respectively. Through studying the individual contribution of each sensor, a sub-optimal solution for the optimal sensor array placement can be obtained.

The verification of sensor robustness to machine noise is based on computerized simulation in the current work. Future investigations could be directed towards introducing more practical

conditions into the optimizing procedure, e.g. the accessibility of the potential sensor locations, and experimentally testing the optimal solutions with the EMA system.

Other applications

The multi-fibre reinforced hyperelastic constitutive equation could be applied to model other biological soft tissues, such as the arm of cephalopods which shares a similar fibrous structure to the tongue. Improved understanding of the mechanical behaviour of these biological tissues could potentially benefit industrial activities in robotics. For instance, Trivedi et al. [2008], Walker et al. [2005] developed a soft continuum robot arm inspired by cephalopods. The soft manipulator is an advancement to conventional rigid robotic arms, which are governed by the theory of rigid body motion. Walker et al. [2005]'s robotic arm is soft and can perform deformations similar to an actual octopus arm. The present constitutive equations and modelling framework could be applied to robotics development for improved mechanical design and controlling system in future work.

The application of the tongue model to sensor placement optimization further demonstrates the possible future application to model-aided instrumentation design. A recent trend in human-computer interface research is the use of tongue motion to control the equipment through a tongue-computer interface. For instance, Struijk [2006] used an inductive pointing device, which measured the tongue-hard palate contact force at various locations, to assist disabled people in controlling a wheel chair. For such applications, the tongue plays a unique role as a controlling instance similar to that of a human hand. The tongue model, presented in the current work, may be applied to improve the development of such controlling devices in the future, for instance, through a more ergonomical design according to tongue mechanics.

Appendices

Appendix A

Subject-specific modelling of the tongue

The FE tongue model, developed in Chapter 4, is based on a subset of the female Visible Human images (VH tongue model). The model may be less accurate when applied to another subject to make movement predictions (i.e., strain, displacement) due to subject-specific variations in muscle fibre arrangements and tongue shape. Therefore, subject-specific modelling of the tongue becomes important when the tongue model is aimed to be applied to subject-specific analysis of tongue mechanics, such as the estimation of muscle activation levels based on inverse modelling.

The shape and internal fibrous structure of the tongue are subject dependent. In a common subject-specific modelling procedure, individual data of the tongue shape and complex internal fibre arrangements need to be acquired for each subject through manual or automatic digitisation of image data. Identification of directions and composition weights (volume fraction) of various fibres would add further work to the model setup. Hence, the development of an automatic or semi-automatic method for generating customised tongue models becomes a crucial step towards applying the VH tongue model to subject-specific measurements.

Customising the shape of a muscular organ and its fibre arrangements based on a template FE model is a challenging task. In this research, subject-specific muscle arrangements within the tongue are considered to share a topological similarity, and thus, the individual geometrical

shape can be approximated by using a generic model with finite steps of transformation. A technique for customising the generic VH tongue model to subject-specific tongue shape and fibrous arrangement is proposed here. It can be divided into three steps: (1) original data registration (Section A.2), (2) customised geometrical modelling (Section A.3) and (3) topological mapping of the fibrous structures (Section A.4). The method is demonstrated using MRI data from a male subject described in Section A.1.

A.1 MR images of the tongue

Subject-specific data was obtained through manual digitisation of a set of MR images acquired by Watson et al. [2009] for a study of analysing the vocal tract shape during the subject's pronunciation of vowels in New Zealand English. Images were obtained for the vowels *i: a: o: e:* and the resting position.

The subject, a 45 year old male, was in a supine position with his head supported to prevent movement throughout the scanning process. The MR images were acquired on a 1.5T Siemens Magnetom Avanto MRI scanner. The scanning was carried out parallel to the sagittal plane in medial-lateral direction. A total of 160 images slices with a voxel resolution of 1 mm $\times$ 1 mm $\times$ 1 mm were taken in the resting position. To reconstruct the 3D vocal track shape in reading vowels, the subject had to maintain a sustained production of each vowel for the entire MRI scan time of 21 seconds. The scanning parameters were: T1-weighted images, 7 mm slice thickness, no gaps between slices, a 200×250 mm field of view, 1600 ms repetition time, 9.4 ms echo time, 1 mm resolution, 20 slices and a total scanning time of 21 seconds. Figure A.1 shows on image in the mid-sagittal plane of the subject in the resting position. Only the subject-specific images in the resting position were digitised and processed to build the customised model in a configuration, which is as close to the reference configuration as possible.

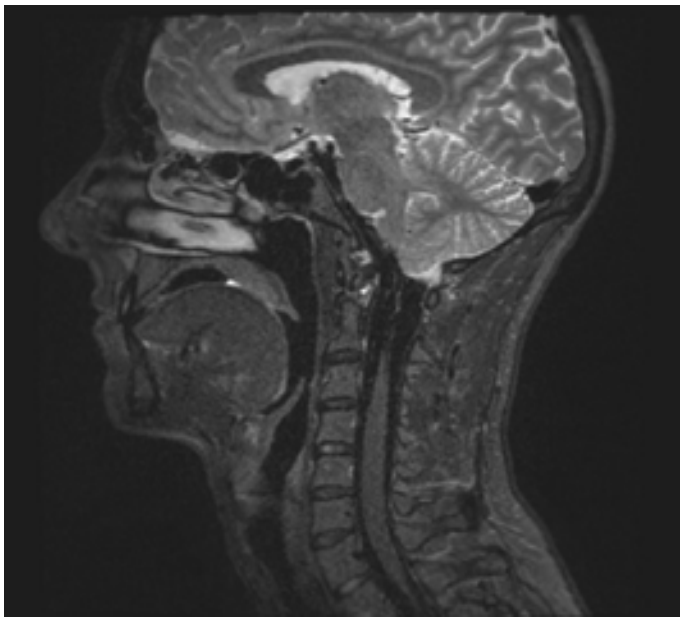

Figure A.1: The mid-sagittal plane view of the MRI image set, obtained by Watson et al. [2009].

A.2 Spatial data registration

The FE model based on the VH image data, developed in Chapter 4, is referred to as the generic model. The MRI scanner defined a subject-specific coordinate system that was not aligned with the spatial coordinate system of the generic tongue model. Furthermore, the width, height, length and curvatures of the subject-specific tongue was significantly different from the generic model. Figure A.2 shows a comparison between the VH tongue model and the data clouds of the subject's tongue. The aim of spatial data registration is to align the orientation of the digitised data with the generic model and apply simple initial scaling techniques to the generic model to ensure the model is sufficiently close to the given data. In other words, the aim is to define a restricted Procrustes transformation between the subject-specific experimental data and the VH tongue model to align the model with the data.

The outer surface of the generic model is approximated by surface data that is denoted as $\mathbf{P}_{\text{model}}$ for which $\mathbf{P}_{\text{model}} = \{\mathbf{P}_1, \mathbf{P}_2, \cdots, \mathbf{P}_{n_{model}}\}$ where n_{model} is the total number of data points. The digitised data of the MR images is denoted as $\mathbf{P}_{\text{image}}$, sharing the same structure as $\mathbf{P}_{\text{model}}$ with n_{image} data points. Considering an ideal case that $n_{\text{model}} = n_{\text{image}}$, and $\mathbf{P}_i$ of $\mathbf{P}_{\text{model}}$ is one-to-one corresponding to the volume element in $\mathbf{P}_{\text{image}}$, a transformation matrix $\mathbf{F}_{\text{registration}}$ can be

introduced, such that

$$\mathbf{P}_{\text{image}} = \mathbf{F}_{\text{registration}}\mathbf{P}_{\text{model}} + \mathbf{T}_{\text{translation}}, \tag{A.1}$$

where $\mathbf{F}_{\text{registration}}$ is the matrix product of the rotation transformation $\mathbf{R}$ and the stretch transformation $\mathbf{U}$. The rotation $\mathbf{R}$ is a 3×3 matrix in which $\mathbf{R} = \mathbf{R}_z(\theta_z)\mathbf{R}_y(\theta_y)\mathbf{R}_x(\theta_x)$, where θ_x, θ_y and θ_z define the rotational angles for the axial rotation matrix $\mathbf{R}_x$, $\mathbf{R}_x$ and $\mathbf{R}_z$ with respect to the x, y and z axis, respectively. The stretch transformation $\mathbf{U}$ is the diagonal matrix

$$\mathbf{U} = \begin{pmatrix} \lambda_x & 0 & 0 \\ 0 & \lambda_y & 0 \\ 0 & 0 & \lambda_z \end{pmatrix}, \tag{A.2}$$

where λ_x, λ_y and λ_z represent scaling factors in x, y and z directions. The definition of $\mathbf{U}$ in Equation A.2 indicates an anisotropic scaling. The translation vector $\mathbf{T}_{\text{translation}}$ is the form $(T_x, T_y, T_z)^T$ representing the translational motion in x, y and z direction. Note that, all transformations introduced so far are with respect to the global coordinate system.

Equation A.1 is based on the assumptions that $n_{\text{model}} = n_{\text{image}}$ and the surface mapping relation between $\mathbf{P}_{\text{image}}$ and $\mathbf{P}_{\text{model}}$ is known. However, such a condition might never hold true in reality. Thus, a searching function f_{search} is introduced to find a subset of $\mathbf{P}_{\text{model}}$ (denoted as $\mathbf{P}^*_{\text{model}}$) as a set of nearest-neighbouring points to $\mathbf{P}_{\text{image}}$. Consequently, a function of the total distance between two sets of data can be formulated as a measure of their similarity, that is

$$E_{\text{error}}(\mathbf{P}_{\text{image}}, \mathbf{P}_{\text{model}}) = \sum_{i=1}^{n_{\text{image}}} \| \mathbf{P}_{i,\text{image}} - \mathbf{P}^*_{i,\text{model}} \|^2, \tag{A.3}$$

where $\mathbf{P}^*_{i,\text{image}} = \mathbf{F}_{\text{registration}}\mathbf{P}^*_{\text{model}} + \mathbf{T}_{\text{translation}}$. To achieve the best match, the function E_{error} needs to be minimised, such that

$$\min \quad E_{\text{error}}(\theta_x, \theta_y, \theta_z, \lambda_x, \lambda_y, \lambda_z, T_x, T_y, T_z), \tag{A.4}$$

under the following conditions

$$0 \leqslant \theta_x < 2\pi,\ 0 \leqslant \theta_y < 2\pi,\ 0 \leqslant \theta_z < 2\pi;$$
$$\lambda_x > 0,\ \lambda_x > 0,\ \lambda_x > 0. \tag{A.5}$$

Once $\mathbf{R}$, $\mathbf{U}$ and $\mathbf{T}_{translation}$ are obtained, the generic model can be aligned with the digitised data. Figure A.2 shows the initial state before registration, while the finial registration results are shown in Figure A.3. The new configuration of the generic model is denoted as $\Omega_{\text{generic},1}$ to distinguish between other configurations (e.g. the reference configuration $\Omega_{\text{generic},0}$) obtained throughout the customising process.

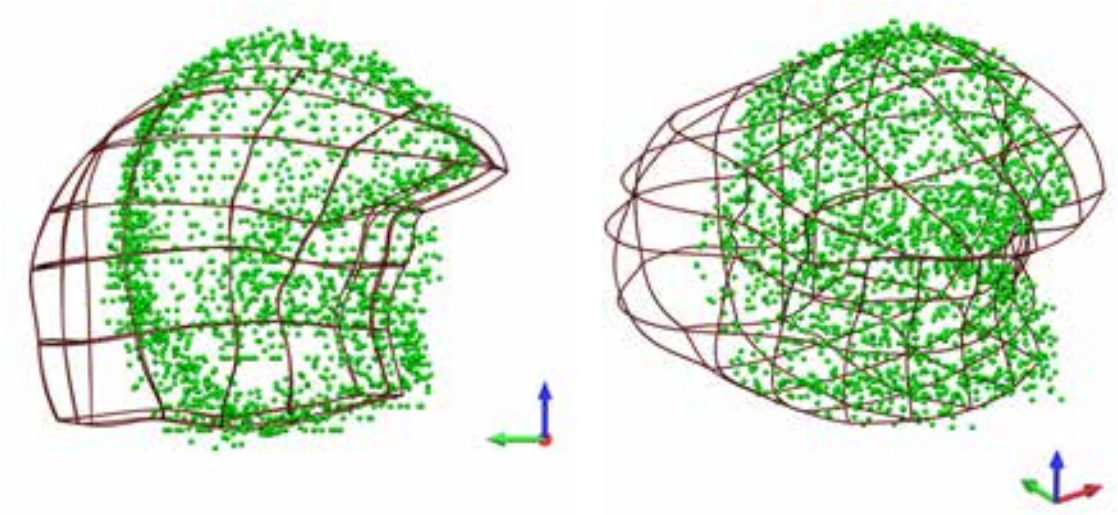

(a) (b)

Figure A.2: The relative positions and shapes between VH tongue model in the $\Omega_{\text{generic},0}$ configuration and the subject-specific image data clouds (green dots), before alignment. Axes are for reference purpose only.

A.3 Customising the geometrical model

The spatial data registration of the generic model in $\Omega_{\text{generic},0}$ leads to the transformed configuration $\Omega_{\text{generic},1}$, which is approximately in line with the subject-specific experimental data. However, the geometrical curves of the generic model still show large discrepancies with the subject-specific data, as seen in Figure A.3. The face fitting method can be adopted to obtain a

customised geometric configuration. However, due to the typical non-convex geometry of the tongue, the direct orthogonal projection of data points in the scope of face fitting is very likely to fail in the search for the ”correct” projection surface that follows the anatomical topology.

The face fitting method, as an optimisation procedure (see Bradley et al. [1997]), has a considerable chance of reaching a local minimum or saddle point, without guaranteeing that the global minimum over the parameter domain (all degree of freedom of the FE model) is achieved. Hence, face fitting may not lead to accurate subject-specific customisation in the case of the tongue. Figure A.3 shows the projection of the digitised data ($\mathbf{P}_{\text{image}}$) for the configuration $\Omega_{\text{generic},1}$, and illustrates the error in the projection due to the mis-matched topological surfaces. For example, in the area of the tip, the image data on the superior surface of the tongue are projected onto the inferior surface of the tongue model.

To reduce the chance of failure in the search for the global optimal configuration, an intermediate configuration $\Omega^{*}_{\text{subject}}$, which is sufficiently close to the configuration $\Omega_{\text{customised}}$, is initially derived using the so-called Host Mesh Fitting (HMF) technique. Subsequently, face fitting is performed on the intermediate configuration to obtain the final solution $\Omega_{\text{customised}}$. The two steps of the customising procedure are outline in the following in Section A.3.1 and A.3.2).

A.3.1 Host mesh fitting

The shape of the tongue is considered to be divided into several sub-domains in accordance with the local curvatures. To capture local shape features, the HMF technique is adopted. The HMF technique was proposed by Bradley et al. [1997]. For instance, Fernandez and Hunter [2005] created a customised model of patello-femoral articulation for diagnostic purposes, and Cheng et al. [2005] adopted the HMF method to model the human torso using ultrasound images.

The main purpose of the HMF procedure in the present work is to obtain an intermediate state, i.e. better starting configuration for face fitting, rather than a final customised configuration as reported in other studies. For HMF, the geometrical domain of the subject-specific data (Ω_{subject}) is divided into several parts, denoted as $\Omega^{e}_{\text{subject}}$. The generic model in configuration

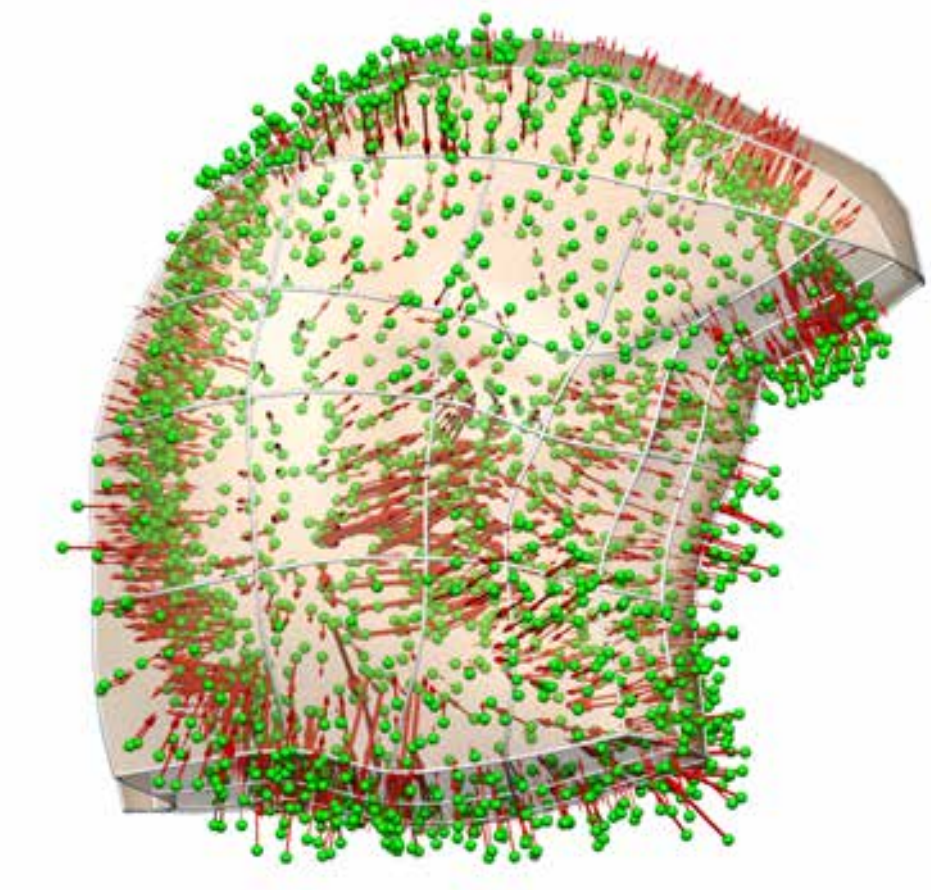

Figure A.3: Projection of $\mathbf{P}_{\text{experiment}}$ onto the outer surface of the tongue model in configuration $\Omega_{\text{generic},1}$. The green dots are members of $\mathbf{P}_{\text{experiment}}$, the red arrows represent the projection direction based on an orthogonal projection function. In the area of the tip, it can be seen that the green dots from the superior surface of the subject-specific data are projected onto the inferior side of the tongue model.

$\Omega_{\text{generic},1}$ is sub-divided into the same number of sub-domains, each of which matches topologically to $\Omega^e_{\text{subject}}$. Note that, the sub-domains of HMF, denoted with the superscript e, do not refer to the finite elements of the generic VH tongue model, but rather comprise a coarse, regional sub-division of the entire object domain.

Following the sub-division outlined above, a local transformation is defined such that $\mathbf{F}^e_T : \Omega^e_{\text{generic},1} \mapsto \Omega^e_{\text{generic},2}$ where $\Omega_{\text{generic},2}$ is an approximation of $\Omega^e_{\text{subject}}$. Theoretically, any given $\mathbf{X}$ in $\Omega^e_{\text{generic},1}$ shall be related to a corresponding position $\mathbf{x}$ in $\Omega^e_{\text{subject}}$, and thus, the transformation $\mathbf{F}^e_T$ is formulated as $\mathbf{F}^e_T = {}^{\partial \mathbf{x}}/_{\partial \mathbf{x}}$. To approximate the transformation field $\mathbf{F}^e_T$, a so-called host mesh is defined which covers the domain of $\Omega^e_{\text{subject}} \cup \Omega^e_{\text{generic}}$. In an ideal case, the host mesh consists of a sufficient number of degrees of freedom to derive the one-to-one transformation from the target points in $\Omega^e_{\text{generic}}$ to the landmark points in $\Omega^e_{\text{subject}}$. In practice, a limited number of target and landmark points are selected from the digitised data and surface points of the generic model. Note that the number of landmarks provides an upper bound on the number of degrees of freedom for the host mesh.

The HMF method is an optimization procedure which seeks the optimal point achieved the minimum or maximum of the objective function. In particular, the optimal mapping between the target and the landmark points by minimising the differences in their spatial positions using

$$H(\mathbf{x}(\boldsymbol{\xi}_d)) = \sum_{d=1}^{D} [\mathbf{x}(\boldsymbol{\xi}_d) - \mathbf{x}_d]^T [\mathbf{x}(\boldsymbol{\xi}_d) - \mathbf{x}_d] + G(\mathbf{x}(\boldsymbol{\xi}_d), \gamma_i), \tag{A.6}$$

where $\mathbf{x}(\boldsymbol{\xi}_d)$ and $\mathbf{x}_d$ are the landmark and corresponding target points, respectively, and D indicates the number of target points within the spatial domain $\Omega^e_{\text{subject}}$. Note that the landmark points are given as functions of local host mesh coordinates $\boldsymbol{\xi}_d$. Thus, $\mathbf{x}(\boldsymbol{\xi}_d)$ can be updated according to the deformed host mesh configuration, and subsequently, the geometrical nodal parameters of the generic FE model in configuration $\Omega_{\text{subject},1}$ can be updated by evaluating $\mathbf{F}^e_T$ [Bradley et al., 1997].

A set of 6 landmarks and corresponding target points were selected. The subdivision of the generic model ($\Omega_{\text{generic},1}$) was in accordance with anatomical features, which contained a

tongue body part ($\Omega^1_{\text{generic},1}$) and a tongue base ($\Omega^2_{\text{generic},1}$) as illustrated in Figure A.4. Through the HMF process, the configuration $\Omega_{\text{generic},2}$ (as shown in Figure A.5) was obtained. Configuration $\Omega_{\text{generic},2}$ was used to derive the final configuration of the subject-specific model using the face fitting technique as outlined in the following.

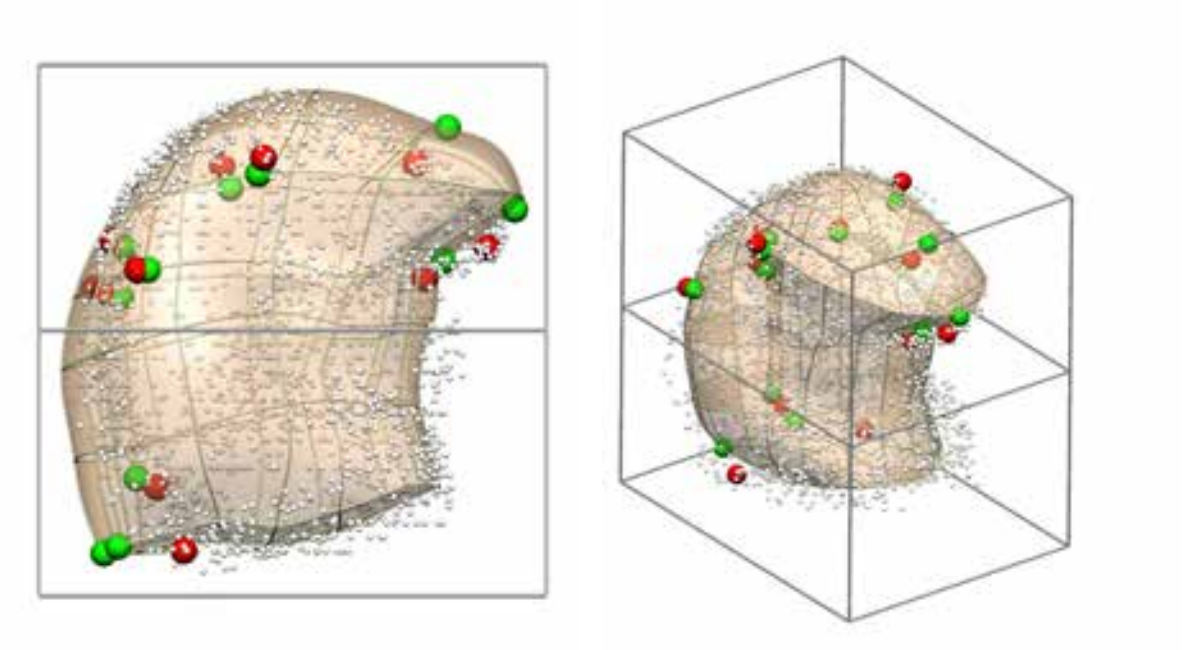

(a) (b)

Figure A.4: Host mesh, landmarks (green dots) and target points (red dots). The white dots are the digitized imaging data points. The host mesh divides the tongue model, given in $\Omega^1_{\text{generic},1}$, into two parts that are $\Omega^1_{\text{generic},1}$ (upper box) and $\Omega^2_{\text{generic},1}$ (lower box).

A.3.2 Face fitting

In the second step of the customisation process, the face fitting technique is used to update the nodal geometrical parameters, $\bar{\mathbf{X}}_a$, including the coordinates and derivatives with respect to the global reference coordinate system by minimising the projections of the data points onto the surface of the model. Face fitting of the tongue model in the configuration $\Omega_{\text{generic},2}$ leads to the configuration $\Omega_{\text{generic},3}$, which is considered the optimal geometrical approximation of Ω_{subject}. Figure A.6 illustrates the customised model after face fitting and the error projection of the digitised data based on the condition of orthogonal projection.

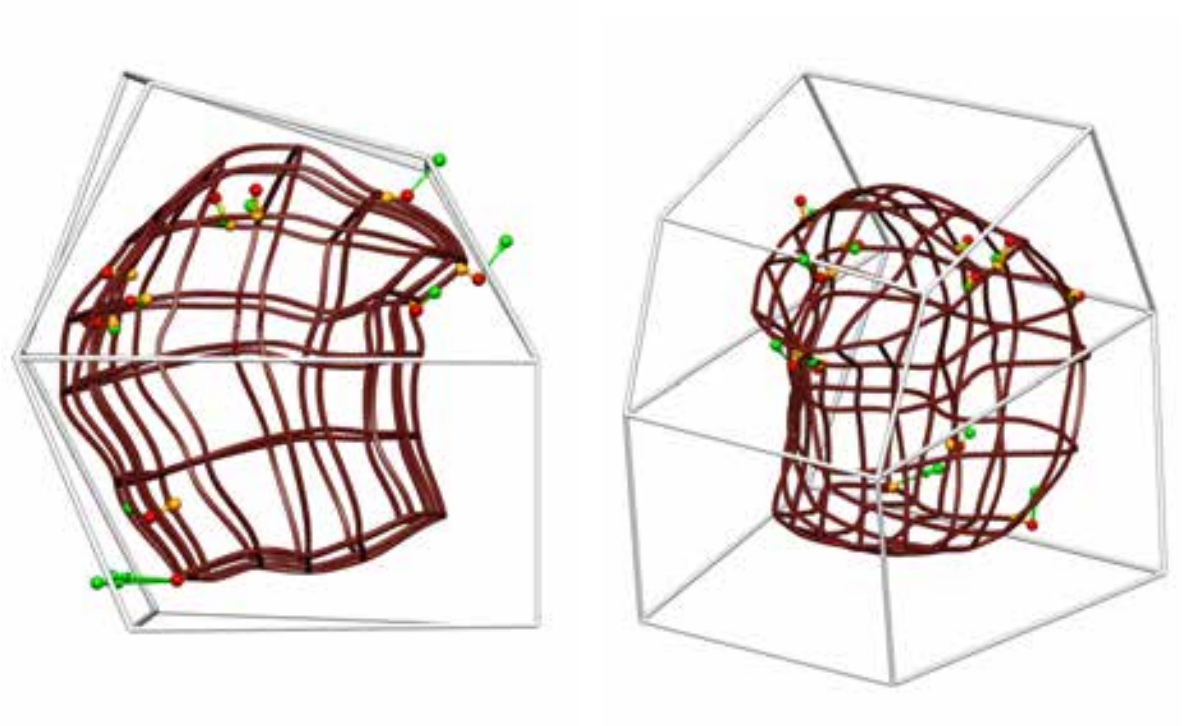

(a) (b)

Figure A.5: The deformed host mesh with the tongue model in configuration $\Omega_{\text{generic},2}$. The red dots represent the target points; the green dots are the landmarks on the tongue in configuration $\Omega_{\text{generic},1}$; and the golden dots are the landmarks in configuration $\Omega_{\text{generic},2}$ after the HMF process. The white arrows indicate the distance between the landmarks and the corresponding target points, and the golden arrows indicate the distance after HMF.

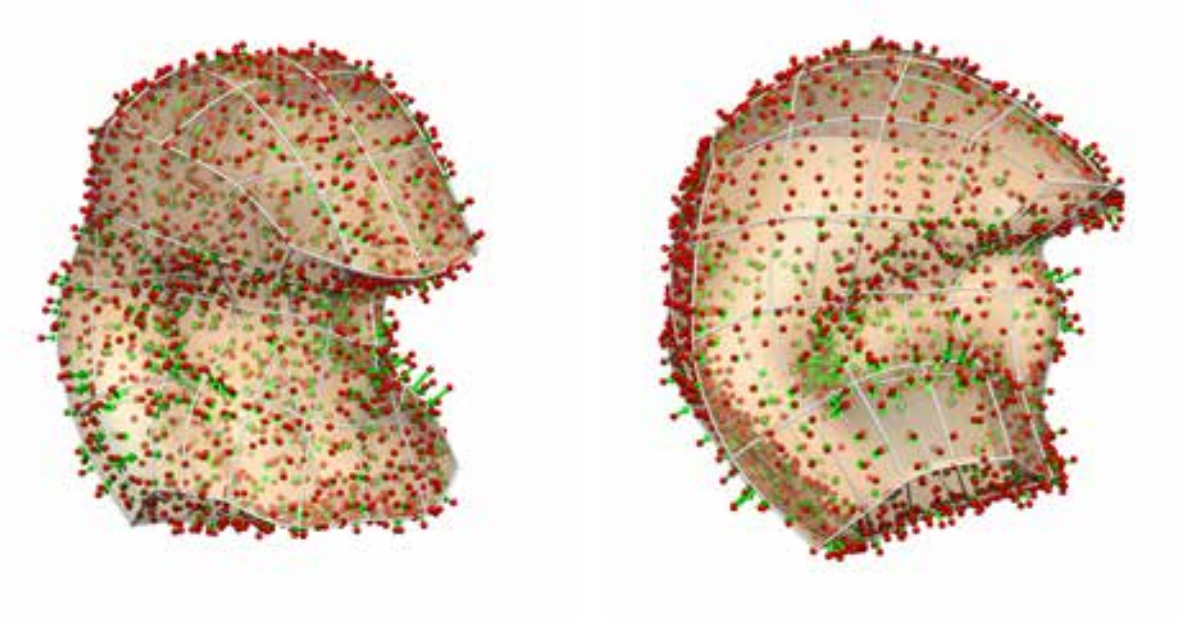

(a) (b)

Figure A.6: The subject-specific geometric tongue model. The red dots represent the actual data points based on MRI images; the green arrows represent the projections of the data point onto the model surface.

.

A.4 Mapping the fibre structure

The internal structure of the generic tongue model has to be redefined for any subject-specific analysis. In an ideal case, the subject-specific arrangement of internal structures, including fibre orientations and volume fractions (distributions), are obtained through direct experimental measurements. However, the acquisition of such data for a subject *in vivo* remains challenging using current measurement techniques. Thus, it is assumed that the internal structure of the tongue muscles (the fibre orientation and distribution) are topologically similar across different subjects. In other words, the relative difference between neighbouring points are preserved while changes might occur in the overall spatial shape and orientation.

During the customisation process, the current configuration $\Omega_{\text{generic},3}$ is obtained through a series of transformations on $\Omega_{\text{generic},0}$. For fibre mapping, we only focus on the rotational transformation which is a path independent process, thus the intermediate rotation transformations can be substituted by one overall rotational process $\mathbf{R}_T$. At any position (i.e. $\mathbf{x}$) of the model in the current configuration $\Omega_{\text{generic},3}$, the local fibre orientation field (a vectorial quantity) has

to be updated with respect to the customised shape; while the topological distribution of a particular muscle population remains constant under the transformation. The fibre directions at a material point $\mathbf{X}$ can be transformed as

$$\mathbf{b}(\mathbf{x}(\boldsymbol{\xi}^e)) = \mathbf{R}_T(\mathbf{X})\mathbf{a}(\mathbf{X}(\boldsymbol{\xi}^e)), \tag{A.7}$$

where $\mathbf{b}(\mathbf{x}(\boldsymbol{\xi}^e))$ denotes the deformed vector (i.e. updated fibre orientation) in the customized model, and $\mathbf{a}(\mathbf{X}(\boldsymbol{\xi}^e))$ are the fibre directions at $\boldsymbol{\xi}^e$. Since the condition of topological mapping is adopted, the volume fraction of muscles will not change during deformation. Thus, the volume fraction in the customised configuration can be derived from

$$d_i(\mathbf{x}(\boldsymbol{\xi}^e)) = d_i(\mathbf{X}(\boldsymbol{\xi}^e)). \tag{A.8}$$

Figure A.7 shows the refitted fibre directions and distributions for the customised model.

A.5 Concluding remarks

A customisation technique was introduced to develop a subject-specific model of the tongue, combining an initial registration process with the HMF technique and face fitting. The customised model contains geometrical and interior structural features based on subject-specific MRI data, which can be used for subject-specific analysis of tongue mechanics.

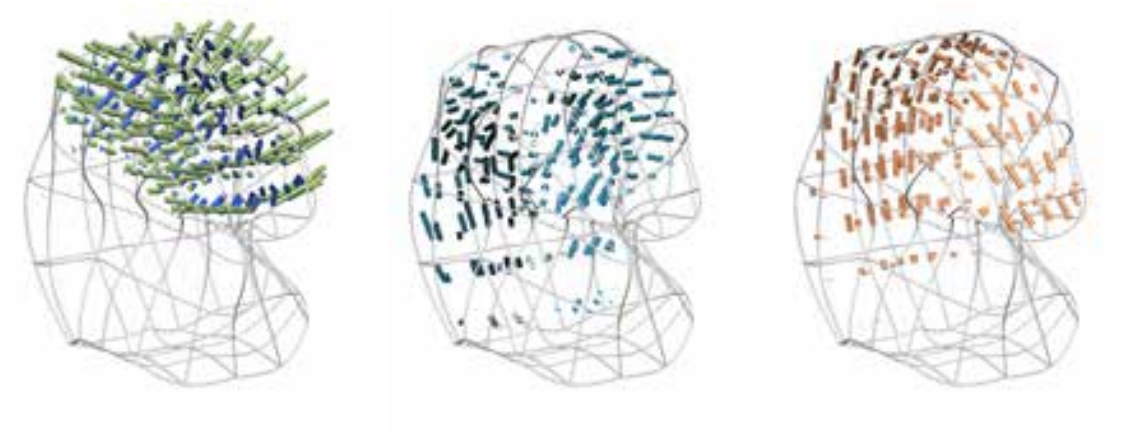

(a) Transversus (green) and verticalis (blue) muscles

(b) Hyoglossus muscle

(c) Longitudinalis muscle

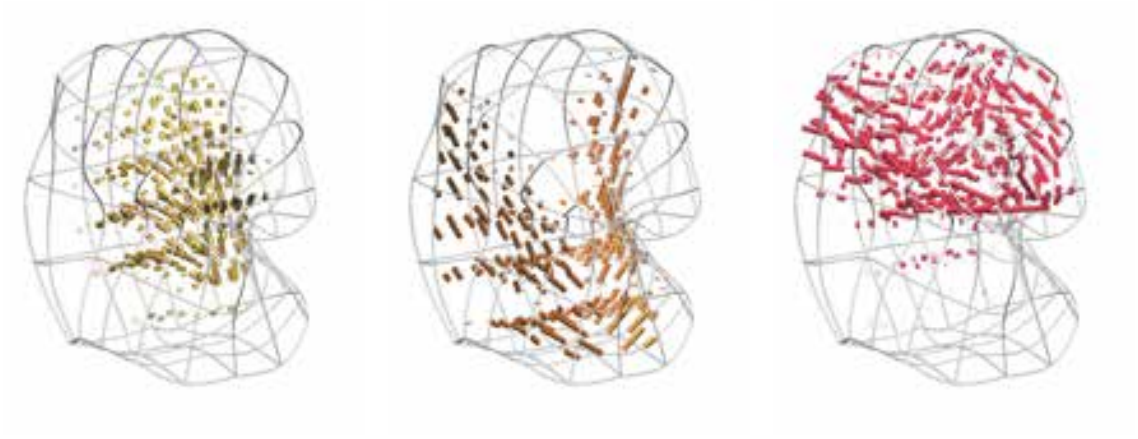

(d) Genioglossus muscle

(e) Mylohyoid muscle

(f) Styloglossus muscle

Figure A.7: The subject-specific model with the fibrous structures. The subject-specific fibrous structures were derived by mapping the interior architecture of the VH tongue model under the assumption of topological similarity.

.

Appendix B

Numerical validation of contact mechanics with muscle activation

B.1 Introduction

The interaction between the tongue and the upper palate is caused by muscle contraction. When one, or more, muscles contract, the shape of the tongue will simultaneously change and establish contact with the upper palate, or other soft tissue on the floor of the mouth. The consideration of contact mechanics within the tongue model is complex, even more so if geometric nonlinearity is added.

Solving the problem of contact mechanics between the tongue and the upper palate with muscular activation is a challenging task. The resulting deformation of the tongue is solved using a Newton iterative method that requires a near-solution initial guess. In other words, an incremental solving path needs to be planned and implemented. The configuration at each intermediate stage ($\boldsymbol{\alpha}$) should benefit the next iterative step of the solving procedure ($\boldsymbol{\alpha} + \Delta\boldsymbol{\alpha}$). Each iterative step has to be numerically stable and solvable.

Since the tongue tissue is idealised to be a hyperelastic material, and the contact interactions are assumed to be frictionless, the deformation of the tongue is independent of the deformation

path. In this study, a simple numerical validation procedure was set up to verify this theoretical statement in a practical manner.

B.2 Method

Three strategies were introduced to solve the contact problem between bony structures and soft tissue with highly nonlinear geometry, material properties and complex boundary conditions. The following simulations are performed:

- First, a rigid-body object gradually approaches the soft tissue object. The size of contact area slowly increases to the target contact size. Thereby, the pre-contact configuration was derived by gradually increasing the contact area, with all muscles remaining in an inactive state ($\boldsymbol{\alpha} = \mathbf{0}$). Subsequently, the deformation was obtained by gradually raising the activation levels.
- Secondly, the deformation is solved by gradually increasing the contact stiffness parameter until it reaches the desired level. Equation 4.42 defines a linear relationship between the geometric penetration and the contact stiffness parameter ε_N. It is obvious that, when $\varepsilon_N = 0$, the contact force equals 0. By increasing ε_N, with g_N remaining at a constant value, the contact force will gradually increase.
- Thirdly, the deformation is initially derived for a specific $\boldsymbol{\alpha}$; followed by the application of contact boundary.

B.3 Numerical experiment

A simplified numerical experiment of the contact between two cubes was conducted. One cube was considered to be a rigid body, such as bone, and the other cube was assigned soft tissue properties with embedded fibres, i.e. muscle, as shown in Figure B.1(a). In the resting state (the

	Case A	Case B
RMS	3.7770×10^{-7}kPa	4.1495×10^{-7}kPa

Table B.1: RMS of contact pressure of case A and B compared to case C.

reference configuration), the two cubes were tightly coupled to each other; though, without mechanical interaction between the two objects. Upon muscle activation, the corresponding tissue cube would self-contract, and due to the volume conservation, the superior surface of the tissue cube would actively press against the rigid body cube. The deformation of the tissue at maximal activation was derived using the three solution strategies as follows

- Case A: rigid cube was gradually lowered from the superior direction of the tissue cube, while simultaneously increasing the activation level of the tissue cube.
- Case B: the contact stiffness parameter was gradually increased with increasing activation level.
- Case C: the activation level was initially set to the maximum level, and then the rigid cube was gradually lowered.

B.4 Results

Figure B.2 shows the contact pressure patterns using the three different solution strategies. Table B.1 shows the RMS of the contact pressure of case A and B compared with case C. The distributions of contact pressure in Figure B.2 show a close match in all three cases. The RMS of case A and B compared with case C indicate a relatively small numerical difference. Thus, the resultant deformations and contact patterns based on the three different solving strategies can be considered to be the same up to same numerical tolerance.

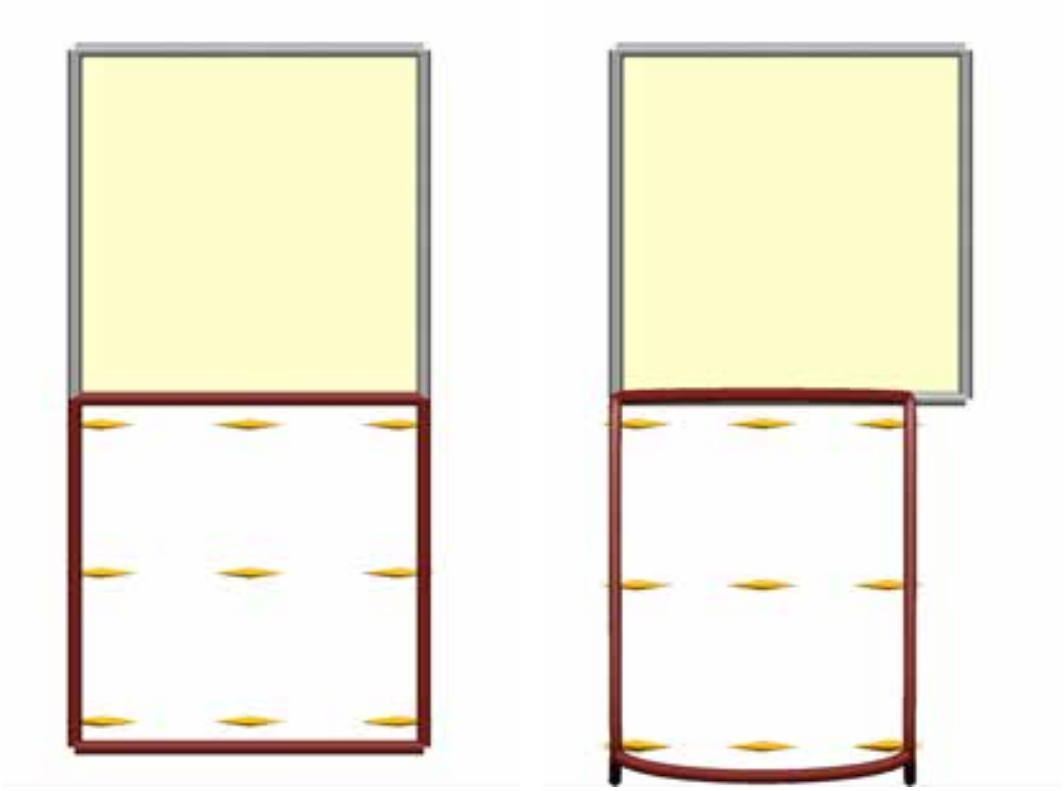

(a) The reference state

(b) The deformed state of maximum muscle activation level

Figure B.1: Testing example for verifying different solving strategies of soft-tissue rigid body contact with muscle activation. The upper cube is a none deformable rigid body; whereas, the lower cube is a tissue block. The golden cones represent the embedded fibre direction within tissue block. When activated, the tissue block will contact with the upper rigid cube, as shown in Sub-Figure B.1(b).

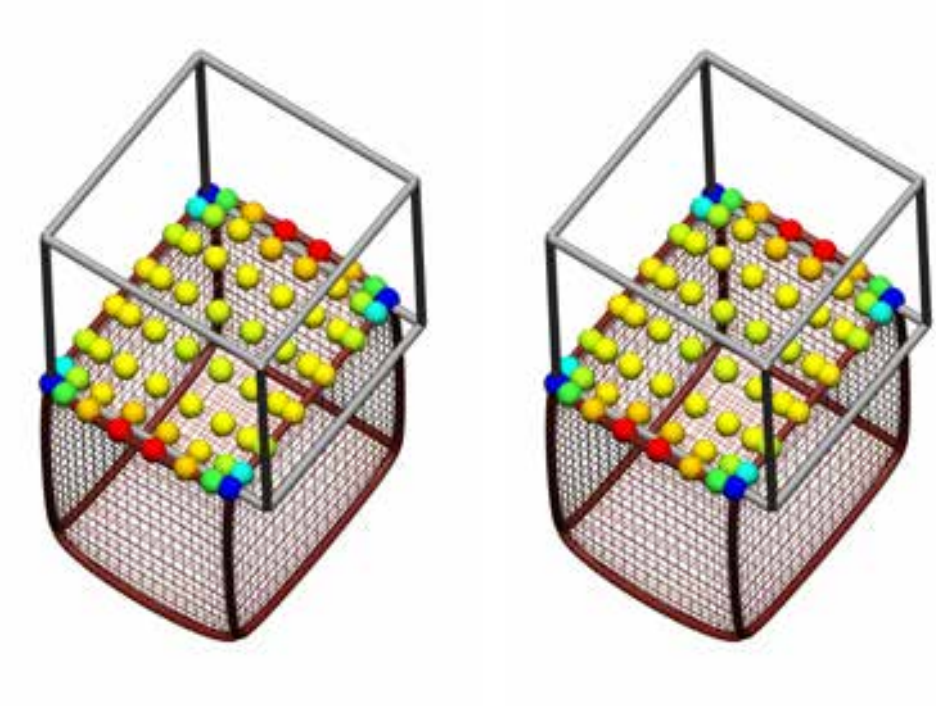

(a) Case A

(b) Case B

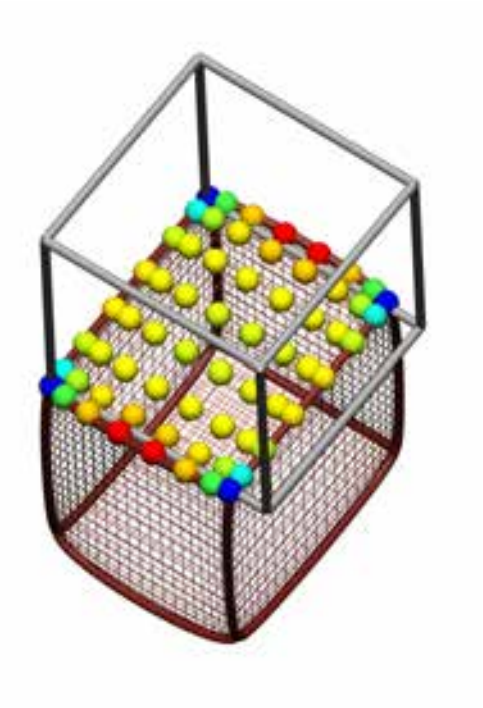

(c) Case C

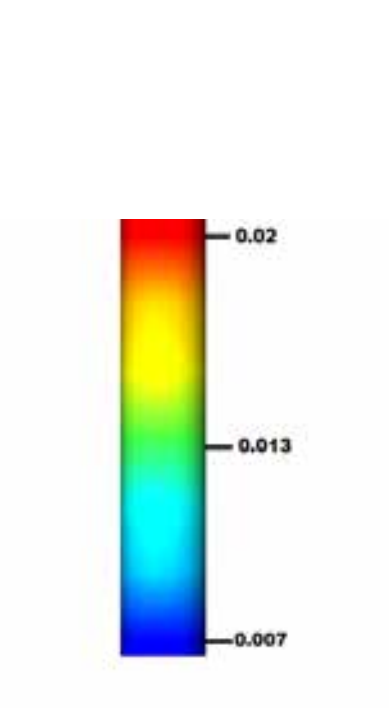

(d) Spectrum, unit in kPa

Figure B.2: The contact pressure patterns based on three different solution procedure, i.e. case A, B and C. The dots are the contact points, with the colors representing the magnitudes of contact force at each contact point.

.

B.5 Remarks

Three different solution strategies are deployed for the contact mechanical problem with muscle contractions. The same results were obtained for the three solution procedures. Therefore, all three solving procedures can be used to derive the resultant tongue deformation with tongue-upper-palate interaction. These three solution strategies provide multiple choices for obtaining the deformation due to the interaction to the upper palate. Hence, they gives more convenient ways to deal with the instability that may occurred during the solution processing, and therefore increases the chance to derive the solution of the deformation.

The solution procedures required a large amount of time to gradually increase the contact loading steps. Reducing the computational costs was considered crucial for application to the inverse problem analysis. In order to reduce the computational costs, the three solution procedures were combined to obtain a pre-stretched state of the tongue. This intermediate configuration was then used as initial configuration for deriving all other configurations which are produced by the contractions of tongue muscles.

Appendix C

Justification for mesh resolution

A fundamental principle of FE modelling is the use of a number of subdivided elements to represent an actual physical object. The number of such subdivisions needs to ensure a mathematical representation that is close to the geometrical shape and mechanical behaviour of the actual object. In other words, the subdivisions (the elements) need to allow the mechanical quantities, e.g. the displacement, to converge to a stable level and remain constant with changes in the number of elements. Therefore, a convergence analysis is required to ensure that the model converges with increasing numbers of degrees of freedom (DOF). Note that, the number of DOF needs to be sufficiently high for an accurate prediction, on the other hand, the number of DOF also needs to maintain in a level which enables the inverse problem to be solved in a reasonable amount of time.

For the convergence analysis, the original model, developed in Chapter 4, was compared to a variety of refined tongue model with different mesh schemes by calculating the root mean square (RMS) of the nodal positions between the refined and unrefined models, as well as the relative RMS. The former metric quantified the RMS difference in predicted coordinate of the nodes for the given levels of activation, the latter scaled the RMS with respect to the overall deformation . The RMS difference was defined as

$$\mathrm{RMS} = \sqrt{\frac{\sum_{i=1}^{n} \|\mathbf{x}_{\mathrm{Refined},i} - \mathbf{x}_{\mathrm{Unrefined},i}\|^2}{n}} \tag{C.1}$$

where i is the index of the node, n is the number of nodes in the original model ($n = 120$ in the present original model); and $\mathbf{x}_{\text{Refined},i}$ is the position of *i-th* node predicted by the refined mesh, and $\mathbf{x}_{\text{Unrefined},i}$ is the corresponding *i-th* nodal coordinate in the original mesh scheme. The relative RMS normalised the RMS with respect to the overall deformation, it was defined as

$$\text{relative RMS} = \sqrt{\frac{\sum_{i=1}^{n} \|\mathbf{x}_{\text{Refined},i} - \mathbf{x}_{\text{Unrefined},i}\|^2}{\sum_{i=1} n \|\mathbf{x}_{\text{Refined},i} - \mathbf{x}_{\text{reference},i}\|^2}} \tag{C.2}$$

where $\mathbf{x}_{\text{reference},i}$ is the nodal coordinate in the reference state.

Four meshes were compared, including the original model and three models which were refined along the ξ_1, ξ_2 and ξ_3 direction, respectively. For convenience, the three refined models are labelled B, C and D, whilst the unrefined model is labelled as A. Figure C.1 presents the refined models based on the original tongue model. All refined models share the same number of DOF (5400).

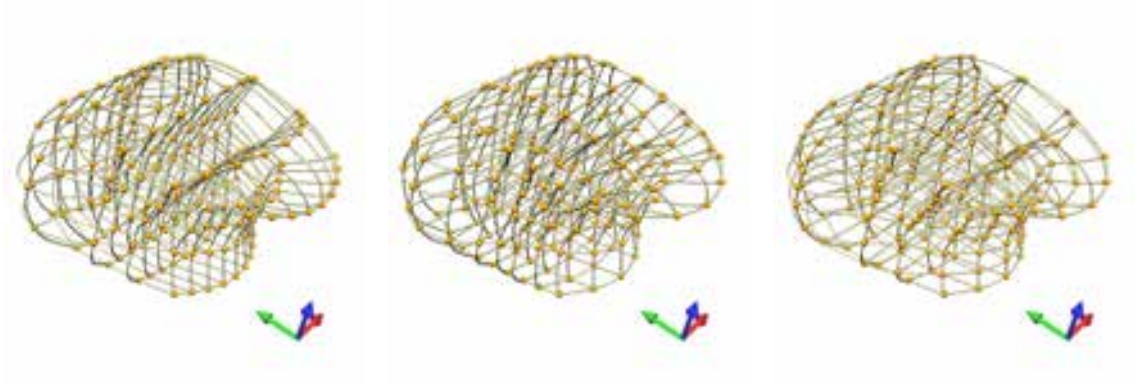

(a) Refining along ξ_1, model B (b) Refining along ξ_2, model C (c) Refining along ξ_3, model D

Figure C.1: The refined tongue models for the convergence analysis

.

Two tongue actions were chosen for comparison reasons, namely, retraction and elongation. Simultaneous contractions of the transversus and styloglossus muscles during retraction are thought to shift the tongue body backwards, while raising the centre dorsum up [Gilbert et al., 2007]. Table C.1 shows the convergence analysis (RMS and relative RMS) comparing the four mesh schemes during retraction when both reached full activation. RMS difference ranged from 0.41 mm to 0.93 mm. However, with respect to the overall deformation, the relative

	Refine ξ_1 (B)	Refine ξ_2 (C)	Refine ξ_3 (D)
RMS	0.41 mm	0.93 mm	0.57 mm
Relative RMS	0.0679	0.1669	0.1017

Table C.1: RMS and relative RMS comparison of different mesh schemes for tongue retraction. Note that each of the refined models had 5400 DOF.

RMS showed showed larger differences ranging from 0.07 to 0.17. The elongation of the tongue body is driven by a co-contraction of the verticalis and transversus muscles. Table C.2 presents the comparison of the four different mesh schemes for tongue elongation when both muscles reached full activation state. Similar to the RMS results presented in the case of tongue retraction, the RMS difference in the elongation varied approximately from 0.46 mm to 0.8 mm, although the relative RMS difference showed a range from 0.11 to 0.18.

	Refine ξ_1 (B)	Refine ξ_2 (C)	Refine ξ_3 (D)
RMS	0.46 mm	0.8 mm	0.5 mm
Relative RMS	0.1116	0.1884	0.1238

Table C.2: RMS and relative RMS comparison of different mesh schemes during tongue elongation. Note that all DOFs of refining ξ_1, ξ_2 and ξ_3 were 5400.

The results from the convergence analysis relied on the mesh schemes (the direction of refinement), as demonstrated in Table C.1 and C.2. In both cases, the range of RMS difference maintained in a similar level that varied from 0.4 mm to 0.9 mm. However, the range of relative RMS difference crossed from 0.06 to 0.19. Recalling the model applications in this thesis, the magnitude of sensor noise of Articulograhy AG500 was about 1.0 mm (Section 2.4); the resolution of MR image in Napadow studies was 1.33 mm $\times$ 1.33 mm (Section 6.1); and the resolution of MR image used in customizing tongue model was 1 mm $\times$ 1 mm (Appendix A). Since the RMS difference showed a range slightly lower than 1 mm, the original model predicated data could sufficiently be used to compare with the data from experiments and literatures, although the comparison of the overall deformation (the relative RMS) showed larger differences. Moreover, the DOFs of the refined models were 5400, implying a longer solution time for a deformed configuration based on given activation levels. The higher DOFs would give rise to serious performance problems in case of an inverse problem analysis. In short, although

the relative RMSs implied that the current model may need to be refined when comparing with high resolution data, the original model is considered a sufficient geometric representation of the actual tongue in terms of computational efficiency and accuracy for the current applications.

Appendix D

Performance testing of the improved inverse problem implementation

In Chapter 4.7, an improved solution procedure was introduced to reduce the computational time for parameter estimation during the inverse problem analysis. The efficiency and robustness of the inverse procedure (parameter estimation) was assessed using a bar model consisting of four groups of fibres. It was expected that the improved solution procedure required less time for the parameter estimation with the same reliability as the conventional solution strategy.

D.1 The bar model

A simple bar model, consisting of four groups of fibres as shown by Figure D.1, was built for testing the efficiency and robustness of the improved solution procedure. The model had a total of 32 tricubic Hermite elements with a total of 81 nodes. Four fibre families were embedded within the model, and arranged parallel with the longest edge of the bar model. Each fibre group occupied a quarter of the model, mainly concentrated near the longest edge of the model and gradually disappearing towards the mid-sagittal and mid-axial planes.

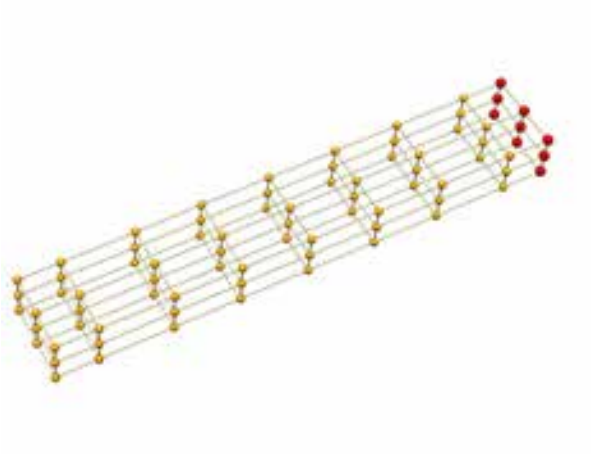

(a) Geometric model

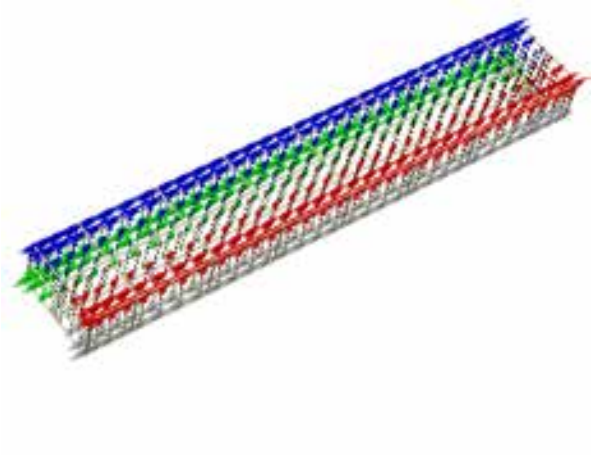

(b) Interior fibrous structure

Figure D.1: The bar model used for testing the optimised inverse procedure. The red nodes in Figure D.1(a) show the fixed nodes. The mirror cones with different colors in Figure D.1(b) show the orientations of the four embedded fibre families and the lengths of the cones indicate the local volume compositions.

.

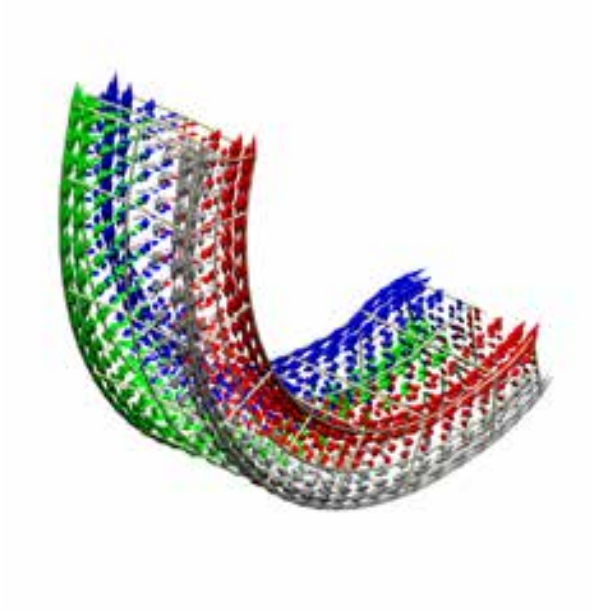

(a)

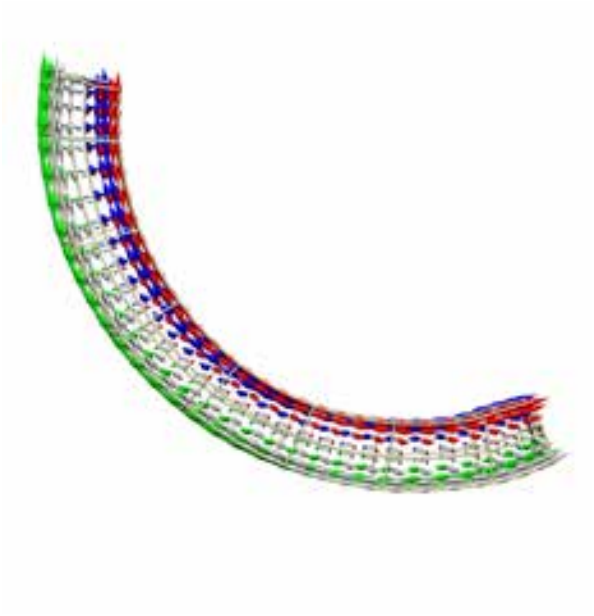

(b)

Figure D.2: The deformed bar model, activated by the red and blue fibre groups simultaneously with the same magnitude. The red, white, blue and green mirror cones present the orientations of the four fibre groups in the deformed configuration.

.

D.2 Problem setting

Two computational experiments using (1) the improved solution procedure (A) and (2) a conventional solution procedure were set up with the bar model for comparison purposes. Both procedures were running on a parallel scheme to evaluate the gradient vector and the Hessian matrix for the inverse parameter estimation. The first and second fibre groups were assumed to be activated, resulting in a 2D parameter space (α_1, α_2). The model deformation state with $(\alpha_1 = 0.4, \alpha_2 = 0.4)$ was chosen as the sample reference configuration.

Procedures A and B were initiated with a set of 9 randomly chosen starting points in the space of (α_1, α_2). The similarity between the model and the reference configuration was evaluated using

$$f(\boldsymbol{\alpha}) = \sum_{i=1}^{n} \parallel \mathbf{x}_{i,\text{model}}(\boldsymbol{\alpha}) - \mathbf{x}_{i,\text{sample}} \parallel, \tag{D.1}$$

where n is the number of nodes (32); and $\mathbf{x}_{i,\text{model}}$ and $\mathbf{x}_{i,\text{sample}}$ are the *i-th* nodes within the model and the given sample reference configuration, respectively. Subsequently, the optimisation problem was formulated as

$$\hat{\boldsymbol{\alpha}} = argmin f(\boldsymbol{\alpha}), \tag{D.2}$$

where $\boldsymbol{\alpha} \in [0,1]^4 = [0,1] \times [0,1] \times [0,1] \times [0,1]$. Both procedures were tested on a standard PC with Intel Xeon E5620 quad core processor. The clock speed of each core was 2.4 GHz with a maximum turbo frequency of 2.66 GHz.

D.3 Results and conclusion

The improved version of the inverse procedure (procedure A) required a total of 75280 seconds of wall clock time for computing the inverse problem with 9 different initial starting points. The average computational time for each starting point was 8364 seconds. The standard version of the inverse procedure (procedure B) required a total of 271600 seconds, with an average computational time of 30177 seconds for each starting point. In short, procedure B required

approximately 3.6 times more computation time compared to procedure A. Both procedures showed the same reliability in their estimated results.

Bibliography

T.L. Allinger, W. Herzog, and M. Epstein. Force-length properties in stable skeletal muscle fibers–theoretical considerations. *Journal of Biomechanics*, 29(9):1235–1240, 1996.

S.M. Altschuler, X. Bao, and R.R. Miselis. Dendritic architecture of hypoglossal motoneurons projecting to extrinsic tongue musculature in the rat. *Journal of Comparative Neurology*, 342(4):538–550, 1994.

M. Aron, E. Kerrien, M. Berger, and Y. Laprie. Coupling electromagnetic sensors and ultrasound images for tongue tracking: acquisition setup and preliminary results. In Hani Camille Yehia ; Didier Demolin ; Rafael Laboissiere, editor, *7th International Seminar on Speech Production - ISSP'06*, Ubatuba, Brésil, 2006. CEFALA - Centro de Estudos da Fala, Acústica, Linguagem e músicA.

P. Badin, G. Bailly, L. Reveret, M. Baciu, C. Segebarth, and C. Savariaux. Three-dimensional linear articulatory modeling of tongue, lips and face, based on MRI and video images. *Journal of Phonetics*, 30(3):533–553, 2002.

T. Baer, P.J. Alfonso, and K. Honda. Electromygraphy of the tongue muscles during vowels in /gpvp/ enviroment. *Annual Bulletin Research Institute of Logopedics and Phoniatrics*, (22): 7–19, 1988.

T. Baer, J.C. Gore, L.C. Gracco, and P.W. Nye. Analysis of vocal tract shape and dimensions using magnetic resonance imaging: Vowels. *Journal of the Acoustical Society of America*, 90(2):799–828, 1991.

E.F. Bailey and R.F. Fregosi. Coordination of intrinsic and extrinsic tongue muscles during spontaneous breathing in the rat. *Journal of Applied Physiology*, 96(2):440–449, 2004.

E.F. Bailey, Y.H. Huang, and R.F. Fregosi. Anatomic consequences of intrinsic tongue muscle activation. *Journal of Applied Physiology*, 101(5):1377–1385, 2006.

R.V. Baratta, M. Solomonow, R. Best, and R. D'Ambrosia. Isotonic length/force models of nine different skeletal muscles. *Medical and Biological Engineering and Computing*, 31(5): 449–458, 1993.

F Barbiera, E Fiorentino, T D'agostino, P Acquaro, L Ferraro, M Parisi, M De Maria, and R Lagalla. Digital cineradiographic swallow study: our experience. *La Radiologia medica*, 104(3):125–133, 2002.

S.S. Blemker and S.L. Delp. Three-dimensional representation of complex muscle architectures and geometries. *Annals of Biomedical Engineering*, 33(5):661–673, 2005.

S.S. Blemker, P.M. Pinsky, and S.L. Delp. A 3D model of muscle reveals the causes of nonuniform strains in the biceps brachii. *Journal of Biomechanics*, 38(4):657–665, 2005.

D.K. Bogen. Strain energy descriptions of biological swelling i: single fluid compartment models. *Journal of Biomechanical Engineering*, 109(3):252–256, 1987.

A. Bothorel, Wioland F. Simon, P., and J.-P. Zerling. *Cineradiographie des voyelles et des consonnes du francais.* Insitut de Phonetique, Universite Marc Bloch, Strasbourg, France, 1986.

C.P. Bradley, A.J. Pullan, and P.J. Hunter. Geometric modeling of the human torso using cubic Hermite elements. *Annals of Biomedical Engineering*, 25(1):96–111, 1997.

E Brandan. Proteoglycans in skeletal muscle. *Brazilian journal of medical and biological research= Revista brasileira de pesquisas medicas e biologicas/Sociedade Brasileira de Biofisica...[et al.]*, 27(9):2109–2116, 1994.

S. Buchaillard, P. Perrier, and Y. Payan. A biomechanical model of cardinal vowel production: Muscle activations and the impact of gravity on tongue positioning. *Journal of the Acoustical Society of America*, 126(4):2033–2051, 2009.

T.J. Burkholder, B. Fingado, S. Baron, and R.L. Lieber. Relationship between muscle fiber types and sizes and muscle architectural properties in the mouse hindlimb. *Journal of Morphology*, 221(2):177–190, 1994.

R.H. Byrd, P. Lu, J. Nocedal, and C. Zhu. A limited memory algorithm for bound constrained optimization. *SIAM Journal on Scientific Computing*, 16(5):1190–1208, 1995.

J. Chen. Food oral processing—a review. *Food Hydrocolloids*, 23(1):1–25, 2009.

C. Cheng, X. Huo, and M. Ghovanloo. Towards a magnetic localization system for 3-d tracking of tongue movements in speech-language therapy. In *Engineering in Medicine and Biology Society, 2009. EMBC 2009. Annual International Conference of the IEEE*, pages 563–566. IEEE, 2009.

C.F. Cheng, C.L. Peng, H.Y. Chiou, and C.Y. Tsai. Dentofacial morphology and tongue function during swallowing. *American Journal of Orthodontics and Dentofacial Orthopedics*, 122(5):491–499, 2002.

L.K. Cheng, G.B. Sands, R.L. French, S.J. Withy, S.P. Wong, M.E. Legget, W.M. Smith, and A.J. Pullan. Rapid construction of a patient-specific torso model from 3d ultrasound for non-invasive imaging of cardiac electrophysiology. *Medical and Biological Engineering and Computing*, 43(3):325–330, 2005.

S. Cheng, SC Gandevia, M. Green, R. Sinkus, and LE Bilston. Viscoelastic properties of the tongue and soft palate using mr elastography. *Journal of Biomechanics*, 44(3):450–454, 2011.

J.H. Clark. A theory of muscle contraction with x-ray diffraction patterns from relaxed and contracted muscles. *American Journal of Physiology–Legacy Content*, 82(1):181–194, 1927.

K.D. Costa, P.J. Hunter, J.M. Rogers, J.M. Guccione, L.K. Waldman, and A.D. Mcculloch. A three-dimensional finite element method for large elastic deformations of ventricular myocardium: I-cylindrical and spherical polar coordinates. *Journal of Biomechanical Engineering*, 118(4):452–463, 1996a.

K.D. Costa, P.J. Hunter, J.M. Rogers, J.M. Guccione, L.K. Waldman, and A.D. Mcculloch. A three-dimensional finite element method for large elastic deformations of ventricular myocardium: Ii-prolate spheroidal coordinates. *Journal of Biomechanical Engineering*, 118(4): 464–472, 1996b.

Jianwu Dang and Kiyoshi Honda. Construction and control of a physiological articulatory model. *The Journal of the Acoustical Society of America*, 115(2):853–870, 2004.

J.H. De Groot and J.L. Van Leeuwen. Evidence for an elastic projection mechanism in the chameleon tongue. *Proceedings of the Royal Society B: Biological Sciences*, 271(1540): 761–770, 2004.

E. Domenech and J. Kelly. Swallowing disorders. *Medical Clinics of North America*, 83(1): 97–113, 1999.

N.J.B. Driessen, C.V.C. Bouten, and F.P.T. Baaijens. A structural constitutive model for collagenous cardiovascular tissues incorporating the angular fiber distribution. *Journal of Biomechanical Engineering*, 127(3):494–503, 2005.

O. Engwall. Combining MRI, EMA and EPG measurements in a three-dimensional tongue model. *Speech Communication*, 41(2):303–329, 2003.

B. Essen, E. Jansson, J. Henriksson, AW Taylor, and B. Saltin. Metabolic characteristics of fibre types in human skeletal muscle. *Acta Physiologica Scandinavica*, 95(2):153–165, 1975.

N. Essen. *Anatomically based modelling of the human masticatory system*. PhD thesis, University of auckland, 2006.

S.M. Felton, T.A. Gaige, T.G. Reese, V.J. Wedeen, and R.J. Gilbert. Mechanical basis for lingual deformation during the propulsive phase of swallowing as determined by phase-contrast magnetic resonance imaging. *Journal of Applied Physiology*, 103(1):255–265, 2007.

J.W. Fernandez and P.J. Hunter. An anatomically based patient-specific finite element model of patella articulation: towards a diagnostic tool. *Biomechanics and Modeling in Mechanobiology*, 4(1):20–38, 2005.

Katrin Fröhlich, Urs Thüer, and Bengt Ingerwall. Pressure from the tongue on the teeth in young adults. *The Angle orthodontist*, 61(1):17–24, 1991.

M. Fujiu, J.A. Logemann, and B.R. Pauloski. Increased postoperative posterior pharyngeal wall movement in patients with anterior oral cancer: preliminary findings and possible implications for treatment. *American Journal of Speech-Language Pathology*, 4(2):24–30, 1995.

Y.C. Fung and S.Q. Liu. Change of residual strains in arteries due to hypertrophy caused by aortic constriction. *Circulation Research*, 65(5):1340–1349, 1989.

A.I. Gafos. *The articulatory basis of locality in phonology*. Routledge, 1999.

H. Gareis, S. Moshe, R. Baratta, R. Best, and R. D'Ambrosia. The isometric length-force models of nine different skeletal muscles. *Journal of Biomechanics*, 25(8):903–916, 1992.

T.C. Gasser, R.W. Ogden, and G.A. Holzapfel. Hyperelastic modelling of arterial layers with distributed collagen fibre orientations. *Journal of the Royal Society Interface*, 3(6):15–35, 2006.

J.M. Gerard, J. Ohayon, V. Luboz, P. Perrier, and Y. Payan. Non-linear elastic properties of the lingual and facial tissues assessed by indentation technique: Application to the biomechanics of speech production. *Medical Engineering & Physics*, 27(10):884–892, 2005.

R.J. Gilbert, L.H. Magnusson, V.J. Napadow, T. Benner, R. Wang, and V.J. Wedeen. Mapping complex myoarchitecture in the bovine tongue with diffusion-spectrum magnetic resonance imaging. *Biophysical Journal*, 91(3):1014–1022, 2006.

R.J. Gilbert, V.J. Napadow, T.A. Gaige, and V.J. Wedeen. Anatomical basis of lingual hydrostatic deformation. *Journal of Experimental Biology*, 210(23):4069–4082, 2007.

J.V. Goozee, B.E. Murdoch, D.G. Theodoros, and P.D. Stokes. Kinematic analysis of tongue movements in dysarthria following traumatic brain injury using electromagnetic articulography. *Brain Injury*, 14(2):153–174, 2000.

J.V. Goozee, L.L. Lapointe, and B.E. Murdoch. Effects of speaking rate on ema-derived lingual kinematics: a preliminary investigation. *Clinical Linguistics &# 38; Phonetics, 17*, 4(5): 375–381, 2003.

D. M. Greig. *Optimisation*. Longman London, 1980.

H. Grey. *Grey's Anatomy*. Churchill livingstone London, 20 edition, 1918.

J. T. Hansen. *Netter's Clinical Anatomy*. Netter Basic Science. Saunders, 2 edition, 2009.

J. Hanson and H.E. Huxley. Structural basis of the cross-striations in muscle. *Nature*, 172 (4377):530–532, 1953.

W.J. Hardcastle, J. Laver, and F.E. Gibbon. *Handbook of Phonetic Science: Part I: Experimental Phonetics*, volume 1. Blackwell, 2 edition, 1999.

I. Hariton, G. DeBotton, T.C. Gasser, and G.A. Holzapfel. Stress-driven collagen fiber remodeling in arterial walls. *Biomechanics and Modeling in Mechanobiology*, 6(3):163–175, 2007.

K. Hashimoto and S. Suga. Estimation of the muscular tensions of the human tongue by using a three-dimensional model of the tongue. *Journal of the Acoustical Society of Japan (E)*, 7 (1):39–46, 1986.

K. Hayashi, M. Sato, H. Handa, and K. Moritake. Biomechanical study of the constitutive laws of vascular walls. *Experimental Mechanics*, 14(11):440–444, 1974.

C.M. He and M.R. Roach. The composition and mechanical properties of abdominal aortic aneurysms. *Journal of Vascular Surgery*, 20(1):6–13, 1994.

K. Hiiemae. Mechanisms of food reduction, transport and deglutition: how the texture of food affects feeding behavior. *Journal of Texture Studies*, 35(2):171–200, 2004.

K.M. Hiiemae and J.B. Palmer. Tongue movements in feeding and speech. *Critical Reviews in Oral Biology & Medicine*, 14(6):413–429, 2003.

A.V. Hill. The heat of shortening and the dynamic constants of muscle. *Proceedings of the Royal Society of London. Series B, Biological Sciences*, 126(843):136–195, 1938.

T.J. Hill, H.J. Field, and W.A. Blyth. Acute and recurrent infection with herpes simplex virus in the mouse: a model for studying latency and recurrent disease. *The Journal of General Virology*, 28(3):341–353, 1975.

G.A. Holzapfel. *Nonlinear Solid Mechanics*, volume 160 of *Solid Mechanics and its Applications*. John Wiley & Sons, 2000a.

G.A. Holzapfel. *Nonlinear Solid Mechanics: A Continuum Approach for Engineering Science*. Springer, 2002.

G.A. Holzapfel and R.W. Ogden. Constitutive modelling of passive myocardium: a structurally based framework for material characterization. *Philosophical Transactions of the Royal Society A: Mathematical, Physical and Engineering Sciences*, 367(1902):3445–3475, 2009.

G.A. Holzapfel, T.C. Gasser, and R.W. Ogden. A new constitutive framework for arterial wall mechanics and a comparative study of material models. *Journal of Elasticity*, 61(1):1–48, 2000b.

J.M. Hombert, J.J. Ohala, and W.G. Ewan. Phonetic explanations for the development of tones. *Language*, 55(1):37–58, 1979.

H. Honda, K.and Miyaka and P. Alfonsao. Electromygraphy of the tongue muscles during vowels in /gpvp/ enviroment. *Annual Bulletin Research Institute of Logopedics and Phoniatrics*, (17):13–22, 1983.

K. Honda. Organization of tongue articulation for vowels. *Journal of Phonetics*, 24(1):39–52, 1996.

K. Honda, T. Kitamura, H. Takemoto, S. Adachi, P. Mokhtari, S. Takano, Y. Nota, H. Hirata, I. Fujimoto, Y. Shimada, S. Masaki, S. Fujita, and J. Dang. Visualisation of hypopharyngeal cavities and vocal-tract acoustic modelling. *Computer Methods in Biomechanics and Biomedical Engineering*, 13(4):443–53, 2010.

K. Hori, T. Ono, and T. Nokubi. Coordination of tongue pressure and jaw movement in mastication. *Journal of Dental Research*, 85(2):187–191, 2006.

C.W. Howden. Management of acid-related disorders in patients with dysphagia. *American Journal of Medicine Supplement*, 117(5):44–48, 2004.

A.W. Hrycyshyn and J.V. Basmajian. Electromyography of the oral stage of swallowing in man. *American Journal of Anatomy*, 133(3):333–340, 1972.

T.JR. Hughes. *The finite element method: linear static and dynamic finite element analysis*. Dover Publications, 2000.

P.A. Huijing. Muscle as a collagen fiber reinforced composite: a review of force transmission in muscle and whole limb. *Journal of Biomechanics*, 32(4):329–345, 1999.

P.J. Hunter, M.P. Nash, and G.B. Sands. Computational electromechanics of the heart. *Computational Biology of the Heart*, 12:345–407, 1997.

A.F. Huxley and R.M. Simmons. Proposed mechanism of force generation in striated muscle. *Nature*, 233:533–538, 1971.

A.F. Huxley et al. Muscle structure and theories of contraction. *Progress in Biophysics and Biophysical Chemistry*, 7:255–318, 1957.

A. Ibrahimbegović. *Nonlinear solid mechanics: theoretical formulations and finite element solution methods*, volume 160. Springer Verlag, 2009.

K. Ito and S.S. Ravindran. A reduced-order method for simulation and control of fluid flows. *Journal of Computational Physics*, 143(2):403 – 425, 1998.

M. Itoh, S. Sasanuma, H. Hirose, and H. YoshiokaTatsujiro. Abnormal articulatory dynamics in a patient with apraxia of speech: X-ray microbeam observation. *Brain and Language*, 11 (1):66–75, 1980.

Samah Jafari, Rebecca A Prince, Daniel Y Kim, and David Paydarfar. Sensory regulation of swallowing and airway protection: a role for the internal superior laryngeal nerve in humans. *The Journal of physiology*, 550(1):287–304, 2003.

C.D. Jennifer, B. Mikoto, and D. SC. Evaluation and treatment of swallowing impairments. *American Family Physician*, 61(8):2453–2462, 2000.

J. Jiang, A. Alwan, P.A. Keating, E.T. Auer, and L.E. Bernstein. On the relationship between face movements, tongue movements, and speech acoustics. *EURASIP Journal on Applied Signal Processing*, 2002(11):1174–1188, 2002.

G.M. Johnson, M. Zhang, and D.G. Jones. The fine connective tissue architecture of the human ligamentum nuchae. *Spine*, 25(1):5–9, 2000.

T. Kaburagi, K. Wakamiya, and M. Honda. Three-dimensional electromagnetic articulography: A measurement principle. *Journal of the Acoustical Society of America*, 118(1):428–443, 2005.

K. Kairaitis. Is the pharynx a muscular hydrostat? *Medical Hypotheses*, 74(3):590–595, 2010.

Y. Kakita and O. Fujimura. Computational model of the tongue: A revised version. *Journal of the Acoustical Society of America*, 62(A):S15, 1977.

I. Kaneko. A cinefluorographic study of hyoid bone movement during deglutition. *Journal of the Oto Rhino Laryngological Society of Japan*, 95(7):974–987, 1992.

D.C. Kanner. Sensor placement for on-orbit modal identification and correlation of large space structures. In *American Control Conference*, pages 2984–2990. IEEE, 1991.

D. Karlsson and R. Tranberg. On skin movement artefact-resonant frequencies of skin markers attached to the leg. *Human Movement Science*, 18(5):627–635, 1999.

W.F. Katz, S.V. Bharadwaj, and B. Carstens. Electromagnetic articulography treatment for an adult with Broca's aphasia and apraxia of speech. *Journal of Speech, Language, and Hearing Research*, 42(6):1355–1366, 1999. ISSN 1092-4388.

M. Kayalioglu, V. Shcherbatyy, A. Seifi, and Z.J. Liu. Roles of intrinsic and extrinsic tongue muscles in feeding: electromyographic study in pigs. *Archives of Oral Biology*, 52(8):786–796, 2007a.

M. Kayalioglu, V. Shcherbatyy, A. Seifi, and Z.J. Liu. Roles of intrinsic and extrinsic tongue muscles in feeding: electromyographic study in pigs. *Archives of Oral Biology*, 52(8):786–796, 2007b.

D. Kennedy, J. Kieser, C. Bolter, M. Swain, B. Singh, and J.N. Waddell. Tongue pressure patterns during water swallowing. *Dysphagia*, 25(1):11–19, 2010.

R.D. Kent. Some considerations in the cinefluorographic analysis of tongue movements during speech. *Phonetica*, 26(1):16–32, 1972.

R.D. Kent and K.L. Moll. Cinefluorographic analyses of selected lingual consonants. *Journal of Speech & Hearing Research*, 15(3):453–473, 1972.

W.M. Kier. The arrangement and function of molluscan muscle. *The Mollusca, Form and Function*, 11(21):211–252, 1988.

W.M. Kier and K.K. Smith. Tongues, tentacles and trunks: the biomechanics of movement in muscular-hydrostats. *Zoological Journal of the Linnean Society*, 83(4):307–324, 1985.

J. Kieser, B. Singh, M. Swain, I. Ichim, J.N. Waddell, D. Kennedy, K. Foster, and V. Livingstone. Measuring intraoral pressure: adaptation of a dental appliance allows measurement during function. *Dysphagia*, 23(3):237–243, 2008.

Y.S. Kim, Z.S. Galis, A. Rachev, H.C. Han, and R.P. Vito. Matrix metalloproteinase-2 and-9 are associated with high stresses predicted using a nonlinear heterogeneous model of arteries. *Journal of Biomechanical Engineering*, 131(1):011009–1–011009–10, 2009.

H. Kolsky. *Stress waves in solids*. Dover Publications, 1963.

C. Kroos. Evaluation of the measurement precision in three-dimensional Electromagnetic Articulography (Carstens AG500). *Journal of Phonetics*, 40(3):453–465, 2012.

Y. Lanir. Constitutive equations for the lung tissue. *Journal of Biomechanical Engineering*, 105(4):374–380, 1983.

S. Lee, E. Bresch, and S. Narayanan. An exploratory study of emotional speech production using functional data analysis techniques. In *Proceedings of 7th International Seminar On Speech Production, Ubatuba, Brazil*, pages 525–532. Citeseer, 2006.

J. Lexell, K. Henriksson-Larsén, B. Winblad, and M. Sjöström. Distribution of different fiber types in human skeletal muscles: effects of aging studied in whole muscle cross sections. *Muscle & Nerve*, 6(8):588–595, 1983.

A. Li, Q. Fang, F. Hu, L. Zheng, H. Wang, and J. Dang. Acoustic and articulatory analysis on mandarin chinese vowels in emotional speech. In *7th International Symposium on Chinese Spoken Language Processing (ISCSLP)*, pages 38–43. IEEE, 2010.

R.L. Lieber. Skeletal muscle adaptability. I: review of basic properties. *Developmental Medicine and Child Neurology*, 28(3):390–397, 1986.

B. Lindblom and I. Maddieson. Phonetic universals in consonant systems. *Language, Speech, and Mind*, pages 62–78, 1988.

B. Lindblom, H.M. Sussman, G. Modarresi, and E. Burlingame. The trough effect: implications for speech motor programming. *Phonetica*, 59(4):245–262, 2002.

B.E.F. Lindblom and J.E.F. Sundberg. Acoustical consequences of lip, tongue, jaw, and larynx movement. *Journal of the Acoustical Society of America*, 50(4B):1166–1179, 1971.

Z.J. Liu, M. Kayalioglu, V. Shcherbatyy, and A. Seifi. Tongue deformation, jaw movement and muscle activity during mastication in pigs. *Archives of Oral Biology*, 52(4):309–312, 2007.

D.G. Lloyd and T.F. Besier. An emg-driven musculoskeletal model to estimate muscle forces and knee joint moments in vivo. *Journal of Biomechanics*, 36(6):765–776, 2003.

P.W. Lucas, J.F. Prinz, K.R. Agrawal, and I.C. Bruce. Food physics and oral physiology. *Food Quality and Preference*, 13(4):203–213, 2002.

S. Maeda. Compensatory articulation during speech: Evidence from the analysis and synthesis of vocal tract shapes using an articulatory model. *Speech Production and Speech Modelling*, pages 131–149, 1990.

Shinji Maeda and Kiyoshi Honda. From emg to formant patterns of vowels: The implication of vowel spaces. *Phonetica*, 51(1-3):17–29, 1994.

A. Malhotra, Y. Huang, R.B. Fogel, G. Pilar, J.K. Edwards, R. Kikinis, S.H. Loring, and D.P. White. The male predisposition to pharyngeal collapse importance of airway length. *American Journal of Respiratory and Critical Care Medicine*, 166(10):1388–1395, 2002.

S.F. Mason. *A History of the Sciences*. Collier Books New York, 1962.

A. Mauro. Satellite cell of skeletal muscle fibers. *The Journal of Biophysical and Biochemical Cytology*, 9(2):493–495, 1961.

K. Meijer, H.J. Grootenboer, H. Koopman, B. Van der Linden, and P.A. Huijing. A hill type model of rat medial gastrocnemius muscle that accounts for shortening history effects. *Journal of Biomechanics*, 31(6):555–563, 1998.

A. Menzel. Modelling of anisotropic growth in biological tissues. *Biomechanics and Modeling in Mechanobiology*, 3(3):147–171, 2005. ISSN 1617-7959.

N. Metropolis and S. Ulam. The monte carlo method. *Journal of the American Statistical Association*, 44(247):335–341, 1949.

K. Miyawaki, H. Hirose, T. Ushijima, and M. Sawashima. A preliminary report on the electromyographic study of the activity of lingual muscles. *Annual Bulletin. Research Institute of Logopedics and Phoniatrics*, 9(91):406–106, 1975.

J.J. Moré and D.C. Sorensen. Computing a trust region step. *SIAM Journal on Scientific and Statistical Computing*, 4(3):553–572, 1983.

L. Mu and I. Sanders. Neuromuscular organization of the canine tongue. *The Anatomical Record*, 256(4):412–424, 1999.

A.R. Muir, A.H. Kanji, and D. Allbrook. The structure of the satellite cells in skeletal muscle. *Journal of Anatomy*, 99(3):435–444, 1965.

B.E. Murdoch and J.V. Goozée. Ema analysis of tongue function in children with dysarthria following traumatic brain injury. *Brain Injury*, 17(1):79–93, 2003.

W.M. Murray, T.S. Buchanan, and S.L. Delp. The isometric functional capacity of muscles that cross the elbow. *Journal of Biomechanics*, 33(8):943–952, 2000.

V.J. Napadow, Q. Chen, V.J. Wedeen, and R.J. Gilbert. Intramural mechanics of the human tongue in association with physiological deformations. *Journal of Biomechanics*, 32(1):1–12, 1999a.

V.J. Napadow, Q. Chen, V.J. Wedeen, and R.J. Gilbert. Biomechanical basis for lingual muscular deformation during swallowing. *American Journal of Physiology- Gastrointestinal and Liver Physiology*, 277(3):695–701, 1999b.

V.J. Napadow, R.D. Kamm, and R.J. Gilbert. A biomechanical model of sagittal tongue bending. *Journal of Biomechanical Engineering*, 124(5):547–556, 2002.

S. Narayanan, K. Nayak, S. Lee, A. Sethy, and D. Byrd. An approach to real-time magnetic resonance imaging for speech production. *The Journal of the Acoustical Society of America*, 115(4):1771–1776, 2004.

S.S. Narayanan, A.A. Alwan, and K. Haker. Toward articulatory-acoustic models for liquid approximants based on MRI and EPG data. Part I. The laterals. *The Journal of the Acoustical Society of America*, 101(2):1064, 1997.

M.P. Nash. *Mechanics and material properties of the heart using an anatomically accurate mathematical model*. PhD thesis, Department of Engineering Science, University of Auckland, 1998.

M.P. Nash and P.J. Hunter. Computational mechanics of the heart. *Journal of Elasticity*, 61(1): 113–141, 2000.

D.M. Needham and D.M. Needham. *Machina carnis: the biochemistry of muscular contraction in its historical development*. Cambridge University Press, 1971.

M.A. Nicosia and J.A. Robbins. The fluid mechanics of bolus ejection from the oral cavity. *Journal of Biomechanics*, 34(12):1537–1544, 2001.

R.W. Ogden. *Non-linear Elastic Deformations*. Dover Publication, 1997.

J.R. O'Kusky and M.G. Norman. Sudden infant death syndrome: increased number of synapses in the hypoglossal nucleus. *Journal of Neuropathology & Experimental Neurology*, 54(5): 627–634, 1995.

A. Oliven, M. Odeh, L. Geitini, R. Oliven, U. Steinfeld, A.R. Schwartz, and N. Tov. Effect of coactivation of tongue protrusor and retractor muscles on pharyngeal lumen and airflow in sleep apnea patients. *Journal of Applied Physiology*, 103(5):1662–1668, 2007.

D. Ong and M. Stone. Three-dimensional vocal tract shapes in/r/and/l: A study of mri, ultrasound, electropalatography, and acoustics. *Phonoscope*, 1(1):1–13, 1998.

T. Ono, K. Hori, and T. Nokubi. Pattern of tongue pressure on hard palate during swallowing. *Dysphagia*, 19(4):259–264, 2004.

E. Otten. Optimal design of vertebrate and insect sarcomeres. *Journal of Morphology*, 191(1): 49–62, 1987.

E.K. Pae and A.A. Lowe. Tongue shape in obstructive sleep apnea patients. *The Angle Orthodontist*, 69(2):147–150, 1999.

C. Papadimitriou, J.L. Beck, and S.K. Au. Entropy-based optimal sensor location for structural model updating. *Journal of Vibration and Control*, 6(5):781–800, 2000.

V. Parthasarathy, J.L. Prince, M. Stone, E.Z. Murano, and M. NessAiver. Measuring tongue motion from tagged cine-mri using harmonic phase (harp) processing. *The Journal of the Acoustical Society of America*, 121(1):491–504, 2007.

Y. Payan and P. Perrier. Synthesis of VV sequences with a 2D biomechanical tongue model controlled by the Equilibrium Point Hypothesis* 1. *Speech Communication*, 22(2):185–205, 1997.

Y. Payan, P. Perrier, and R. Laboissiere. Simulation of tongue shape variations in the sagittal plane based on a control by the equilibrium-point hypothesis. volume 2 of *In Proceeding on International Congress of Phonetic Sciences*, pages 474–477. Stockholm Sweden, 1995.

J-P. V. Pelteret and B. D. Reddy. Computational model of soft tissues in the human upper airway. *International Journal for Numerical Methods in Biomedical Engineering*, 28(1): 111–132, 2012.

C.L. Peng, P.G. Jost-Brinkmann, R.R. Miethke, and C.T. Lin. Ultrasonographic measurement of tongue movement during swallowing. *Journal of Ultrasound in Medicine*, 19(1):15, 2000.

J. Perkell. *A physiologically- oriented model of tongue activity in speech production*. Unpublished doctoral dissertation, Department of Electrical Engineering, MIT., 1974.

J. S. Perkell. *Physiology of speech production: results and implication of a quantitative cineradiographic study*. Combridege, Massachusetts: MIT Press, 1969.

D. Pette and R.S. Staron. Myosin isoforms, muscle fiber types, and transitions. *Microscopy Research and Technique*, 50(6):500–509, 2000.

W.R. Proffit, H.W. Fields, and D.M. Sarver. *Contemporary Orthodontics*. Mosby Inc, 2007.

C. Prudhomme, D.V. Rovas, K. Veroy, L. Machiels, Y. Maday, A.T. Patera, and G. Turinici. Reliable real-time solution of parametrized partial differential equations: Reduced-basis output

bound methods: Special section on quantifying uncertainty in cfd. *Journal of Fluids Engineering*, 124(1):70–80, 2002.

W. Pytlik. Abnormal tongue position in swallowing as a cause of ankylosis and abnormal tooth eruption. *Fortschritte Der Kieferorthopadie*, 43(5):380–393, 1982.

J.Y. Rho, M.E. Roy II, T.Y. Tsui, and G.M. Pharr. Elastic properties of microstructural components of human bone tissue as measured by nanoindentation. *Journal of Biomedical Materials Research*, 45(1):48–54, 1999.

O. Röhrle and A.J. Pullan. Three-dimensional finite element modelling of muscle forces during mastication. *Journal of Biomechanics*, 40(15):3363–3372, 2007.

O. Röhrle, J.N. Waddell, K.D. Foster, H. Saini, and A.J. Pullan. Using a motion-capture system to record dynamic articulation for application in cad/cam software. *Journal of Prosthodontics*, 18(8):703–710, 2009.

R.Y. Rubinstein and D.P. Kroese. *Simulation and the Monte Carlo method*, volume 707. Wiley-interscience, 2007.

H. Saini, J.N. Wadell, A.J. Pullan, and O. Röhrle. Automatically generating subject-specific functional tooth surfaces using virtual mastication. *Annals of Biomedical Engineering*, 37 (8):1646–1653, 2009.

H. Saito and I. Itoh. Three-dimensional architecture of the intrinsic tongue muscles, particularly the longitudinal muscle, by the chemical-maceration method. *Anatomical Science International*, 78(3):168–176, 2003.

V. Sanguineti, R. Laboissiere, and Y. Payan. A control model of human tongue movements in speech. *Biological Cybernetics*, 77(1):11–22, 1997.

S. Schiaffino, L. Gorza, S. Sartore, L. Saggin, S. Ausoni, M. Vianello, K. Gundersen, and T. LØmo. Three myosin heavy chain isoforms in type 2 skeletal muscle fibres. *Journal of Muscle Research and Cell Motility*, 10(3):197–205, 1989.

S. Schmitt and M. Günther. Human leg impact: energy dissipation of wobbling masses. *Archive of Applied Mechanics*, 81(7):887–897, 2011.

M.F. Schneider. Control of calcium release in functioning skeletal muscle fibers. *Annual Review of Physiology*, 56(1):463–484, 1994.

T.H. Shawker, B.C. Sonies, and M. Stone. Soft tissue anatomy of the tongue and floor of the mouth: an ultrasound demonstration. *Brain and Language*, 21(2):335–350, 1984.

D.U. Silverthorn. *Human physiology*, volume 67 of *Recherche*. 2 edition, 2009.

K.K. Smith and W.M. Kier. Trunks, tongues, and tentacles: moving with skeletons of muscle. *American Scientist*, 77(1):28–35, 1989.

B.C. Sonies, T.H. Shawker, T.E. Hall, L.H. Gerber, and S.B. Leighton. Ultrasonic visualization of tongue motion during speech. *The Journal of the Acoustical Society of America*, 70(3): 683–686, 1981.

B.C. Sonies, B.J. Baum, and T.H. Shawker. Tongue motion in elderly adults: initial in situ observations. *Journal of Gerontology*, 39(3):279–283, 1984.

A.J.M. Spencer. *Deformations of fibre-reinforced materials*. Oxford, 1972.

V. Spitzer, M.J. Ackerman, A.L. Scherzinger, and D. Whitlock. The visible human male: a technical report. *Journal of the American Medical Informatics Association*, 3(2):118–130, 1996.

P. Stål, S. Marklund, L.E. Thornell, R. De Paul, and P.O. Eriksson. Fibre composition of human intrinsic tongue muscles. *Cells Tissues Organs*, 173(3):147–161, 2003.

I. Stavness, J. E Lloyd, Y. Payan, and S. Fels. Coupled hard–soft tissue simulation with contact and constraints applied to jaw–tongue–hyoid dynamics. *International Journal for Numerical Methods in Biomedical Engineering*, 27(3):367–390, 2011.

J.R. Steedle and W.R. Proffit. The pattern and control of eruptive tooth movements. *American Journal of Orthodontics*, 87(1):56–66, 1985.

C.M. Steele and P. Van Lieshout. An ultrasound examination of tongue movement during swallowing. *Dysphagia*, 1(2):78–83, 1986.

C.M. Steele and P. van Lieshout. Use of electromagnetic midsagittal articulography in the study of swallowing. *Journal of Speech, Language, and Hearing Research*, 47(2):342–352, 2004.

C.M. Steele and P. Van Lieshout. The dynamics of lingual-mandibular coordination during liquid swallowing. *Dysphagia*, 23(1):33–46, 2008.

C.M. Steele and P. Van Lieshout. Tongue movements during water swallowing in healthy young and older adults. *Journal of Speech, Language and Hearing Research*, 52(5):1255–1267, 2009.

K.N. Stevens. *Acoustic Phonetics*, volume 30. The MIT press, 2000.

M. Stone. A three-dimensional model of tongue movement based on ultrasound and x-ray microbeam data. *The Journal of the Acoustical Society of America*, 87(5):2207–2217, 1990.

M. Stone. A guide to analysing tongue motion from ultrasound images. *Clinical Linguistics & Phonetics*, 19(6):455–501, 2005.

M. Stone and T.H. Shawker. An ultrasound examination of tongue movement during swallowing. *Dysphagia*, 1(2):78–83, 1986.

M. Stone, E. P. Davis, A. S. Douglas, M. NessAiver, R. Gullapalli, W. S. Levine, and A. Lundberg. Modeling the motion of the internal tongue from tagged cine-MRI images. *The Journal of the Acoustical Society of America*, 109(6):2974–2982, 2001.

M. Stone, M.A. Epstein, and K. Iskarous. Functional segments in tongue movement. *Clinical Linguistics & Phonetics*, 18(6):507–521, 2004.

L.N.S.A. Struijk. An inductive tongue computer interface for control of computers and assistive devices. *IEEE Transactions on Biomedical Engineering*, 53(12):2594–2597, 2006.

S. Takano and K. Honda. An MRI analysis of the extrinsic tongue muscles during vowel production. *Speech Communication*, 49(1):49–58, 2007.

H. Takemoto. Morphological analyses of the human tongue musculature for three-dimensional modeling. *Journal of Speech, Language, and Hearing Research*, 44(1):95–107, 2001.

G.A. Thibodeau and K. T. Patton. *Anatomy & Physiology*. Mosby Elsevier, 2003.

J.T. Thompson, A.D. Lowe, and W.M. Kier. The columellar muscle of prosobranch gastropods: morphological zonation and its functional implications. *Invertebrate Biology*, 117(1):45–56, 1998.

I.R. Titze. Mechanical stress in phonation. *Journal of Voice*, 8(2):99–105, 1994.

D. Trivedi, C.D. Rahn, W.M. Kier, and I.D. Walker. Soft robotics: Biological inspiration, state of the art, and future research. *Applied Bionics and Biomechanics*, 5(3):99–117, 2008.

D. Ucinski. Optimal sensor location for parameter estimation of distributed processes. *International Journal of Control*, 73(13):1235–1248, 2000.

M. Van Loocke, C.G. Lyons, and C.K. Simms. Viscoelastic properties of passive skeletal muscle in compression: Stress-relaxation behaviour and constitutive modelling. *Journal of Biomechanics*, 41(7):1555–1566, 2008.

M.A. Volonte, M. Porta, and G. Comi. Clinical assessment of dysphagia in early phases of parkinson's disease. *Neurological Sciences*, 23(2):121–122, 2002.

I.D. Walker, D.M. Dawson, T. Flash, F. Grasso, R. Hanlon, B. Hochner, W.M. Kier, C. Pagano, C.D. Rahn, and Q. Zhang. Continuum robot arms inspired by cephalopods. In *Proceedings of the SPIE Conference Unmanned Ground Vehicle Technology IV*, pages 303–314, 2005.

Y.K. Wang, M. P. Nash, A. J. Pullan, J. A. Kieser, and O. Röhrle. Model-based identification of motion sensor placement for tracking retraction and elongation of the tongue. *Biomechanics and Modeling in Mechanobiology*, 12(2):383–399, 2013.

C.I. Watson, C.W. Thorpe, and X.B. Lu. A comparison of two techniques that measure vocal tract shape. *Acoustics Australia*, 37(1):7–11, 2009.

W. Weber and R. W. Henry. Sheet plastination of body slices-e12 technique, filling method. *Journal of the International Society for Plastination*, 7(1):16–22, 1993.

V.J. Wedeen, T.G. Reese, V.J. Napadow, and R.J. Gilbert. Demonstration of primary and secondary muscle fiber architecture of the bovine tongue by diffusion tensor magnetic resonance imaging. *Biophysical journal*, 80(2):1024–1028, 2001.

R. Wilhelms-Tricarico. Physiological modeling of speech production: Methods for modeling soft-tissue articulators. *The Journal of the Acoustical Society of America*, 97(5):3085–3098, 1995.

R. Wilhelms-Tricarico. Geometric representation of a human tongue for computational biomechanical modeling. 2005. Retrieved June 2010, `http://webpages.charter.net/reinerwt/JSHLRmanuscript.pdf`.

W. Woźniak and P.A. Young. Further observations on human hypoglossal nerve. *Anatomischer Anzeiger*, 125(2):203–205, 1969.

P. Wriggers. *Computational contact mechanics*. Springer, 2006.

K. Yabunaka, H. Sanada, S. Sanada, H. Konishi, T. Hashimoto, H. Yatake, K. Yamamoto, T. Katsuda, and M. Ohue. Sonographic assessment of hyoid bone movement during swallowing: a study of normal adults with advancing age. *Radiological Physics and Technology*, 4(1):73–77, 2011.

Masaki Yanagishita. Function of proteoglycans in the extracellular matrix. *Pathology International*, 43(6):283–293, 1993.

Y. Yuan. A review of trust region algorithms for optimization. In *Proceedings of the Fourth International Congress on Industrial and Applied Mathematics*, pages 271–282. Oxford University Press, 2000.

Y. Yunusova, J.R. Green, and A. Mefferd. Accuracy assessment for AG500, electromagnetic articulograph. *Journal of Speech, Language, and Hearing Research*, 52(2):547–555, 2009.

Faisal N Zaidi, Paul Meadows, Ofer Jacobowitz, and Terence M Davidson. Tongue anatomy and physiology, the scientific basis for a novel targeted neurostimulation system designed for the treatment of obstructive sleep apnea. *Neuromodulation: Technology at the Neural Interface*, 16(4):376–386, 2013.

F.E. Zajac. Muscle and tendon: properties, models, scaling, and application to biomechanics and motor control. *Critical Reviews in Biomedical Engineering*, 17(4):359–410, 1989.

X. Zhong, F.H. Epstein, B.S. Spottiswoode, P.A. Helm, and S.S. Blemker. Imaging two-dimensional displacements and strains in skeletal muscle during joint motion by cine DENSE MR. *Journal of Biomechanics*, 41(3):532–540, 2008.

C. Zhu, R.H. Byrd, P. Lu, and J. Nocedal. Algorithm 778: L-bfgs-b: Fortran subroutines for large-scale bound-constrained optimization. *ACM Transactions on Mathematical Software (TOMS)*, 23(4):550–560, 1997.

P.K. Zysset, X. Edward Guo, C. Edward Hoffler, K.E. Moore, and S.A. Goldstein. Elastic modulus and hardness of cortical and trabecular bone lamellae measured by nanoindentation in the human femur. *Journal of Biomechanics*, 32(10):1005–1012, 1999.